Luminosity Functions using New Radio Surveys

Josephine Peters

Worcester College

University of Oxford

A thesis submitted for the degree of

Doctor of Philosophy

Trinity 2019

Abstract

Galaxy evolution at radio wavelengths is often measured using luminosity functions which are commonly based on the luminosity (L) and redshift (z) of individual sources as well as the overall distribution for a sample. However, an important factor when K-correcting radio sources to their rest-frame luminosity is the spectral index (α). This is often assumed to be a constant value for the entire sample. In reality, there is a distribution in α which affects the rate at which sources drop below the flux limit of the survey. If not accounted for, the differing rates at which sources become unobservable can be mistaken as a genuine decline in source numbers and affect the evolution of the radio luminosity function (RLF).

To tackle this, I estimate RLFs incorporating the α-distribution for both active galactic nuclei (AGN) and star forming galaxies (SFGs). Data from the Low-Frequency Array (LOFAR) and the Very Large Array (VLA) are used to formulate 150 MHz RLFs for a sample of AGN. MeerKAT and VLA data are used to measure and model the 1.4 GHz RLFs for a sample of SFGs. Markov Chain Monte Carlo sampling is used to find parameters to fit models based on ρ(L,z) and ρ(L,z,α) for comparison.

The main findings of this work are that the accurate modelling of the α-distribution has a significant effect on not only the shape of the RLF, but the value of the evolution parameter k, parameterised as $(1+z)^k$ in pure evolution and pure density evolution. This is true for both AGN and SFGs.

The AGN RLF model has higher values of k when accounting for the α-distribution. Steep spectrum sources drop out of the flux limit of a survey earlier and therefore drive the RLF to evolve faster.

The SFG RLF model has lower values of k when α is accounted for, since high values of k are found to compensate for the absence of α information. Since the aim of RLFs is to measure the evolution of galaxies, it is imperative that the α-distribution be included to obtain accurate estimates of the strength of any evolution.

Future work would aim to improve on this further through including another factor that affects the visibility of a source; the angular or projected linear size of the source. In this thesis, observations of the same field but using different antenna configurations have shown that high-resolution, long baseline imaging needs to be supplemented with short baseline observations to fully capture all scales of emission and all sources. Therefore, a radio telescope with an abundance of both short and long baselines is necessary. MeerKAT is such a telescope, as will be the SKA. Therefore, my work has set out the way forward for towards properly understanding the evolution of radio sources in the Universe.

Statement of Originality

This is to certify that the thesis has been written by myself, and that all intellectual content within this thesis is my own, unless explicitly stated otherwise.

The work in this thesis has not been submitted for a degree to any other university, institution or professional body.

This work is the intellectual property of the author.

Acknowledgements

First and foremost, a giant thank you to my supervisor Matt Jarvis. Thank you first of all for agreeing to take me on, even though I was already mid-way into my DPhil. I don't know what I would have done otherwise and I am immensely grateful that you took that risk. I have always enjoyed our meetings and it has been a pleasure being supervised by you. Thank you for all of the knowledge you have imparted, invaluable advice, as well as trips to The Fishes and coming to see some improv! (I will always remember that the best activity to do in Derby is "nothing").

Another huge thank you goes to Ian Heywood. Your radio know-how surely makes you the Chief Wizard of Interferometry. Thank you for all the time you have spent with me at my desk, grappling with dodgy PSFs and trying to find a decent spot of wifi. I am sure my images would look like garbage without you. Pub trips and seeing you in the Wheatsheaf audience for some Monday-night improv has also been fun.

A big woop woop to my best astro-buddies; Jaz, Laura and James. You made me feel at home in the department, our numerous tea and coffee breaks have been my favourite parts of the day. Dear Laura, it was such a joy to be desk-mates with you. You are a wonderful friend and I miss laughing and talking with you so often since you left for the States. Jaz my creative pal, our drawing/origami sessions accompanied with endless teapots of Rooibos are something we have to keep up! You are going to kick-ass in your new job and end up saving the world some day. I'm so pleased we made this astro-journey together through all the ups and downs of DPhil life. Thank you James for many pub trips and laughs at coffee. And thank you all three of you for your support in coming to see me improvise, it makes such a difference to see your faces and hear your suggestions (- Is, ... is there a theme here?).

An extra shout-out to Ed, Verity, Dawn, Lydia, Archie and Chloe. I may have partied, giggled and chatted with you for hundreds of hours. Ed, Verity and Dawn I value your abilities to turn any situation into a volcano of fun, joy, hilarity and expression. You three hold a special place in my heart. Archie, our Mighty Boosh sessions and impersonations in coffee shops while we work has been an utter delight. Cracking up at doing silly voices and characters has made me smile and cackle. Lydia, we have had so many conversations going through our DPhils together! It has been

so good to put the world to rights with you. Chloe, I love our Harry Potter film times and the loveliness that is getting to know you that comes with them, you are a truly wise (and fantastically funny) person.

Can I get a "woop woop", can I get a "hell yeah" for my longest surviving housemate, Frankie. The biggest part of making our little house a home is sharing it with you. I am so pleased that our friendship has grown. You are a fantastic human being. I love our chats and the silly things we laugh about. I have so much fun spending time with you. May it continue, where ever our new lives take us.

Thank you to my extended family of many aunties, uncles and cousins! I am lucky to have such a caring family. Dear Aunty Sam, thank you so much for keeping me going - especially near the end! I appreciate all your support and everything you have done for me.

Thank you of course to my Mum. For keeping me company on the phone most of the mornings on my journey to the DWB. Thank you for all your advice and listening to all my thoughts and feelings. Your cheerleading of "Yes, this is my daughter, she's doing a PhD... in Astrophysics...at Oxford" to anyone who will listen has been hilarious and I am glad to make you proud. It is all possible because of you.

Finally, thank you to Jonny. You bring so much positivity, light, warmth and understanding to my life. You've even helped fix things in astrophysics a couple of times! You are such a kind and fun person, I am so happy I get to share so many moments with you.

To the Oxford Imps.

You have been a shining beacon of fun and support. Our laughter, creativity and friendship has fuelled me through my time here. I admire each and every one of you and am honoured to call you my friends. You have allowed me to truly be myself, and that is the greatest gift I have ever received. I LOVE YOU.

"Come with us now...

on a journey through time...

and space."

- *The Mighty Boosh.*

Contents

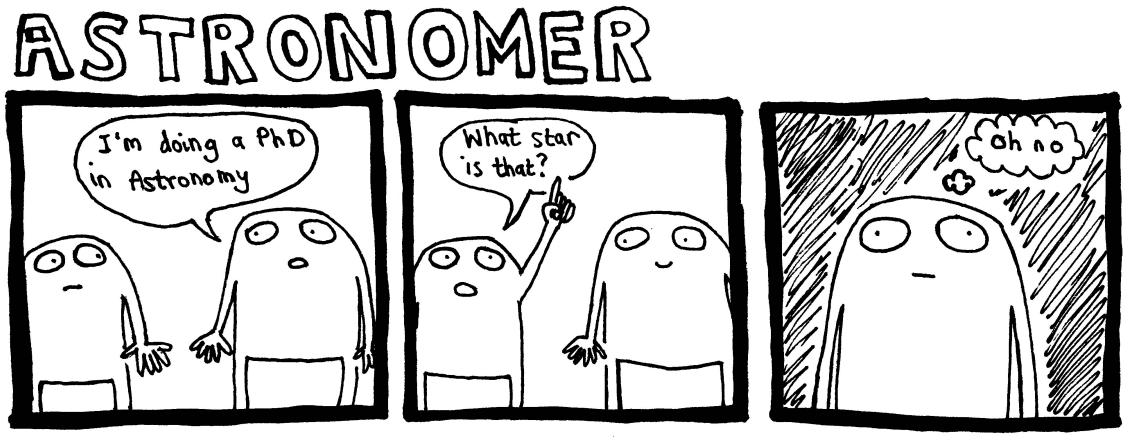
ASTRONOMER
I'm doing a PhD in Astronomy
What star is that?
oh no

Chapter 1

Galaxy Evolution

We live in a galaxy, there's another one a few mega-parsecs away and to be honest they're all over the Universe. There are billions of galaxies. They are the birthplaces and gatherings of stars, dust, gas and super-massive black holes (SMBHs). Some are big, some are small, blue, red, spiral-shaped or big amorphous blobs. They are so ubiquitous, that to truly understand the Universe itself we must understand how galaxies work and how they came to be. The shaping of the evolution of galaxies is a direct result of the history of the Universe as its conditions and ingredients change through time. Therefore, we get a bonus 2 for 1 when studying galaxy evolution as we also gain insight into the life of the Universe too. Studying the colour and composition of early galaxies not only reveals the chemical make-up of those galaxies in their beginnings, but also what was available cosmologically at the time. Similarly, a peak in cosmic star formation reveals when in cosmic history levels of cold, molecular gas were most readily accessible to galaxies.

There are a long list of factors that contribute to the life of a galaxy: levels of star formation, black hole activity, minor and major mergers, the density of the cluster or group it lives in, the surrounding availability of cool gas to fuel further evolution (relevant reviews include Kormendy & Ho, 2013; Conselice, 2014). Even processes that can be secular such as the formation of a bar, or radial migration of stars within a galaxy can also have a significant impact on the shape and colour of a galaxy (Sellwood & Binney, 2002; Kormendy & Kennicutt, 2004; Sellwood, 2014).

There are some general rules that roughly apply to finding out more about a galaxy's history, e.g. elliptical galaxies tend to be redder and spiral ones bluer, though even this requires further analysis as counter-cases have been found (e.g. Schawinski et al., 2009; Masters et al., 2010). Galaxy evolution is a complex process and one could examine a small subset of galaxies up close to work out specific mechanics (e.g. Davies et al., 1983; Emsellem et al., 2007; Cappellari et al., 2011) or a large sample

to see the general behaviour over time (e.g. Beswick et al., 2008; Donoso et al., 2009; Smolčić et al., 2017c). Not only the types of galaxies, but the properties one measures can too vary wildly; the morphology of a galaxy, the colour, velocity measurements in dispersion and rotation, cluster properties, chemical analysis and luminosity.

Luminosity measurements, with their relative simplicity, lend themselves to allowing us to probe the furthest reaches of the Universe as sensitivity is one of the main limiting factors of the observations, whereas angular resolution is paramount for observing other properties. By using the luminosity of a sample of galaxies as a proxy to measure the evolution of the general population, we can stretch deep into the Universe's history and map out a timeline of events, compared to using forensic investigation on smaller samples.

Two processes cause big impacts in the luminosity of a galaxy: star formation and active galactic nuclei (AGN) activity. Star formation is self-explanatory, the more stars a galaxy is making the brighter the galaxy will be. An AGN is an actively feeding black hole that produces extremely luminous emission from different aspects of the process depending on the viewing wavelength and orientation. An AGN may outshine its galaxy due to the material forming the accretion disc around the SMBH heating up as it reaches the event horizon, or from the enormous jets sometimes present when observed at radio wavelengths.

Both of these are thought to play major roles in shaping a galaxy and are highly dependent on the availability of cold gas in the local environment, and thus correlate with the changing of the Universe over time. In this thesis, I explore the contribution of star formation and AGN in galaxy evolution using large samples of galaxies.

1.1 Star Forming Galaxies

Actively star forming galaxies are typically young, lower-mass, disk-like and blue with new starlight from massive stars. Star formation evolves a galaxy chemically (e.g. Timmes et al., 1995; Korobkin et al., 2012), by producing elements up to iron through nuclear fusion in the core of stars and elements beyond iron (in the periodic table) in the death of massive stars through the explosive forces of supernovae or mergers of neutron stars (e.g. Korobkin et al., 2012). Star formation can even inhibit or slow down further star formation, as the expulsion of gas via supernovae (e.g. Dekel & Woo, 2003) or the locking up of gas in low-mass, long living stars constricts the supply of available gas to the galaxy.

The higher the level of star formation, the greater the impact on the galaxy as a whole. Star formation enriches a galaxy with metals, which over time reddens the galaxy since the elements in the envelopes of metal rich stars preferentially absorb blue light.

Higher star formation rates of course increase the luminosity of a galaxy, not only by simply having more and newer stars, but, depending on the initial mass function (IMF), by the increase in massive stars (> 8 $M_\odot$). Massive stars are brighter and bluer than lower-mass stars, but live shorter lives. After ~ 8 Myr the most massive of these will have expired, and so when a galaxy is bright with light from these stars we can infer that star formation is occurring at the time of observation. Even when observed at radio wavelengths, we detect synchrotron emission which massive stars produce in their death as supernovae, it is still safe to assume that star formation is ongoing because of their short lifetimes.

If the level of star formation is so high or the IMF is particularly top-heavy (i.e. a considerable proportion of high-mass stars are being produced), then the explosive energy from the supernova explosions that occur at the end of a massive star's life can blow away reservoirs of cool gas nearby. Violent cycles such as this can leave long periods between star formation activity and affect the appearance and dynamics of the galaxy. It is necessary to include these processes in simulations of galaxy populations to reproduce the distribution of galaxies seen in the Universe (e.g. Vogelsberger et al., 2014; Crain et al., 2015). Without the addition of stellar feedback, simulations predict galaxies that are more massive as well as higher number densities of galaxies at the low mass end than is observed. Gas that would have been heated, or ejected entirely, by supernovae is permitted to cool and form into stars (e.g. Hopkins et al., 2014).

1.1.1 Measuring Star Formation

To find the star formation rate (SFR) of a galaxy, unless the galaxy is the Milky Way, Andromeda or one of the Magellanic clouds, it is unlikely to be possible to detect and count each star within that galaxy. Even in our own galaxy, regions in the Galactic plane towards and behind Sgr A are obscured and difficult to observe. Let alone considering galaxies at high redshift that are unresolved. Instead, estimates can be made by measuring emission known to originate from the most massive stars ($M > 8$ $M_\odot$) within a galaxy. Not only do they dominate the UV light radiated from a galaxy, but they are better indicators of star formation itself. Massive stars typically have short lifetimes between 2-15 Myr, and so when a population of massive stars is observed, it can be reliably inferred that star formation is either ongoing or

has recently taken place. Therefore, this makes massive stars an ideal population to estimate SFRs from.

Across the electromagnetic spectrum different aspects of star formation can be observed. The most commonly used wavebands for this task are Ultra-Violet (UV), optical, infrared (mid and far) and radio.

1.1.1.1 UV Emission

UV emission is the most sensitive wavelength range to measure the star formation rate as it is predominantly produced by the most massive, and youngest stars. Emission by young, blue OB stars dominates the light produced by an actively star forming galaxy, whereas lower mass, dwarf stars collectively dominate the overall mass and near-infrared emission. The rest-frame UV is highly sensitive over an extensive redshift range, with detections confirming galaxies at $z \sim 7$ (e.g. Finkelstein et al., 2013), and candidates found at $z \sim 11$ (e.g. Bouwens et al., 2015). The most commonly used UV wavelength is 1500Å in the near-UV (NUV). NUV measurements are preferable as the emission is dominated by the light of younger stars, whereas mid-UV wavelengths (e.g. 2800Å) can be contaminated with the light of older stars (Madau & Dickinson, 2014). This is due to the rate of decline of the emission, where the 1500Å drops off sharply after ∼250 Myr longer wavelengths such as 2800Å experience a more exponential decline. The high sensitivity and consistency of UV emission make it a desirable candidate for quantifying star formation rates over redshift and using it to investigate the evolution of galaxies.

1.1.1.2 Optical Emission

Young, massive stars are, by nature, formed in cocoons of gas. The energetic UV photons they produce photoionise electrons in the surrounding Hydrogen gas (HII regions). The recombination of the electrons emits light in the optical regime (recombination line emission). The close association with the OB stars that ionise these electrons, means that recombination line emission has a near direct correlation with star formation. Recombination line emission can be produced by electrons moving to many different energy states and dropping and being raised from different levels. There are several Hydrogen series (e.g. Lyman, Balmer, Paschen) and numbers of energy levels. The series denotes the orbit that the electron jumps down to and Greek letters denote the quantity of levels transitioned. For example, Lyα equates to an electron that transitions from quantum number $n = 2$, to $n' = 1$, whereas Paβ transitions

from n = 5 to n′ = 3. The most prominent and commonly used optical recombination line is Hα = 656.8 nm, from the Balmer series. Hα is generally considered the most reliable of the recombination lines due to having relatively lower extinction (Madau & Dickinson, 2014), which is imperative for studies that span wide redshift ranges. Other lines in the Hydrogen series can be useful in specific cases, (e.g. Paα in nearby, dusty galaxies) but Hα is more consistent universally. Heavier elements also produce recombination lines at optical wavelengths (e.g. [OII], [OIII]), but have greater dependencies on interstellar medium (ISM) properties such as metallicity and so are not as closely linked with star formation activity.

1.1.1.3 Infrared Emission

As the Universe ages, more dust is produced by the life cycle of stars. As such, new born stars typically find themselves in not only gas-rich, but dust-rich regions of a galaxy. While the photoionised gas re-radiates starlight at optical wavelengths through recombination line emission, dust re-radiates UV starlight in the infrared. Mid- and far-infrared (MIR, FIR) emission (8 - 1000 μm) is predominantly associated with massive stars, while near-infrared emission is more indicative of older stellar populations (Meneses-Goytia et al., 2015; Kotilainen et al., 2012).

The type of infrared emission depends on the size or type of the dust grain that absorbs the UV emission and the temperature. There are three main contributors: polycyclic aromatic hydrocarbons (PAHs), small dust grains (diameter $< 0.0025\mu$m) and large dust grains (diameter $> 0.1\mu$m).

PAHs are easily heated by the absorption of a single UV photon and re-radiate this emission in the MIR. PAHs are a key component of the ISM and produce 7 major emission features over 3-17μm (3.3, 6.2, 7.7, 8.6, 11.2, 12.7, and 16.4 μm). Since these emission features are excited by individual UV photons, they are particularly bright in regions of young, massive stars and can be used as a tracer of star formation. (For more on PAHs, see a review by Tielens (2008)). However, PAHs can depend strongly on the metallicity of the ISM and so can vary over redshift and between galaxy types.

Small dust grains also reach high temperatures (> 1000 K) upon the absorption of UV photons, and they too radiate in the MIR (< 30 μm). The MIR is often dominated by re-radiated starlight and can be a good indicator of star formation. However, at higher redshifts where galaxies become unresolved, there is the possible contamination from AGN that also produce strong UV emission and are often surrounded by hot, dusty tori or clouds. However, unless selecting for them directly, they are thought to

be relatively rare and can be separated by using additional features (e.g. an excess of radio emission, optical emission lines that relate to AGN etc.).

Large dust grains contribute to the FIR emission of a galaxy. At $\sim$60μm FIR emission is still considered warm, and so corresponds to star forming regions. Beyond $\sim$ 100μm the FIR light is dominated by an "infrared cirrus" that is a more extended region of dust (Kennicutt, 1998) and is comparatively cold (15-60 K). While FIR can be separated from the complications that MIR emission has with possible AGN contamination, there is evidence that FIR emission can have a significant contribution from older stars which heat dust to cooler temperatures (Bendo et al., 2015).

Another issue with longer infrared wavelengths is resolution. FIR instruments such as *Herschel* SPIRE achieve resolutions of (18.1, 25.2, 36.6)$''$ for wavelengths of (250, 350, 500)μm respectively (Griffin et al., 2010). Ground-based FIR instruments such as SCUBA (Holland et al., 1999) on the JCMT can achieve slightly higher resolution, but are still on the order of tens of arcseconds with resolutions of (7.8, 13.8)$''$for (450, 850)μm respectively. Poor resolution blurs multiple sources together. Therefore, while the FIR may be sensitive, some of this may be due to multiple sources combining together, affecting the inferred luminosities of supposedly individual sources and reducing number counts. However, high resolution may not fix these issues as instruments such as ALMA can struggle to observe a large number of sources above $z > 3.5$ due to the drop off in high mass sources with redshift (Dunlop et al., 2017) requiring large areas for a survey, or a pre-selection for targeted follow up. Another issue is because of the ratio of the total SFR compared to the UV-visible SFR, and when observing galaxies at these redshifts the rest-frame wavelength is in the UV. Higher mass galaxies experience much greater levels of dust obscuration and become invisible at these wavelengths. High mass galaxies are required since at high redshift lower mass galaxies will drop below the flux limit of the observation. Another trade off with high resolution with ALMA can be that the higher the resolution, the smaller the maximum observable angular scale is of the observation which can limit the detection of more nearby sources due to resolving out larger scale structures with the interferometer.

A consequence of dust, is that UV emission suffers extinction and UV measurements on their own are not sufficient to derive star formation rates. Even Lyman-break galaxies, which are selected based on their high UV emission, can have as much as 80% of that UV emission attenuated by dust (Reddy et al., 2012). Galaxies that are dustier, with higher star formation rates suffer from this even more. The ratio of IR to UV emission can reach factors of more than 100 times. To still utilise UV,

optical and IR emission their measurements can be combined to accommodate UV photons that both escape their galaxy and are absorbed by dust (e.g. da Cunha et al., 2008; Smith et al., 2011).

Either estimates can be made on the severity of dust attenuation based on the specific wavelength, or a more rigorous multi-wavelength approach. However, a way to avoid complications with dust is to use a waveband that is not affected by dust.

1.1.1.4 Radio Emission

Radio emission has an advantage over higher frequency emission since the long wavelengths of radio waves can traverse through the dust that inhibits shorter wavelengths. This means a window to otherwise cloaked parts of galaxies and the Universe. As well as being able to see otherwise hidden aspects of the Universe, radio emission can also show us the path of mechanical processes (non-thermal emission); some of which are invisible to us without the use of radio astronomy. Examples of these include jets and supernovae which propel cosmic rays into the surrounding medium. In addition to the benefits of passing through astrophysical obstacles, radio emission is useful because it can be observed from the ground. Whereas at higher frequencies the atmosphere is either opaque or severely impairs observations causing targets to twinkle, the atmosphere is transparent for the majority of the radio spectrum. This means that observing in the radio is substantially lower in cost as it is not necessary to send radio telescopes to the tops of mountains, in deserts or into space. The main source of interference one has to look out for is man-made. The use of mobile phones and satellites near to a telescope can cause Radio Frequency Interference (RFI) and disrupt observations. However, this is not applicable to all radio bands and can be avoided by choosing sites away from busy towns and cities, and knowing the travel paths and times of satellites in order to avoid them when scheduling an observation.

Radio continuum emission from extragalactic sources comes in two forms: thermal and non-thermal. Below I describe both of these in further detail, discussing the physics that produces the radio waves and the astrophysical sources from which they originate. In particular, I discuss a property of non-thermal radio emission that can vary: the spectral index, which is particularly pertinent for this thesis.

1.1.2 Free-free

Free-free (or thermal) radio emission comes from the scattering of a free-electron by an ion with no electron capture (i.e. it remains free). It is 'free-free'. This dominates

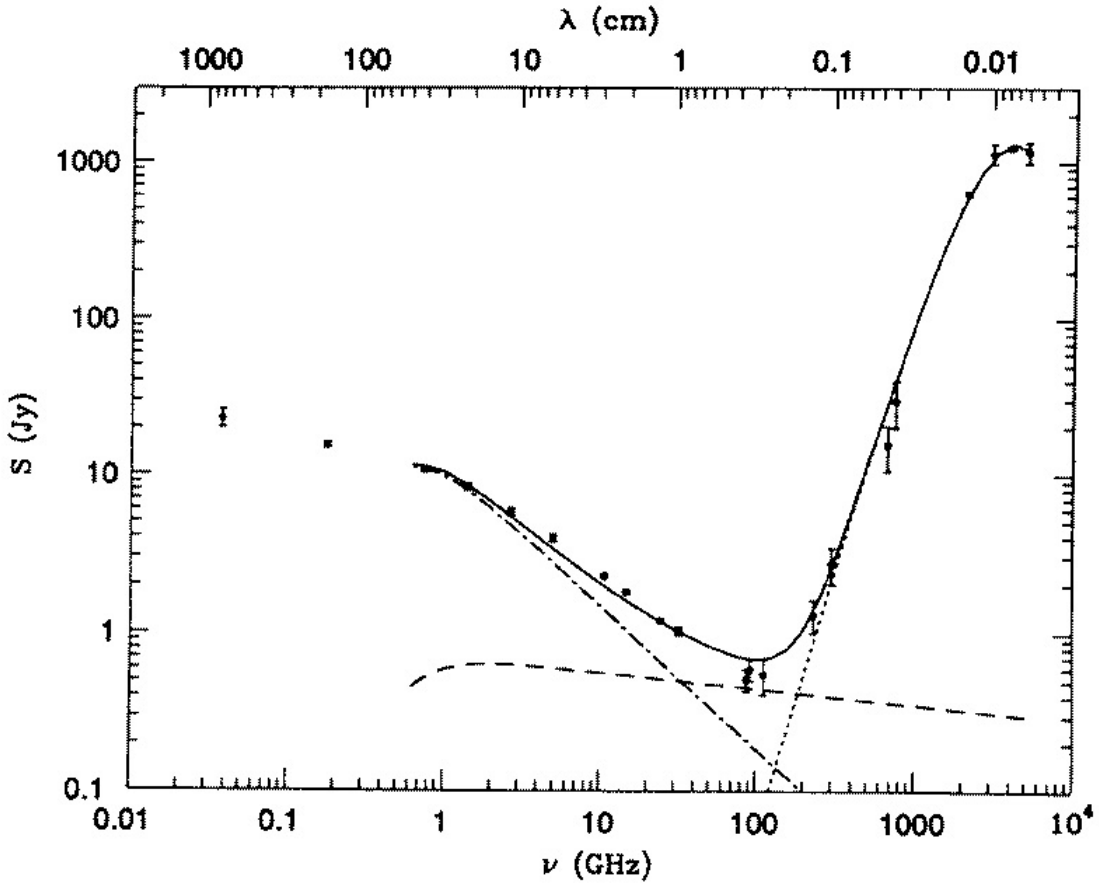

Figure 1.1: The radio-infrared spectrum of galaxy M82 broken down into its constituent components. *Solid:* The sum of the constituent parts, *Dotted:* Far-infrared emission, *Dashed:* Free-free emission, *Dot-dashed:* Synchrotron emission. *Image credit:* Condon (1992)

the higher frequency end of the radio (> 10 GHz) and has a flat spectrum ($\alpha \sim 0.1$, where $S_\nu \propto \nu^{-\alpha}$. See Figure 1.1 for an example).

The main source of free-free emission is HII regions, i.e. ionised hydrogen around new born stars. The intense radiation from young stars and active star formation produces ions for free electrons to scatter off. Thus free-free emission is proportional to the photo-ionisation rate of stars and can be used as a tracer of star formation rates in galaxies. However, the fact that free-free emission spectrum overlaps with that of the synchrotron and is relatively faint means that the two have to be disentangled to use free-free measurements reliably. Observing at multiple frequencies is one way to do this as the spectrum of the synchrotron emission can be measured and therefore the synchrotron emission can be accurately removed. This is only necessary for free-free since the contributions to the overall emission are relatively close at these higher frequencies. At lower frequencies, synchrotron emission dominates so substantially that removing the free-free contribution is not needed to measure the synchrotron emission accurately.

1.1.3 Synchrotron

Synchrotron emission is generated by the acceleration of relativistic electrons around magnetic field lines. The population of electrons produce a much steeper spectrum than free-free emission (typically $\alpha \sim 0.7$). The steepness of the spectrum is determined by the initial power law distribution of the electron energies. Longer wavelengths trace the peak of the energy emitted by electrons that have spiralled around magnetic fields for longer.

Processes that emit synchrotron radiation are typically in the form of a shock-waves, such as the forefront of a supernova (SN) explosion. While SNe mark the end of a massive stars life, the lifespan of a massive star is so short relative to other stellar lifetimes that it can still be used as an indicator of active star formation in a galaxy.

There are two main producers of synchrotron emission on different scales. Within a galaxy, supernova remnants in regions of active star formation expand into the interstellar medium. Beyond the scale of the galaxy, radio jets from AGN expel huge amounts of matter large distances away from the host galaxy. Both of these processes involve powerful shock-waves either at the edges of the supernova explosion or the forefront of the jets reaching out into the intergalactic medium. The acceleration of the nearby electrons in turn produces the synchrotron emission.

The reliability of synchrotron radio emission as a tracer of star formation is bolstered by a phenomenon known as the FIR-radio correlation. Over many scales,

galaxy types and redshifts a tight correlation between FIR and radio emission from the same galaxies holds (Helou et al., 1985; de Jong et al., 1985; Appleton et al., 2004; Calistro Rivera et al., 2017). Though Active Galactic Nuclei (AGN) can contribute to synchrotron emission as produced by jets, the FIR-radio correlation can be used to disentangle these from a sample. Since FIR is known to correlate with star formation, sources with an excess in radio emission compared to what is expected from the FIR-radio correlation can be inferred to be AGN. This removes the need for more complex methods of identifying AGN such as using spectral lines, which can be more prone to error from different viewing angles, or if the AGN is obscured by dust at optical wavelengths. The benefit of using radio measurements is the superior resolution that can be achieved with the long baselines of radio interferometry. High resolution enables the localization of individual star forming regions within nearby galaxies, and makes it possible to distinguish sources in close proximity to one another. Whereas the relatively poorer resolution of FIR observations can blur sources together. Often, when comparing radio with IR emission, the radio resolution has to be degraded with a smoothing kernel to compare the emission accurately.

Synchrotron emission dominates the radio spectrum at frequencies < 10 GHz. As discussed above, the relative contributions of synchrotron emission and free-free are substantial enough that removing the free-free component is not necessary at ≤ 2 GHz.

However, while the majority of the synchrotron radio spectrum is readily observable from the ground, at the lowest frequencies ($\lesssim 300$ MHz) effects of the ionosphere interfere with observations. These ionospheric variations can cause "twinkling" effects that can impede not only the flux measurement, but the observed position of sources. Though there are calibration methods around this (Lonsdale, 2005; Intema et al., 2009; van Weeren et al., 2016), it is increasingly difficult and can impact the sensitivity of an observation. Additionally, though the majority of the synchrotron spectrum is a power law, spectral curvature and a low-frequency turn-over can be an issue at MHz frequencies.

1.1.3.1 Spectral Index

Synchrotron emission can be characterised by a spectral index (α) that captures the power law of emission over a range of radio frequencies. Although on average this falls in the range $\alpha \sim 0.7 - 0.8$, there are factors which can cause this value to deviate:

1. **Ageing**: Over time energy losses in synchrotron emission scale with $\frac{\mathrm{dE}}{\mathrm{dt}} \propto \nu^2$ and so the photons with the highest energy radiate away their energy first. This

steepens the spectrum over time if no further injections of energy occur. Deciphering the spectral aging that occurs, especially in radio galaxies with jets, can provide an insight into the physical processes that underly the structures. As such, models of spectral aging have been created to find the ages and dynamics of these radio structures (e.g. Carilli et al., 1991; Tribble, 1993; Komissarov & Gubanov, 1994; Hardcastle & Krause, 2013). Assumptions such as whether the source has had a single injection of energy and the initial electron energy distribution are included in these models. Factors such as synchrotron and Inverse Compton losses also have to be considered to model spectral aging accurately. These are described in the remaining bullet points.

2. **Inverse Compton Scattering**: The relativistic electrons that release Synchrotron emission close in energy to that of the Cosmic Microwave Background (CMB), up-scatter CMB photons to higher energies. Since this is at microwave wavelengths energy is lost from the system at higher frequencies (with the CMB peaking at $\sim$ 100 GHz) this results in a steepening of the spectral index.

3. **Synchrotron self absorption**: self-absorption occurs when a Synchrotron photon is absorbed by a relativistic electron, exactly the kind that produces the synchrotron emission in the first place. Hence, "self"-absorption. Synchrotron losses via self-absorption are due to the density of the medium that produces the synchrotron emission. Not all synchrotron photons produced by a source are able to escape to reach the observer. Longer wavelength photons produced are more likely to interact with Synchrotron electrons than shorter wavelength photons, and so get absorbed on the low-frequency end. For particularly dense mediums this means that the majority of longer wavelength photons that are observed are being emitted from the surface. As one moves to higher frequencies one can gradually see deeper into the source.

4. **Orientation**: Depending on the orientation of a radio source with jets, there are differing effects on the spectral index. Observing jets perpendicular to their axis, or edge on, will give a steeper spectrum, whereas viewing jets along the direction of travel leads to beaming effects that create a flatter spectrum. The reason for these differences is to do with optical thickness.

   When observing edge on, we are able to observe the full range of the jets. Near the core, the concentration of electrons is so dense that only the highest energy photons can escape, i.e. it is optically thick. As the jets dissipate into the

surrounding intergalactic medium, photons of longer wavelengths can escape these optically thin regions and reach the observer. However, since the denser regions are more energetic and release more emission, these areas dominate the resulting spectrum observed. Leading the spectrum to be steeper, but with a positive gradient.

When observing directly down the jet, the spectra of the core and lobe regions sum together. Not only that, but as the jets are relativistic the core emission is Doppler-boosted, or "beamed". Beaming shifts the emission to the bluer end of the spectrum. At the lower-frequency end, Synchrotron self-absorption comes into play in these dense regions. Therefore, the individual spectra are peaked, and also get Doppler-boosted to higher frequencies depending on the distance within the core. Summing peaked spectra at frequencies that shift gradually along the Radio Spectral Energy Distribution produces a flat spectrum overall (Wills & Browne, 1986; Jarvis & McLure, 2002, 2006).

Spectral aging, Inverse Compton Scattering and Synchrotron self-absorption affects both star forming and AGN galaxies, whereas the effects of observing sources from different angles exclusively affects AGN dominated galaxies.

1.2 Active Galactic Nuclei

Active Galactic Nuclei (AGN) are galaxies with actively feeding super-massive black holes (SMBHs). The emission from AGN comes from material falling onto the SMBH at the centre of the galaxy, heating up as it accelerates towards the SMBH and producing mainly thermal emission. Like star formation, AGN activity is an indicator of the level of gas available to power these systems throughout the history of the Universe and directly impact galaxy evolution. There are several varieties of AGN that have been discovered.

Below I discuss the different types of AGN and the possible impact they have on their host galaxy.

1.2.1 Types of AGN

Many types of AGN have been observed, each with different morphological and emission-based properties. A unification scheme is the currently favoured model, which explains these characteristic signatures in terms of different view-points and/or processes (Urry & Padovani, 1995; Antonucci, 1993; Tran, 2003; Tadhunter, 2008) (See

Figure 1.2 for a visual representation and Netzer (2015) for a recent review). If an AGN has radio jets, it can be categorised depending on viewpoint;

1. a Blazar is viewing directly down the axis of the jet,
2. a radio galaxy is viewing the jets perpendicular to the axis of the jet,
3. a quasar is viewing between these two extremes.

A sub-type of Blazars are BL Lacertae (BL Lac) objects, which are highly variable in their radio flux measurements. This variability is thought to be due to the fact that the line of motion is so close to the line of sight of the observer and slight variations in this cause variability in the observed emission. Another blazar sub-type is flat spectrum radio quasars (FSRQs). FSRQs is a term that encompass previously separate types of quasars; optically violent variable-, highly polarised-, core dominated- and flat spectrum radio quasars (Urry & Padovani, 1995). FSRQs look similar to BL Lacs with high variability, polarisation and bright core emission, but are differently classified based on the strength of their emission lines (Landt et al., 2004).

Quasars are extremely luminous AGN that dwarf any emission from their host galaxy. Quasars were first discovered by radio astronomers (Matthews & Sandage, 1963), these bright, point like sources outshining their host galaxy were named quasi-stellar objects by their star-like appearance. Although first observed in the radio, they emit over the electromagnetic spectrum and it is now known that only 10% of quasars produce significant radio emission. When jets are present they would fall under the "radio loud" category, as they emit strong radio emission. Quasars without strong radio emission are categorised as "radio quiet" (RQ).

Other types of RQ AGN also exist. Seyfert galaxies are still highly luminous, but it is possible to detect and image their host galaxy. Seyfert I AGN and their host galaxies are viewed face on. Seyfert II AGN and their host galaxies are viewed edge on. Both have narrow emission lines in their spectra and show an excess of FIR emission compared to what is expected from star formation that is estimated consistently over other wavelengths. However, Seyfert I also show broad emission lines in their spectra, whereas Seyfert II do not. This is an artefact of the viewing angle, as the region that emits broad line emission lies between the accretion disc and the dusty torus (see Figure 1.2). When viewed edge on, this region is obscured by the torus.

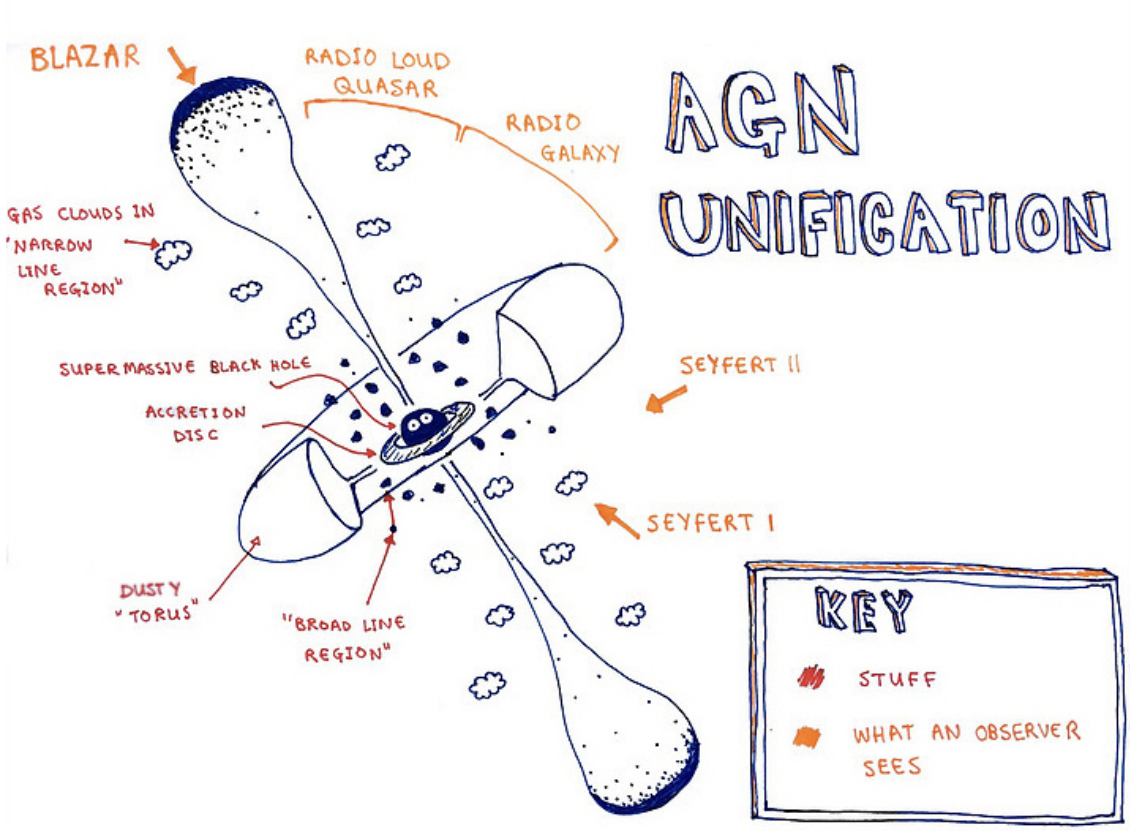

Figure 1.2: The AGN unification model reasons that the variety of AGN we see are the same type of object viewed from different angles, with or without a radio jet.

Low-ionisation nuclear emission-line region (LINER) galaxies (Heckman, 1980) are the final category I will discuss. They are a type of galaxy with core emission that displays low-ionisation emission lines in their spectra. There is debate as to whether the ionisation is caused by AGN (Kewley et al., 2006), warm gas (Yan & Blanton, 2012), older stellar populations (Singh et al., 2013) or various sources of shocks (Molina et al., 2018) in the nuclear region of LINERs, but they are more commonly grouped with AGN.

Though there is a unification scheme, that is not to say that all AGN are the same type viewed from different angles. Not all AGN produce radio jets, hence the distinction between radio loud and radio quiet quasars. And even if an AGN does have jets, there is more than one kind of jet it could have.

One can obtain more information on a particular AGN by using multiple wavebands and spectroscopy. This not only helps identify the specific type of AGN, but also helps gain an accurate picture of the full power exuded by it.

1.2.2 Feedback

As mentioned in Section 1.1, lower-mass simulated galaxies at the faint end of the luminosity function require input from stellar feedback to recreate what is seen in the Universe (e.g. Hopkins et al., 2014). The same is true for the bright end of the luminosity function. However, at the bright end, far more powerful processes are needed to generate sufficient levels of feedback to placate further star formation and galaxy growth. AGN can provide such levels of feedback. There are two main modes that are the currently favoured models:

1. Wind / Radiative / Quasar mode

2. Jet / Kinetic / Mechanical / Maintenance mode

Winds are expected to be generated by quasars in regions near the centre of the host galaxy as material is accelerated towards the SMBH. These winds expel material away from the accretion disc. They have not been directly observed, but are inferred through direct and in-direct evidence from optical spectroscopic measurements (e.g. Arav et al., 2008; Moe et al., 2009; Alexander et al., 2010; Liu et al., 2013).

As noted, powerful jets are found to be present in 10% of AGN. It is generally thought that jets are formed through the spin of the SMBH twisting nearby magnetic field lines (e.g. Rees, 1978; Rawlings & Saunders, 1991; Narayan & Quataert, 2005; Ballantyne, 2007) generated by the accretion disk which then channel on-falling material into bipolar jets. It is also possible that jets are formed not by the spin of the black hole but by spin of the accretion disk (Lu, 1991; Natarajan & Pringle, 1998; Koide et al., 1999; Sauty et al., 2002) or by a mis-match of the spins of the two (Caproni et al., 2004). The vast amount of energy involved can eject a galaxy's reservoirs of cold gas. Not only does this mechanism remove gas from the vicinity of the galaxy, but it heats it too. Starving the galaxy of its cold gas reservoirs can halt any ongoing star formation and black hole growth. This makes an AGN's production of jets a likely feedback process and one that is invoked in simulations to reproduce many properties of large samples of observed galaxies including the stellar mass function, luminosity functions, star formation history, mass-metallicity relations, morphological variance and more (e.g. Schaye et al., 2015; Sijacki et al., 2007; Vogelsberger et al., 2013; Bower et al., 2006; Dubois et al., 2016).

Jets of radio galaxies have been observed directly at radio wavelengths, though they can also be inferred from X-ray measurements that show the hot cavities of gas left behind from the jets (see Figure 1.3, Fabian & Crawford (1990); Pedlar et al.

(1990)). Radio images reveal that there are in fact two kinds of jet. They are distinguished morphologically and have traditionally been classified by the Fanaroff-Riley (Fanaroff & Riley, 1974) scheme of FRI and FRII (Figure 1.4). FRI jets are brightest near the centre and gradually tail off in luminosity with distance from the galaxy. FRII jets are characterised by hot spots at the edges of large radio lobes at the ends of the jets.

These two types of jets differ in terms of the power and efficiency that fuel them. A radio galaxy with FRI jets indicates a generally weaker and inefficient source as they lose power with distance from the galaxy, whereas FRII jets indicate a more powerful source as they efficiently transport energy to the outer reaches of the far-extending lobes. The hot-spots at the end of the radio lobes display the shock from the jets pushing out into a dense intergalactic medium.

Additionally, FRIs and FRIIs are observed to be present in different kinds of galaxies. FRII jets are more likely found in younger, bluer galaxies whereas FRIs are found in more massive galaxies at the centre of clusters (Hill & Lilly, 1991; Rodman et al., 2019). This leads on to the type of feedback mode they are *commonly* associated with, though not exclusively.

FRII jets are usually associated with the radiative mode, whereas FRIs are typically thought to be coincident with maintenance mode. So, although maintenance mode is also known as jet mode, that does not mean that jets are only present in 'jet' mode. Here it is to do with the most powerful processes in these modes. FRII jets are considerably more powerful and luminous than FRI jets and so are generally observed originating from galaxies undergoing the radiatively efficient quasar mode. Whereas FRIs originate from older galaxies surrounded by hot gas that they eventually dissipate into.

The fact that we see these two modes in distinct categories of galaxies implies they are active at different stages in a galaxy's life. Radiative mode is typically observed in younger galaxies. Meanwhile, jet, or maintenance mode, is observed in older, massive galaxies and as the name suggests, maintain the bulge and black hole of the galaxy. The maintaining aspect of this is that over time, the expelled gas gradually cools and settles back down onto the galaxy, meaning that while these feedback processes can inhibit activity they eventually feed future sessions of star formation and/or black hole growth.

Lastly, in recent years there has been growing evidence for a third kind of jet morphology, FR0 (Baldi & Capetti, 2009; Ghisellini, 2011; Baldi et al., 2015, 2018, 2019; Whittam et al., 2016, 2017). Geometrically, they appear similar to FRIs, but

Figure 1.3: An Optical and X-ray multi-wavelength image of a group of galaxies, NGC 5813. This image demonstrates the cavities left behind by jets from repeated SMBH activity over 50 million years. Several cavity sites can be seen in the holes of the X-ray emission which is coloured purple. Image credits: X-ray : NASA/CXC/SAO/S.Randall et al., Optical: SDSS

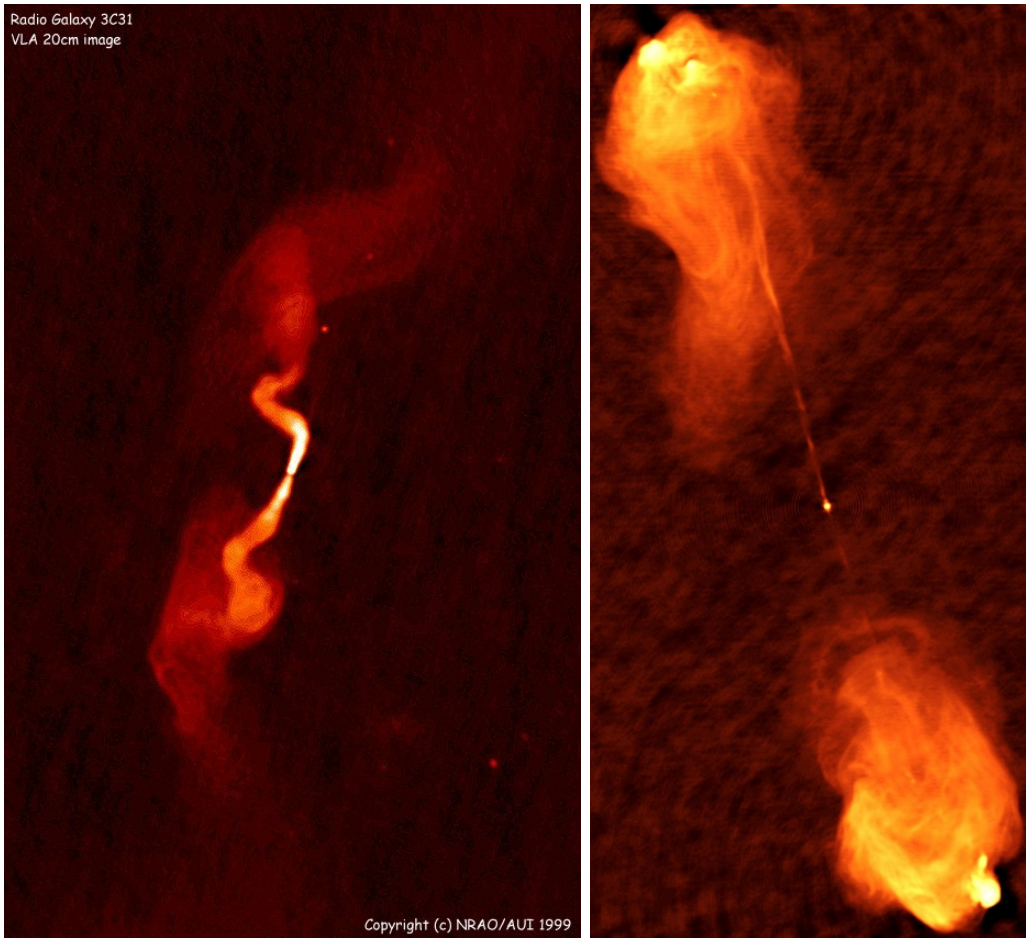

Figure 1.4: Examples of FRI (*left*) and FRII (*right*) type jets. The image on the left is of radio galaxy 3C31 which displays FRI type jets, exemplified by the bright emission near the core. Cygnus A shown in the image on the right is radio galaxy with FRII type jets, it shows bright hot spots at the end of the radio lobes and compact jets near the core. Image credit: NRAO/AUI

their core emission is around 30 times brighter than an FRI and the extended emission is weaker.

An additional layer on the AGN cake are objects called high- and low-excitation radio galaxies (HERGs and LERGs). The properties of high and low excitation refer to emission lines seen in the optical spectra of radio-loud AGN. As the nomenclature suggests, AGN with optical spectra where high excitation lines are present are denoted HERGs, an absence of these lines and a radio source will be a LERG. HERGs and LERGs are now thought to correspond to two different accretion modes. Counter-intuitively, though they show the presence of high levels of energy, HERGs are sometimes referred to as AGN being in 'cold mode'. The "coldness" relates to the efficiency of the accretion, where HERGs are radiatively efficient. This radiatively efficient process ties in with 'radiative mode' that I referenced earlier. Therefore, the mode of accretion is that of a highly luminous, geometrically thin accretion disc that is unobscured and generates powerful winds. It produces both broad and narrow line emission and is typically associated with powerful FRII jets.

LERGs on the other hand, are 'hot mode'. They are radiatively inefficient. They are unable to successfully transport energy to the ends of their jets and are commonly found to have FRI type jets. 'Hot' also references that there is no evidence for an accretion disc or torus, and so the accretion is that of *hot gas* from a surrounding halo. The environment at the centre of clusters is a typical location for plentiful hot gas, and so lends itself to hosting LERGs. LERGs are also typically redder and more massive.

This additional criteria for separating out AGN provides a deeper insight into galaxy evolution and SMBH growth. The rates of individual accretion modes over time and the density of both types of sources can unveil more about the underlying physics. For example, there is evidence to show that HERGs and LERGs evolve differently. HERGs appear to evolve over the redshift range $0 < z < 0.3$, whereas LERGs show no such evolution (Best & Heckman, 2012). In the same study, though HERGs and LERGs are found at all luminosities, there is a bigger population of LERGs below $L_{1.4GHz} \sim 10^{26}$ WHz^{-1}. Above this, HERGs can evolve by factors as high as $\sim$ 1,000 when increasing out to $z \sim 2$ (e.g. Willott et al., 2001; Sadler et al., 2007). From $0.5 < z < 0.75$ HERGs continue to evolve more rapidly (Pracy et al., 2016).

Though there seem to be many different ways to classify radio AGN, having a variety of ways to discern between them allows astronomers to get a precise handle on the variety of physics that is occurring within these systems. Pin-pointing when

certain populations outnumber the other or become more or less active, all adds more detail to the story of galaxy evolution.

1.3 Luminosity Functions

Galaxy evolution is a cocktail of secular and environmental processes, all of which fundamentally influence the levels of star formation and AGN activity. Both of these processes can be quantified by luminosity. Thus, a straightforward way of measuring galaxy evolution is by measuring the change in luminosity for a population of galaxies over cosmic time. For this we use luminosity functions (LFs). LFs measure the number density of galaxies (Φ) within a certain redshift (z) and luminosity (L) bin. This can be done across many wavelength regimes which offer different physical insights: γ (quasars, e.g. Chiang & Mukherjee, 1998; Ajello et al., 2012), X-ray (supernova remnants and hot gas heated by AGN, e.g. Miyaji et al., 2000; Aird et al., 2010), ultraviolet (starlight from young, blue, massive stars, e.g. Bouwens et al., 2015; Finkelstein et al., 2015), optical (young, massive blue stars and hot tori around AGN, e.g. Boyle et al., 1988, 2000; Vigotti et al., 2003; Croom et al., 2004; Prescott et al., 2009; Westra et al., 2010), infrared (hot dust heated by stars or in tori around AGN, e.g. Le Floc'h et al., 2005; Lake et al., 2017), Radio (supernova remnants and jets from AGN, e.g. Peacock, 1985; Condon, 1989; Willott et al., 1998; Machalski & Godlowski, 2000; Snellen et al., 2000; Sadler et al., 2002; Clewley & Jarvis, 2004; Mauch & Sadler, 2007; Sadler et al., 2007; Donoso et al., 2009; McAlpine & Jarvis, 2011; Simpson et al., 2012; McAlpine et al., 2013; Prescott et al., 2016; Pracy et al., 2016) and bolometric (e.g. Hopkins et al., 2007) LFs.

UV and optical LFs tend to use a high number of sources and so obtain better measurements for the LF, but require correcting for emission absorbed by dust. Mid-infrared traces only the hot dust, and so can miss emission that escapes freely from a galaxy. At the other end of the spectrum, radio LFs (RLFs) have the benefit of skewering through the dust, but the sources are typically less numerous. This is down to a sensitivity issue that will be resolved with the advent of new radio telescopes.

The LF can be used to measure the evolution of both SFGs and AGN. A sample of galaxies over a range in redshift can be used to document the changes in the luminosity of the population over time. This could be a change in the bright or faint end of the LF, finding peaks in luminosity at a certain redshift or a steady decline/increase in the LF with redshift. The evolution of the LF is often described by a parameter k, in

the form of a single power law $(1 + z)^k$ as a factor of the LF. This assumes a constant rate of evolution of the LF over redshift and is therefore a simple parameterisation.

The many wavelengths it is possible to calculate LFs from offer different insights into galaxy evolution, both in star formation and AGN activity. Below I discuss what LFs at different wavelengths can offer.

1.3.1 UV, Optical and infrared luminosity functions for tracing star formation

To quantify how levels of star formation activity change throughout time, luminosity distribution of galaxies at wavebands dominated by star formation can be measured over redshift. By comparing the rest-frame luminosity for large enough samples of galaxies the number density at a given luminosity can be calculated. Luminosity functions (LFs) of multiple wavelengths can then be compared to see if the trends they observe in star formation activity agree. This includes not only when a peak in SF occurred in the Universe's past, but also the rate of which any changes evolve and steepness of the bright and faint ends of LFs over many wavelengths.

1.3.1.1 UV LFs

UV LFs are highly sensitive and thus can be calculated over a vast range in redshift, where to observe in the rest-frame UV one turns to optical and NIR photometry (Ellis & Jones, 2004; McLure et al., 2009; Bowler et al., 2015). Confirmed detections of sources all the way to z $\sim$ 7 (Bowler et al., 2014) exist and have been used to measure the UV LFs. With a high number of sources and an extensive range in redshift this has allowed astronomers to document a detailed account of the peak of star formation in cosmic history. Beginning relatively recently in 1996 (Lilly et al., 1996), even with the earliest measurements a trend has been seen that star formation peaks in the window between $1 < z < 2$. However, subsequent studies have predominantly observed at higher redshifts, past this window. This is because, at $z < 1$, to observe rest-frame UV emission at shorter wavelengths, which is recommended due to the stability over redshift as mentioned in the previous section, requires the use of space telescopes. Also, identifying galaxies at high redshift provides an insight into other aspects of the history of star formation in the Universe and so observing using ground-based optical telescopes becomes preferable.

1.3.1.2 Optical LFs

Optical LFs that aim to measure SF are typically constructed using measurements of Hα (Gallego et al., 1995; Gunawardhana et al., 2013). It is the most reliable recombination line, as it is bright since it is not as susceptible to effects that other lines in the Hydrogen series suffer from, such as Lyα which scatters easily and is quickly extinct. Heavier elements pose problems with dependence on metallicity and also experiencing higher rates of extinction. Observing using Hα will only detect sources as far as z < 0.5. To reach beyond this observations are required at near-IR (NIR) wavelengths using spectrographs to identify and measure Hα lines (Yan et al., 1999; Hopkins et al., 2000; Shim et al., 2009).

1.3.1.3 IR LFs

IR LFs have been measured across the IR range. Due to the nature of IR emission, IR LFs are prone to tracing the evolution of highly dusty, and therefore exceptionally bright and highly star forming galaxies. This means that the bright end of the IR LF is well probed and can reach back to high redshift. Accessing the highest redshifts is done by observing at sub-millimeter wavelengths. The recent advance of sub-millimeter instrumentation such as ALMA has pushed the limits of possible sensitivity in this area, and thus the distances as well as number counts of distant rest-frame IR sources. Dusty, luminous galaxies have been detected at redshifts as high as $z \sim 6.3$ (e.g. Riechers et al., 2013). As with any wavelength, it becomes more difficult to detect faint objects as redshift increases, and so it is difficult to constrain the faint end of the LF. However, evidence from IR LFs agrees with other wavelengths, that the peak of cosmic star formation lies between $1.5 < z < 2.5$ (Duivenvoorden et al., 2016; Dunlop et al., 2017).

1.3.2 Radio Luminosity Functions

Radio luminosity functions are the topic of this thesis. The way they are referenced is in a slightly different way to other luminosity functions. At shorter wavelengths, the luminosity function is often fitted to a Schechter function (Schechter, 1976) and the steepness of the faint and bright slopes are independently characterised and compared from study to study. At radio wavelengths it is more common to use a double power-law of which two separate models are fitted : Pure Density Evolution (PDE) and Pure Luminosity Evolution (PLE). They represent two modes of evolution in which

different physical processes cause the evolution of the RLF to change. I describe them in more detail in the following two sections.

1.3.2.1 Pure Density Evolution

Pure Density Evolution (PDE) is the evolution in the number density of galaxies such that with redshift, galaxies are presumed not to change luminosity but become less or more numerous. This could primarily be through mergers or for radio sources, the general availability of fuel to supply radio jets.

The most common way to incorporate PDE into a LF is with a factor,

$$\Phi_z(L, z) = (1 + z)^k \Phi_0(L) \tag{1.1}$$

where k is a free parameter that determines the rate of evolution. This is a simple parameterisation that assumes a constant rate of evolution, more complex models must be invoked to incorporate a potential turnover or change in evolution rates over redshift.

1.3.2.2 Pure Luminosity Evolution

Pure Luminosity Evolution (PLE) assumes that the physical number of galaxies does not change, but that galaxies become dimmer or brighten over time. Physical reasons for dimming include quenching of star formation due to AGN activity, loss of star fuel through ram-pressure stripping or excessive supernova activity and stellar winds blowing gas reservoirs out of the galaxy. Conversely, a galaxy may increase in luminosity due to accretion of cold molecular gas from filaments or secular processes such as a central bar funneling gas into a condensed region and triggering starburst activity.

PLE is incorporated in a similar fashion into a LF but such that L changes with redshift,

$$\Phi_z(L) = \Phi_0 \left(\frac{L}{(1 + z)^k} \right) \tag{1.2}$$

where again, k is a free parameter to fit the extent of the evolution. Again, the factor of $(1 + z)^k$ is a simple parameterisation for a constant rate of evolution. A more complex form would be required to model for differing rates of evolution of redshift.

1.3.2.3 Star Formation Over Cosmic Time

Radio LFs (RLFs) for star forming galaxies (SFGs) generally trace synchrotron emission. The current sensitivity of radio instruments means that free-free emission is not currently a viable option for tracing star formation for a wide redshift range over wide area, though this may change with the dawn of more sensitive radio telescopes (Murphy, 2009). Synchrotron emission is more robust over redshift, though because of its steep spectrum, to sample high redshift emission in the radio one has to extend to lower frequencies. For more distant galaxies, low frequencies are probing rest-frame high frequencies in the radio, which are significantly less luminous due to the typically steep spectrum. However, for more nearby galaxies the low frequency end is the brightest part of the spectrum and can help to detect greater numbers of local galaxies. Sensitivity also currently limits the depth of synchrotron detections, however, with the advent of new radio telescopes such as the SKA, advances in sensitivity and subsequently the redshift range of radio observations will open the door for further study at radio wavelengths.

SFGs galaxies dominate the low luminosity end, but the overlap between SFGs and AGN can be significant. To gain confidence that the sample of sources (especially at low redshift) is not contaminated by AGN, it is often necessary to provide more than a luminosity cut to distinguish between the two groups. Sadler et al. (2002) used optical spectra to split their sample into SFG and AGN, resulting in 272 SFGs. Their radio data came from 1.4 GHz VLA observations over 325 $\deg^2$ and at $z < 0.48$. Best et al. (2005) found that their 1.4 GHz RLF at $z < 0.3$ that was also split into SFG and AGN by using optical spectra, matched well with all other current RLFs at the time. Additionally, they compared their RLF with one from the FIR. They found them to agree well at high luminosities, but not low luminosities, suggesting that the FIR-radio correlation breaks down below $L_{1.4GHz} \sim 10^{22}$ WHz^{-1}. Mauch & Sadler (2007) provide one of the most statistically robust RLFs at local redshifts. They used a sample of a total of 7824 radio sources at 1.4 GHz at z < 0.1 over an effective area of 7076 $\deg^2$. The sample was divided into SFG and AGN through inspecting individual optical spectra, which resulted in 4625 SFG sources. The resulting RLFs show that SFGs begin to dominate the local RLF at $L_{1.4GHz} < 10^{23}$ WHz^{-1}.

Other combinations of several sets of data can provide tight constraints on the evolution of the SFG RLF for significant redshift ranges. Hopkins (2004) compiled 1.4 GHz source counts from 6 studies, including that of Sadler et al. (2002), as well as UV, optical, mid and far-infrared as well as one X-ray study to constrain the RLF. This makes it one of few studies that models for a PDE and PLE for SFGs, finding

$\Phi \propto (1+z)^{2.70\pm0.60}$ for PLE and $\Phi \propto (1+z)^{0.15\pm0.60}$ for PDE. The reason this is not usually the case is that SFGs dominate at lower luminosity, and also lower-redshift. Since with current sensitivities SFGs are not found in large enough number beyond local redshifts, it is often statistically unreliable to calculate evolution parameters.

Padovani et al. (2011) show that SFGs dominate at certain flux densities. Their RLF is constructed from 1.4 GHz observations from the VLA, but at a much narrower and deeper field of view (0.11 deg^2 down to 43μJy). These deeper observations (up to z $<$ 2.3 for SFGs) also allow fitting of evolution terms, of which the best fit is $\Phi \propto (1+z)^{2.89\pm0.1}$ for a PLE model. The sample is divided in SFG and AGN via their own classification scheme using multi-wavelength data, spanning X-ray, optical, near and far-infrared and radio wavelengths. Padovani et al. (2011) find that below 10 mJy, SFGs dominate the RLF over AGN. Detailed studies such as this and Mauch & Sadler (2007) allow further studies to use these luminosity or flux cuts to make reasonable estimations of a limit by which to segregate a sample into distinct SF and AGN categories.

McAlpine et al. (2013) use 1.4 GHZ VLA observations from Bondi et al. (2003) over 1 deg^2 area of sky, down to 100μJy sensitivity. They use the Mauch & Sadler (2007) local RLFs for SFGs and AGN to fit their data and observe trends in the two populations. For example, to analyse the separate evolution of SFG and AGN in their sample they estimate the PDE RLF by,

$$\Phi_{\rm PDE}(z) = (1+z)^{k_1}\Phi_{\rm SFG} + (1+z)^{k_2}\Phi_{\rm AGN} \tag{1.3}$$

where k_1 and k_2 measure the evolution of SFG and AGN respectively. Using this technique, they find that SFGs push the evolution of the combined RLF at z $<$ 1.2 and that the evolution of SFGs is best fitted by a PLE model, $\Phi \propto (1+z)^{-2.47\pm0.12}$.

So far the works I have mentioned all use 1.4 GHz measurements, but other parts of the radio spectrum can provide their own benefits. Prescott et al. (2016) estimate the RLF using the 325 MHz GMRT survey. Lower frequencies are of interest for SFGs since the part of the synchrotron spectrum they probe is the brightest region, therefore allowing some sources that may not have otherwise been above the flux limit to be detected. The large survey area of 138 deg^2 is large enough to dispel effects of cosmic variance. Through matching each radio source with optical spectra from GAMA (Galaxy and Mass Assembly survey) they were able to separate out SFG and AGN, as well as obtaining accurate redshift information from the spectra. They find that the SFG RLF matches well with existing 1.4 GHz RLFs. The majority of the

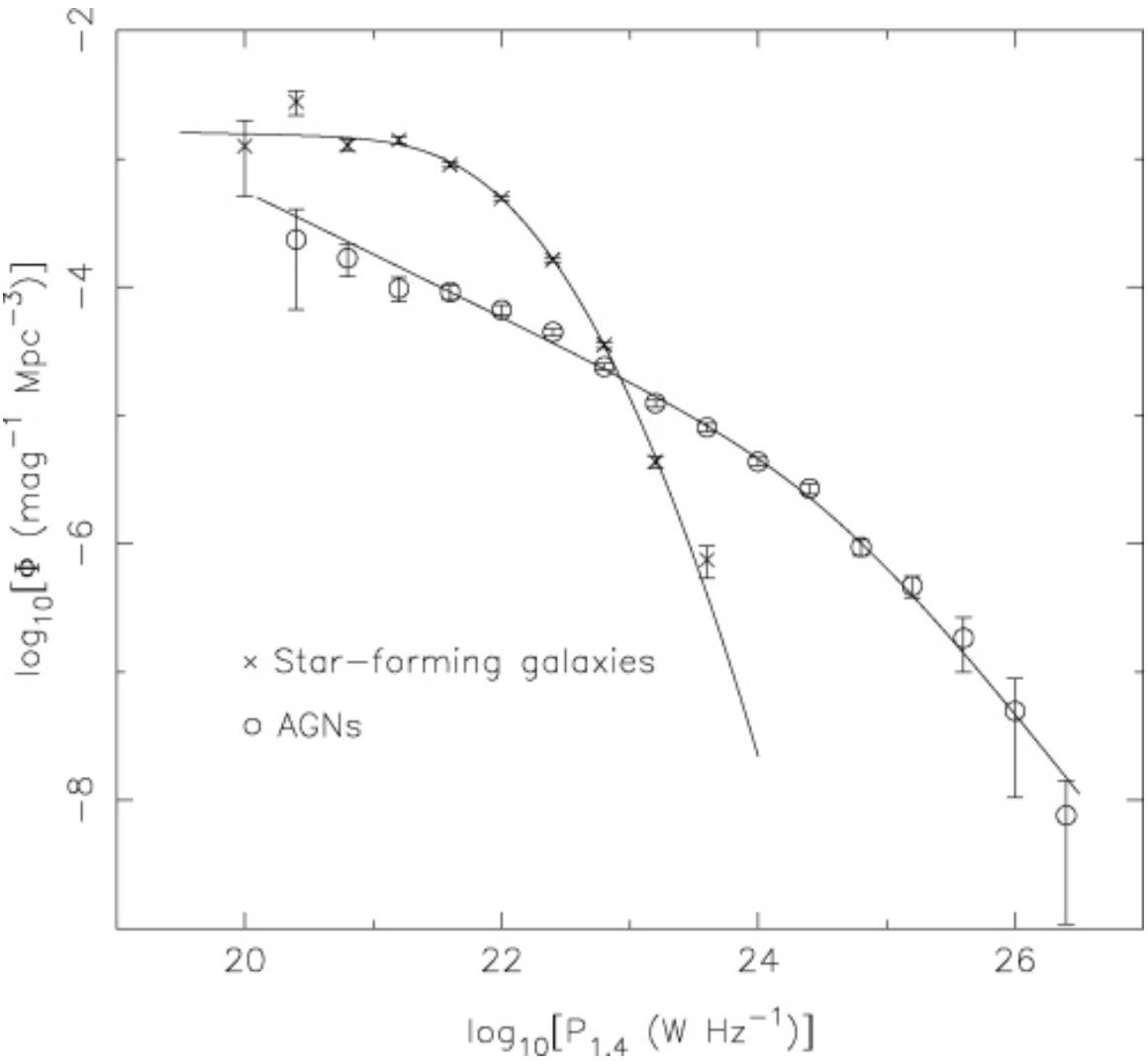

Figure 1.5: The local RLF at 1.4 GHz from Mauch & Sadler (2007). The sample is separated into SFG and AGN. SFGs begin to dominate the local RLF at $L_{1.4GHz} < 10^{23}$ WHz^{-1}. Credit: Mauch & Sadler (2007)

SFGs lie below z < 0.1, with only 6 sources z > 0.1, thus it was not possible to measure evolutionary terms.

Going up to higher frequencies, work by Novak et al. (2017) uses data from the VLA-COSMOS 3 GHz survey (Smolčić et al., 2017a). The VLA-COSMOS 3 GHz survey is a deep survey conducted over 384 hours of observations down to $\sim 2.3\mu$Jy over 2 deg^2. The star forming population consists of 5915 sources out to z < 5 and are identified using optical counterparts. They find a fit for PLE translated to 1.4 GHz of $\Phi_{1.4GHz} \propto (1+z)^{3.16\pm0.2-(0.32\pm0.07)z}$. They do not fit PDE since they argue that the faint end of the RLF is not well constrained enough over redshift to get a reliable PDE fit. A surprising result is that they find the peak of star formation rate

density lies at a higher redshift than previously reported, $2 < z < 3$. They reason that this higher redshift range is due to the greater proportion of dust-obscured sources they detect, around 15-20% of the SFR at z $\gtrsim$ 4 than studies that use Lyman break galaxies (optical measurements).

Significant evidence has been collected to confirm the local SFG RLF and to disentangle SFGs from AGN. With the advance of more sensitive radio telescopes (e.g. the SKA and its precursors MeerKAT and ASKAP, as well as the improved sensitivities on the VLA) and surveys dedicated to extremely deep surveys, the wealth of data that will surface on the faint end of the RLF will provide even more opportunity for closely detailing the evolution of SFGs.

1.3.2.4 AGN Activity Over Cosmic Time

While RLFs can be used to track star formation activity, the brightest radio sources in the Universe are AGN. Being the brightest means they can be observed to the furthest reaches and provide a more detailed story than is currently possible with observing star forming radio galaxies.

Many of the studies discussed in Section 1.3.2.3 also provided AGN RLFs as samples were split into SFG and AGN. The main purpose of Sadler et al. (2002), Best et al. (2005) and Mauch & Sadler (2007) were to provide robust RLFs showing the distinct forms associated with SFGs and AGN, all using optical measurements to split their samples. In the chronology of these three studies they each increased in number, with Sadler et al. (2002) using 441 AGN, Best et al. (2005) using a sample of 2215 AGN and Mauch & Sadler (2007) a sample of 2864 AGN.

Building on the numbers game, Donoso et al. (2009) estimate the RLF out to $z \sim 5$ using 14,453 radio-loud AGN. The RLF agrees well with other studies, but due to the size of the sample has considerably smaller error bars. They identify a characteristic luminosity of $\sim 10^{25}\mathrm{WHz}^{-1}$, above which sources evolve strongly and below evolve weakly with redshift.

Padovani et al. (2011) also looked at AGN as well as SFGs. The AGN in the sample stretched as far as $z \sim 5$ and the RLFs estimated actually did not agree with previous studies, but were in fact 2-4 times higher than the results of Sadler et al. (2002) and Mauch & Sadler (2007). However, this is due to the fact that their sample contained not only radio-loud AGN, but also radio-quiet AGN. In radio-quiet AGN it appeared that the radio emission is originating solely from star formation processes in these sources as the evolution closes matches that of the SFG population. Radio-loud AGN showed little to no evolution, whereas radio-quiet AGN evolved as strongly as

SFGs in the RLF. When removing radio-quiet AGN from their sample and sources in the highest redshift, most sparsely populated bins, the RLFs match well with previous studies.

The different evolutionary paths for AGN and SFG are also evident in McAlpine et al. (2013). Their 1.4 GHz RLFs show AGN to be best fit by a PLE model of $\Phi \propto (1+z)^{1.18\pm0.21}$. Compared to their result of $\Phi \propto (1+z)^{2.47\pm0.12}$ for SFGs, AGN evolve much more slowly. While at lower redshifts ($z < 1.2$), SFGs dominate, at higher redshifts ($1.2 < z < 2.5$) low-luminosity AGN dominate and their weaker evolution slows down the overall evolution of the combined RLF.

Dissecting the RLF in multiple ways, Prescott et al. (2016) categorise their AGN sample into both HERGs and LERGs and steep ($\alpha > 0.5$) and flat ($\alpha < 0.5$) spectrum AGN. For the combined sample of AGN, they find fits to both PDE and PLE models of $\Phi \propto (1+z)^{0.92\pm0.95}$ and $\Phi \propto (1+z)^{2.13\pm1.96}$ respectively which fits well with other studies. The further refined samples are too small (full sample is 453 AGN) to do evolutionary analysis on, but other trends are examined. They find that steep spectrum AGN are more numerous and span wider luminosity ranges, but also that when considering steep and flat-spectrum sources as different viewing angles of each other their RLFs are consistent between one another. This can be done by assuming that flat-spectrum sources are the same as steep-spectrum sources but viewed along the direction of the jet (see Section 1.1.3.1). This provides support for AGN unification and that flat-spectrum sources are a subset of steep-spectrum sources.

In terms of HERGs and LERGs, Prescott et al. (2016) find that between $10^{23} < L_{325MHz} < 10^{26}$ WHz^{-1} LERGs dominate, and the fraction of HERGs decreases when going from bins $0.002 < z < 0.25$ to $0.25 < z < 0.5$. Work by Pracy et al. (2016) uses a much larger number of 5026 radio AGN separated into HERGs and LERGS by their optical spectra, and so is able to study their evolution up to $z = 0.75$. The difference in strength of evolution is substantial. Fitting for PDE, the best fit for LERGs is $\Phi \propto (1+z)^{0.06^{+0.17}_{-0.18}}$, which is almost no evolution at all. Whereas for HERGs, the fit for PDE follows $\Phi \propto (1+z)^{2.93^{+0.46}_{-0.47}}$. In PLE models the difference is even more severe, with LERGs following $\Phi \propto (1+z)^{0.46^{+0.22}_{-0.24}}$ and HERGs evolving as $\Phi \propto (1+z)^{7.41^{+0.79}_{-1.33}}$. These starkly contrasting evolutionary parameters support the idea that HERGs and LERGs are powered by different accretion modes (see Section 1.2.2). However, the redshift range is small.

Extending to higher redshifts, recent work by Smolčić et al. (2017c) find 1.4 GHz RLFs out to $z \sim 5$. Using data from VLA-COSMOS 3 GHz Large Project, they assume a mean spectral index of $\alpha = 0.7$ to convert to 1.4 GHz. With their sample

of 1800 radio AGN they find that the AGN evolve as $\Phi \propto (1+z)^{(2.00\pm.18)-(0.60\pm0.14)z}$ when fitting for PDE, and $\Phi \propto (1+z)^{(2.88\pm.82)-(0.84\pm0.34)z}$ when fitting for PLE. As with previous studies, they find the PLE model to evolve more strongly. They discuss the potential implications of their sample which contains both accretion modes. They separate into radiatively efficient (quasar mode) and radiatively inefficient (jet mode) via X-ray and mid-infrared measurements, the presence of which indicates a quasar mode AGN, as well as the rest-frame colours of the galaxies. They find that 30-40% of their sample are quasar mode AGN and so there is a significant contribution from both modes in their sample. Factors such as this are useful to consider, as the combination of two differently evolving populations can explain effects such as Φ values being higher than the best fit.

The range of AGN RLFs is complex with many different aspects and populations of AGN to consider, whether they are radio-loud or radio-quiet, viewed from different orientations or experiencing different accretion modes. It is clear that they evolve at contrasting paces and these are important factors to consider if not accounted for. It is also prudent to examine effects that are less well examined, such as using a parametric model compared to the studies which use non-parametric forms for the RLF, or the effects of modelling accurately the distribution of the spectral index instead of assuming the mean value for all sources.

1.4 Thesis Outline

In this thesis I explore galaxy evolution through the use of radio luminosity functions calculated from new radio surveys. I begin by introducing Radio Interferometry in Chapter 2. This includes its theory, imaging techniques, interferometers, surveys conducted by those interferometers and selection effects that affect observations.

In Chapter 3 and 4 I measure RLFs at 150 MHz and 1.4 GHz respectively. In Chapter 3 I use data over the XMM-LSS field with LOFAR and the VLA. The work in Chapter 4 uses observations of the COSMOS field (Scoville et al., 2007) taken by the VLA and MeerKAT.

In Chapter 5 I present the reduction of C- and D-configuration data observed with the VLA of the XMM-LSS field (Pierre et al., 2004). I then explore the impact of the longest and shortest baselines on the luminosity of sources observed by interferometers. To do this I compare the flux ratios of C+D configuration data to higher resolution B-configuration observations of the same field.

I conclude this thesis and discuss topics for future work in Chapter 6. Throughout, I adopt a ΛCDM cosmology of $\Omega_m = 0.7$, $\Omega_l = 0.3$ and $H_0 = 70$ km/s/Mpc. All fluxes are measured in Janskys (Jy) unless stated otherwise and α is defined by $S \propto \nu^{-\alpha}$.


€€
'18

Chapter 2

Radio Interferometry

The data in this thesis is observed using radio interferometers. In this Chapter, I introduce basic interferometry theory, the most commonly used algorithm for imaging interferometric data - CLEAN, specific interferometers and examples of surveys they have conducted.

2.1 Fundamentals

An interferometer is the collection of 2 or more telescopes working together as a single instrument. An interferometer observes the sky as if it is a single dish with a diameter as wide as the longest distance (or baseline) between any two antennas in the interferometer. The remaining antennas fill in the gaps in the collecting area of the 'dish' size created by the two furthest antennas.

The longest baseline of an interferometer determines the resolution of the images that are observed from the full width half maximum (FWHM) of the synthesised beam,

$$\theta = \frac{\lambda}{b_{max}}, \tag{2.1}$$

where θ is the resolution in radians, λ is the wavelength of the emission and b_{max} is the longest baseline. Whereas the diameter of the individual dishes in the array relates to the field of view of the interferometer described by the same equation as Equation 2.1, but where b is replaced by D, the diameter of a single dish size of one of the antennas.

The signals from an astronomical source need to be received *in phase* to interfere constructively and to accurately image the target source. However, given that some interferometers have baselines as long as several kilometers, a delay term has to be

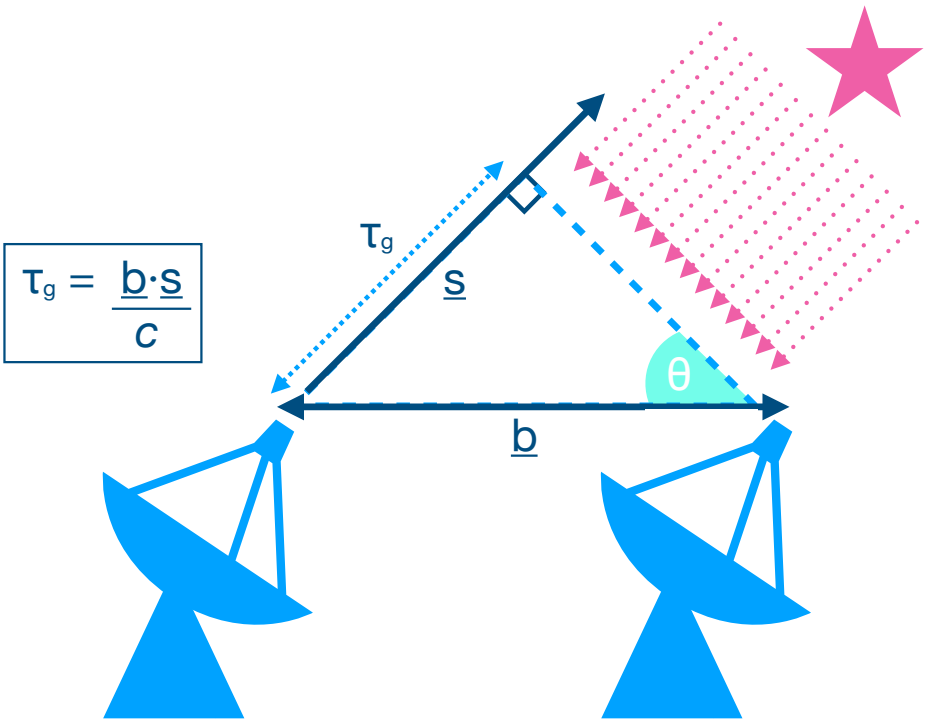

Figure 2.1: A diagram showing the geometry of two interferometers and the delay term that has to be added for incoming signals to sample the same phase. The pink star and arrows represent the target source and its emission.

added to the received signals between antennas to correct for the different distances they have travelled,

$$\tau_{ij} = \frac{\vec{b} \cdot \hat{s}}{c}, \tag{2.2}$$

where τ_{ij} is the delay term between antennas i and j, $\vec{b}$ is the baseline, $\hat{s}$ is the unit vector from the direction of the source and c is the speed of light (see Figure 2.1). Once these signals have been adjusted to be in phase there are two ways in which the incoming radiation to the antennas can be combined : adding and correlating.

An adding interferometer adds together the signals from individual antennas. This is a fast method as the processing load is low and so the beam can be formed instantaneously. It is best for observations that need a quick response and high time resolution, such as in the event of observing transients or the period of a pulsar. However, this in turn means they are susceptible to time dependent sources of interference

such as man-made signals, variability of noise in the instrument and atmospheric disturbances.

A correlation interferometer multiplies and averages the inputs from the antennas. Although this is more computationally intensive, the multiplication and averaging may resolve out sources of noise that are present in the observations from adding interferometers described above. A correlation interferometer is optimal for making high resolution images. The interferometers used for the work in this thesis are correlation interferometers, and shall be described in further detail in the rest of this Chapter.

When imaging with an interferometer, the aim is to sample the brightness distribution $B(\theta, \varphi)$ of the source. This is done via the spatial coherence function (SCF) from the Van Cittert-Zernike Theorem (van Cittert, 1934; Zernike, 1938),

$$< C(x_1, y_1)C(x_2, y_2) > = \iint B(\theta, \varphi) e^{-\frac{i2\pi}{\lambda}[(x_1 - x_2)\theta + (y_1 - y_2)\varphi]} \mathrm{d}\theta \mathrm{d}\varphi. \tag{2.3}$$

The SCF measures the degree of spatial coherence between a fixed point (x_1, y_1) and a variable point (x_2, y_2) in the amplitude of the diffraction pattern from the observed emission. The left hand side is the SCF and the right hand side is the Fourier transform of the brightness distribution of the target source. A correlation interferometer observes the SCF and so observations occur in Fourier space. Each baseline of the interferometer contributes a Fourier Component (FC) to the SCF.

The coordinate units in Fourier space are given in terms of (u,v). The definitions of u and v are,

$$u = \frac{bx}{\lambda} \qquad\qquad v = \frac{by}{\lambda},$$

where b is the length of the baseline and λ is the observing wavelength. (u,v) coordinates translate the physical units of (x, y) to be in units of wavelength.

When the SCF is converted into (u,v) coordinates, it becomes the visibility equation $V(u, v)$,

$$V = Ae^{i\phi}, \tag{2.4}$$

where A is the amplitude and ϕ is the phase of the spatial coherence measured. These are expanded as follows in their relation to the components of the Fourier transform

of the brightness distribution of the target source,

$$A = [R_{\cos}(u,v)^2 + R_{\sin}(u,v)^2]^{\frac{1}{2}},$$

$$\phi = \arctan\left[\frac{R_{\sin}(u,v)}{R_{\cos}(u,v)}\right],$$

$$R_{\cos} = \iint_{\text{source}} B(\theta,\varphi)\cos[2\pi(u\theta + v\varphi)]\,\mathrm{d}\theta\mathrm{d}\varphi,$$

$$R_{\sin} = \iint_{\text{source}} B(\theta,\varphi)\sin[2\pi(u\theta + v\varphi)]\,\mathrm{d}\theta\mathrm{d}\varphi.$$

In the (u,v) plane, long baselines correspond to small angular scales on the sky and vice-versa. In the (u,v) plane, there are twice as many points as baselines. Since in Fourier space we deal with the complex conjugate of any point, and so sample the (u,v) plane twice. It corresponds to the fact that a single baseline is counted twice, i.e. from antenna 'a' to antenna 'b', and antenna 'b' to antenna 'a'.

As mentioned already, an interferometer is akin to a single dish with many gaps, but there are several ways to fill the (u,v) plane:

1. Add more antennas
2. Rearrange antennas
3. Increase the bandwidth of the observation
4. Observe for longer

Adding more antennas helps fill the (u,v) plane in a couple of ways. Not only does it fill the (u,v) plane with more points, but adding more antennas in a combination of various baselines increases the number of angular scales observed. Having a lack of short or long baselines means that observations do not include the large or small scale structure that correspond to those baselines. One of the major pitfalls of interferometers is that it is impossible to have a 'zero' baseline, meaning there is always some limit on the largest scale emission observed with an interferometer. To compensate for this, one can observe with a single dish radio telescope to access these large angular scales.

Rearranging antennas is another useful way to increase (u,v) coverage. Though this is only possible if combining data from several observations, the different baseline lengths introduce new FCs to the (u,v) plane.

Increasing the bandwidth of observations is akin to adding additional baselines in terms of (u,v) coverage due to (u,v) distance being measured in units of wavelength. Thus multi-frequency synthesis imaging (Conway et al., 1990) fills out the (u,v) plane radially.

Lastly, as the Earth rotates, the interferometer scans across the sky and lengthens the (u,v) plane tracks (see Figure 2.2) or projected baselines. This is because, in relation to the sky, the interferometer has changed position and thus samples more spatial frequencies.

A final aspect of observing with an interferometer to consider is the sensitivity (ΔT) of the instrument, measured in Kelvin. ΔT is reliant on several factors and is given by the Radiometer equation;

$$\Delta T = \frac{T_{\rm sys}}{(\Delta\nu \cdot \tau)^{\frac{1}{2}}(D^2/Nd^2)} \tag{2.5}$$

The system temperature T_{sys} is clearly a factor to keep as low as possible, though other properties of the interferometer and observations can help improve ΔT. The observing bandwidth ($\Delta\nu$) not only helps add additional FCs, but is generally a source of more data and thus increases the signal to noise ratio (S:N). The integration time (τ) works similarly. The diameter of the synthesised aperture (D) contributes in that it is increasing the size of the collecting area of the synthesised aperture. The number of antennas (N) increases the number of baselines and thus FCs and there are simply more dishes and so the actual collecting area is higher. Though each antenna brings noise to the system. Lastly, the diameter of the individual antennas (d). d determines the field of view of the observations as well as collecting area of the interferometer.

2.2 Imaging

The raw data requires a lot of work before the final radio image is produced. During the observation process, several factors can affect the quality of the data. A particular antenna or baseline in an observation may have been under-performing, or a strong source of Radio Frequency Interference (RFI) may have crossed the sky during observation.

There is also the task mentioned above of filling the (u,v) plane to obtain information on all spatial scales. Although one can try to fill the (u,v) plane with as many

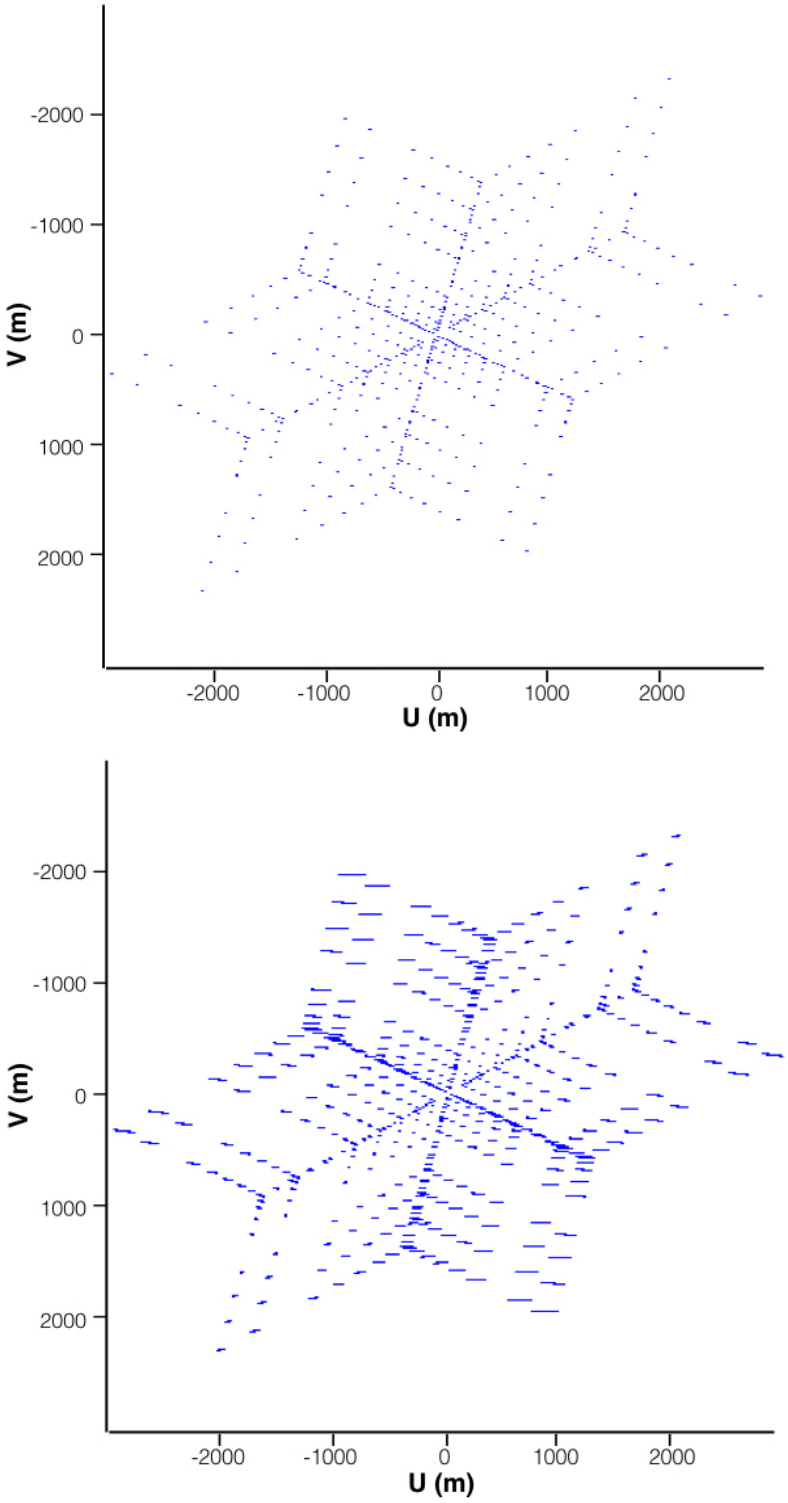

Figure 2.2: Comparison of (u, v) tracks while observing using the VLA for 1 minute of observing time (*top*) compared to the full observing schedule for this particular observation (24 minutes, *bottom*). One can clearly see that the (u, v) plane starts to fill up with longer observations.

antennas, a wide bandwidth and long observations as possible, there will always be gaps. As such, to achieve an image some reconstruction has to take place to make a well-educated guess as to what is in the gaps in spatial frequency. These gaps mean that there is missing data, which corresponds to the scales on the sky not represented by baselines on the ground.

The imaging process is a combination of estimating missing information, removing noise and disentangling the target source ($T(x, y)$) from the beam created by the interferometer ($S(x, y)$). The two result in the 'dirty image', $T^D(x, y)$,

$$T(x, y) \star S(x, y) = T^D(x, y) \tag{2.6}$$

$$V(u, v) \times S(u, v) = V^S(u, v) \tag{2.7}$$

$S(x, y)$ is also know as the synthesised beam and is *convolved* ($\star$) with the true flux distribution of the sky, $T(x, y)$. The Fourier transform of the true sky distribution is the visibility function $V(u, v)$ which I have mentioned previously in this Chapter. The PSF becomes the sampling function, $S(u, v)$, which is a function of how the interferometer samples the (u,v) plane plane. $V^S(u, v)$ is the sampled visibility function in Equation 2.7. The PSF corresponds to the resolution, e.g. a large PSF will smear and distort any source smaller than it.

Bad antennas and RFI can be manually flagged and removed through the use of the Common Astronomy Software Applications (CASA McMullin et al., 2007). CASA enables plotting of various aspects of the observation against another, e.g. amplitude against time, antenna, baseline etc. Through visual inspection, one can select data points that appear contaminated and look for correlations with time, antenna, spectral window and remove these problem factors from the observation.

The task of removing the effects of the beam and extrapolating over the informational gaps is achieved by the algorithm CLEAN.

2.2.1 CLEAN

CLEAN (Högbom, 1974; Schwarz, 1978) works on the premise of iteratively constructing a model of the sky for a particular observation. It is based on two key assumptions,

1. The sky is positive,

2. The sky is comprised of point-like sources.

The steps are as follows:

1. Fourier Transform the sampled visibility function $V^S(u,v)$ and the sampling function $S(u,v)$ to obtain the dirty map $T^D(x,y)$ and the PSF $S(x,y)$ respectively.

2. Identify the brightest point in the dirty map,

3. Subtract a model of the PSF centred on that point, this is a CLEAN component.

4. Update the map.

5. Go back to step 1 and repeat until the residual map has no peaks greater than the noise.

6. Finish the process by convolving all of the CLEAN components (CCs) with an idealised 'CLEAN' version of the PSF, modelled on the central lobe of the PSF, and adding to the residual image.

This is the most basic version of CLEAN, known as `Hogbom`-CLEAN (Högbom, 1974). It is a continually iterative approach and is performed entirely in the image domain, meaning only *minor* cycles are done after the first major cycle (Fourier Transforming from (u,v) space to the image domain). Computationally, this makes it an efficient method as Fourier Transforms are expensive. However, if an image has a PSF with high sidelobes then the `Högbom` method is susceptible to errors, especially if an inappropriate weighting scheme is chosen. A weighting scheme is the method of choosing different weights to the visibility points.

A similar method was developed by Clark (1980), but differs by using a cropped version of the PSF. This speeds up the minor cycle process, but is unsuitable for observations with a wide field of view. `Clark`-CLEAN also involves *major* cycles. In a major cycle, the point source model of the CCs is fast Fourier Transformed to the (u,v) plane, multiplied by a weighted sampling function, fast Fourier Transformed back to the image domain and then subtracted from the dirty map. A major cycle is triggered when the brightest peak in the residual map is below the first sidelobe level of the brightest source in the initial residual map.

CSCLEAN (Schwab & Cotton, 1983) is a commonly used version of CLEAN and also uses a combination of major and minor cycles. However, the difference with CSCLEAN is that the CCs are subtracted while in the (u,v) plane, where the data is un-gridded. The data is then re-gridded to form a new residual image. The way in which the data is re-gridded depends on the chosen weighting scheme.

The aforementioned CLEAN algorithms are implemented in the Common Astronomy Software Applications (CASA, McMullin et al. (2007)). CASA is one of the most widely used applications for reducing and imaging radio data, along with the NRAO's Astronomical Imaging Processing System (AIPS). Other software exists which help to tackle specific issues more efficiently than AIPS or CASA. For example, WSCLEAN (Offringa et al., 2014) was developed to image wide field of view observations more efficiently than is possible with the w-projection method in CASA (Cornwell et al., 2008).

2.2.1.1 Important CLEAN parameters

The weighting of the data that occurs in major cycles is an important and adjustable parameter. There are two extremes: Natural and Uniform weighting. In simple terms, Natural weighting weights each visibility point equally, whereas Uniform weighting weights each visibility point inversely proportionally to the number of points within an image cell. In relation to how the data is gridded, this translates that each image cell under a Natural weighting will have a different weight, whereas under Uniform weighting each cell has the same weight by definition.

More precisely, the Natural weighting scheme allocates a weight for each visibility point that is inversely proportional to the noise at that point and is the natural sensitivity of the interferometer. i.e., for the i^{th} visibility point, the weight (W_i) is given by,

$$W_i = \frac{1}{\sigma_i^2}, \tag{2.8}$$

where σ_i is the rms noise contribution. This means that points in areas of low noise are weighted more highly. Natural weighting is preferable if the aim is to achieve high sensitivity in the image, since the image benefits from regions of high signal to noise ratio. However, in some interferometers the visibility points are more densely populated at the centre of the (u,v) plane(e.g., which in turn means that less weight is given at the edges. Since the points furthest from the centre on the (u,v) plane determine the resolution of the image, natural weighting substitutes high resolution for the sensitivity it achieves.

On the other end of the scale, Uniform weighting sacrifices sensitivity for high angular resolution. A Uniform weight is initially calculated as in the Natural weighting, but after all of the data is weighted and then gridded onto a number of cells in the (u,v) plane, it is then re-weighted such that each cell has a uniform weighting. By giving equivalent weight to points on the edge of the (u,v) plane as in the centre, it

reduces the sidelobes of the PSF and obtains the highest possible resolution. However, the sensitivity is diminished, as the regions with the most visibility points are down-weighted relative to long baselines.

Between these two weighting schemes is a compromise, Robust weighting (Briggs, 1995). The 'robust' parameter allows the user to determine the balance between a natural or uniform weighting scheme. A robust parameter of 2 represents purely Natural weighting, and a robust value of -2 is equivalent to weighting uniformly. Often values in the middle are chosen to obtain a balance of sensitivity and resolution in an image.

The size of the cells used to grid the data are determined by the diameter of the synthesised beam (Equation 2.1). The synthesised beam needs to be sampled at least twice according to the Nyquist-Shannon sampling theorem (Shannon, 1949) to ensure that the original signal is accurately reconstructed. Often the synthesised beam is sampled more times than this for good measure.

2.2.1.2 Difficulties with interferometric imaging

The two key assumptions of CLEAN; (i) the sky is always positive, (ii) the sky is populated by point-like sources, are largely reliable. However, the object of an observation may be to observe a nearby object, and wide field of view images of large samples of galaxies may contain extended sources that are present even in low resolution observations (e.g. FRI and FRII type sources, see Chapter 1). To model targets like this with CLEAN's assumption of point-like sources, they can be CLEANed interactively by gradually building a model of the source by conglomerating several points in the model map. Adopting multiple scales may also be necessary (Cornwell, 2008).

Other issues can arise depending on the configuration of the interferometer. If the baselines are long enough, the standard assumption that the Earth is flat (for the area of the interferometer) is no longer true as the curvature of the Earth comes into play. Wide-angle imaging is a difficult task with many additional factors to account for. The curvature of the Earth elongates the PSF of the interferometer when observing furthest from the zenith and can distort the PSF depending on the position. Additionally, calibration of sources is more complicated over wide angles as the conditions of the atmosphere can change over the observed field. With these issues in mind, it becomes necessary to include the direction of the sources in the image in the calibration stages. There are two approaches to overcome this: faceting and projection methods.

Faceting divides the sky into smaller components (or facets) and calibrates independently for each facet, basing that calibration on the brightest point in the facet (e.g. DDFacet; Tasse et al., 2018). The A-Projection method (Bhatnagar et al., 2008, 2013) works by including extra direction-dependent terms in the imaging process, so that calibration is changed based on the position in the image.

2.3 Interferometers

In this thesis, the data I use has been taken by several interferometers. I give a brief overview of them here.

2.3.1 VLA

The Karl J. Jansky Very Large Array (JVLA, or VLA) is a 27-dish interferometer situated in Socorro, New Mexico, US. The antennas are arranged in a Y-shape and are movable on a track-system to construct 7 different configurations. The configurations range from the largest baseline of 36.4km ('A' configuration) to the smallest of 0.035km ('D' configuration) with 2 in between; 'B' and 'C' configuration, as well as 3 hybrid configurations that have a combination of baselines ('AnB', 'BnC', 'CnD'). The VLA observes from 74MHz to 45GHz and each dish is 25m in diameter.

2.3.2 LOFAR

The LOw Frequency ARray (LOFAR) is a phased-array, primarily based in the Netherlands (see Figure 2.3). A phased array is one which electronically generates multiple beams simultaneously, adding the benefits of not only being able to cut down in observing time, but it is able to observe several parts of the sky at once. It is unlike other interferometers in that it utilises many small sensors instead of using a relatively low number of large dishes. It observes over the frequency range 10-240MHz using the Low (LBA : 30-80MHz) and High-Band Antennas (HBA : 120-240MHz). 13 of the 51 LOFAR stations reside outside the Netherlands in Germany, Poland, France, the UK, Sweden and Ireland.

2.3.3 MeerKAT

MeerKAT, originally the Karoo Array Telescope, is an SKA (Square Kilometre Array) pre-cursor radio interferometer consisting of 64 antennas, based in the Northern Cape of South Africa. Each dish is 13.5m in diameter; most of which (48/64) are

Figure 2.3: *Top:* an aerial view of the land that houses 6 of the LOFAR stations. *Bottom left:* the Low-Band Antennas (LBAs) that observe 30-80 MHz. *Bottom right:* the black casings that cover the High-Band Antennas (HBAs) that observe 120-240 MHz. *Image credits:* aerial view - Top-Foto, Assen; LBAs and HBAs - ASTRON.

concentrated within a central 1km region. The longest baseline is 8km. MeerKAT was designed to observe over the frequency range 0.58-14.5 GHz.

2.4 Surveys

Here I provide examples of surveys that have been, will be, or are in the process of being undertaken by the previously mentioned interferometers in Section 2.3. All of the mentioned surveys include an aim to understand galaxies and their evolution.

2.4.1 CHILES Con Pol

The COSMOS HI Large Extragalactic Survey Continuum Polarization (CHILES Con Pol) is a 1000 hour survey conducted with the VLA (Hales & Chiles Con Pol Collaboration, 2014). It covers a 0.2 $\deg^2$ region of the COSMOS field and is being observed at 1.4 GHz in full continuum polarization. At this frequency and in the VLA 'B' configuration, the resolution $\sim 5''$.

The COSMOS field is a well observed region of the Universe and so can be combined with existing data (e.g. McCracken et al., 2012; Laigle et al., 2016) to gain more insight than from an observation of a less well studied field. The goal of this particular survey is to be one of the deepest yet, aiming to reach 500 nJy sensitivities. A sensitivity level which, in the future, should be easily attainable with the Square Kilometre Array (SKA). This not only allows science to be done on faint and distant objects in the radio sky, but can be used as preparation in terms of methods and science goals for the SKA-era. The addition of polarisation data means that magnetic fields can also be investigated. CHILES Con Pol began observing in 2013 and is expected to finish in 2019, with a full data release in 2020.

2.4.2 LoTSS

The LOFAR Two-metre Sky Survey (LoTSS) is both a deep and wide survey that will cover the entire Northern sky (Shimwell et al., 2017). The bandwidth is 120-168 MHz and each of the 3170 pointings will be observed for 8 hours, aiming to reach a sensitivity of $\sim$100 μJy. This totals an observing time of 25,360 hours for the complete survey. For most of these pointings the resolution will be $5''$, depending on declination (e.g. Hale et al., 2019). The LOFAR baseline distribution of a highly compact core of stations with long international baselines mean that the survey will access both large and small scales.

As well as galaxies and their evolution, LoTSS aims to explore the formation and evolution of black holes, galaxy clusters and large scale structure. The survey will provide a unique perspective as low-frequency radio astronomy is less common than observations at Gigahertz frequencies. LoTSS began observing in 2014.

2.4.3 MIGHTEE

The MeerKAT International GHz Tiered Extragalactic Exploration (MIGHTEE) survey (Jarvis et al., 2016) is a radio survey conducted by the MeerKAT array in South Africa. It will survey 20 deg^2 at 900-1640 MHz down to $\sim 1\mu$Jy sensitivity. It is expected to reach $\sim 6''$resolution. The four extragalactic fields that make up the 20 deg^2 are some of the most observed and so have ancillary data to aid with further understanding extragalactic pursuits. These four fields are: XMM-LSS (Pierre et al., 2004), COSMOS (Scoville et al., 2007), ECDFS (Weiß et al., 2009) and ELAIS-S1 (Oliver et al., 2000; Rowan-Robinson et al., 2004).

2.4.4 Selection Effects

When conducting radio surveys, or any observation, selection effects occur from limitations of the observation. These selection effects prescribe the subset of sources or emission that ends up in the final data set. To be sure that sources are real and not an artefact of selection effects, one has to be aware of what these effects are.

Several factors which contribute to the selection of sources are:

1. Luminosity,
2. Redshift,
3. Spectral Index,
4. Angular size / diameter / source morphology

Luminosity and redshift (L and z) affect all types of observations. How bright and how far away sources are determines whether or not they are picked up by the observing telescope, given the flux limit of the survey. Even if a source is incredibly nearby, but faint, or intensely luminous but distant, it may not be picked up by the telescope. The factor of spectral index also affects this. The spectral index (α) is the measurement of the slope of the synchrotron radio emission,

$$S_\nu \propto \nu^{-\alpha} \tag{2.9}$$

where S is the flux density and ν is the associated frequency. α is used to K-correct the luminosity at a specific frequency given the redshift of the source. Thus the spectral index determines the severity with which a source becomes fainter as it is redshifted. A source with a steeper spectral index will drop out of a survey much faster than a flat-spectrum source with redshift. This not only affects observations on a source-by-source basis, but inevitably the limiting boundary on the L-z plane of the entire survey.

Often it is assumed sources have the same spectral index, typically between 0.7-0.8 (e.g. Sadler et al., 2002) which is often the mean spectral index value of a sample (e.g. Prescott et al., 2016; Smolčić et al., 2014; Mauch et al., 2013). However, a variety of reasons can cause the spectral index of a source to steepen or flatten whether due to age, orientation or absorption (e.g. Harwood et al., 2013; Orr & Browne, 1982).

In summary, to accurately try and understand anything about a sample of galaxies, one must take into account all the selection effects which determine the sample one ends up with after observing. Else, it may appear that there are physical processes occurring in the Universe when in fact it is just a lack of modeling distributions of sources in luminosity, redshift, spectral index and angular size. When properly accounted for, it is possible to see real trends and then uncover the physics behind them.

For example, many studies have seen a correlation between α and z, with high redshift sources exhibiting steep spectral indices ($\alpha > 1.2$). So much so in fact, that a steep spectral index is often used as selection criteria for finding high-redshift galaxies (e.g. van Breugel et al., 1999; De Breuck et al., 2000). However, Morabito & Harwood (2018) find that this criteria can be relaxed to lower values of 0.9 or 0.8 when taking into account properly selection effects to find more high redshift sources. They also find that the steepening of the spectra that can be replicated by including increased Inverse Compton Losses in models. This is due to the increased density of the Cosmic Microwave Background at high redshift interacting with photons at the higher frequency end of the radio spectral energy distribution. By combining these two effects of one observational and the other physical onto local galaxies, they are able to reproduce the trends seen at high redshift.

With this in mind, it motivates the work produced in this thesis, to determine robust, reliable and convincing RLFs to find out more about the underying physical processes affecting galaxies and their evolution.

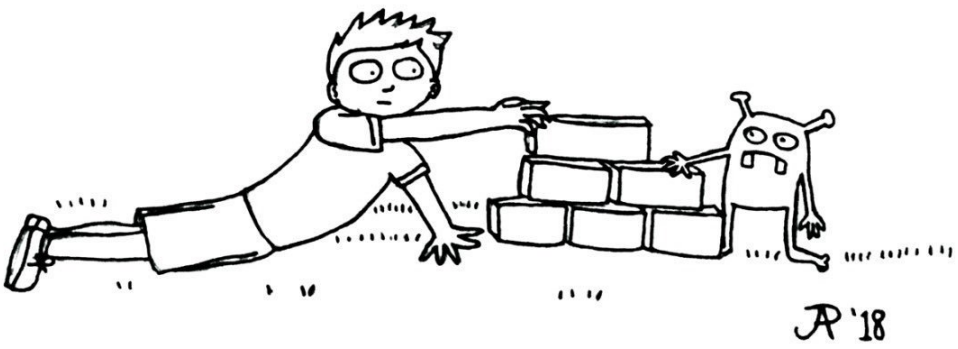
'18

Chapter 3

150 MHz Radio Luminosity Functions Of The XMM-LSS Field

3.1 Introduction

As outlined in Chapter 1, there is a great deal of motivation for including spectral index information, for individual sources and the sample as a whole, in the calculation of RLFs. It is with this in mind that I present the application of the methods outlined in Jarvis & Rawlings (2000); Jarvis et al. (2001) and Yuan et al. (2016) to new ~ 1.5 GHz and ~ 150 MHz observations of the XMM-LSS field with the Very Large Array (VLA) and Low Frequency Array (LOFAR) respectively.

In Section 3.2 I describe the data used in this study. In Section 3.3 I go into detail describing the model fitting process. I present my results in Section 3.4, and discuss these in Section 3.5, ending with conclusions and summary in Section 3.6.

3.2 Data

To model the RLF over luminosity (L), redshift (z) and spectral index (α) observations at different frequencies are required. The radio data sets used in this Chapter are Very Large Array (VLA) and Low Frequency Array (LOFAR) observations at 1.5 GHz and 150 MHz respectively. The 150MHz observations provide the base for the RLFs and the 1.5 GHz measurements are used to measure the spectral index for each source. Redshift information for each source comes from optical and near-infrared observations from the VISTA Deep Extragalactic Observations (VIDEO) survey (Jarvis et al., 2013) and optical measurements by Canada France Hawaii Telescope (CFHT) and Subaru. The following sections describe these data sets.

3.2.1 Karl J. Jansky Very Large Array (VLA)

The 1.5 GHz observations were taken using the Karl J. Jansky Very Large Array (VLA) (Heywood et al., prep). They cover $\sim$6.8 deg^2 of the XMM-LSS field and were observed using L-band (1-2 GHz) while the VLA was in B configuration, which gives the image an angular resolution of $\sim$4.5″.

The observations were taken in 90 minute observing blocks for each of the 32 pointings that make up the final map. The time on source was 67.5 minutes per pointing. This length of observing time gives a final map with a median depth of 16 μJy beam^{-1}.

The data were processed and imaged by Dr Ian Heywood, I provide a very brief summary here. The observations initially went through the CASA pipeline before being examined visually to identify any sources of RFI and then through a second round of the CASA pipeline. The imaging was performed using WSCLEAN (Offringa et al., 2014), also using PyBDSF to identify significant features in the images that could then be masked in subsequent imaging stages. Direction-dependent calibration was also applied due to the wide area of the map.

Source catalogues were constructed using ProFound (Robotham et al., 2018; Hale et al., 2019) and PyBDSF. I use the PyBDSFcatalogue, which comprises 7,185 sources, for ease of comparison with the LOFAR data. PyBDSFwas initially designed to extract sources from LOFAR data, but can decompose radio images observed by any interferometer. It works by calculating the background rms and using a set threshold (of a defined σ above the background emission, in this case 5σ) to find islands of emission above this set threshold. Each island is fit with multiple Gaussians and a catalogue is produced which can be of each island or each Gaussian individually. Over the 4.5 deg^2 area overlap with the VIDEO data (described below) the catalogue has an rms of 16μJy/beam and the catalogue is 50% complete at 100μJy/beam. These data are used again in Chapter 5 where I present further details on the data reduction, for full information see Heywood et al. (prep).

3.2.2 Low Frequency Array (LOFAR)

To measure the spectral index of the sources I require a second set of observations at another frequency. Lower frequencies are preferable because the synchrotron emission dominates (see Chapter 1).

In this Chapter I use data from 12 hours of observations at 150 MHz from LOFAR (Hale et al., 2019). The observations were taken over three four-hour observing blocks

on 22 December 2015, 27 February and 1 March 2018. The High Band Antenna (HBA) was used with a frequency range that spans 120-168 MHz.

The data were processed using the LOFAR pipeline to ensure the calibration was accurate for each LOFAR station. Direction-independent calibration was performed first, followed by direction-dependent calibration. The direction-dependent calibration utilised the faceting technique (see Chapter 2) to divide the large sky area into smaller facets that can be independently calibrated depending on their direction. Both DDFacet and killMS were used to calibrate and image the data in a direction-dependent way.

The final image was corrected for the primary beam and created over a restricted region to only include regions that had a primary beam response $\gtrsim 50\%$. The data covers a 27 deg^2 elliptical image of the sky with a resolution of 7.5″ by 8.5″ and a central rms of 280 μJy beam^{-1}. The ellipse is in the North-South direction and is centred at a J2000 declination of $-4.5°$. The central frequency is 144 MHz.

To extract sources from the image to form a catalog, Hale et al. (2019) used PyBDSF. The final catalog contains 3,044 sources once correcting for individual radio components of the same source that had been identified as multiple sources. See Hale et al. (2019) for more details.

3.2.3 VIDEO

The VIDEO survey (Jarvis et al., 2013) covers 12 deg^2 of sky and is observed in the near-infrared using Z, Y, J, H and K_s bands. The survey area encompasses three fields: XMM-LSS (Pierre et al., 2004), ECDFS (Weiß et al., 2009) and ELAIS-S1 (Oliver et al., 2000; Rowan-Robinson et al., 2004). The design of the survey is such to examine the evolution of galaxies and large scale structures from $z = 4$ to present day as well as AGN and the most massive galaxies as far back as the epoch of reionization.

The VIDEO survey data has been combined with visible wavelength data from a combination of HyperSuprimeCam (HSC; Miyazaki et al., 2006) and CFHT Legacy Survey (Cuillandre et al., 2012) imaging, and photometric redshifts are estimated using LePhare (Arnouts et al., 1999; Ilbert et al., 2009). The photometry and photometric redshifts were supplied by the VIDEO team, namely Matt Jarvis, Rebecca Bowler and Nathan Adams. I used these data, which cover 4.5 deg^2 along with the radio data in this Chapter. The accuracy of the photometric redshifts is $\sigma = 0.023$ (from the Normalised Median Absolute Deviation, Jarvis et al. (2013)). This is well

within the redshift bin width of $z = 0.5$ that I will use in this work and so will not affect the analysis or results.

3.2.4 Cross-matching

The final sample is derived from combining the VIDEO, VLA and LOFAR data. The deep VLA data is first cross-matched with the VIDEO data, so that each galaxy is associated with a galaxy with a photometric redshift estimate. This is initially done via likelihood ratio (McAlpine et al., 2012) and then followed by visual inspection to ensure that radio sources with multiple components are not identified as separate galaxies in the VIDEO data. The visual inspection of sources was carried out by Matt Jarvis, Leah Morabito and Catherine Hale. Every source was categorised as to whether it was a compact source, a component of a source with multiple radio components or unidentifiable. As well as the category, the most probable candidate from the VIDEO catalogue was also identified from visual inspection. After the individual inspections of the sources, the final consensus on the nature of each source was decided as a group to ensure reliability in the classifications.

The cross-matching between the VIDEO and the VLA data has been performed for both unresolved and extended sources, although I note that the beam may "resolve" out larger scale emission from a galaxy that is resolved (see Chapter 2).

The VLA sample is then cross-matched with the LOFAR data where both observations overlap in the VIDEO-XMM-LSS field. The area of overlap between the LOFAR and VLA observations is $\sim$6.8 deg^2. I match all galaxies that are within $5''$ of one another. Further to this, remaining galaxies are then visually inspected to find any remaining matching counterparts.

3.2.5 Final sample

The cross-matched sample is composed of 560 sources over a redshift range $0.04 < z < 5.77$ and spectral index range of $-0.5 < \alpha < 3.8$. Every radio galaxy is matched to a VIDEO-ID and thus the sample is 100% complete in terms of redshift. A flux limit of 1800 μJy is imposed at 150 MHz which brings the sample count to 534 sources. This high flux limit is imposed to ensure that the flux cut off of the sample at low frequencies is consistent and well above the rms noise across the whole of the part of the image used and also to ensure we are not biased against very steep spectrum sources given the flux-density limit of the VLA sample. With this flux-density limit

Catalogue	Area (deg^2)	Sources	Flux Limit	Sensitivity Threshold	Completeness
VLA	6.8	7,185	0.08 mJy/beam	5σ	N/A
LOFAR	27	3,044	1.4 mJy/beam	5σ	50%
VIDEO	12	$> 10^6$	$K_s < 23.7$	5σ	90%
Sample Used	4.5	432	1.8 mJy/beam	6.4σ	70%

Table 3.1: Summary table showing the content and characteristics of the parent samples and cross-matched sample. The flux limit of the cross-matched sample is determined by the adopted flux limit of the LOFAR catalogue as this is the highest, and only sources present in both catalogues are used. As noted in the text, the sensitivity of the VLA data permits cross-matching to sources with a spectral index as steep as $\alpha = 1.4$. Furthermore, we adopt a low-luminosity cut in the LOFAR selection at $L_{150\mathrm{MHz}} > 10^{24}\mathrm{WHz}^{-1}$ to select AGN only.

we are able to measure spectral indices as steep as $\alpha = 1.4$ for the radio sources at the detection limit.

However, the luminosity range is such that I am probing two luminosity functions: those of star forming galaxies and AGN. Mauch & Sadler (2007) show that star-forming galaxies dominate up to a luminosity at 1.4 GHz of $L_{1.4\mathrm{GHz}} = 10^{23}\,\mathrm{WHz}^{-1}$. I restrict the sample to only include sources with $L_{150\mathrm{MHz}} > 10^{24}\mathrm{WHz}^{-1}$ to ensure only AGN are selected. Including only sources likely to be AGN reduces the sample by 88 sources down to 446.

The AGN sample spans a redshift range of $0.04 < z < 5.77$ (Figure 3.2). Since there are few sources with redshifts above $z \sim 3$, and those that are have much higher photometric redshift uncertainty, only sources with $z < 3$ are used in this Chapter. This further reduced the sample by only 14 sources, to the final sample of 432 galaxies, which includes only AGN. The sample has a spectral index range of $-0.13 < \alpha < 3.8$ (see Figure 3.3). 15.7% of the sample is considered 'flat' by the definition $\alpha < 0.5$. The mean spectral index is $\alpha = 0.88$. The overall span in luminosity range is 10^{24} $\mathrm{WHz}^{-1} \lesssim L_{150\mathrm{MHz}} \lesssim 10^{29}$ WHz^{-1}.

As mentioned in Chapter 2, there is evidence for a correlation between high redshift sources and a steep spectral index (e.g. Roettgering et al., 1997; Saxena et al., 2018). If present in this sample, the modelling of the α-distribution would require a dependence on z. However, the sources in the final sample show no evidence of correlation (see Figure 3.4) with a Pearson's r correlation coefficient of 0.02.

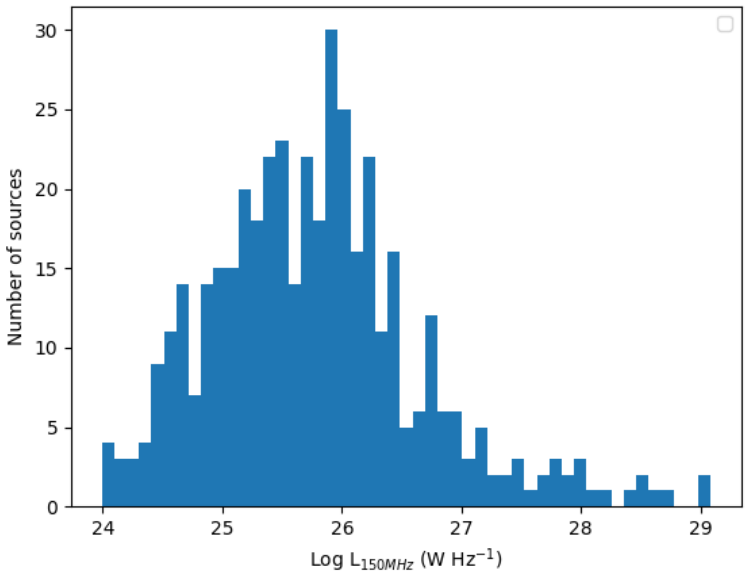

Figure 3.1: Histogram showing the radio luminosity distribution of the final sample of 432 AGN.

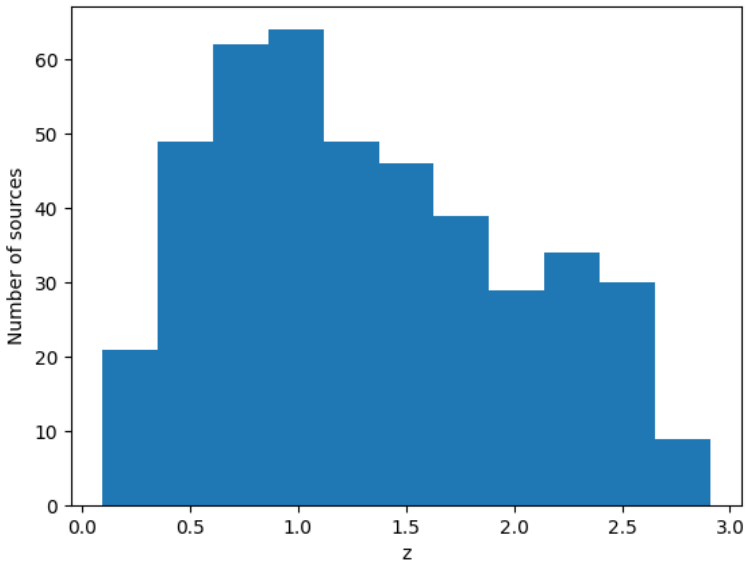

Figure 3.2: Histogram showing the redshift distribution of the final sample of 432 AGN.

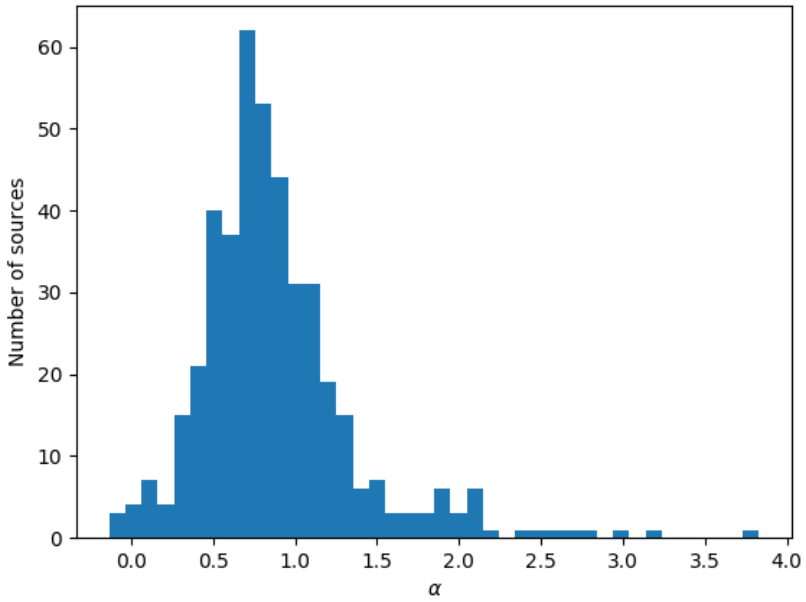

Figure 3.3: Histogram showing the distribution of the sample in Spectral Index between 1.5 GHz and 150 MHz.

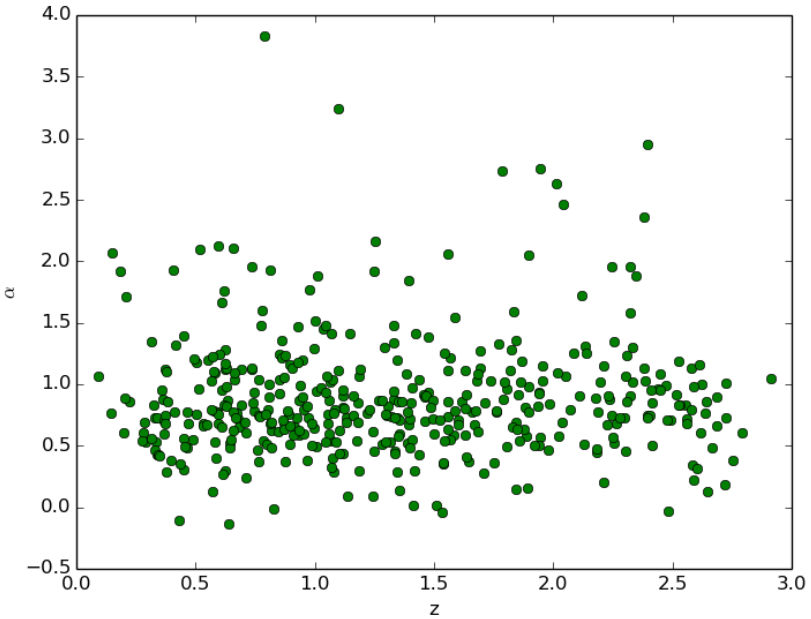

Figure 3.4: The data points in the final sample are shown in green, plotted according to their spectral index (α) and redshift (z) values. The data points appear to be evenly distributed and indeed have a Pearson's r correlation coefficient of 0.02, showing no evidence for a correlation.

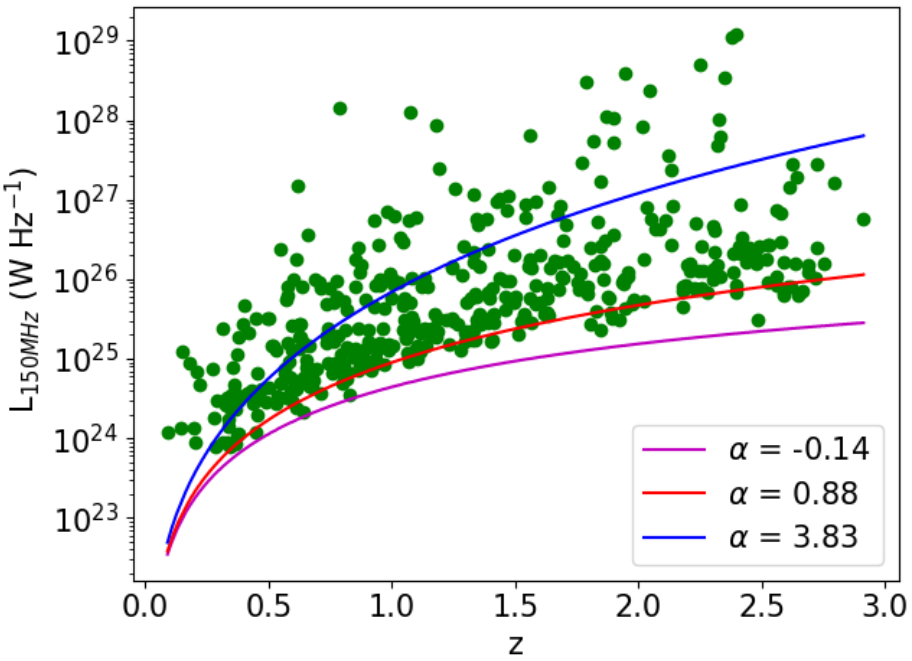

Figure 3.5: 150 MHz luminosity against redshift for the AGN sample (*green markers*). Over-plotted are the truncation boundaries calculated from the minimum (*magenta*, $\alpha = -0.14$), mean (*red*, $\alpha = 0.88$) and maximum (*blue*, $\alpha = 3.83$) spectral indices.

3.3 The Radio Luminosity Function

Here I describe the most commonly used non-parametric method to calculate luminosity functions ($\frac{1}{\mathrm{V_{max}}}$; Schmidt, 1968), along with the parametric models that encompass the two most commonly used parameterisations of redshift evolution (Pure Density Evolution described in Section 1.3.2.1 and Pure Luminosity Evolution described in Section 1.3.2.2). In Section 3.3.2 I describe the parametric models using luminosity, redshift and spectral index.

3.3.1 $\frac{1}{\mathrm{V_{max}}}$

LFs are typically measured using a non-parametric method known as $\frac{1}{\mathrm{V_{max}}}$ (Schmidt, 1968). For a sample of N data points contained in a luminosity bin of width ΔL the $\frac{1}{\mathrm{V_{max}}}$ LF is estimated by,

$$\phi_{1/V_{\mathrm{max}}(L,z)} = \frac{1}{\Delta L} \sum_{i=1}^{N} \frac{1}{V^i_{\mathrm{max}}}, \tag{3.1}$$

where V^i_{max} is the maximum volume available to observe a specific source of a given luminosity and spectral shape given the flux limit and area of a survey. V^i_{max} is de-

termined by finding the maximum observable redshift, $z^i_{\rm max}$, by iteratively increasing the redshift of the source by some Δz. This is increased until the source falls below the flux limit of the survey. The resulting $\phi_{1/V_{\rm max}}(L, z)$ gives us the number density of sources for a given redshift z and luminosity L.

3.3.2 Parametric models

It is common to estimate RLFs using the $\frac{1}{\rm V_{max}}$ method described in Section 3.3.1. While $\frac{1}{\rm V_{max}}$ works well locally, at higher redshifts it becomes unreliable for sources near the flux limit. $\frac{1}{\rm V_{max}}$ accounts for changes in volume and redshift through the fact that it is constructed using the comoving volume, but the increasing changes in the truncation boundary due to the increasing prevalence of the flux limit and decreased range in observable spectral indices with redshift means that estimations of the RLF near the flux limit can be unreliable. A way to address this is through parametric modeling of the RLF.

Parameterizing the distribution of galaxies over observed variables means that we are not relying on our observations to tell the whole story, but that they are consistent with some model of the number density of galaxies. This helps remove the impact of selection effects on a sample, i.e. how the flux limit of a survey needs to be considered at the low luminosity end.

First, I discuss the bivariate model which integrates over luminosity (L) and redshift (z). Second, I cover the improvements that can be made in measuring the RLF by including spectral index (α) information. α is highly significant for accurately determining radio luminosity functions as it affects the K-corrections for adjusting the rest-frame luminosity given the redshift and therefore influences the redshift that a given galaxy can be observed to.

3.3.2.1 ρ(L,z)

Bivariate modeling of the RLF parameterises the distribution of galaxies over luminosity and redshift. Typically, a double power law is used (e.g. Mauch & Sadler, 2007),

$$\rho_L = \frac{\rho_0}{\left(\frac{L_*}{L}\right)^A + \left(\frac{L_*}{L}\right)^B}, \tag{3.2}$$

where ρ_0 is the normalisation at $2L_*$ and A and B are the parameters that describe the two power-laws that combine to form a double power law. Equation 3.2 is then fitted in each redshift bin.

There is also the option to model the redshift evolution of population of sources. In this case,

$$\Phi_0 = \rho_L \times \rho_z \tag{3.3}$$

where ρ_z is often assumed to be a single power law in $(1 + z)$. I use $\rho_z \propto (1 + z)^k$. A reason for adopting this parameterisation is for the most direct comparison with the literature, in which this format is commonly used. A drawback of this is that it assumes a constant evolution by the use of a single evolution parameter k. If there is a significant slow down in evolution at high redshift, fitting of the parameters might reduce the value of k to compensate for the change in rate of evolution over time. However, the majority of our sources will be at an intermediate redshift and the primary aim with this work is to compare the addition of the distribution of the spectral index with bivariate models in the literature. By using a parameterisation that resembles that used in other studies, the comparison of the incorporation of the spectral index alone is more evident.

Bivariate modeling considerably improves the measurement of the RLF. The shape is more consistent with the real RLF, whereby $\frac{1}{V_{max}}$ cannot measure the low luminosity end of the RLF as redshift increases as there are no sources in that part of parameter space in a flux-density limited survey. However, it does necessarily assume that the shape of the RLF does not evolve in a way that is not characterised by the parametric model. However, the use of a single spectral index means that there is a single flux limit for every sources in the survey, regardless of the spectral shape of an individual source. Furthermore, even if the individual spectral indices for each source are used, this also does not give the full picture as the model does not have a description of the underlying model of the spectral index distribution. I discuss this further in the next section.

3.3.2.2 ρ(L,z,α)

The value of the spectral index (α, where $S_\nu \propto \nu^{-\alpha}$) affects the maximum distance an object could be observed to be above the flux limit of a survey. This is known as the truncation boundary, i.e. the curve on the $L - z$ plane (see Figure 3.5). A flatter spectrum allows a source to be seen at greater redshifts and so the truncation boundary is flatter, providing a greater area in the $L - z$ plane. A steeper spectrum has the opposite effect. If all sources had the same spectral index, then the truncation boundary would be a single line. With multiple spectral indices in a sample, the boundary is a combination of multiple truncation boundaries with differing weights either side

depending on the distribution of spectral indices. Some studies include α when applying the K-correction in calculating $\frac{1}{\mathrm{V_{max}}}$, but the crucial aspect here is looking at the entire distribution of α's. The weights of the multiple truncation boundaries can be mistaken as a physical property of the sample and affect the calculation of the RLF.

A clear example of how this can be misinterpreted is the appearance of a "redshift cut-off" in the RLF (Dunlop & Peacock, 1990). The cut-off is a reported drop in number density with redshift, and whether this is luminosity dependent such that the most powerful radio sources drop off at higher redshifts than lower luminosity sources. On first inspection this seems like Malmquist bias; brighter objects can be seen to further distances. Jarvis & Rawlings (2000) and Jarvis et al. (2001) investigated this further by looking at the evolution of the most luminous flat and steep spectrum sources respectively. They find that for flat spectrum sources there is not enough co-moving volume to decidedly determine whether a cut-off exists and that for steep spectrum sources a constant co-moving density (i.e. no cut off) is the best fitting model. More recently, Yuan et al. (2016) (see their Figure 3) show that a redshift cut-off can be generated by $\frac{1}{\mathrm{V_{max}}}$hitting the flux limit of the survey, when in fact, there is no such physical evolution. If one ignores the fact that there is a distribution of spectral indices, then it may seem as if the number density of galaxies is physically dropping off as opposed to merely the differing individual truncation boundaries of each source.

Another artefact that can arise from forgoing the α-distribution is the underestimation of the rest frame luminosity of low-luminosity sources. If one assumes $\alpha = 0.7$ when in fact the real α is much flatter, the calculated rest-frame luminosity would be much lower than it actually is. Furthermore, if a sample contains a non-negligible fraction of flat-spectrum sources, then the RLF will be lower than it should be if calculated using $\alpha = 0.7$ for the sample (Yuan et al., 2016). When considering flat-spectrum sources separately from the rest of the sample, the low-luminosity end of the RLF can be underestimated by as much as an order of magnitude when not incorporating the distribution of α values.

Conversely, a population of steep spectrum sources being ignored can effect the RLFs in the opposite way. Both of these also impact the evolution parameter k, a surplus of flat-spectrum sources decreases the rate of evolution in luminosity whereas a surplus of steep-spectrum sources will increase it. This is due to the observational volume that these distinct groups of sources occupy. Flat spectrum sources can be observed further where steep spectrum sources have a much more limited observing

volume. By modelling the α-distribution and accounting for the α values a more reliable value for k can be found that is not subject to these observational influences which can appear physical.

Trivariate modeling accounts for the distribution in α and therefore corrects for this particular selection effect of a sample. A simple Gaussian form can be adopted,

$$\rho_\alpha = \exp\Big[-\frac{1}{2}\Big(\frac{\alpha-\mu_\alpha}{\sigma_\alpha}\Big)^2\Big] \tag{3.4}$$

where μ_α and σ_α are the mean and standard deviation of the spectral index distribution respectively. If required, these can be fitted for flat and steep spectrum samples separately or more complicated distribution models could be considered. Combining these with the more standard bivariate RLF is modelled as,

$$\Phi_{\rm PLE}\Big(\frac{L}{(1+z)^k}\Big) = \rho_0 \times \rho_L \times \rho_\alpha \tag{3.5}$$

for the PLE model and

$$\Phi_{\rm PDE}(L) = \rho_0 \times \rho_L \times \rho_z \times \rho_\alpha \tag{3.6}$$

for the PDE model. ρ_0 is the normalisation factor (where the $z = 0$ normalisation is incorporated into for PDE), ρ_L is the distribution in luminosity, ρ_α is the distribution in spectral index and, where applicable, ρ_z is the distribution in redshift.

3.3.3 Fitting the model

I use a trivariate model RLF as outlined above and test it against bivariate models as well as $\frac{1}{\rm V_{max}}$. For the $\frac{1}{\rm V_{max}}$ analysis on the sample I use increments of $\Delta z = 0.001$ to calculate $z_{\rm max}$. Individual values of α are included in the calculation of $V^i_{\rm max}$ for each source.

For the trivariate modelling I initially use an RLF model that contains 7 parameters to be fit: ρ_0, L_0, A, B, k, μ_α and σ_α, whereas the bivariate model only uses 5 as μ_α and σ_α are not included. k can be interchanged between PDE and PLE. These parameters will model the distributions of L, z and α in the sample and constrain the RLF.

To find the best fit to the model the maximum likelihood method is used, which is defined as $-2\ln\mathcal{L}$ where $\mathcal{L}$ is the likelihood function (See Marshall et al., 1983; Jarvis & Rawlings, 2000; Jarvis et al., 2001). This is re-labelled, where $-2\ln\mathcal{L} = S$,

$$\begin{aligned} S = &-2\sum_{i=1}^{N}\ln[\rho(L_{150i},\,z_i,\,\alpha_i)] \\ &+2\iiint \rho(L_{150},\,z,\,\alpha)\,\Omega(L_{150},\,z,\,\alpha)\,\frac{\rm dV}{\rm dz}\,{\rm d(log_{10}L_{150})}\,{\rm dz}\,{\rm d}\alpha, \end{aligned} \tag{3.7}$$

which, in order to maximise the likelihood, is minimised. Here $\Omega(L_{150}, z, \alpha)$ is the sky area available if a source has a flux that is above the flux limit of the sample, $\frac{\mathrm{dV}}{\mathrm{dz}}$ is the differential comoving volume element and $\rho(L_{150}, z, \alpha)$ is the model distribution as defined in Equations 3.5 and 3.6. The 150 MHz luminosity is used in this Chapter for it is the most reliable measurement in terms of being dominated by synchrotron emission, and also has the higher flux limit. Any source would drop out of the observations in 150 MHz before 1400 MHz. I model the data with the RLF evolving both as PLE and PDE.

3.3.4 Searching the parameter space

I use the popular Monte-Carlo Markov Chain (MCMC) python package EMCEE (Foreman-Mackey et al., 2013) to find the best fits for the parameters. EMCEE is an affine-invariant MCMC ensemble sampler that allows multiple walkers to sample the parameter space simultaneously. To test the reliability of this method I first apply it to a self-constructed simulated data set for which the input parameter values are known.

This is trialled in several stages. Integrating over:

1. luminosity (with fixed z and α),
2. luminosity and redshift (with fixed α),
3. the full parameter space.

Here I test the reliability of the parameter search.

The self-constructed data set is constrained by upper and lower limits for each variable and randomly samples the distributions in L, z and α. I use a simulated sample size of 600 to roughly mirror the real observations.

The results of the EMCEE run on the simulated data set converge well to the input parameter values (Table 3.2 and Figure 3.6). The parameter values are arbitrarily chosen, but are in the same prior range as expected from real observations (see also Table 3.2 for the priors).

After confirming that the parameter fitting is successful, this can now be applied to the real data. The form of the code remains the same, the only difference is that the true parameter values are unknown. The initial guesses for parameters are based on visual inspection of the $\frac{1}{\mathrm{V_{max}}}$ points for L_0, A and B and the calculated mean and variance of the spectral index measurements for μ and σ respectively. To speed

Table 3.2: The results of the RLF fitting on the simulated data. Input parameter values, lower and upper priors and measured values. The uncertainties are derived from the 16^{th} and 84^{th} percentiles.

	$\log_{10}\rho_0$	A	B	$\log_{10}L_0$	k	μ	σ
Input	-	1.5	0.5	23	3.7	0.7	0.3
Lower prior	-6.0	0.0	0.0	21.0	-2.0	0.0	0.0
Upper prior	-2.5	2.0	2.0	25.0	5.0	2.0	2.0
Result	$-3.95^{+0.22}_{-0.87}$	$1.41^{+0.13}_{-0.23}$	$0.43^{+0.06}_{-0.08}$	$22.7^{+0.24}_{-0.61}$	$3.75^{+0.02}_{-0.14}$	$0.70^{+0.01}_{-0.004}$	$0.31^{+0.01}_{-0.003}$

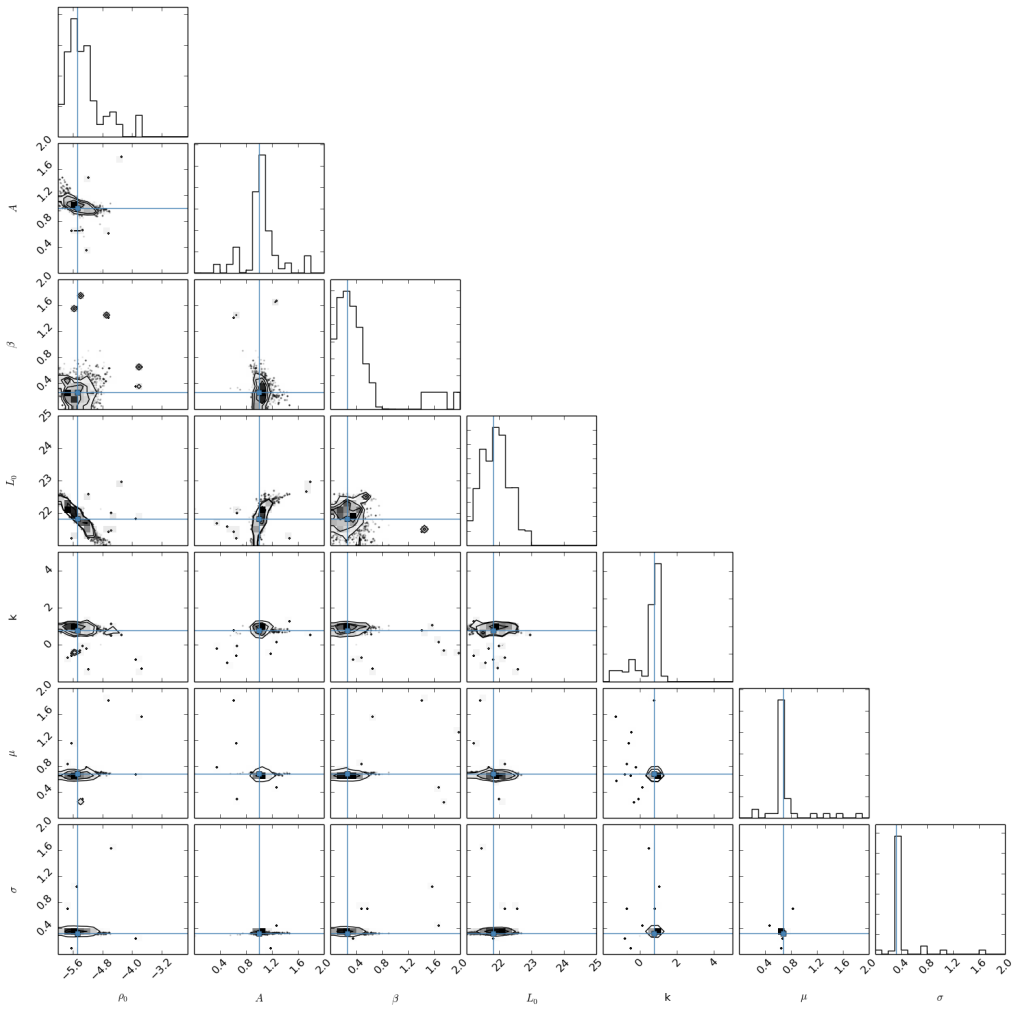

Figure 3.6: The results of the Emcee run on the simulated data set. The single peaks for each parameter shows the code to reliably find the input parameter values. Non-circular distributions in likelihood show a degeneracy between parameters. This particular run had 100 walkers that took 500 steps into parameter space.

up computation time I run the EMCEE process in parallel using IPYPARALLEL. The code is written in Python.

3.4 Results

The results for the parameters for the trivariate parameterisation are listed in Table 3.3. The corner plots for both PLE and PDE models (Figures 3.7 and 3.8) show the spread of values for each parameter and any degeneracies between the parameters, which are exemplified by non-circular distributions in parameter space. There is one case of a strong degeneracy: between L_0 and ρ_0, which is unsurprising as these two values determine the placement of the RLF on the $L - \phi$ plane. ρ_0 determines the normalization and thus the position of the RLF on the ϕ axis, whereas L_0 is responsible for the position of the knee in the RLF.

Figures 3.9 and 3.10 shows the fits of luminosity and redshift against the distribution of the data when corrected for the effects of the flux limit of the observations. These close fits between the data and the corrected model demonstrates the credibility of the fits. However, the mean value of α is skewed towards $\alpha = 1.0$, which is steeper than the median of the sample (see Figure 3.11) and the usual value of 0.7-0.8. The tail at the steep end ($\alpha > 1.5$), which consists of 35 sources, has skewed the mean away from the bulk of the sources. Therefore, this does not appear to be a good parameterisation of the α distribution. I discuss this further below. Using a Kolmogorov-Smirnov (KS) test I find that the probability of the data being drawn from the same underlying distribution as the model is only $p = 1.8 \times 10^{-7}$ for the PLE model and $p = 1.8 \times 10^{-7}$ for the PDE model.

The RLFs that emerge (in both cases) are close to a single power law (i.e. A and B are close in value to one another), encompass the $\frac{1}{V_{max}}$ points (Figure 3.12, 3.13 and 3.14) and there is little separation between the PLE and PDE models with similar likelihoods.

3.4.1 Pure Density Evolution

The parameter values for the results of the PDE model can be found in Table 3.3 and shown graphically in Figures 3.12, 3.13 and 3.14. In general, it fits within the error of the data for the $\frac{1}{V_{max}}$ points, with some deviation at the lowest and highest redshift bins due to the lower number of sources meaning the $\frac{1}{V_{max}}$ points are poorly constrained. The observed and predicted luminosity distributions match well (K-S test p value = 0.92 that the two samples are consistent with being drawn from

Model	ρ_0	A	B	L_0	k	μ	σ	$-2\ln L$
PLE, ρ(L,z,α)	$-5.15^{+0.55}_{-0.55}$	$0.67^{+0.07}_{-0.08}$	$0.65^{+0.06}_{-0.09}$	$25.2^{+0.84}_{-0.85}$	$0.83^{+0.17}_{-0.17}$	$0.98^{+0.02}_{-0.02}$	$0.52^{+0.02}_{-0.02}$	12483.05
PDE, ρ(L,z,α)	$-5.18^{+0.56}_{-0.53}$	$0.68^{+0.06}_{-0.07}$	$0.66^{+0.06}_{-0.07}$	$25.2^{+0.82}_{-0.81}$	$0.57^{+0.14}_{-0.12}$	$0.99^{+0.02}_{-0.02}$	$0.52^{+0.02}_{-0.02}$	12482.5
PLE, ρ(L,z)	$-4.8^{+0.33}_{-0.67}$	$0.74^{+0.07}_{-0.05}$	$0.39^{+0.12}_{-0.19}$	$24.9^{+1.09}_{-0.63}$	$0.51^{+0.24}_{-0.24}$	–	–	11882.8
PDE, ρ(L,z)	$-4.85^{+0.32}_{-0.66}$	$0.73^{+0.06}_{-0.04}$	$0.39^{+0.12}_{-0.19}$	$24.9^{+1.09}_{-0.63}$	$0.32^{+0.16}_{-0.16}$	–	–	11882.8

Table 3.3: Results. 150 walkers, PLE: 951 steps, PDE: 1324 steps. ρ(L,z), PLE: 17045 steps, PDE: 7407 steps.

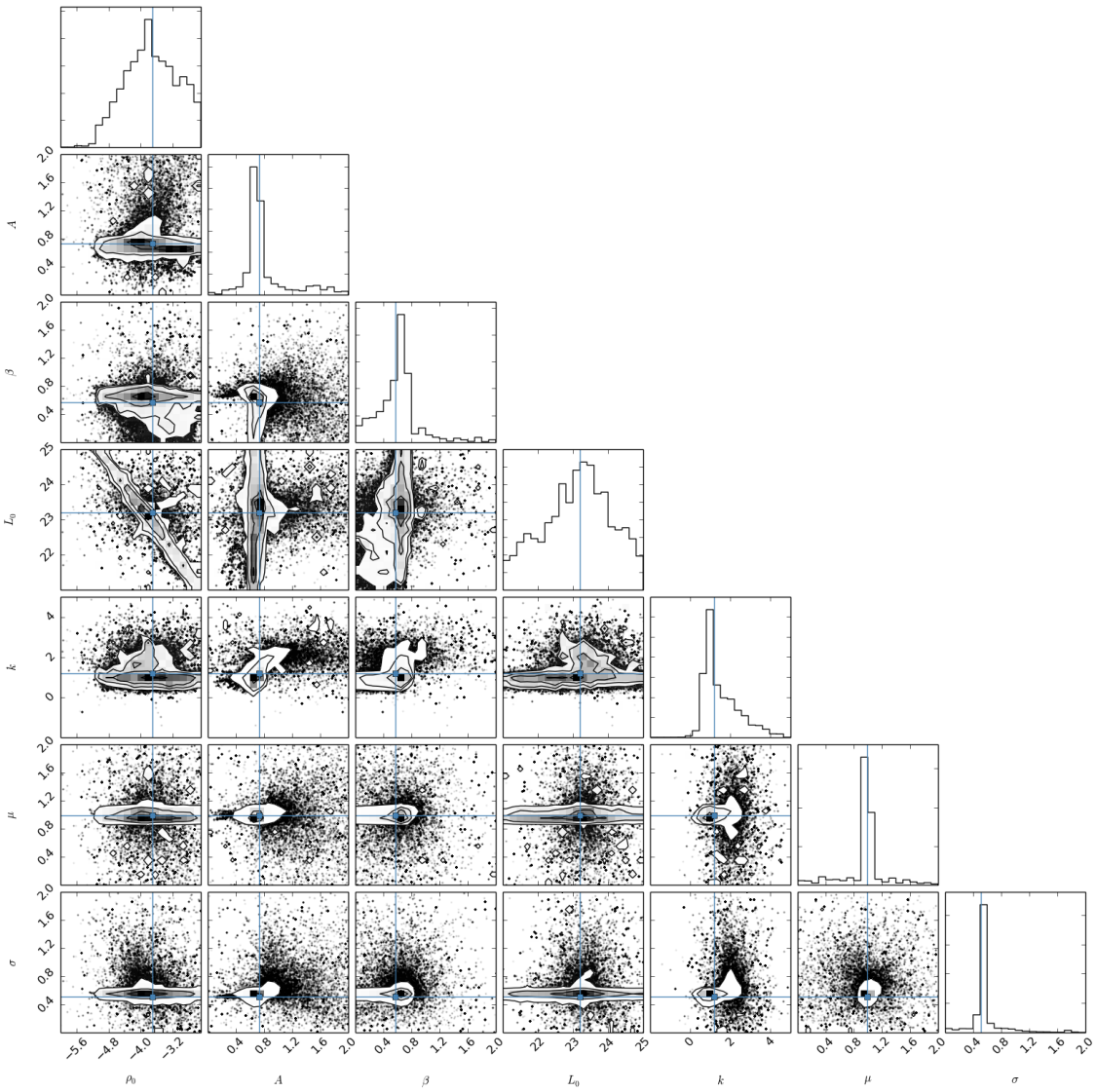

Figure 3.7: The results of the ρ(L,z,α) PLE model for parameters ρ_0, A, β, L_0, k, μ and σ respectively. The scatter plots show the relationships between all parameters where regions of high density show the most sampled regions of the prior from the MCMC algorithm, determined by minimising the likelihood. The histograms show the individual distributions in sampling the prior ranges.

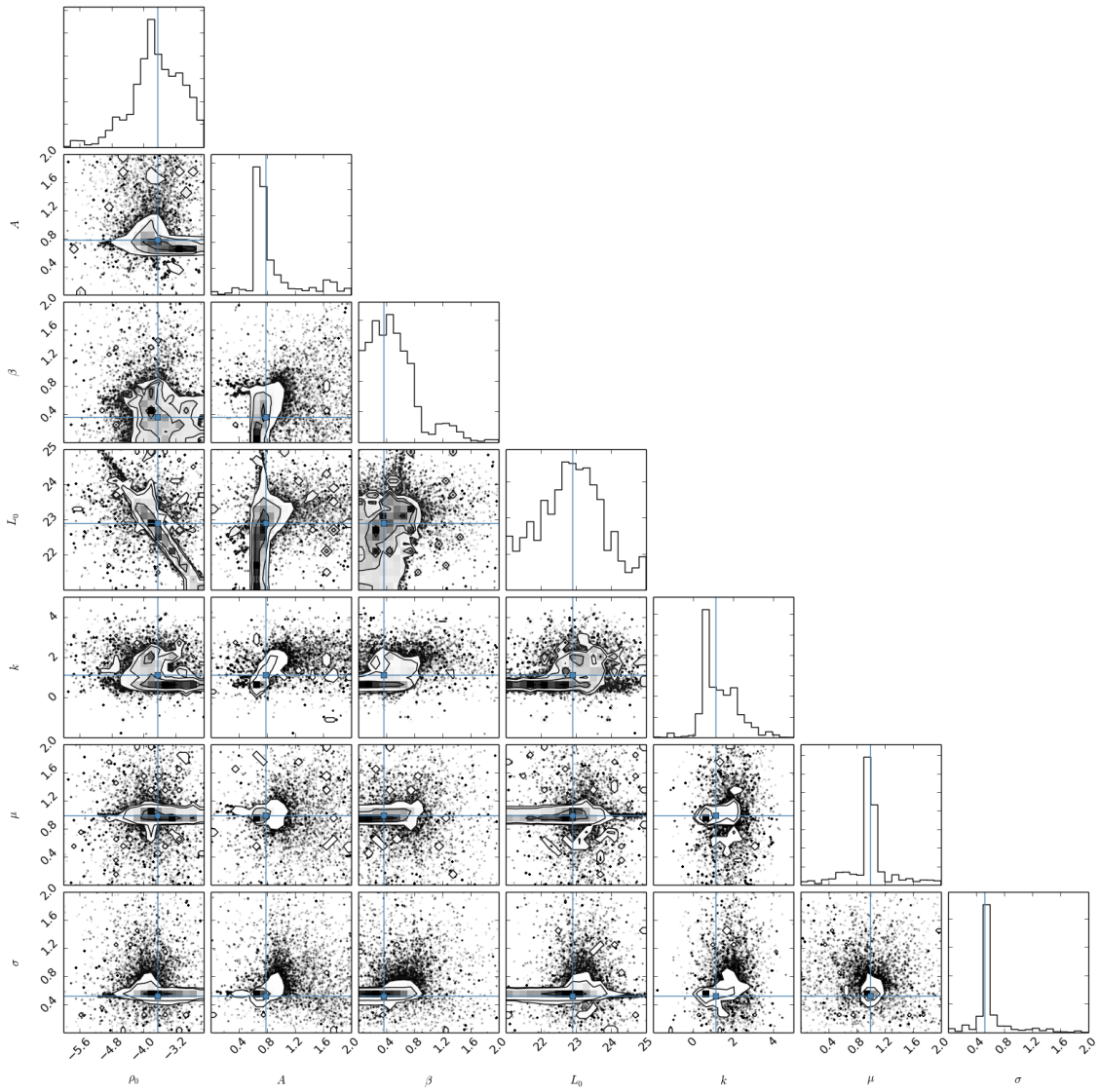

Figure 3.8: As with Figure 3.7, but for the ρ(L,z,α) PDE model.

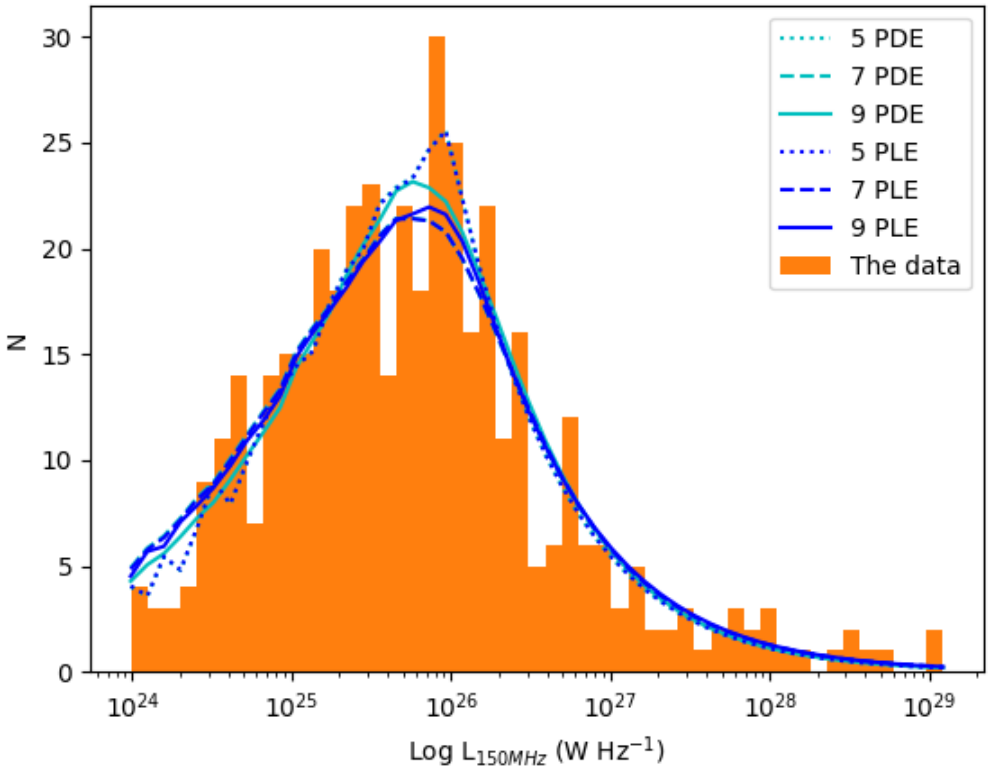

Figure 3.9: The distribution in luminosity. The orange histogram shows the distribution of the data. The blue and cyan lines show the fit from the model for the PLE and PDE models respectively. The ρ(L,z) PLE and PDE models lie on top of one another. The dotted, dashed and solid lines show the ρ(L,z), ρ(L,z,α) 7 parameter and ρ(L,z,α) 9 parameter models respectively.

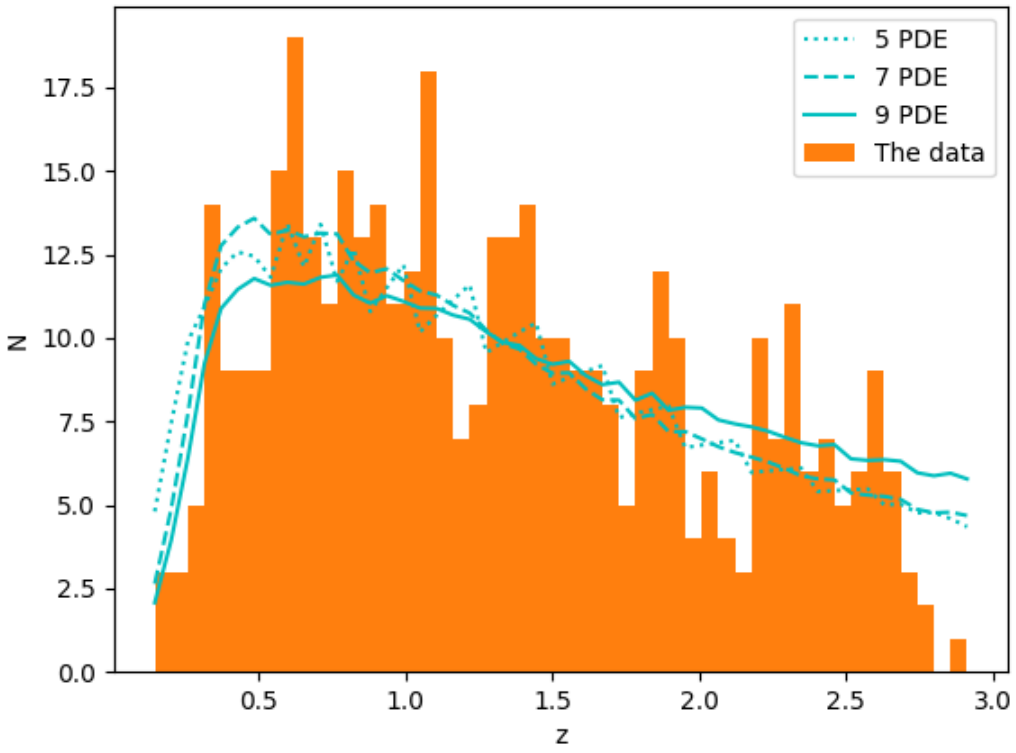

Figure 3.10: The distribution in redshift. The orange histogram shows the distribution of the data. The dotted, dashed and solid lines show the ρ(L,z), ρ(L,z,α) 7 parameter and ρ(L,z,α) 9 parameter PDE models respectively.

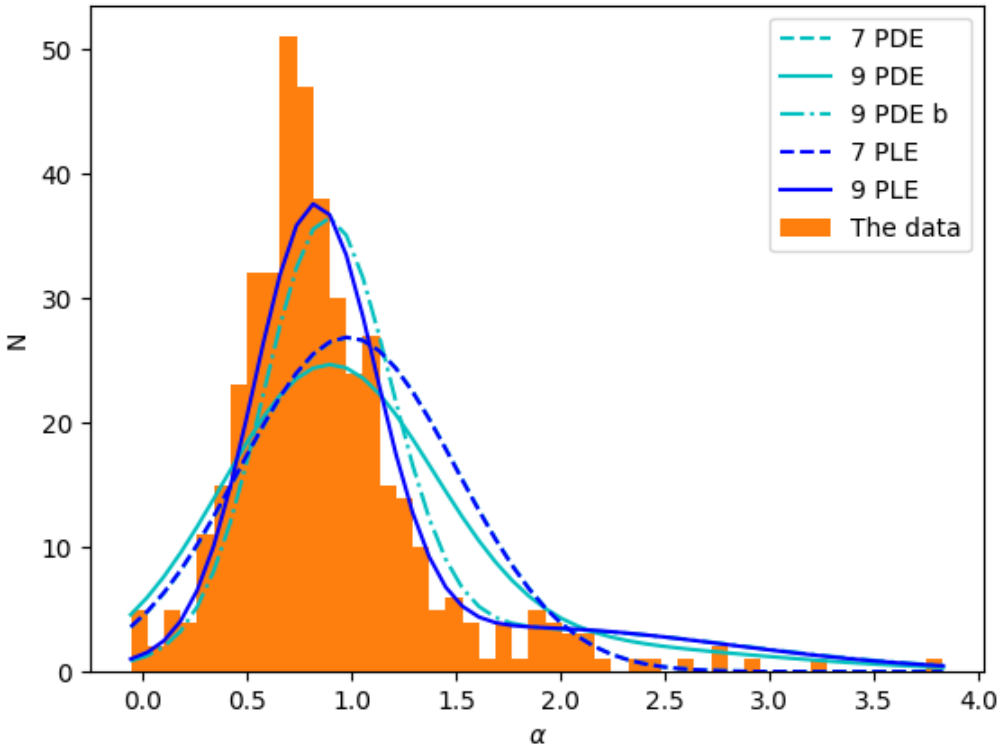

Figure 3.11: The model fits of the spectral index distribution, including an additional two parameters compared to the standard ρ(L,z,α) model to account for the tail in the distribution of the data. The orange histogram shows the distribution of the data. The blue and cyan lines show the fit from the model, corrected for observational effects of PLE and PDE models respectively. The dashed lines represent the 7 parameter ρ(L,z,α) model and the solid lines represent the 9 parameter ρ(L,z,α) model. Both 7 parameter ρ(L,z,α) models lie on top of one another. A second 9 parameter ρ(L,z,α) PDE model ('PDE b') where the value for σ_1 comes from the peak value in the histogram of sampled values instead of the median value, is shown as a dot-dashed blue line.

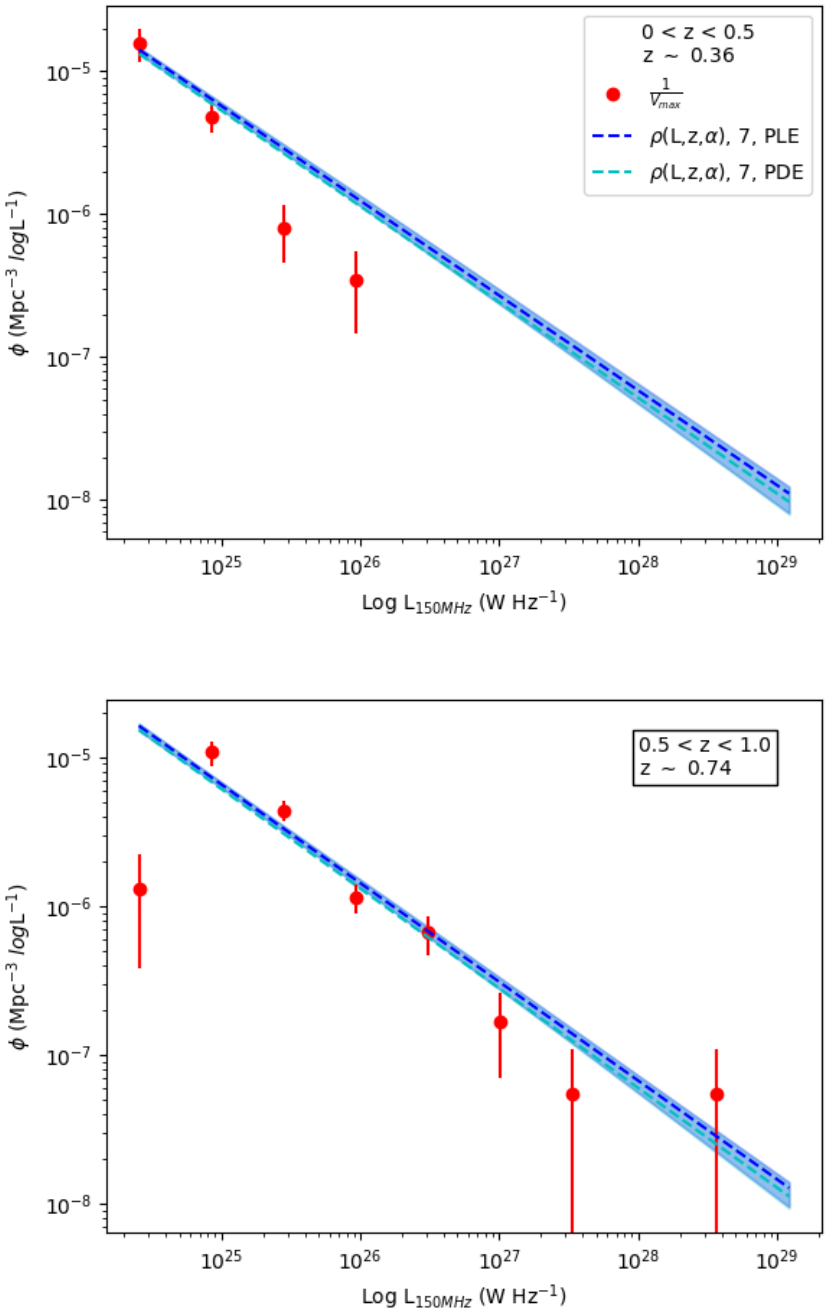

Figure 3.12: The $\frac{1}{V_{max}}$ and ρ(L,z,α) RLFs. The red points denote the $\frac{1}{V_{max}}$ points. The dashed lines show the ρ(L,z,α) models. PLE models are in blue, PDE models are in cyan. The uncertainties from the 16th and 84th percentiles are presented as the width either side of the RLF.

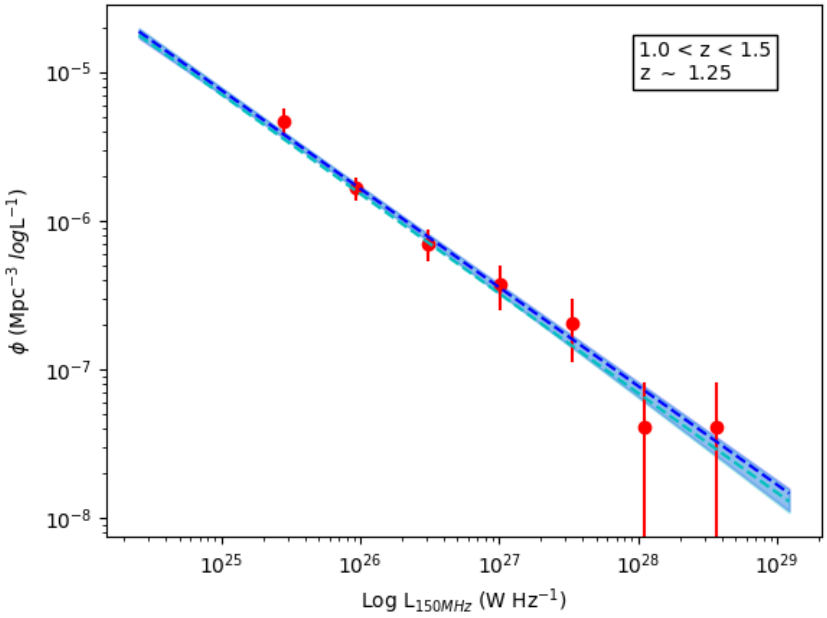

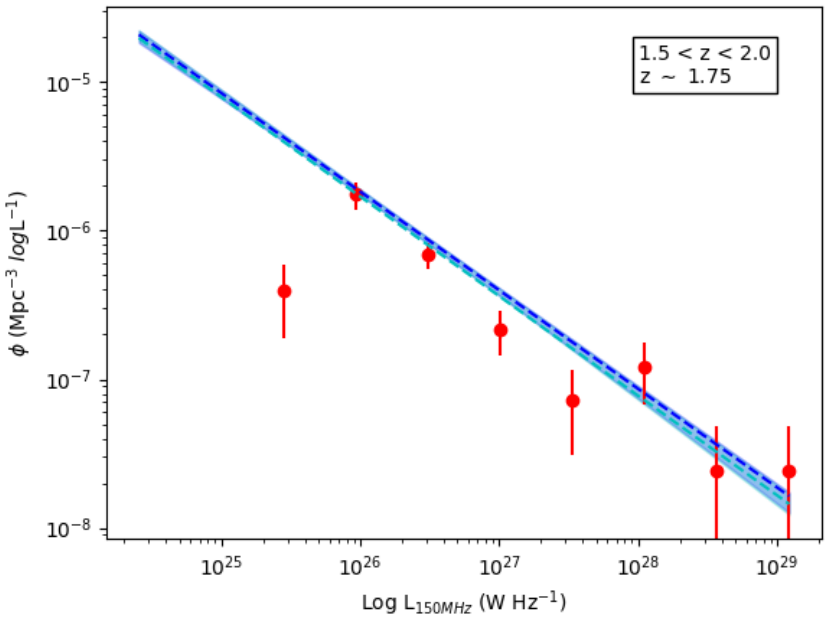

Figure 3.13: Figure 3.12 continued.

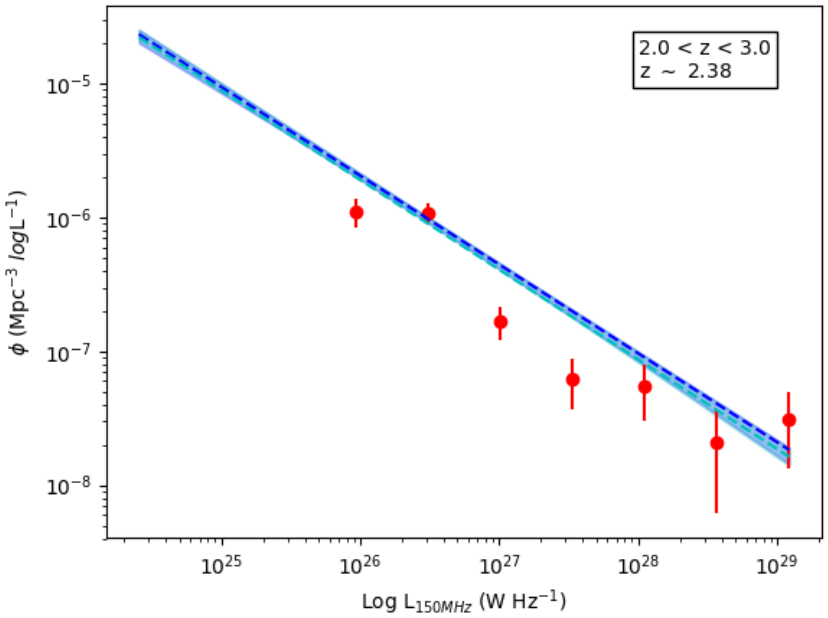

Figure 3.14: Figure 3.12 continued.

the same underlying distribution) when the predicted distribution is corrected for selection effects (i.e. the flux limit of the survey, Figure 3.9). The redshift distribution corrected for the flux limit of the survey also matches the observations well (Figure 3.10, p value = 0.03).

The distribution of spectral indices is modelled using a Gaussian distribution with a peak at $\alpha = 0.98$ and a width of $\sigma = 0.52$ (Figure 3.11). However, this is not a good fit to the underlying distribution (K-S test $p = 1.8 \times 10^{-7}$). The location of the peak does not match the data, and the overall shape is also inconsistent with the data. The presence of a small population of steep spectrum sources means that the resulting fit from the model deviates from the dominant population at a flatter spectral index. The evolution in density follows a power law with $k = 0.57^{+0.14}_{-0.12}$.

3.4.2 Pure Luminosity Evolution

The results of the PLE RLF are almost identical to those of the PDE RLF (See Table 3.3), with the exception of the evolution parameter k. The PLE model has a value of $k = 0.83^{+0.17}_{-0.17}$, which is higher than the PDE model value of 0.57. In terms of the movement on the Φ-L axis, this implies the RLF evolving more strongly along the L-axis compared to the PDE model which moves the RLF along the Φ-axis.

The PLE model has a good fit to the luminosity distribution (K-S test $p = 0.4$), but again fits poorly for the α distribution (K-S test $p = 1.58 \times 10^{-8}$).

3.4.3 Bivariate (ρ(L,z)) models

The ρ(L,z) models come close to appearing as a single power law, as A and B are found to still be close for both PLE and PDE models (see Table 3.3). Both models have a weak evolution term, that again, is the only substantially differing factor between PDE and PLE models. They appear to lie directly on top of one another in each redshift bin and are within each others errors (see Figures 3.15, 3.16 and 3.17). The ρ(L,z) models are often within the constraints of the errors from the $\frac{1}{\mathrm{V_{max}}}$ points, though they deviate at the lowest redshift bins due to the smaller number of sources, as with the ρ(L,z,α) models. The fitting of the RLF is constrained to the regions where there are the most sources which direct the fit, hence the lack of agreement in regions where the number of sources is lower.

3.5 Discussion

The reason for undertaking this work is to provide a more robust RLF than those measured previously using a fixed α or using $\frac{1}{\mathrm{V_{max}}}$. To assess this I compare with $\frac{1}{\mathrm{V_{max}}}$, bivariate ρ(L,z) models and results from the literature. I also investigate the addition of a further two parameters to model the spectral index distribution more fully.

3.5.1 ρ(L,z,α) vs. $\frac{1}{\mathrm{V_{max}}}$

Both PLE and PDE models are in agreement with the $\frac{1}{\mathrm{V_{max}}}$ points, with the exception of the lowest redshift bin ($z < 0.5$) where the models are higher on the ϕ-axis. This is likely a result of the fact that the k parameter is determined by a single power law and does not account for the downturn of cosmic AGN activity beyond $z \sim 2$ (e.g. Rigby et al., 2015). By assuming a constant rate of evolution the value of k has to compensate for changes by accommodating an increase and decrease in activity. Beyond $z \sim 0.5$, where the bulk of the sources lie, they are a satisfactory match. The ρ(L,z,α) and $\frac{1}{\mathrm{V_{max}}}$ models agree most at $1.0 < z < 1.5$ where the number of sources in the sample is highest and thus constrains RLF well. The agreement worsen either side of this redshift bin.

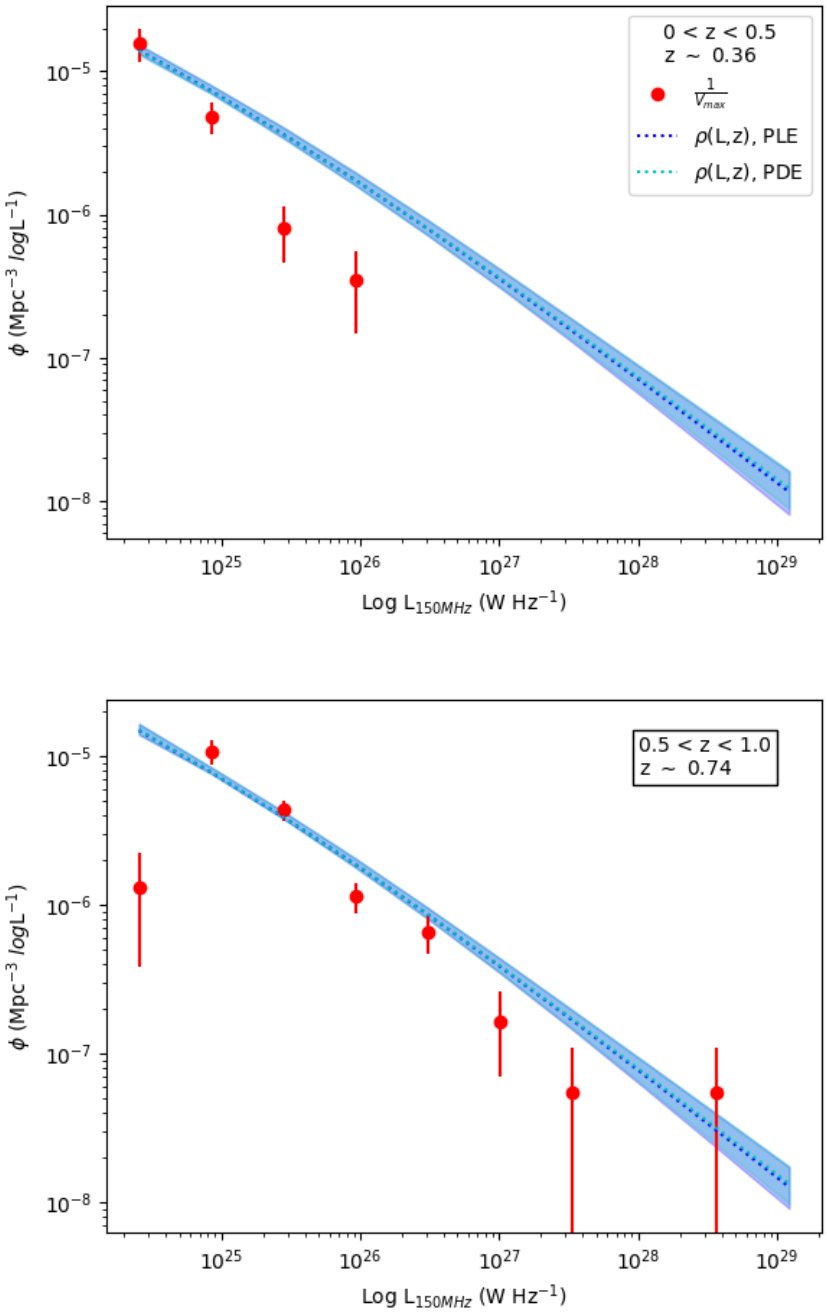

Figure 3.15: The $\frac{1}{V_{max}}$ and ρ(L,z) RLFs. The red points denote the $\frac{1}{V_{max}}$ points. The dotted lines show the ρ(L,z) models. PLE models are in blue, PDE models are in cyan. The uncertainties from the 16th and 84th percentiles are presented as the width either side of the RLF.

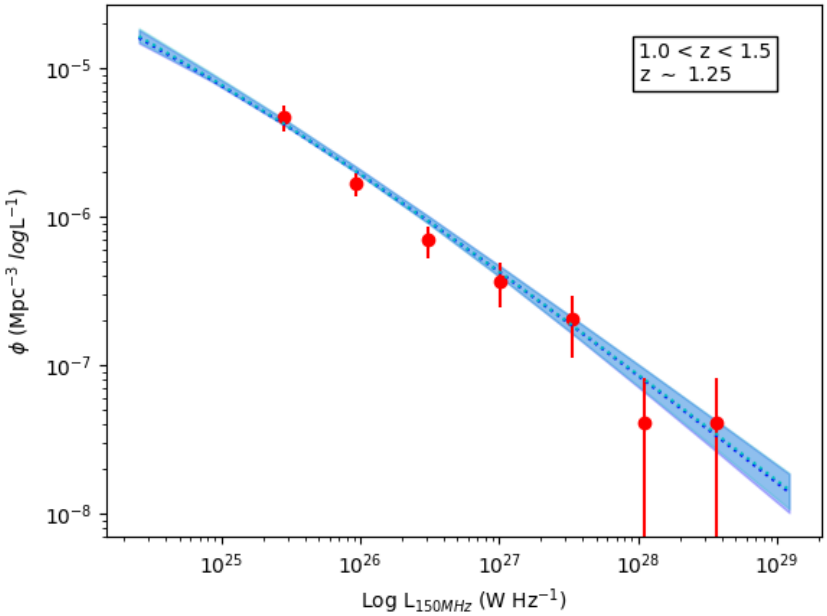

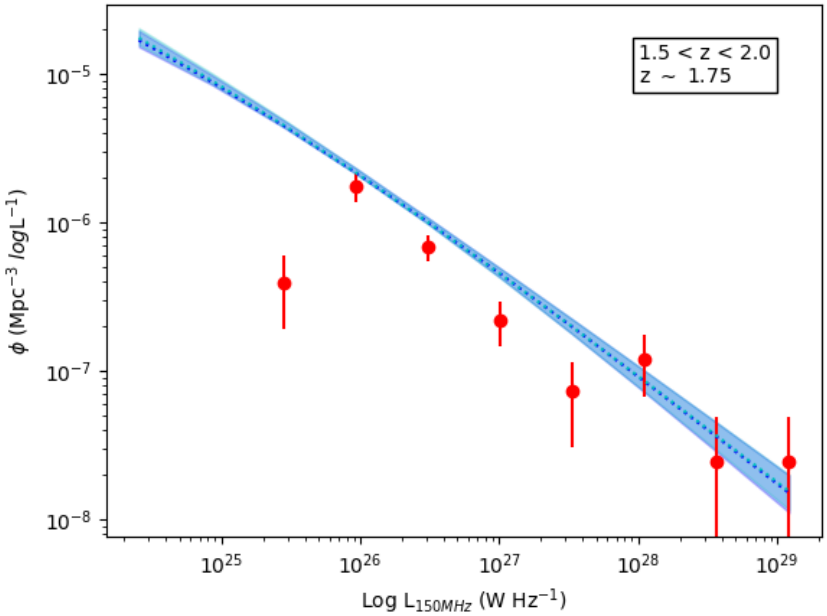

Figure 3.16: Figure 3.15 continued.

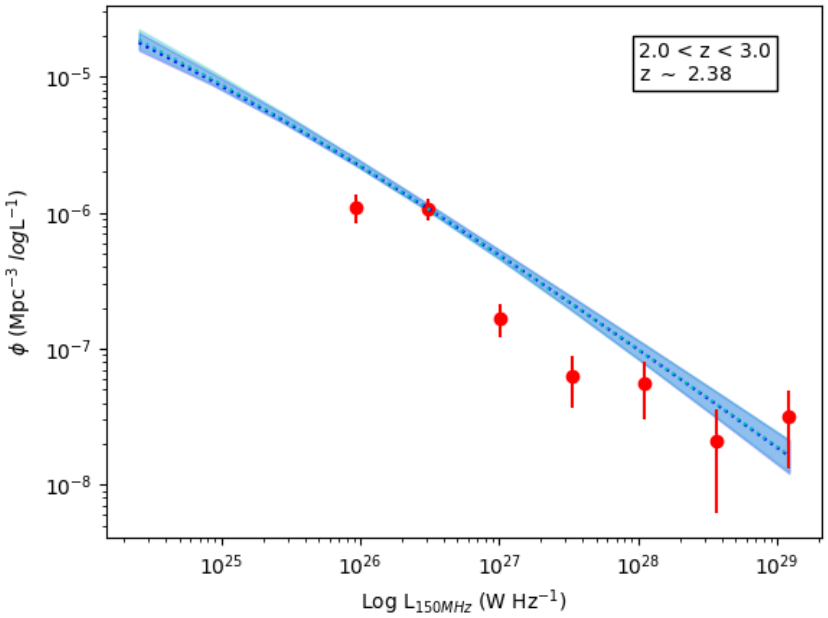

Figure 3.17: Figure 3.15 continued.

At the highest redshift bins the poorer agreement between the $\frac{1}{V_{max}}$ points and the models could be due to a lack of sources at these higher redshifts or, the fact that the k parameter is in reality not constant. By having a constant value for k I assume no change in the form of the evolution, and the RLF continues to evolve positively with increasing redshift. This does not allow for a plateau or a turn down. For this reason it may be why the models over estimate the number of sources compared to the $\frac{1}{V_{max}}$ points.

In general the results are in keeping with what is expected and the error bars largely contain both ρ(L,z,α) and ρ(L,z) RLFs.

3.5.2 ρ(L,z,α) vs. ρ(L,z)

When visually examining the two sets of RLFs it is difficult to detect a difference between them at all. Both sets of RLFs lie close to one another, where in each case the PLE and PDE models show little difference. The most significant differences between the two sets of models are between the values for the RLF parameters ρ_0, k, A and B.

For the normalisation, the mean values are $\log_{10}\rho_0 = -5.165$ and -4.825 for the ρ(L,z,α) and ρ(L,z) models respectively (and the PLE and PDE models are very similar). The ρ(L,z,α) model is lower, which shifts the entire RLF down the ϕ axis.

This is evident from visually inspecting the plots as the ρ(L,z,α) RLFs lie lower in the L-ϕ plane. Though this is only a small difference. There are slightly differing shapes of the two sets of models (i.e. that in ρ(L,z,α) the A and B values are almost equal, whereas there is a marginal distinction between them in the ρ(L,z) models).

The k-values for the sets of ρ(L,z,α) and ρ(L,z) models retain the relationship in that the PDE models have smaller evolution parameters. When looking at the two sets of models side by side, the mean evolution parameters are $k = 0.70$ for ρ(L,z,α) models and $k = 0.42$ for ρ(L,z) models. Including the spectral index distribution is highly determinate of how strongly the sample is predicted to evolve. ρ(L,z,α) models predict a much stronger evolution than ρ(L,z) models. When the individual and sample distribution of spectral index is taken into account, the observable volume of the sources and the sample is modeled more accurately. By examining the α-distribution (Figure 3.11) a tail is evident at steeper spectral index values, which in turn reduces the observable volume. This reduction in volume leads to a stronger evolution in density over redshift. This has substantial consequences for understanding galaxy evolution using RLFs that do not account for this.

Finally, another consequence of including the α-distribution is on the A and B parameters. Including the spectral index distribution has the effect of steepening the RLF overall by providing almost equal A and B values compared to the starkly differing ones seen in the ρ(L,z) models. The B parameter reflects the faint end slope, and when accounting for a variety of spectral index values, it increases. This is due to accounting for a population of sources with flatter α's than 0.7, which, when K-corrected, have a lower luminosity than they would have otherwise been given. Therefore the faint end population increases. Over redshift, the ρ(L,z,α) models predict a greater number density than the ρ(L,z) models in the low-luminosity regions ($L \sim 10^{26}\mathrm{WHz}^{-1}$), while both maintaining similar predictions at the high-luminosity end. In the ρ(L,z) models the more extreme values of A and B reflected this and thus called for a weaker evolution term.

The dearth of low-luminosity points for $\frac{1}{\mathrm{V_{max}}}$ is due to a lack of sources at these luminosities in our survey, and ρ(L,z) is lower than ρ(L,z,α) due to a lack of accounting for the spectral index distribution in the ρ(L,z) model. There is little to no-data at this end of the luminosity scale and the increased prediction with redshift in this region is pure extrapolation. While it makes sense, more data is needed to confirm whether these fits are accurate at the low luminosity end.

3.5.3 A 9 parameter model

When inspecting the fit for both ρ(L,z,α) models on the distribution of the spectral index (Figure 3.11) it is clear that the model fit is shifted to the right, towards steeper α values, by a tail at the steep end. This shifts the mean value from the expected range of 0.7-0.8 to ∼1.0. To see whether this had a substantial effect on the model fits, I added an additional two parameters to improve the fit of the spectral index distribution. The factor of the RLF that fits the α distribution is now,

$$\rho_\alpha = \exp\Big[-\frac{1}{2}\Big(\frac{\alpha-\mu_1}{\sigma_1}\Big)^2\Big] + 0.1 \times \exp\Big[-\frac{1}{2}\Big(\frac{\alpha-\mu_2}{\sigma_2}\Big)^2\Big] \tag{3.8}$$

where μ_1 and σ_1 refer to the mean and variance of the dominant peak in the α distribution and μ_2 and σ_2 refer to the second, smaller peak at the steep end. In a bid to reduce computational demand and save time, I fix the normalisation of the 2$^{\text{nd}}$ Gaussian at 0.1, since this is the ratio between the two single most populated bins in each half of the histogram $\alpha \leq 1.5$ and $\alpha > 1.5$.

Before performing an MCMC run, I checked whether it was possible to find a reasonable fit on the spectral index distribution using Equation 3.8. By visual inspection I estimated values for the parameters related to the α-distribution of $\mu_1 = 0.75$, $\sigma_1 = 0.25$, $\mu_2 = 1.8$ and $\sigma_2 = 0.5$ which appear to fit the α-distribution well (see Figure 3.18). From this point onward I proceeded to fit the parameter values using Emcee.

3.5.3.1 Results & Discussion

The values for all parameters from the 9 parameter PLE and PDE model can be seen in Figures 3.19 and 3.20 respectively, with the resulting RLFs in Figures 3.21, 3.22 and 3.23.

The results of these additional parameters on the fitting of the spectral index distribution can be seen in Figure 3.11. The PLE model is somewhat close to what is seen in the data for the α distribution, although the peak of the fit is still pulled to the right by steeper sources. The shape of the fit to the α-distribution, however, is fairly close to the sample and with a K-S test $p-$value between the data and the model of $p = 0.02$. The PLE model agrees with the luminosity distribution well, with a K-S test $p = 0.56$.

Though the PDE model appears to be close to the PLE model in the α-distribution the μ_1 value is actually higher than the PLE model (0.88 c.f. 0.82) and the fit fails to pass the K-S test on any confidence level with a p value = 1.197×10^{-6}. When looking at the sample distribution in Figure 3.20 the median value for σ_1 lies in the middle of

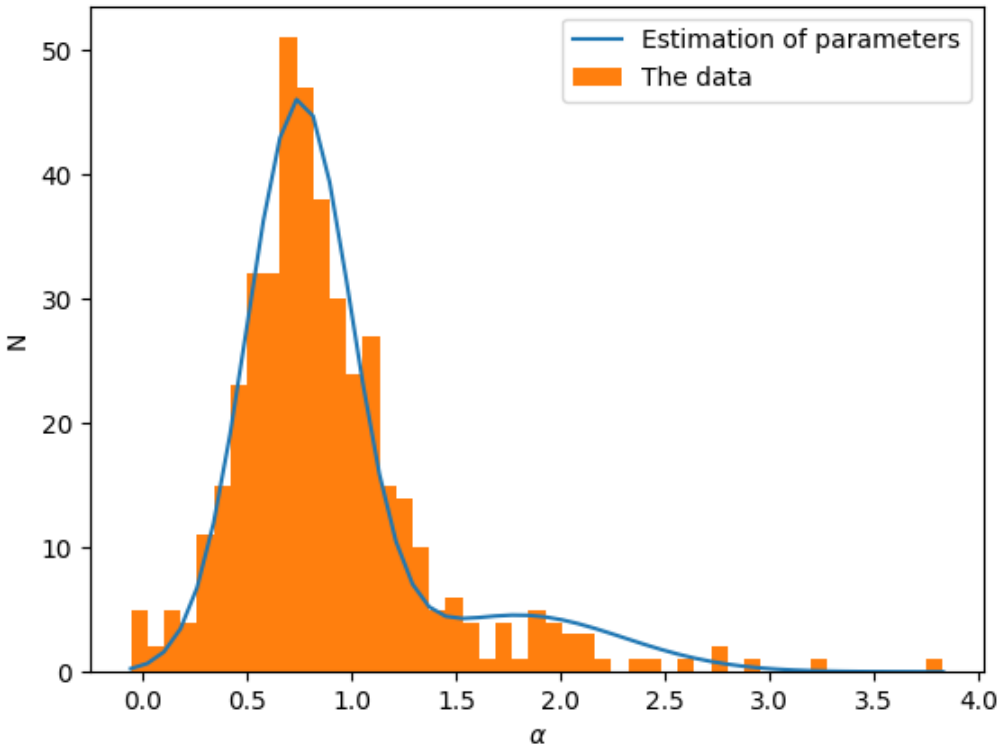

Figure 3.18: The orange histogram displays the data for the distribution in spectral index, α. The blue line shows my estimation of the parameters via visual inspection ($\mu_1 = 0.75$, $\sigma_1 = 0.25$, $\mu_2 = 1.8$ and $\sigma_2 = 0.5$) for using Equation 3.8 in the RLF.

the values, though a peak is seen to the left at lower values of σ_1. In the eventuality that with more steps taken the value may have drifted towards that peak, I examined the effects this other value has on the value of σ_1, the fit to the α-distribution and the likelihood.

Zooming in to the values for σ_1 (Figure 3.24), the most populated histogram bin lies closer to 0.30 than the median value of 0.51 (Table 3.5.3.1). Taking the central value of the most populated histogram bin I label this as 'PDE b' in Table 3.5.3.1. The $-2\ln L$ value actually improves with this new σ_1 value (reducing from 12666.1 to 12483.3), as does the shape to the fit of the α-distribution in Figure 3.11. Yet it still fails the K-S test with a p value = 1.4×10^{-5}.

However, there is still room for further improvement, as the fit is better than the previous 9 parameter ρ(L,z,α) PDE model and the 7 parameter ρ(L,z,α) PDE model, the peak of the fit does not correspond accurately enough to the underlying distribution of the data. This is merely speculation on the fit of the α-distribution, as the changing of one value may alter the others when fitting for the entire RLF and so it is not appropriate to expand on this to the full RLF. If there was more time, a refitting of the model with priors restricting σ_1 around this region would be appropriate.

This shows that even with a model that *is* able to replicate the underlying distribution (Figure 3.18) this is still difficult to do so. If there was more time, it could be appropriate to use an alternative form for the modelling of the α-distribution or allow the EMCEE search to run for more steps.

Although the fits to the α-distribution are not optimum, they are improved and the overall RLFs continue to fit the $\frac{1}{V_{max}}$points well in both PLE and PDE models (see Figures 3.21, 3.22 and 3.23). It is still possible to see what even marginal improvements have on the parameter values that are found by using the 9 parameter ρ(L,z,α) PLE and PDE models.

However, it is evident in Figure 3.20 and from the large error bars in Figures 3.21, 3.22 and 3.23 that the PDE model fails to converge.

In general, for assessing how well parameters in a model *are* converging, many approaches can be taken. The autocorrelation function measures the degree of correlation of the MCMC chains of a parameter with a time lagged repeat of themselves. If a correlation is found, it can be a sign that the chains for the parameter are converging.

The Gelman-Rubin statistic (G-R statistic Gelman & Rubin, 1992) is another standard method for assessing convergence. It requires the use of several chains with

independent starting points. If a model is converging, the variance between multiple chains should match the variance within a single chain. If the variance within chains is too high then the G-R statistic will have a value greater than 1 which indicates that one or more chains have not yet converged. The methodology in EMCEE means that even though multiple chains are run, they begin with the same starting point and thus the G-R statistic is not applicable for the work done here without repetitions of EMCEE to create independent chains.

I show this more explicitly in the time series plots for the PLE and PDE models in Figures 3.25 and 3.26 respectively. While the PLE model shows A, B, k, μ_1 and σ_1 converge, with the remaining parameters at least showing signs of mixing, the PDE model in Figure 3.26 shows the chains to be predominantly unmixed and no clear signs of convergence for any parameter. For this reason, the 9 parameter PDE model is too unreliable and shall be removed from any detailed discussion. Time series plots are the most basic way for identifying a lack of convergence. A way to improve this can be to run the chains for longer. Although, this technique has failed for the PDE model which ran for 2615 steps compared to the 683 steps for the PLE model.

Another remedy for the 9 parameter PDE model could have been a simplification of the model to reduce the number of parameters and ease convergence. As seen in Figures 3.21, 3.22 and 3.23 and the values for A and B in Table 3.5.3.1, the resulting RLFs look like a single power law for both PLE and PDE models. The double power law describing the luminosity distribution could have been reduced to a single power law to simplify the model without compromising accuracy.

However, a factor that has not been considered is that there is an in-built reason as to why the PDE model struggles to fit the data here. The PDE model tracks evolution in terms of the movement of the RLF on the ordinate axis (the Φ-axis). Due to the shape of the RLF, this means that the faint end of the RLF, where the slope is flatter, more strongly constrains this movement. Conversely, the PLE model is more strongly constrained by the bright end, beyond the break, of the RLF as it moves along the abscissa (L-axis). The only way to overcome such a degeneracy is to acquire more data at the faint-end of the RLF to more strongly limit the explored range in parameter space for the PDE model.

3.5.3.2 Comparing the 7 and 9 parameter models

The PLE model shows little change from 7 to 9 parameters. There is a greater separation between A and B which adds a shallow break to the RLF, as well as a change in μ_1 and σ_1 which is to be expected by design of the new model.

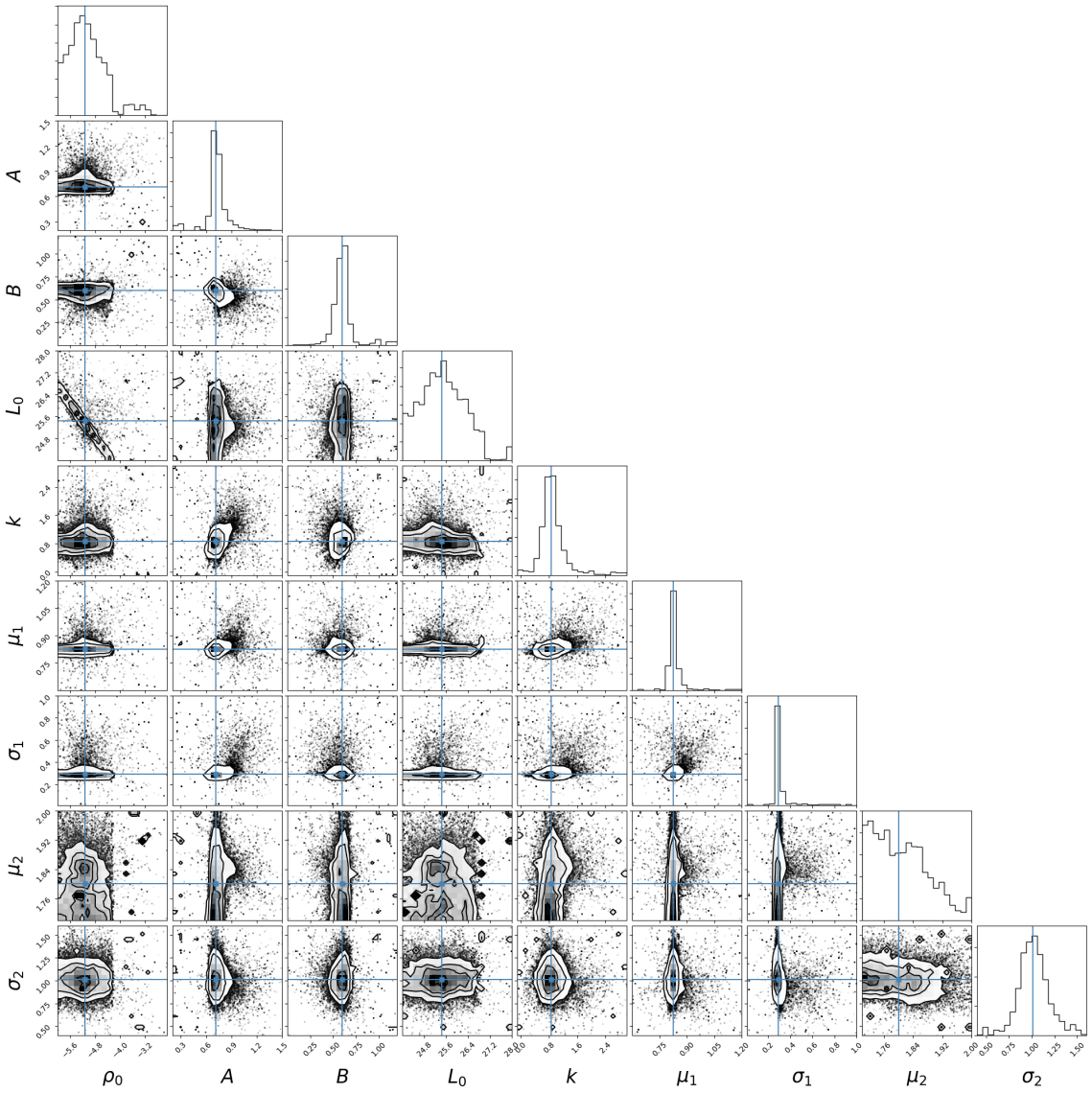

Figure 3.19: The results of the 9-parameter ρ(L,z,α)PLE model for parameters ρ_0, A, β, L_0, k, μ_1, σ_1, μ_2 and σ_2 respectively. The scatter plots show the relationships between all parameters where regions of high density show the most sampled regions of the prior from the MCMC algorithm, determined by minimising the likelihood. The histograms show the individual distributions in sampling the prior ranges.

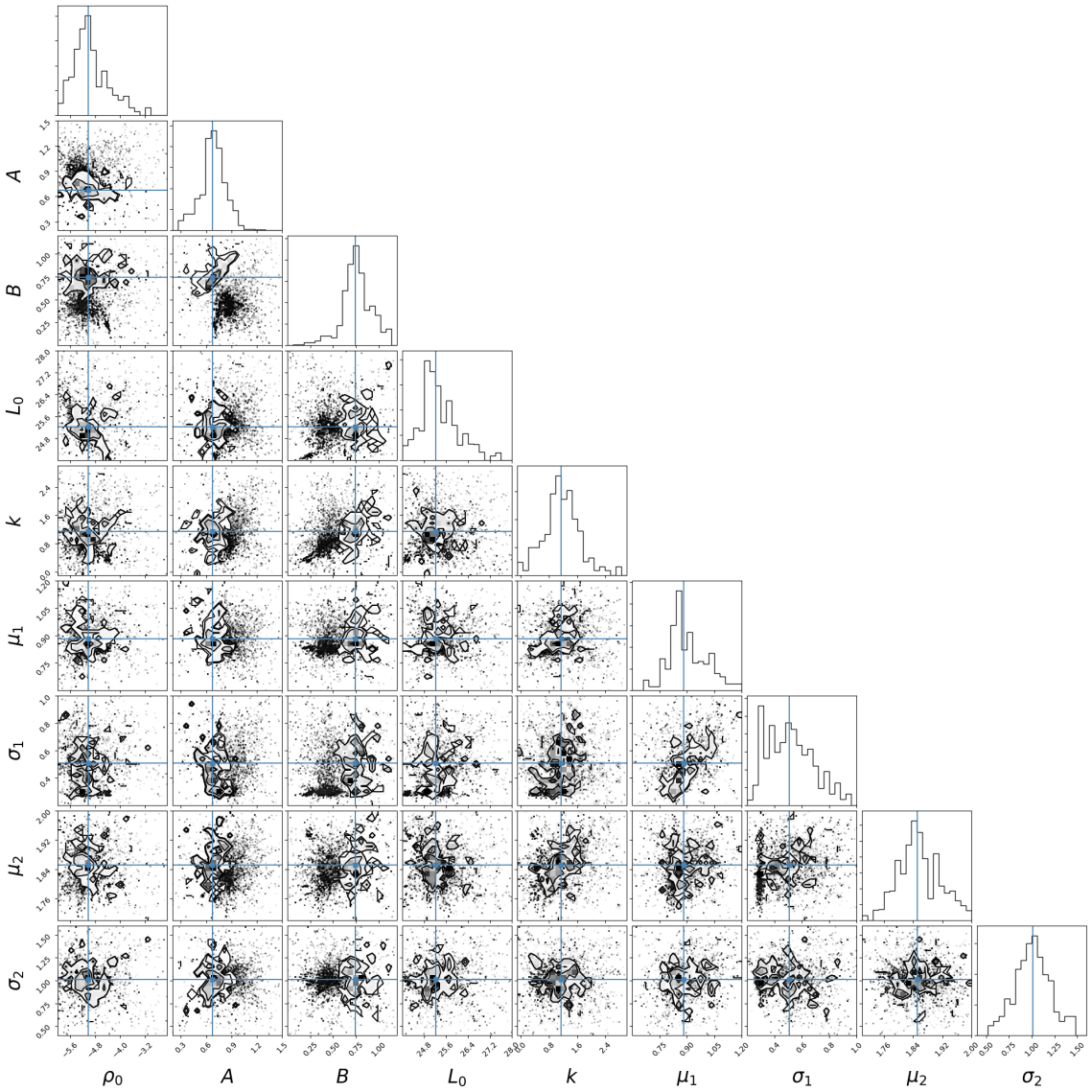

Figure 3.20: As with Figure 3.19, but the results of the 9-parameter ρ(L,z,α) PDE model.

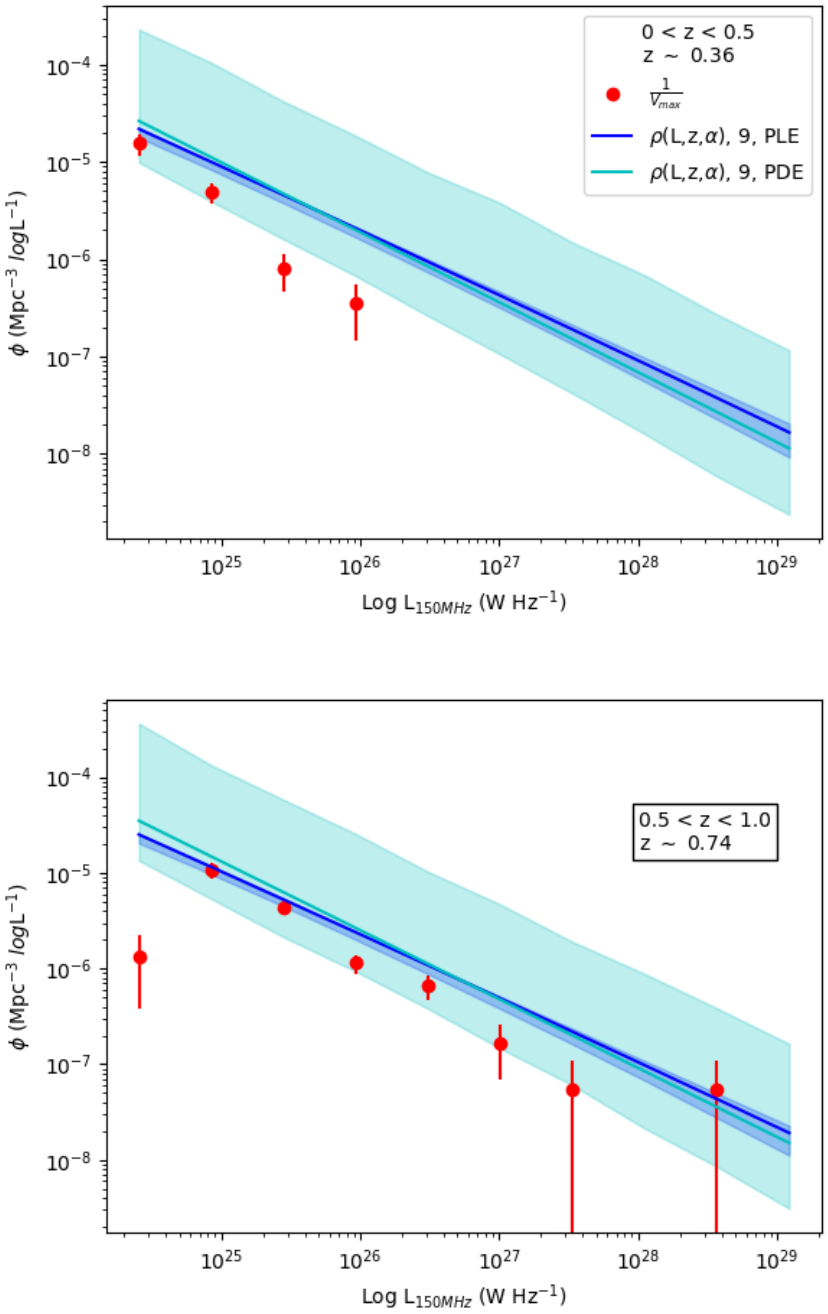

Figure 3.21: The $\frac{1}{V_{max}}$ and ρ(L,z,α) RLFs. The red points denote the $\frac{1}{V_{max}}$ points. The solid lines show the 9 parameter ρ(L,z,α) models. PLE models are in blue, PDE models are in cyan. The uncertainties from the 16th and 84th percentiles are presented as the width either side of the RLF.

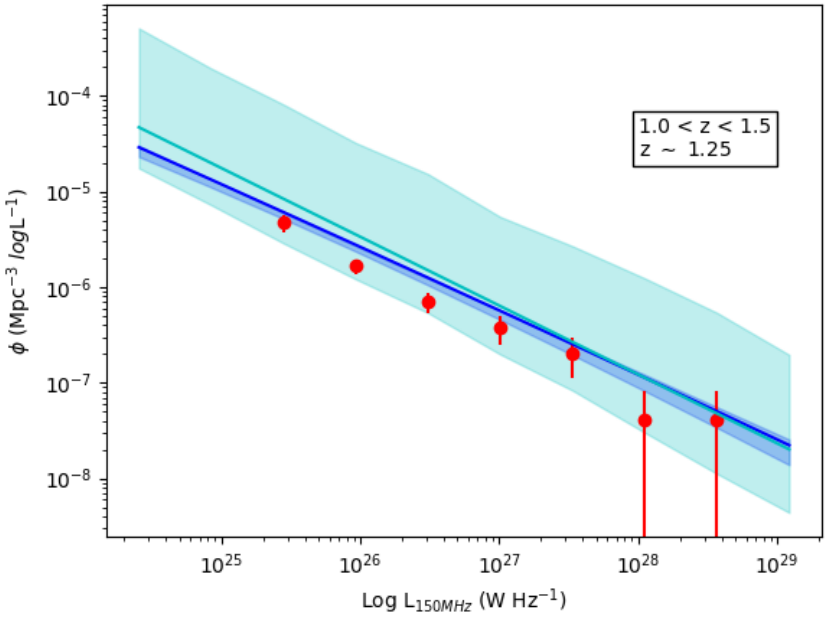

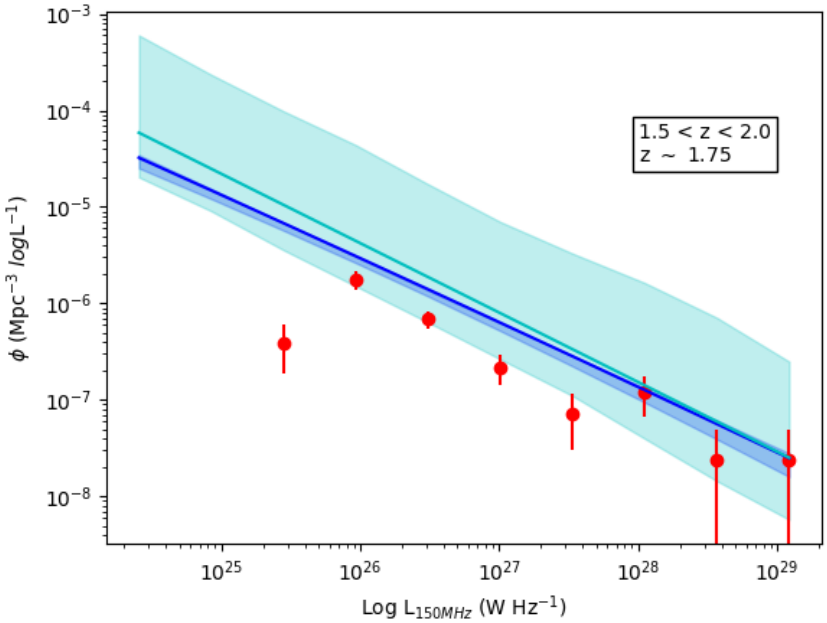

Figure 3.22: Figure 3.21 continued.

Model	ρ_0	A	B	L_0	k	μ_1	σ_1	μ_2	σ_2	-2
PLE	$-5.13^{+0.60}_{-0.50}$	$0.72^{+0.08}_{-0.05}$	$0.60^{+0.06}_{-0.07}$	$25.4^{+0.85}_{-0.84}$	$0.85^{+0.29}_{-0.22}$	$0.82^{+0.02}_{-0.02}$	$0.29^{+0.03}_{-0.01}$	$1.80^{+0.09}_{-0.07}$	$1.01^{+0.16}_{-0.14}$	12364.0
PDE	$-5.03^{+0.68}_{-0.44}$	$0.68^{+0.15}_{-0.15}$	$0.75^{+0.17}_{-0.12}$	$25.2^{+0.78}_{-0.46}$	$1.14^{+0.48}_{-0.49}$	$0.88^{+0.14}_{-0.07}$	$0.51^{+0.18}_{-0.18}$	$1.85^{+0.07}_{-0.05}$	$1.01^{+0.19}_{-0.19}$	12666.1
PDE b	”	”	”	”	”	”	$0.30^{+0.02}_{-0.02}$ *	”	”	12483.3

Table 3.4: Results for the 9 parameter ρ(L,z,α) models. The EMCEE run used 150 walkers and per walker each model performed PLE: 683 steps, PDE: 2615 steps. The median value for each parameter is listed alongside uncertainties from the 16^{th} and 84^{th} percentiles. *This value comes from choosing the peak value in the histogram of sampled values for this parameter, σ_1. The uncertainty for this parameter comes from the width of the histogram bins in Figure 3.24.

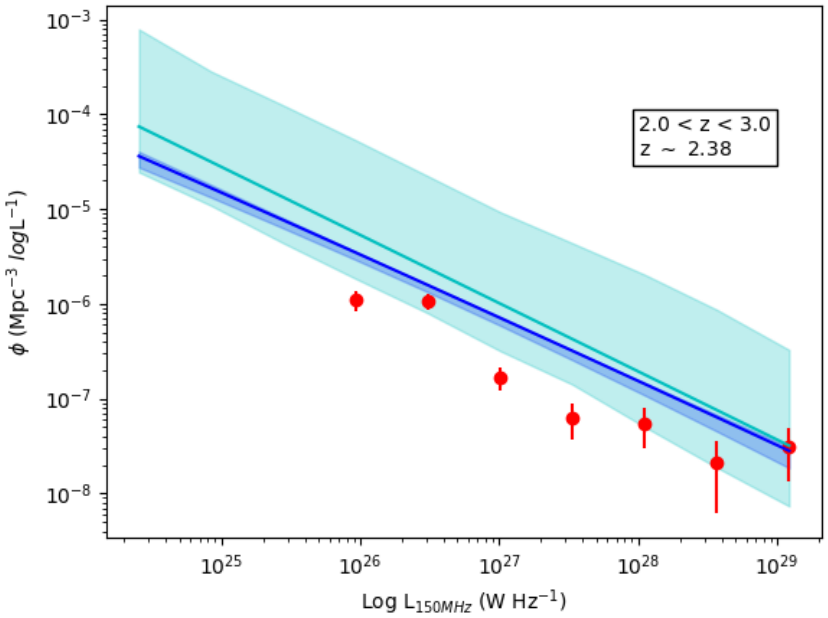

Figure 3.23: Figure 3.21 continued.

On the $L-\phi$ plane although the ρ_0 values are similar to the 7 parameter ρ(L,z,α) models, the 9 parameter RLFs lie above the 7 parameter RLFs. This difference becomes more distinct with redshift, as to be expected from the higher values of k for the 9 parameter models.

These models also show the only noticeable difference between the PDE and PLE RLFs. A difference that increases with redshift. Another interesting point is that while the 7 parameter ρ(L,z,α) model lies below the ρ(L,z) models, the 9 parameter ρ(L,z,α) model lies above it. The 9 parameter ρ(L,z,α) model predicts a greater number of sources than simpler models do. This is due to that fact that outlying sources with steeper spectral indices are more accurately considered and known by the model to be more difficult to observe.

In summary, the 9 parameter models, in general, predict a great number density at all luminosities and redshifts than other models, as well as stronger changes in evolution. Both models also fit the α distribution more accurately.

3.5.4 Comparing with other studies

Due to the limited survey area and the flux-limit of our sample, the low-redshift RLF cannot be adequately constrained. Theerefore, in the following, I concentrate on comparing the model RLFs in this work, with the work in the literature which

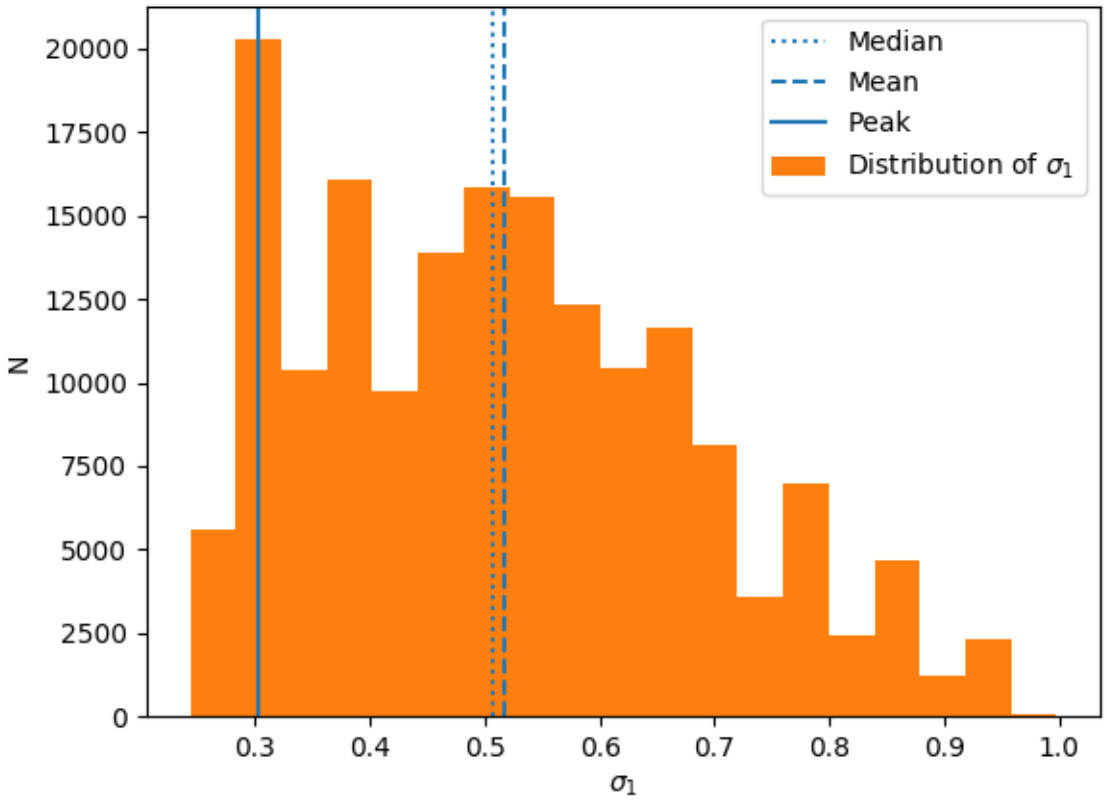

Figure 3.24: A close-up view of the values sampled by the EMCEEalgorithm for σ_1 in the 9 parameter ρ(L,z,α) PDE model. The underlying sample distribution is the orange histogram. The median value, which is originally chosen, is the vertical dotted line. The mean is shown by the vertical dashed line and the peak value corresponding to the most populated histogram bin is shown as a solid line, centred on the middle of the histogram bin in which it lies. The y-axis (N) denotes the number of times a value was visited during the EMCEEsampling. The number of histogram bins here is the same as in the corner plot Figure 3.20.

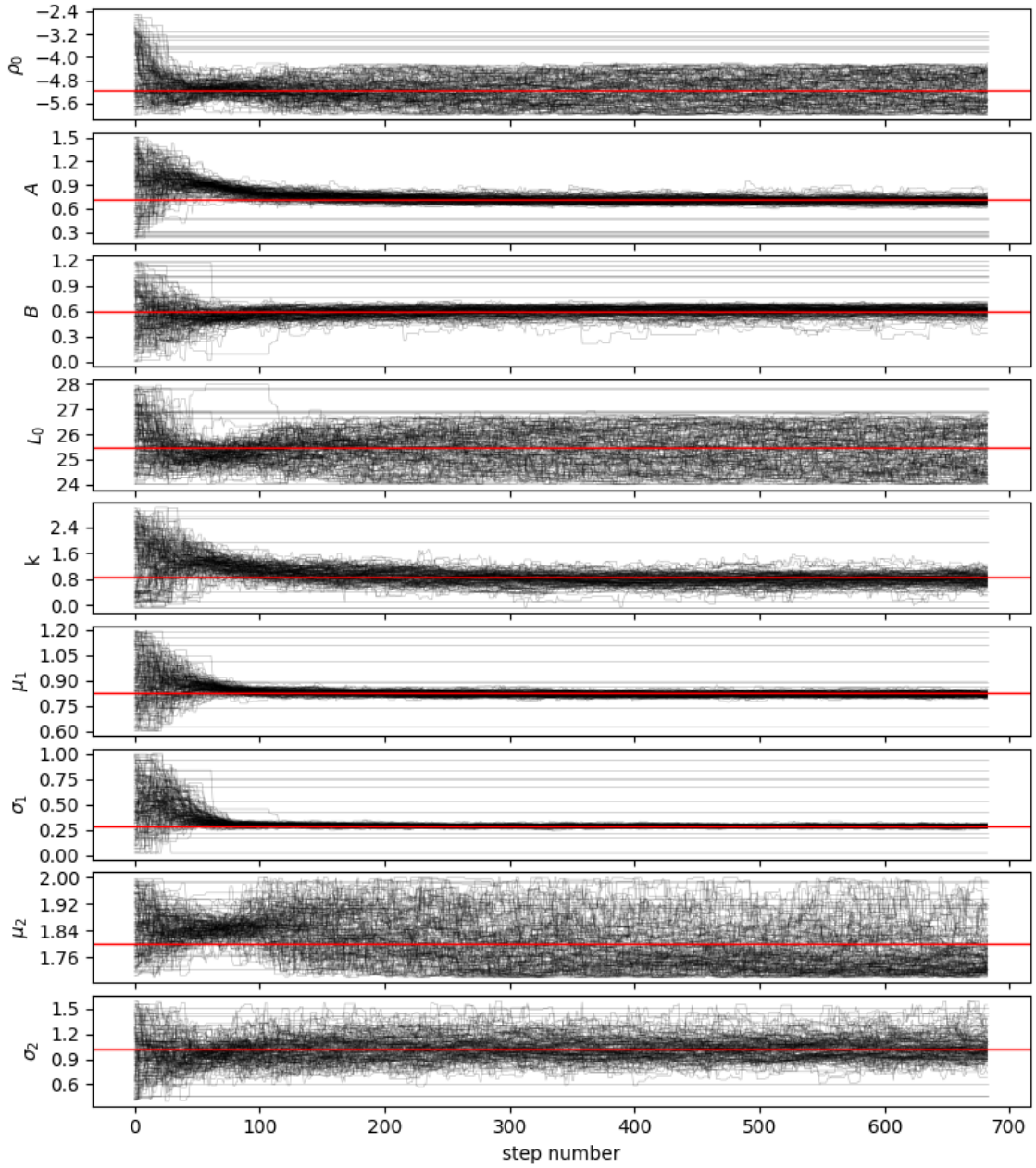

Figure 3.25: The time series plots of the 9 parameter PLE model at all steps for each chain for each parameter. The black lines are the individual chains and the red line is the resulting median value. While ρ_0, L_0, μ_2 and σ_2 show poor signs of convergence, A, B, k, μ_1 and σ_1 appear to converge well for this model.

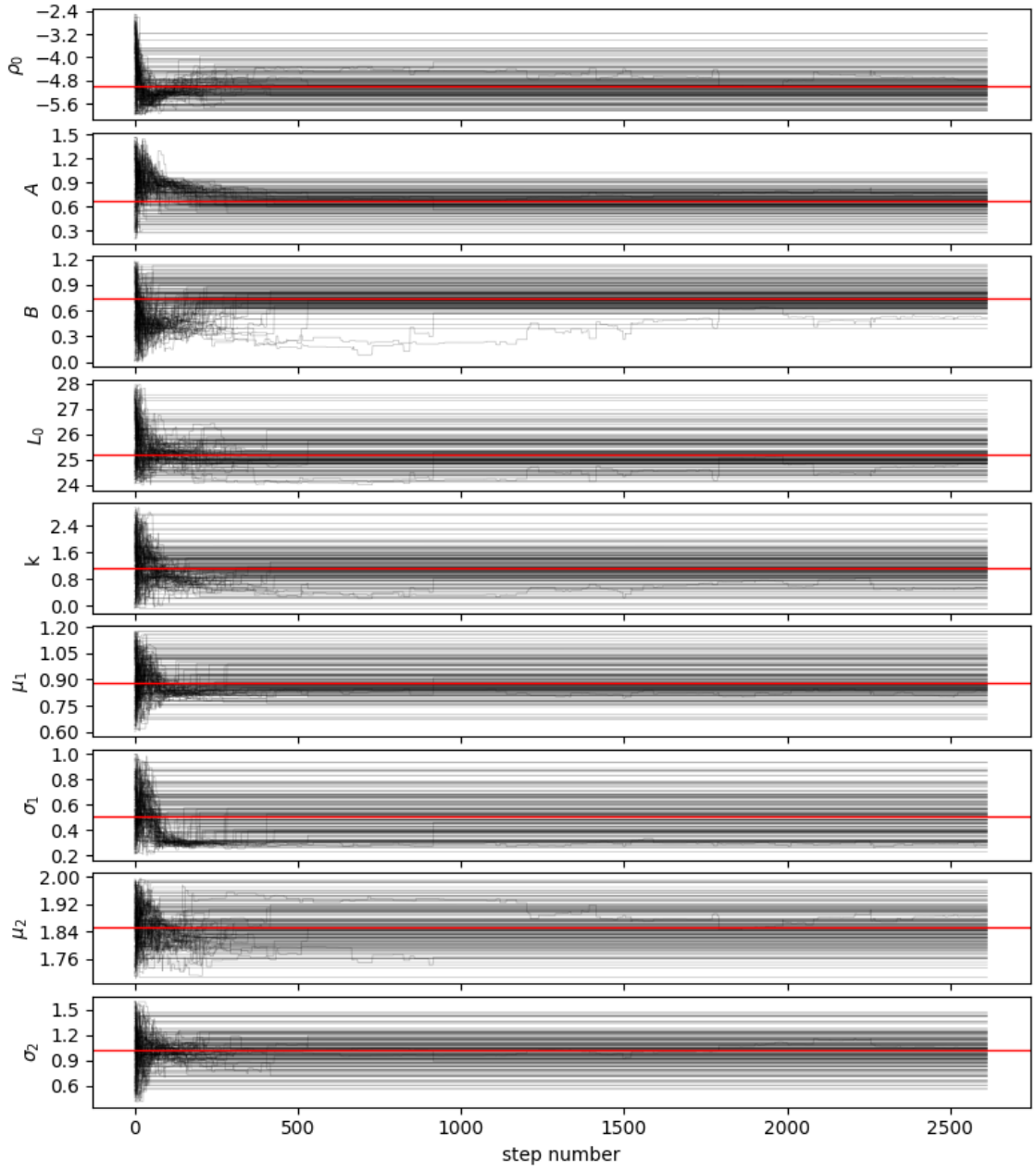

Figure 3.26: The time series plots of the 9 parameter PDE model at all steps for each chain for each parameter. The black lines are the individual chains and the red line is the resulting median value. There exists little evidence of convergence for any of the parameters for this model, even with a significantly greater number of steps than that seen in Figure 3.25.

concentrates on the evolutionary form of the RLF towards higher redshift. When comparing to the RLFs from the literature (Figures 3.27, 3.28, 3.29 and 3.30) it is evident that although the data used here is limited to $\gtrsim 10^{24}\mathrm{WHz}^{-1}$, the $\frac{1}{\mathrm{V_{max}}}$points and models are in keeping with the trends (within the errors) discussed.

Specifically, there is agreement of the 9 parameter PLE model with the studies of Smolčić et al. (2009), McAlpine et al. (2013) and Smolčić et al. (2017c). The points from these studies support the low luminosity end of the model, even though it is not sampled completely at $z > 0.5$ with the data used in this thesis. This suggests that the low luminosity end, which is well populated in the lower redshift bins ($0.5 < z < 1.0$ and $1.0 < z < 1.5$) and thus most influences the fitting of the low luminosity end of the RLF, adequately describes the faint end of the RLF at higher redshift measured directly in other studies. This suggests that once the faint end is fixed at low redshift, the best fit evolution term from our PLE model is in agreement with other deeper studies on smaller fields.

The new constraints from this study, lie at the bright end at higher redshifts. Indeed, as discussed earlier, this is why we do not find an reasonable PDE model. We can directly compare the strength of the evolution for the PLE model with other work that used similar parametric modelling for the form of the evolving RLF. Reassuringly we find close agreement with Smolčić et al. (2009), McAlpine et al. (2013) and Smolčić et al. (2017c) (Table 3.5) who also studied the evolution of AGN in their samples.

Pracy et al. (2016) investigated the evolution of the RLF for both LERGS and HERGs as distinct populations. The k term from the PLE model (and also the literature cited previously) lies between the values for these separate populations suggesting there is a mix of the two in the data here, which could account for the differences. The spectroscopic data required to separate HERGS and LERGS in the data used here is not available, therefore this conjecture cannot easily be tested directly. However, future spectroscopic surveys in this field are planned with future multi-object spectrographs such as the Multi-Objects Optical-Near-infrared Spectrograph (MOONS; Cirasuolo et al., 2014).

If a PLE model is preferred for a sample of AGN, this indicates that a primary factor that determines the evolution of the AGN population is the increase and decrease in activity for AGN over time, dominating over the activation or termination of AGN activity. However, the sampling of the RLF over cosmic time is very coarse compared to the duty cycle of AGN activity, which is estimated to be $10^7 - 10^9$ years (e.g. Murgia et al., 1999; Martini & Weinberg, 2001; Gilli et al., 2009). Therefore, it is difficult to establish a one-to-one mapping of population evolution to the evolution

of individual AGN. What we can say is that over the redshift range $z \sim 3 \rightarrow 0$ the AGN population is dimming as a whole, i.e. the physical process that can activate a large population of very powerful AGN at $z \sim 2$ is no longer playing a signifcant role at low redshift. Given that AGN power, and thus radio power from AGN, has been found to depend on the black hole mass (e.g. McLure & Jarvis, 2004), and black holes only grow with time, then it must be the lack of fuel that is causing this evolution. So in summary, it is the combination of black hole growth, which still allows radio-AGN activity to be observed, coupled with a relative dearth of fuel that acts to shift the RLF to lower luminosities.

It is therefore also worth noting that more information on this could be gleaned by separating the mode of accretion following (e.g. Pracy et al., 2016; Prescott et al., 2016). If these studies are accurate, then the PLE evolution is largely driven by the HERG population, which is in line with our understanding that HERGS dominate the bright end of the RLF. Thus it is specifically the lack of efficient accretion of cold gas that is driving the evolution of the radio galaxy population, but this evolution is stronger than is measured when considering the radio source population as a whole.

3.6 Conclusions

I have used a sample of 432 galaxies over a redshift range of $0.04 < \mathrm{z} < 3.0$, with a spectral index distribution ranging $-0.15 < \alpha < 3.8$ from the VIDEO-XMM-LSS field, which is a 4.5 deg^2 patch of sky. I used observations at 150 MHz with LOFAR and 1.5 GHz with the VLA, and use these two frequencies to measure the spectral index of each source. The sample was cross-matched with data from the VIDEO survey to gain redshift information.

I then performed MCMC analysis using two parameterizations, ρ(L,z,α) and ρ(L,z) , and fitting for both PLE and PDE to find the 150 MHz RLF. I found that both PDE and PLE ρ(L,z,α) RLFs match the ρ(L,z) RLFs with little difference. Both ρ(L,z,α) and ρ(L,z) are consistent with the $\frac{1}{\mathrm{V_{max}}}$ points. The most significant difference between the ρ(L,z,α) and ρ(L,z) models is the evolution parameter, k. ρ(L,z,α) models evolve more strongly due to the accurate representation of both individual and sample-wide spectral index values. The data include a significant population of steep-spectrum sources, that when accounted for, greatly limit their observable volume and hence affects the available number of sources at a given redshift range. This remains true when modelling the α-distribution more accurately with a further two parameters (9 parameters in total) that model the steep end. This exemplifies

Study	PLE	PDE	z range	Sky area (deg^2)
This work, 7 parameter	0.83 ± 0.17	$0.57^{+0.14}_{-0.12}$	$0.0 < z < 3.0$	4.5
This work, 9 parameter	$0.85^{+0.29}_{-0.22}$	-	$0.0 < z < 3.0$	4.5
Smolčić et al. (2009)	0.8 ± 0.1	1.1 ± 0.1	$0.4 < z < 1.3$	1.5
McAlpine et al. (2013)	1.18 ± 0.21	1.16 ± 0.09	$0.0 < z < 2.0$	1.0
Pracy et al. (2016), LERGs	$0.06^{+0.17}_{-0.18}$	$0.46^{+0.22}_{-0.24}$	$0.005 < z < 0.75$	900
Pracy et al. (2016), HERGs	$2.93^{+0.46}_{-0.47}$	$7.41^{+0.79}_{-0.13}$	$0.005 < z < 0.75$	900
Smolčić et al. (2017c)	$2.88\pm0.82-(0.84\pm0.34)z$	$2.0\pm0.18-(0.6\pm0.14)z$	$0.1 < z < 5.5$	2.0

Table 3.5: Values of evolution parameter k across the literature for both PLE and PDE. Both 7 parameter models from the work conducted in this thesis are listed, as well as the 9 parameter PLE value of k. The 9 parameter PDE model is not included due to the lack of convergence in Emcee.

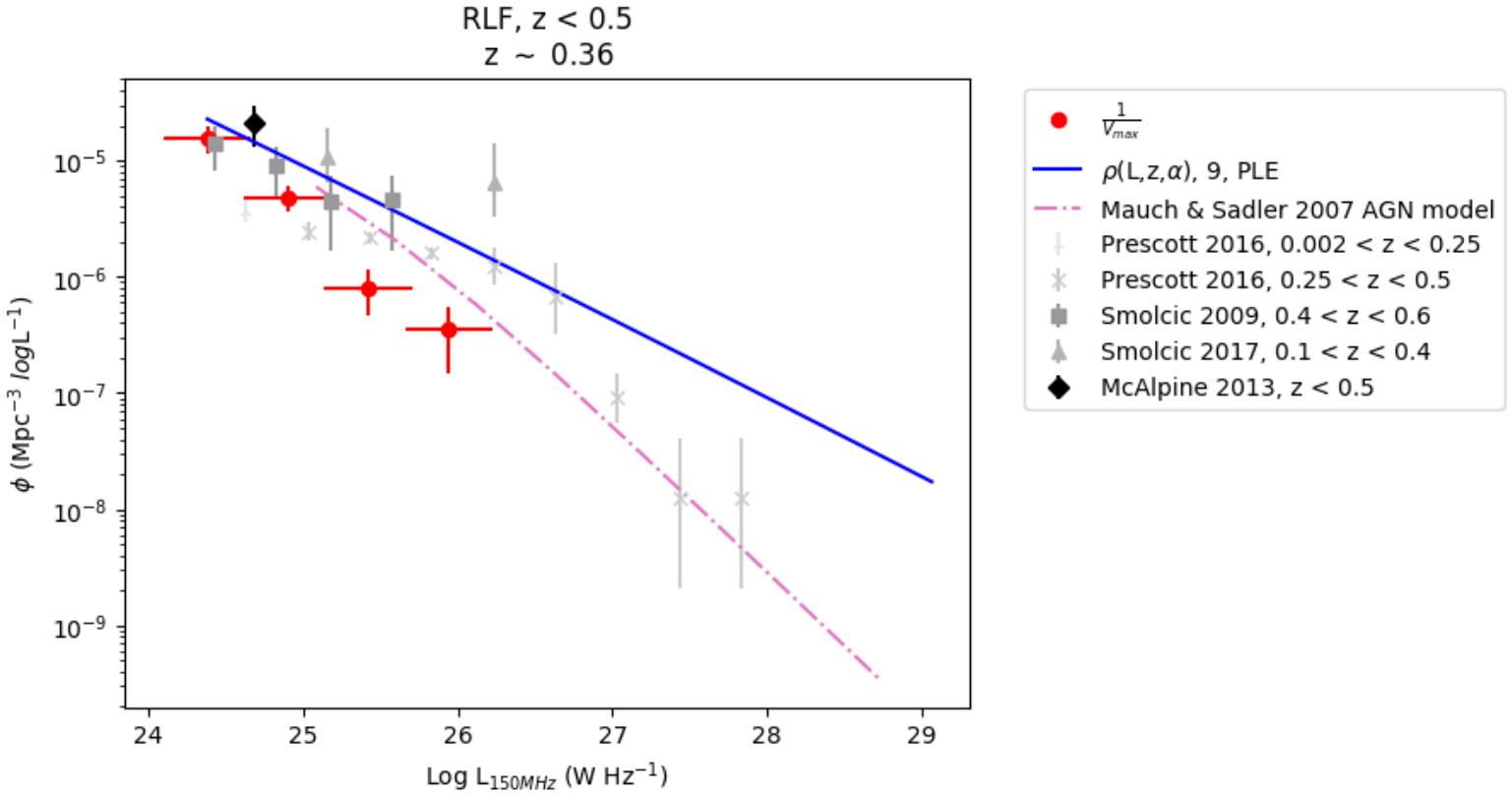

Figure 3.27: Comparing ρ(L,z,α), ρ(L,z)and $\frac{1}{V_{max}}$RLFs with RLFs from the literature. All literature RLFs are from samples exclusively populated by AGN. The red markers represent the $\frac{1}{V_{max}}$points, and the solid lines show the RLFs of 9 parameter ρ(L,z,α) models. The PLE RLF is shown in blue and the PDE RLF is shown in cyan. This plot shows RLFs in the redshift bin $0 < z < 0.5$. The tri up, cross, square, triangle and square markers show the RLFs from Smolčić et al. (2009) $0.4 < z < 0.6$, Prescott et al. (2016) $0.002 < z < 0.25$, Prescott et al. (2016) $0.25 < z < 0.5$, Smolčić et al. (2017c) $0.1 < z < 0.4$ and McAlpine et al. (2013) $z < 0.5$ respectively.

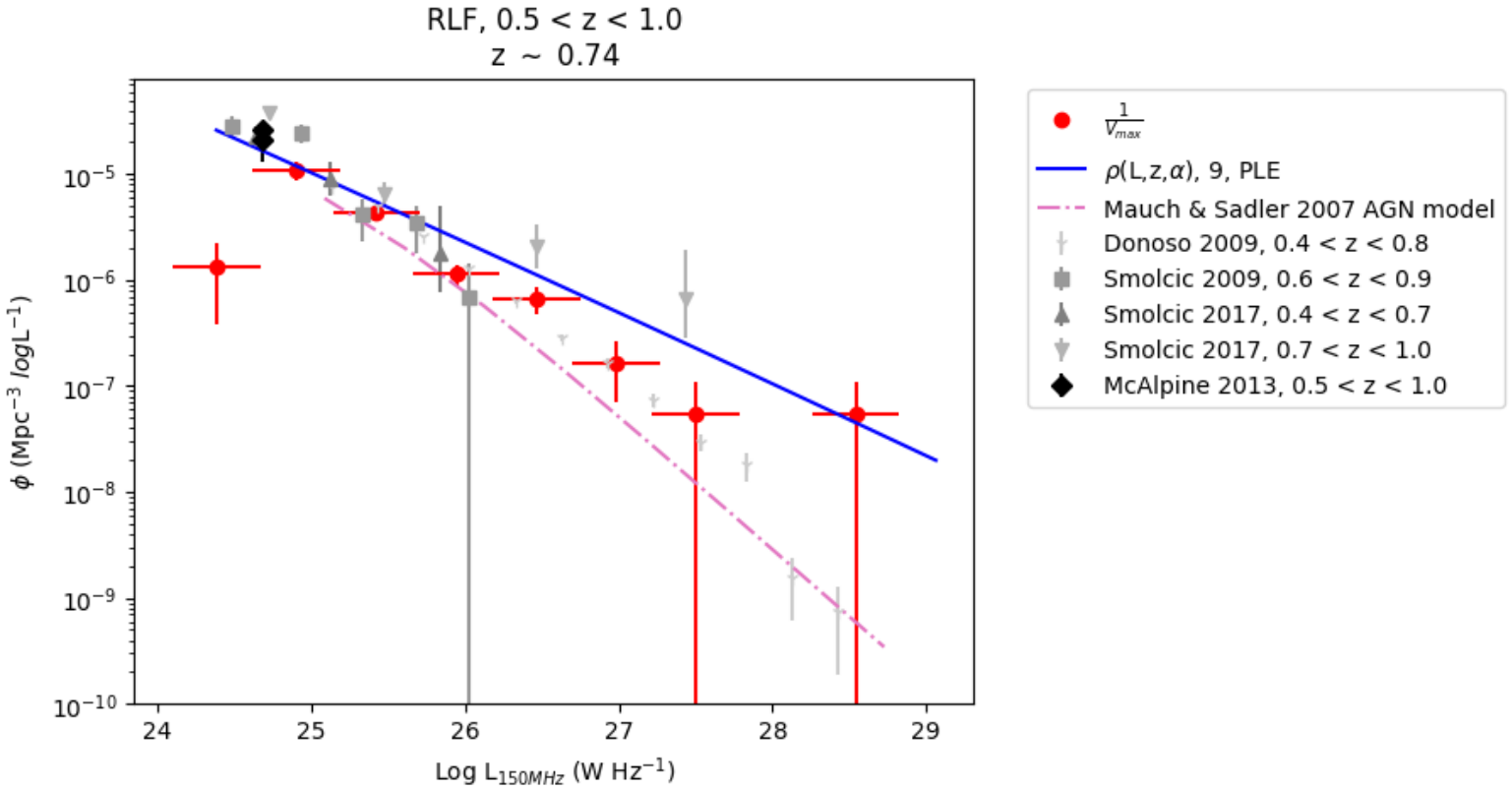

Figure 3.28: Figure 3.27 continued for RLFs in the redshift bin $0.5 < z < 1.0$. The tri down, square, triangle, downward-triangle and diamond markers show the RLFs from Donoso et al. (2009) $0.4 < z < 0.8$, Smolčić et al. (2009) $0.6 < z < 0.9$, Smolčić et al. (2017c) $0.4 < z < 0.7$ and $0.7 < z < 1.0$ and McAlpine et al. (2013) $0.5 < z < 1.0$ respectively.

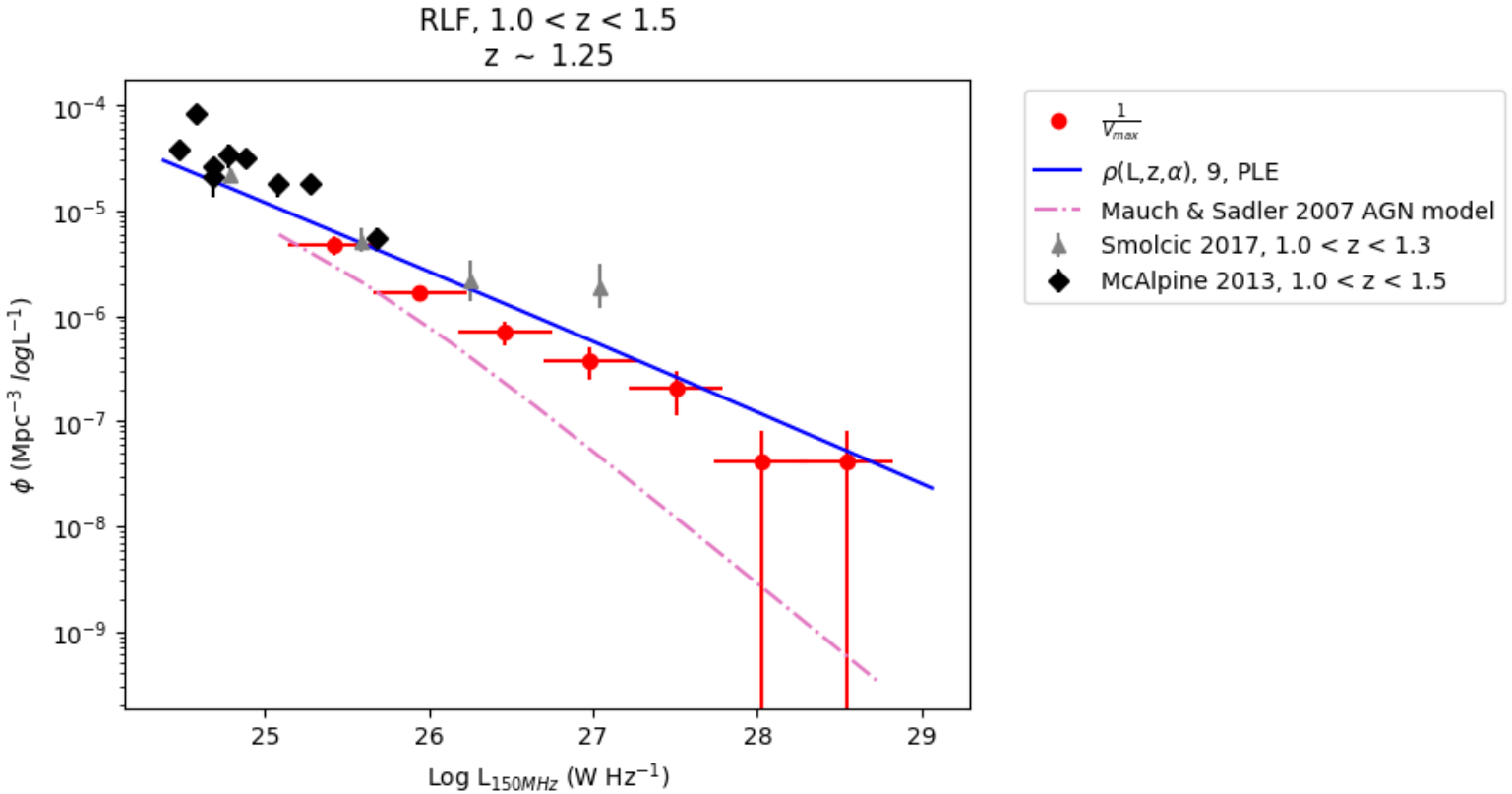

Figure 3.29: Figure 3.27 continued for redshift range $1.0 < z < 1.5$. The triangle and the diamond markers show the RLFs from Smolčić et al. (2017c) $1.0 < z < 1.3$ and McAlpine et al. (2013) $1.0 < z < 1.5$ respectively.

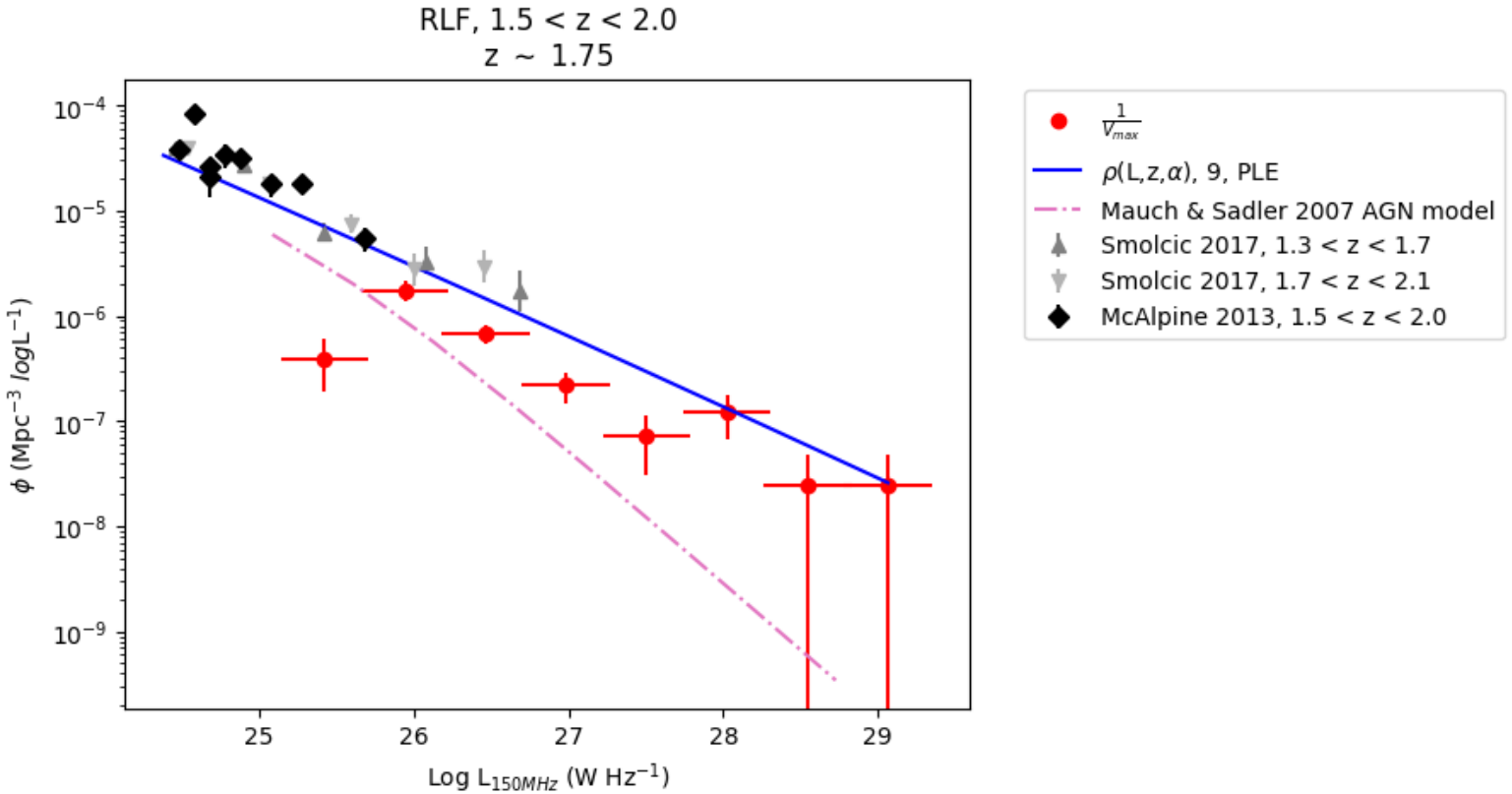

Figure 3.30: Figure 3.27 continued for redshift range $1.5 < z < 2.0$. The triangle, downward triangle and diamond markers show the RLFs from Smolčić et al. (2017c) ranges $1.3 < z < 1.7$, $1.7 < z < 2.1$ and McAlpine et al. (2013) $1.5 < z < 2.0$ respectively.

how the value of the evolution parameter k is dependent on whether one includes spectral index information of a sample, and how well it is modelled. Comparing to the literature the models are largely consistent for the PLE models.

When fitting a 9 parameter PDE model with relatively few data points at the faint end of the RLF, there is simply not enough information to constrain such a high number of parameters and produce satisfactory fits. Therefore, it unsurprising that almost no convergence is seen in the PDE model here. This is also evident in the form of the RLF, where a single power law appears reasonable, as there is not enough data at the faint end to give the RLF the characteristic double power law shape. Since the spectral index mean and distribution affects the truncation boundary of a survey (and thus the faint end) it would be interesting to compare with other PDE models using a sample populated by fainter sources.

When visually inspecting the ρ(L,z,α) and ρ(L,z) RLFs it is difficult to distinguish any major differences between them when comparing to data from the literature. However, for future surveys that are more sensitive and cover larger areas, it may be possible to constrain both the high and low luminosity ends more accurately and obtain a better handle on the RLFs.

However, when examining the individual fits of L, z and α it is evident how the advanced models perform. The clear marker as to why modelling of the α-distribution is important is the result of the evolution parameter, k. The value of k changes drastically with the inclusion of the α-distribution. When this is one of the primary outcomes of RLFs it is evident this factor should be included in future works of this type, to truly get a physical grasp on the evolution of galaxies throughout the history of time.

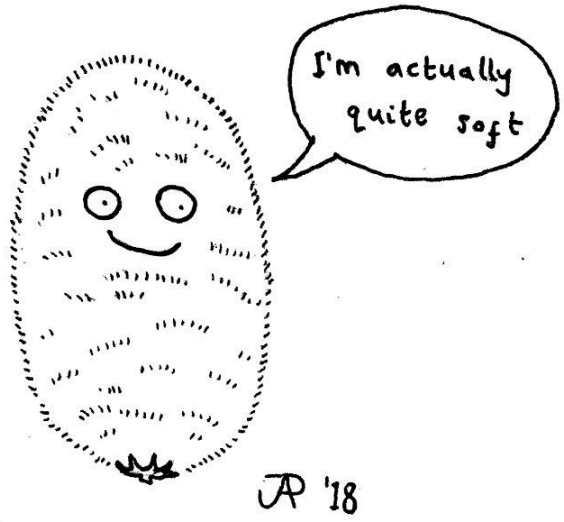
I'm actually quite soft
JP '18

Chapter 4

1.4 GHz Radio Luminosity Functions for SFGs in the COSMOS Field

4.1 Introduction

In this Chapter, the same methodology as Chapter 3 is used. Whereas previously, I investigated the RLFs of AGN, in this Chapter I examine the RLFs of Star Forming Galaxies (SFGs) made possible with the better sensitivity of the data in the COSMOS field. I compare how including the spectral index changes the RLF compared with those from the literature without spectral index information, but also I can contrast the RLFs on the lower-luminosity end of the spectrum that rely on a different physical process for generating the radio emission.

This Chapter is organised as follows. I begin by describing both the VLA and MeerKAT observations and data reduction used for this study in Section 4.2. Since the method is the same as the previous Chapter 3, I provide a brief reminder in Section4.3. I present the results in Section 4.4. Discussion of the results and conclusions are presented in Sections 4.5 and 4.6 respectively.

4.2 Data

For this Chapter, I use existing VLA observations at 3 GHz and new MeerKAT observations at 1.4 GHz of the COSMOS field.

4.2.1 VLA

The VLA data comes from the VLA-COSMOS 3 GHz Large Project (Smolčić et al., 2017a). The observations totalled 384 hours at S-band (2-4 GHz). The bandwidth of 2048 MHz was centred at 3 GHz and separated into 16 spectral windows of 128 MHz each. 324 hours of the data were observed while the VLA was in A-configuration (angular resolution $\sim 0.65''$at S-band) and 60 hours in C-configuration (angular resolution $\sim 7''$at S band). The observations were taken during November 2012 - January 2013, June - August 2013 and February - May 2014. Each observing run was either 5 or 3 hours long and typically used 26 antennas.

To cover the full two square degree COSMOS field and obtain a uniform rms across the map, there were 192 individual pointings. These comprise of three sets of 64 pointings laid out in a grid. The second and third sets were shifted versions of the first set of 64 pointings. The second was shifted by $5'$ in Right Ascension (RA) and Declination (Dec) and the third was shifted by -$5'$ in RA.

The data was calibrated using the Astronomical Imaging Process System (AIPS) based pipeline AIPSLite developed by Bourke et al. (2014), though it was adapted for these specific observations by Smolčić et al. (2017a). Self-calibration was applied to 44 of the 192 pointings, those which had a source of peak brightness > 5mJy beam^{-1}.

In brief, the imaging process was done using a variation on the algorithm CLEAN (see Chapter 2) implemented in CASA. Smolčić et al. (2017a) used multi-frequency synthesis with two Taylor terms (nterms = 2) and a Briggs weighting with a robust parameter of 0.5 to balance between sensitivity and resolution. Each pointing was imaged individually and then mosaicked together using a custom process in `IDL` combined with AIPS task `FLATN`. For full details on the data reduction see Smolčić et al. (2017a). The final map has a resolution of $0.75''$ down to a median rms of 2.3 μJy beam^{-1} for the full 2 square degrees of the COSMOS field.

To extract the sources into a catalogue they used `blobcat` developed by Hales et al. (2012). Resolved and unresolved sources were separated by comparing the peak flux and the total flux for each source, if the ratio is 1 then the source is unresolved. These are labelled in the catalogue. For this work, I aim to only consider the emission from star-forming galaxies. I therefore only use the unresolved sources, which should select all star-forming galaxies at moderate to high redshift, where the typical size of a star forming galaxy is $\lesssim 1''$ (Lindroos et al., 2018). This also ensures that the total emission from each source is captured.

Multi-wavelength counterparts to the VLA-COSMOS data are presented fully in Smolčić et al. (2017b). Briefly, there is data at near-UV, infrared, X-ray and optical

wavelengths, which includes spectroscopic and photometric redshift measurements, the most reliable of which are selected in Delvecchio et al. (2017). Many wavelength counterparts are implemented for the distinction between AGN and SFGs; including X-ray, mid-infrared, spectral energy distribution fitting, UV/optical colour selection and detecting excess measurements in the radio (compared to what is expected for SFGS, to signal the presence of an AGN).

4.2.2 MeerKAT

The MeerKAT data is some of the first collected by the array for the MIGHTEE survey (Jarvis et al., 2016). The observations were taken over $\sim$ 24 hours on three dates; 11, 19 April and 6 May 2018 with 54, 64 and 62 antennas respectively. A total of $\sim$19 hours were spent on target with the remaining 20% of the time observing calibration sources. The central frequency of the observations is 1.4 GHz from an observing band of 856 - 1712 MHz ($\Delta\nu$ = 856 MHz). The observations cover 0.785 deg^2 of the COSMOS field.

The data was reduced by Dr. Ian Heywood and I produce a summary below.

4.2.2.1 Flagging and calibration

To begin with, the data was flagged to remove any forms of interference or bad data. This involved first removing autocorrelations and visibilities with an amplitude of 0. Visibilities with exceptionally high amplitudes ($>$ 50 Jy) were then clipped and a mask was applied to regions known to be troubled by persistent RFI : [944$\sim$947MHz, 1160$\sim$1310MHz, 1476$\sim$1611MHz, 1670$\sim$1700MHz]. From here the `TFCrop` autoflagger in CASA was used under its default settings on the remaining data, the resulting mask was then expanded by one time or frequency point to account for any interference that had not already been captured. Between 30-40% of the data was lost due to RFI.

Delay, bandpass and absolute flux scale calibration was then performed using primary calibrator J0408-6545. This was then followed by time dependent gain calibrations using the secondary calibrator 3C237. These calibration corrections were applied to the target and then split from the remainder of the measurement set (MS) for imaging. All target data was imaged simultaneously.

4.2.2.2 Imaging

An initial image was first produced using WSCLEAN with automasking enabled. The phases were self-calibrated using CUBICAL and then re-imaged again after this calibration using WSCLEAN. From this second image, a CLEANing mask was made using a threshold technique `MakeMask`[1] from DDFACET. This mask was then implemented for the next imaging stage performed using DDFACET. Through visual inspection of this third image, directions were identified to form facets for direction dependent imaging. 11 facets were identified in total for the COSMOS map. KILLMS[2] was then used to derive time-frequency based gain corrections for each of these facets that are then applied on the fly by DDFACET in a further round of imaging. Following this, a primary beam (PB) correction was applied to account for the change in the gain of the telescope as distance from the centre of the field increases. This corrects the flux measurements of sources towards the edge of the map that will have been underestimated due to the decreasing sensitivity of the telescope. The sources were then extracted using PYBDSF.

The predominant type of source in the sample should be SFGs. Since the observations look intensely at a small patch of sky ($\sim$1 deg^2) down to $\sim 2\,\mu$ Jy rms sensitivity, I am able to detect fainter, more numerous sources. The nature of the sources is confirmed after cross-matching with the VLA-COSMOS 3 GHz catalogue which contains all information from the extensive multi-wavelength cross matching done as part of that project. The process of narrowing down to the final sample is described below.

4.2.3 Final Sample

I cross-matched the two radio catalogues by RA and Dec to within $2''$. I separated the SFGs from the sample using the classifications from the VLA-COSMOS project (specifically, whether the SFG flag was labelled 'true') and remove sources labelled as having multiple components. For consistency in this thesis the sample is restricted to redshifts $z < 3$. This resulted in 792 sources at a conservative flux cut of $50\,\mu$Jy at 1.4 GHz. This flux cut is imposed to ensure that the sources near the flux limit are reliable and that again we can measure the spectral indices between 1.4 GHz and 3 GHz accurately. Given that the 5σ limit of the 3 GHz data is 11.5μJy over the

[1] https://github.com/cyriltasse/SkyModel/blob/master/MakeMask.py
[2] https://github.com/saopicc/killMS

Catalogue	Area (deg^2)	Sources	Flux Limit (μJy/beam)	Sensitivity Threshold (σ)
VLA	2	10,633	11.5	5
MeerKAT	0.785	3,952	10	5
Sample used	0.785	792	50*	-

Table 4.1: Summary table define the content and characteristics of the cross-matched sample. *The flux limit of the cross-matched sample is manually imposed to ensure reliability of sources near the flux limit.

region of overlap, this ensures that we are sensitive to spectral indices as steep as $\alpha = 1.92$ for sources near the flux limit.

The distribution in redshift is shown in Figure 4.1. There are a large number of sources at $z \leq 1$, a slight resurgence at $z \sim 2$ and then a steady decline in number counts towards higher redshifts. The redshift range spans $0.0618 \leq z \leq 2.9987$, with a mean $z \sim 1.093$.

The α distribution spans $-1.025 \leq \alpha \leq 2.527$ and so covers the full range of very flat and quite steep spectrum sources. Due to a small surplus of steep spectrum sources visible in Figure 4.2, the mean spectral index of the sample is $\alpha = 0.943$. This is more evident when compared to the median $\alpha = 0.898$.

Figure 4.3 shows the effect of the flux limit of the survey on the ($L_{1.4\mathrm{GHz}}$,z) plane. As sources become more sparse at higher redshift it is easier to see how the truncation boundary becomes less distinguished.

4.3 Method

Following the work presented in Chapter 3; $\frac{1}{\mathrm{V_{max}}}$ (Section 3.3.1), 5-parameter ρ(L,z) (Section 3.3.2.1), 7-parameter ρ(L,z,α) (Section 3.3.2.2) and 9-parameter ρ(L,z,α) (Section 3.5.3) models are tested against each other. I use a 9-parameter ρ(L,z,α) model from the offset as by visually inspecting Figure 4.2 it is clear that there is again a small population of steep spectrum sources in the α-distribution. As with Chapter 3, I make an estimation for parameters related to the α-distribution to assess whether the form of ρ_α is suitable (Equation 3.8, see Figure 4.4).

With all parametric models I aim to minimise $-2 \ln L$ as defined in Equation 3.7. I again use the package EMCEE (Foreman-Mackey et al., 2013) to perform MCMC analysis to find parameters to fit the models. All models take the same form as used previously in Chapter 3.

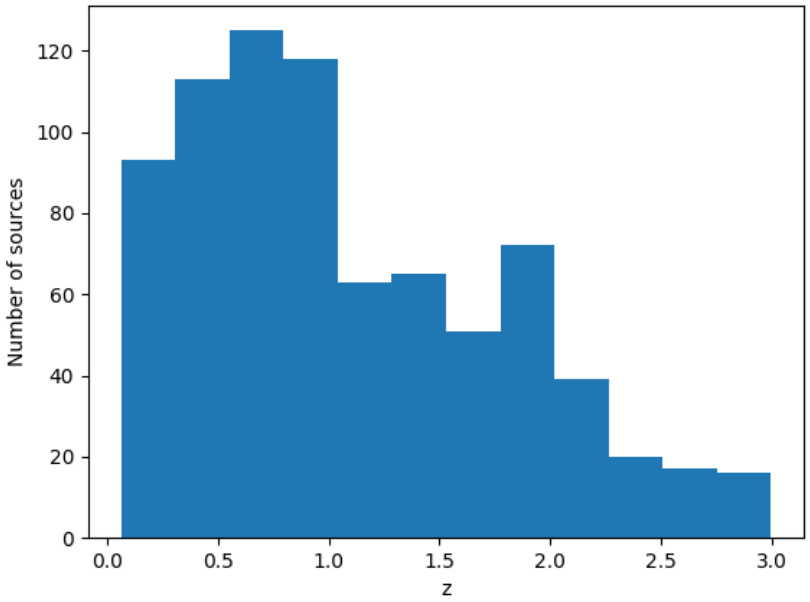

Figure 4.1: Histogram showing the redshift distribution of the MeerKAT-VLA COSMOS sample.

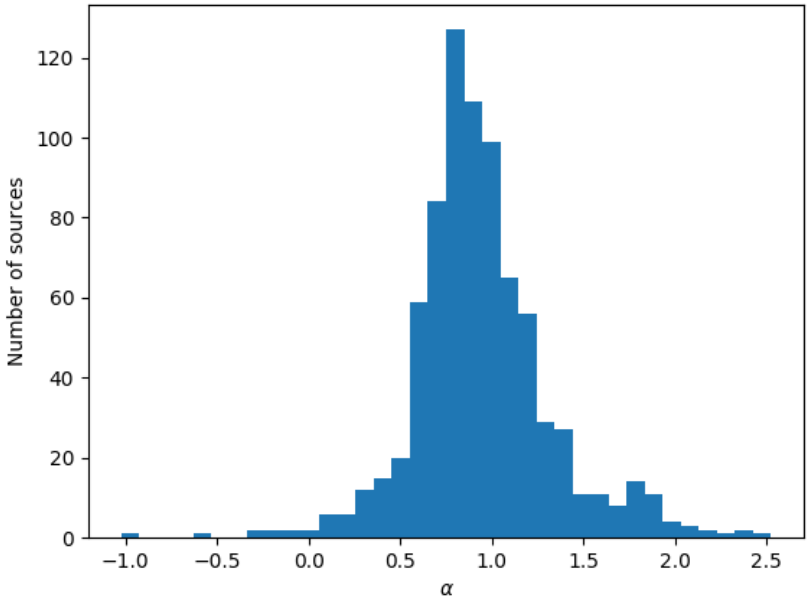

Figure 4.2: Histogram showing the distribution of spectral indices for the MeerKAT-VLA COSMOS sample.

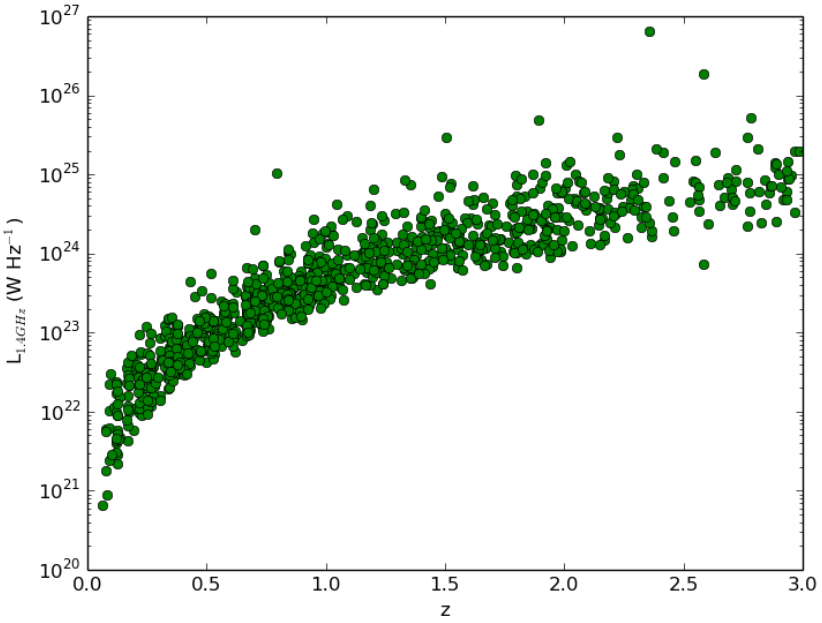

Figure 4.3: The 1.4 GHz luminosity ($L_{1.4}$) versus redshift for the final MeerKAT-VLA COSMOS sample.

4.4 Results

4.4.1 5 parameters

The results of the 5 parameter models can be seen in Figures 4.5, 4.6 and 4.7. I discuss the results of the PLE and PDE models separately below.

4.4.1.1 PLE

The fitting of the parameters for the ρ(L,z) PLE model are clearly defined (see Figure 4.5). The values in Table 4.4 show the PLE model has a strong evolution parameter $k = 2.53^{+0.11}_{-0.11}$. The double power law described by A and B suggests a steep bright-end slope ($A \sim 2$) and a relatively flat faint-end slope ($B \sim 0$). The ρ(L,z) PLE model fits well alongside the $\frac{1}{\mathrm{V_{max}}}$ points (see Figure 4.7), although the $\frac{1}{\mathrm{V_{max}}}$ points sometimes appear higher, this mainly due to the width of the redshift bin over which the $\frac{1}{\mathrm{V_{max}}}$ points are meausred over, whereas the RLF model is shown for the median redshift of the bin. When two RLFs are plotted using the boundaries of the bin for the z value, the model and the $\frac{1}{\mathrm{V_{max}}}$ points are close to one another. However, another factor is due to the simple form of the model.

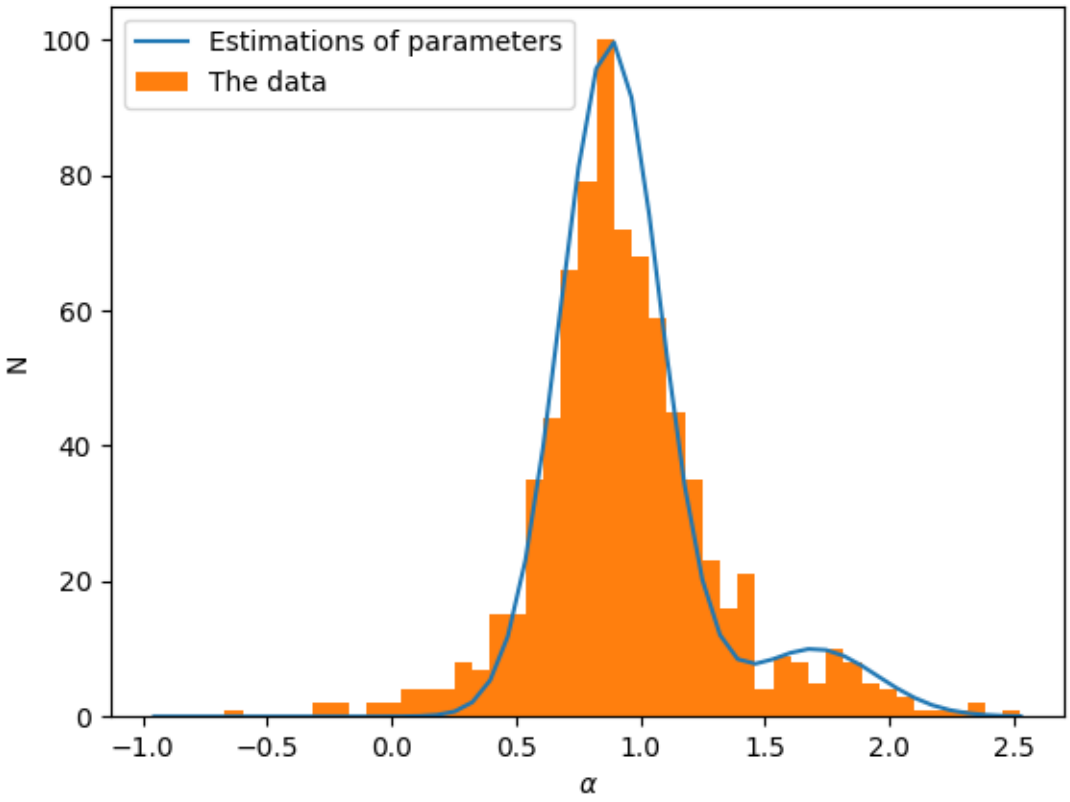

Figure 4.4: The orange histogram shows the data for the α-distribution and the blue line shows my estimation of the parameters to fit the α-distribution. Following Equation 3.8, I estimate via visual inspection parameter values of $\mu_1 = 0.88$, $\sigma_1 = 0.20$, $\mu_2 = 1.7$ and $\sigma_2 = 0.25$.

Parameters	Model	ρ_0	A	B	L_0	k	μ_1	σ_1	μ_2	σ_2	-2ln L
5	PLE	$-2.98^{+0.05}_{-0.27}$	$2.12^{+0.07}_{-0.07}$	$0.05^{+0.25}_{-0.13}$	$22.4^{+0.13}_{-0.05}$	$2.68^{+0.06}_{-0.07}$	-	-	-	-	16019.5
5	PDE	$-4.09^{+0.11}_{-0.10}$	$2.13^{+0.06}_{-0.07}$	$0.68^{+0.06}_{-0.08}$	$22.9^{+0.07}_{-0.07}$	$5.50^{+0.24}_{-0.27}$	-	-	-	-	15998.8
7	PLE	$-3.28^{+0.12}_{-0.56}$	$1.84^{+0.12}_{-0.30}$	$0.45^{+0.13}_{-0.12}$	$22.54^{+0.39}_{-0.11}$	$2.49^{+0.13}_{-0.69}$	$1.09^{+0.02}_{-0.03}$	$0.38^{+0.12}_{-0.01}$	-	-	16820.3
7	PDE	$-4.21^{+0.28}_{-0.19}$	$1.86^{+0.09}_{-0.39}$	$0.74^{+0.09}_{-0.26}$	$23.17^{+0.18}_{-0.16}$	$3.99^{+0.48}_{-1.88}$	$1.10^{+0.02}_{-0.02}$	$0.38^{+0.10}_{-0.01}$	-	-	16809.9
9	PLE	$-3.42^{+0.32}_{-0.52}$	$1.59^{+0.18}_{-0.16}$	$0.52^{+0.15}_{-0.13}$	$22.68^{+0.46}_{-0.23}$	$2.13^{+0.29}_{-0.56}$	$0.95^{+0.03}_{-0.03}$	$0.26^{+0.27}_{-0.02}$	$1.95^{+0.13}_{-0.19}$	$0.87^{+0.24}_{-0.11}$	16780.6
9	PDE	$-4.09^{+0.26}_{-0.27}$	$1.79^{+0.12}_{-0.36}$	$0.74^{+0.11}_{-0.17}$	$23.2^{+0.16}_{-0.16}$	$3.63^{+0.50}_{-1.66}$	$0.96^{+0.02}_{-0.01}$	$0.25^{+0.10}_{-0.01}$	$1.83^{+0.15}_{-0.14}$	$0.78^{+0.09}_{-0.07}$	16685.2

Table 4.2: A summary of the fitted parameters found for each model. All models used 150 walkers in the MCMC process. The number of steps per walker varied from model to model depending on how long it took for a model to converge or time constraints. 5 parameter ρ(L,z) models, PLE: 2515 steps, PDE: 2241 steps. 7 parameter ρ(L,z,α) models, PLE: 298 steps, PDE: 344 steps. 9 parameter ρ(L,z,α) models, PLE: 218 steps, PDE: 356 steps.

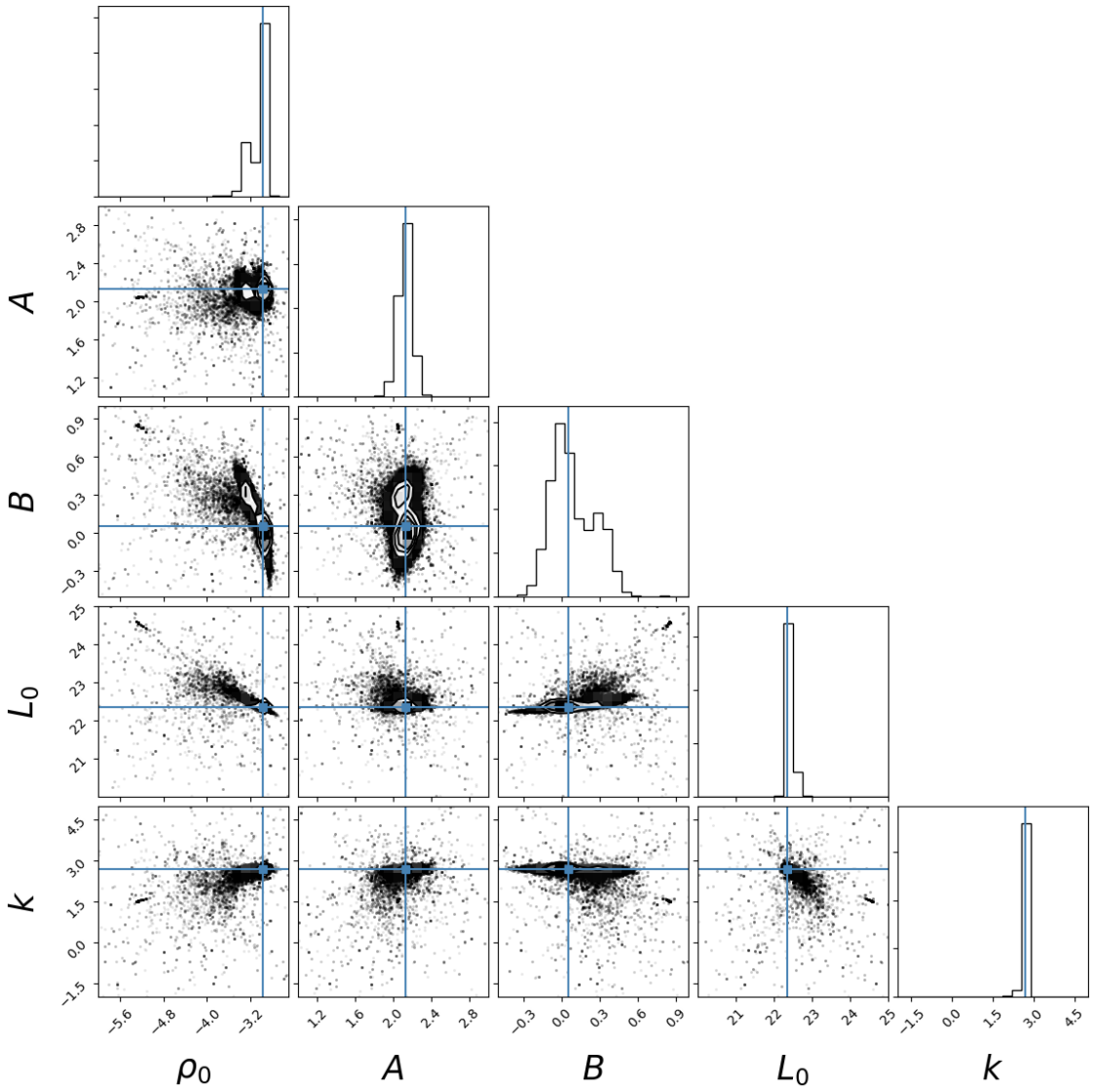

Figure 4.5: The corner plot showing the fits of the parameters for the ρ(L,z) PLE model. The blue lines show the median values that are listed in Table 4.4.

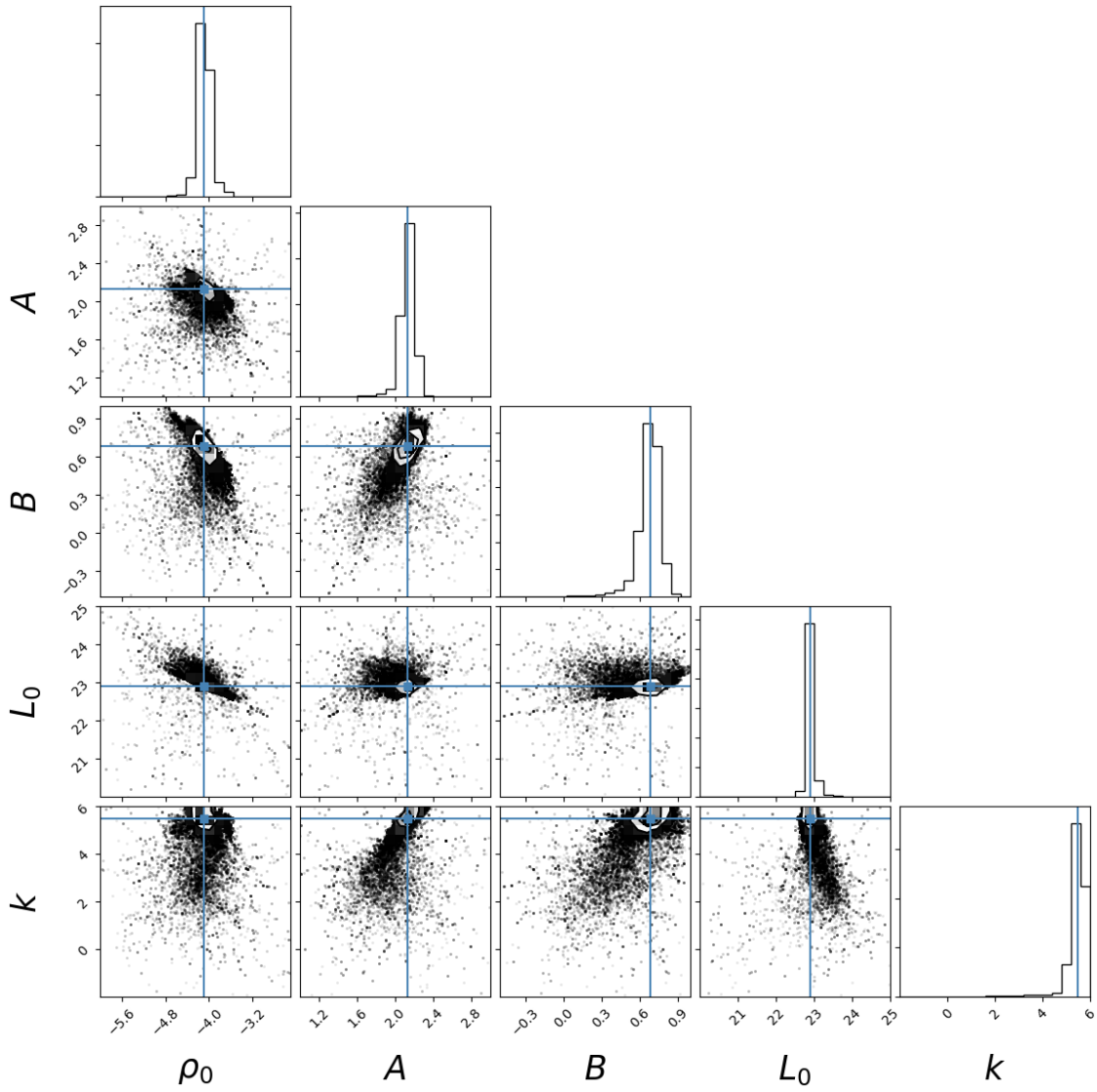

Figure 4.6: The corner plot showing the fits of the parameters for the ρ(L,z) PDE model. The blue lines show the median values that are listed in Table 4.4.

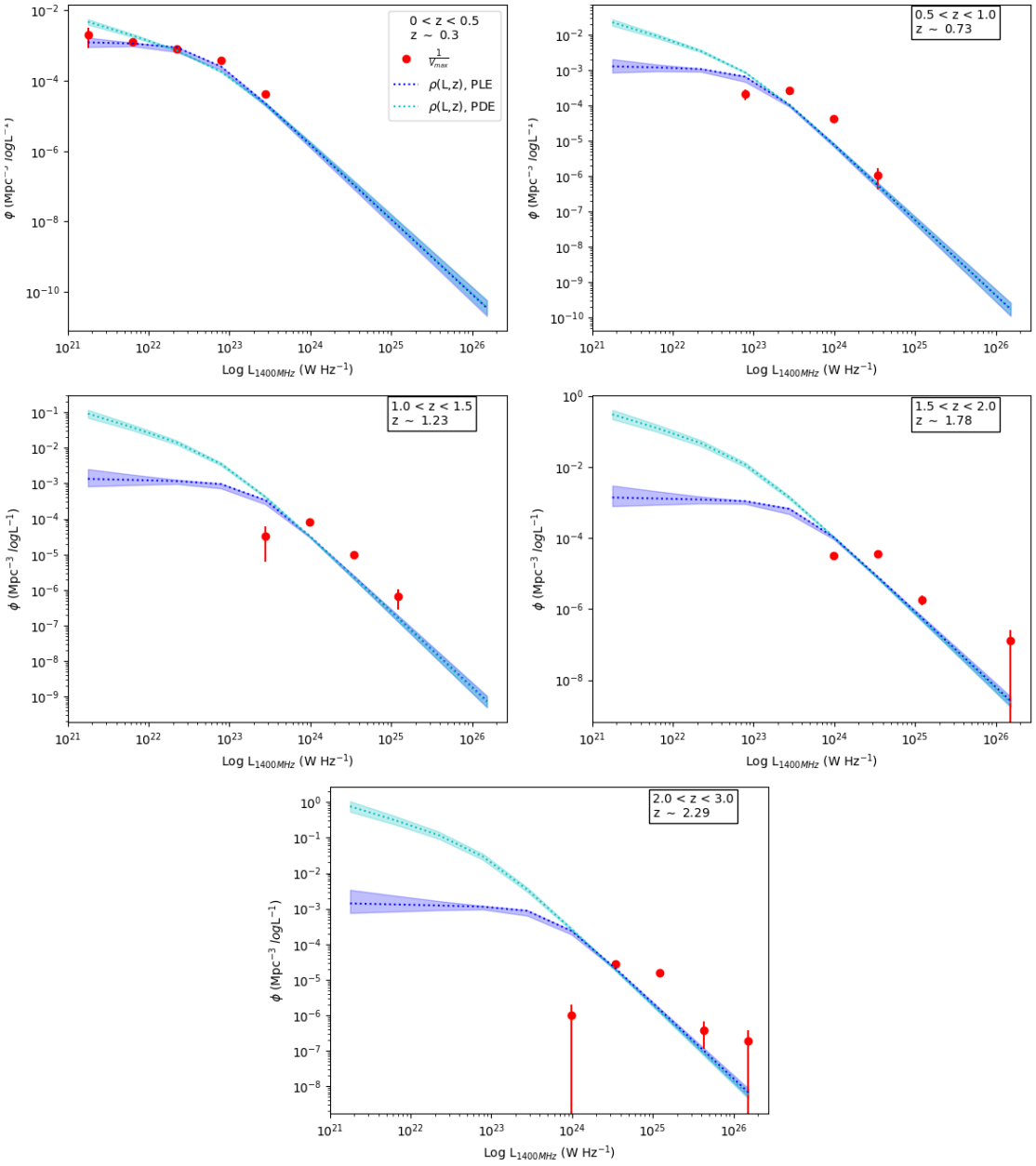

Figure 4.7: The $\frac{1}{\mathrm{V_{max}}}$ and ρ(L,z) RLFs. *Red points:* $\frac{1}{\mathrm{V_{max}}}$ points. *Dotted:* ρ(L,z) models based on the median parameter values from the MCMC sampling. The RLFs are plotted based on the mean $\alpha = 0.94$ for the sample, and the median z for the z-bin. *Blue:* PLE model. *Cyan:* PDE model.

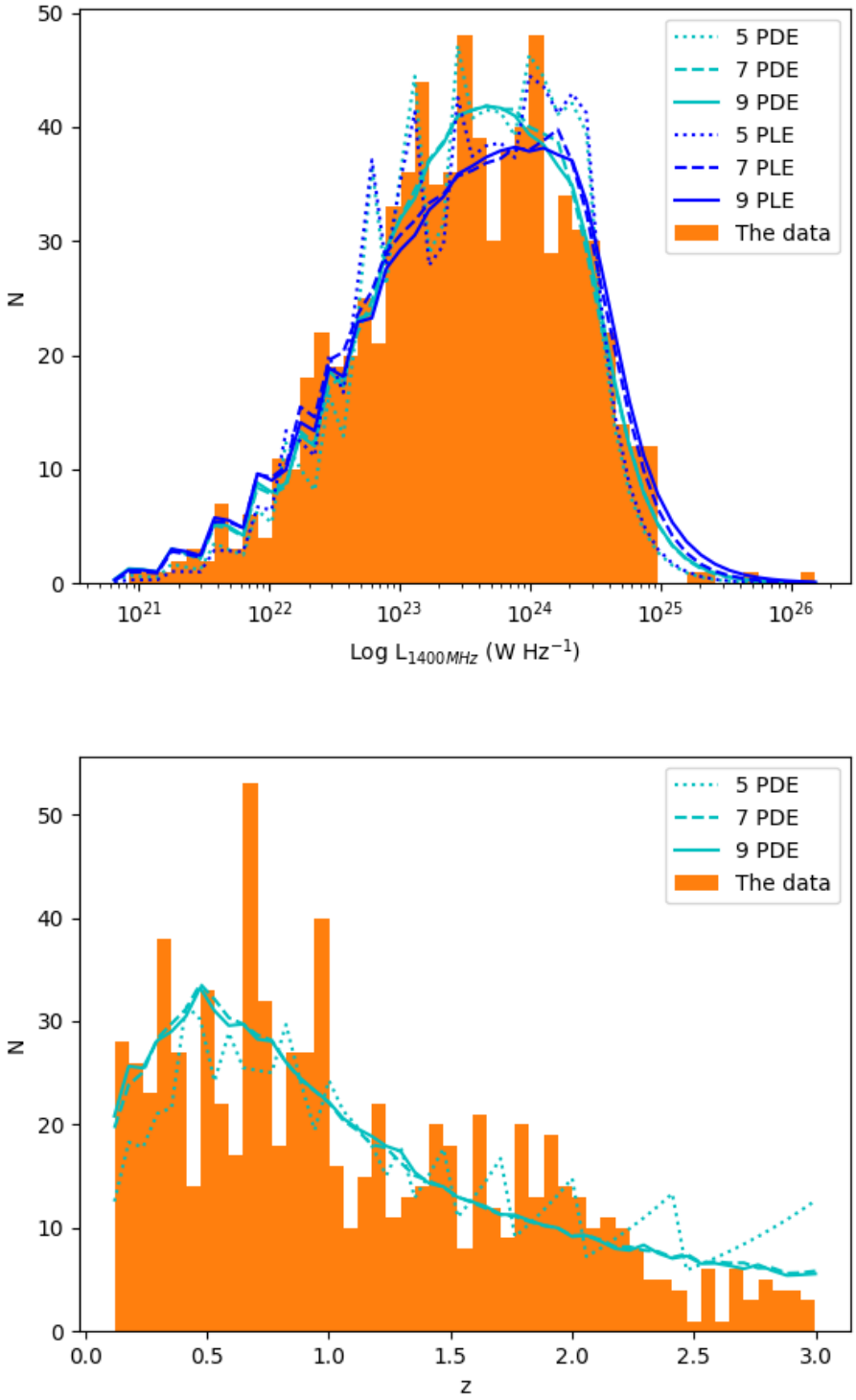

Figure 4.8: Histrogram showing the fits of the models compared to the individual distributions of the data across L and z accounting for the flux limit of the survey. *Upper:* the fit for L. *Lower:* the fit for z.

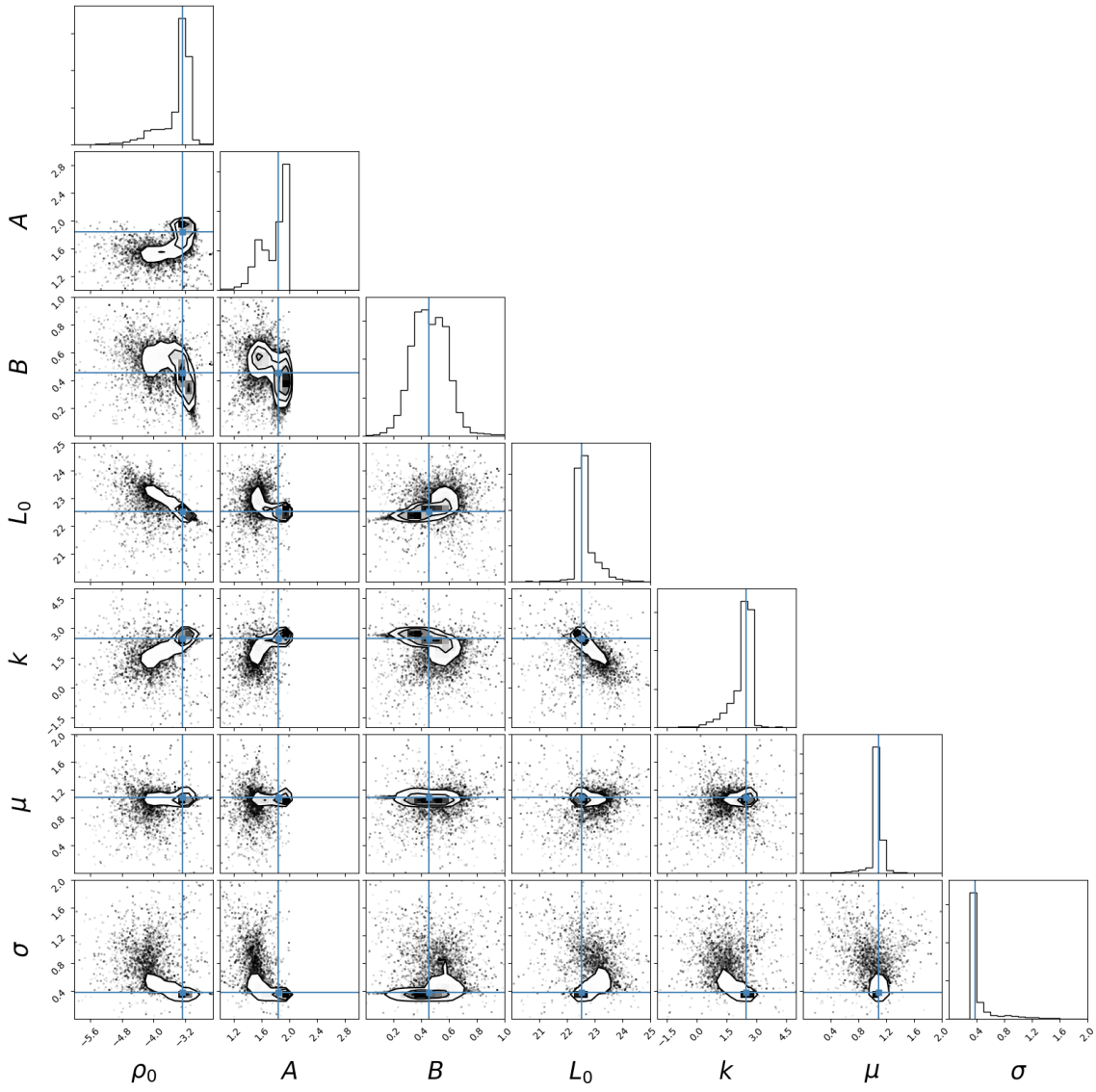

Figure 4.9: The corner plot showing the fits of the parameters for the ρ(L,z,α) 7 parameter PLE model. The blue lines show the median values that are listed in Table 4.4.

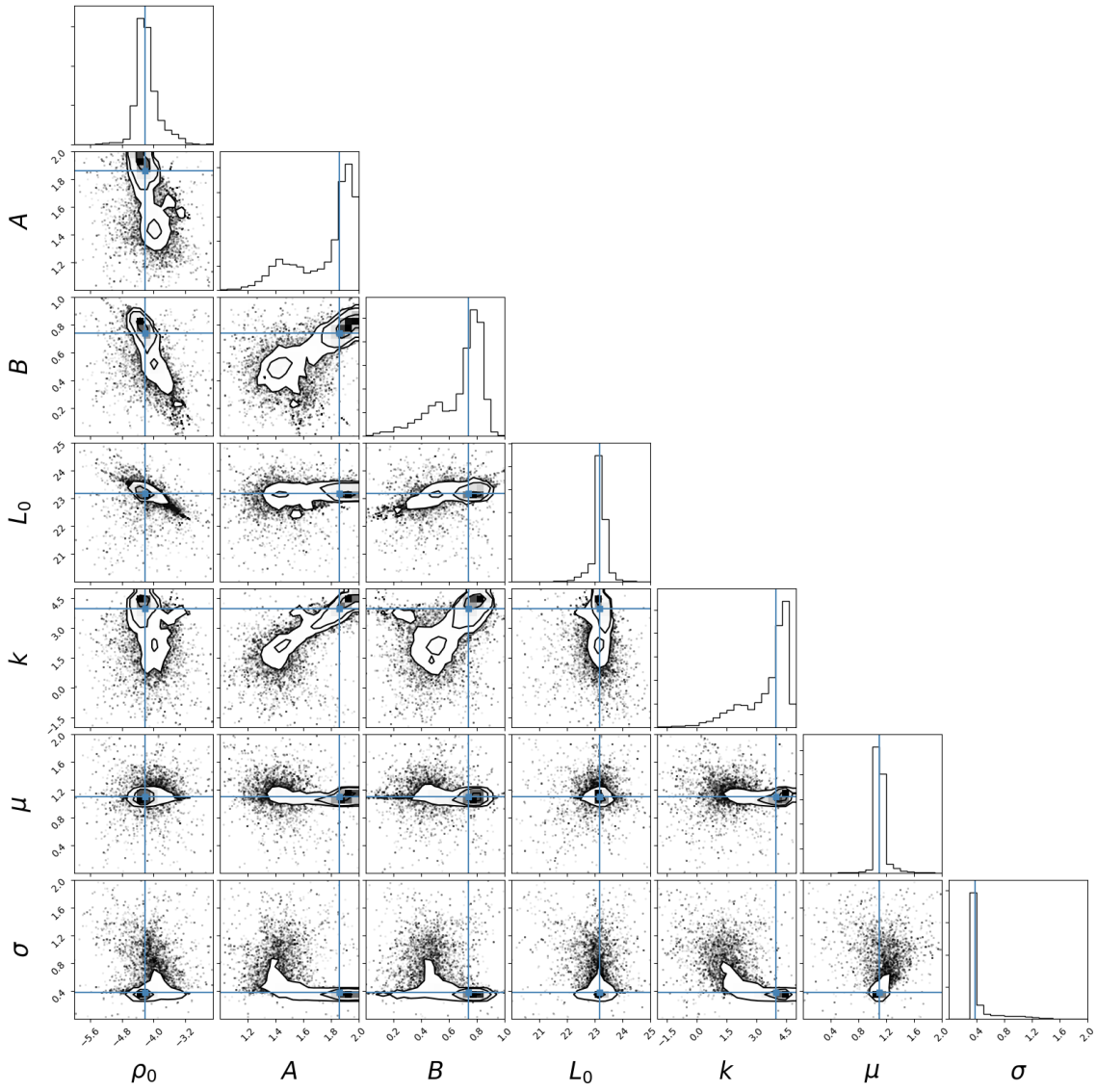

Figure 4.10: The corner plot showing the fits of the parameters for the ρ(L,z,α) 7 parameter PDE model. The blue lines show the median values that are listed in Table 4.4.

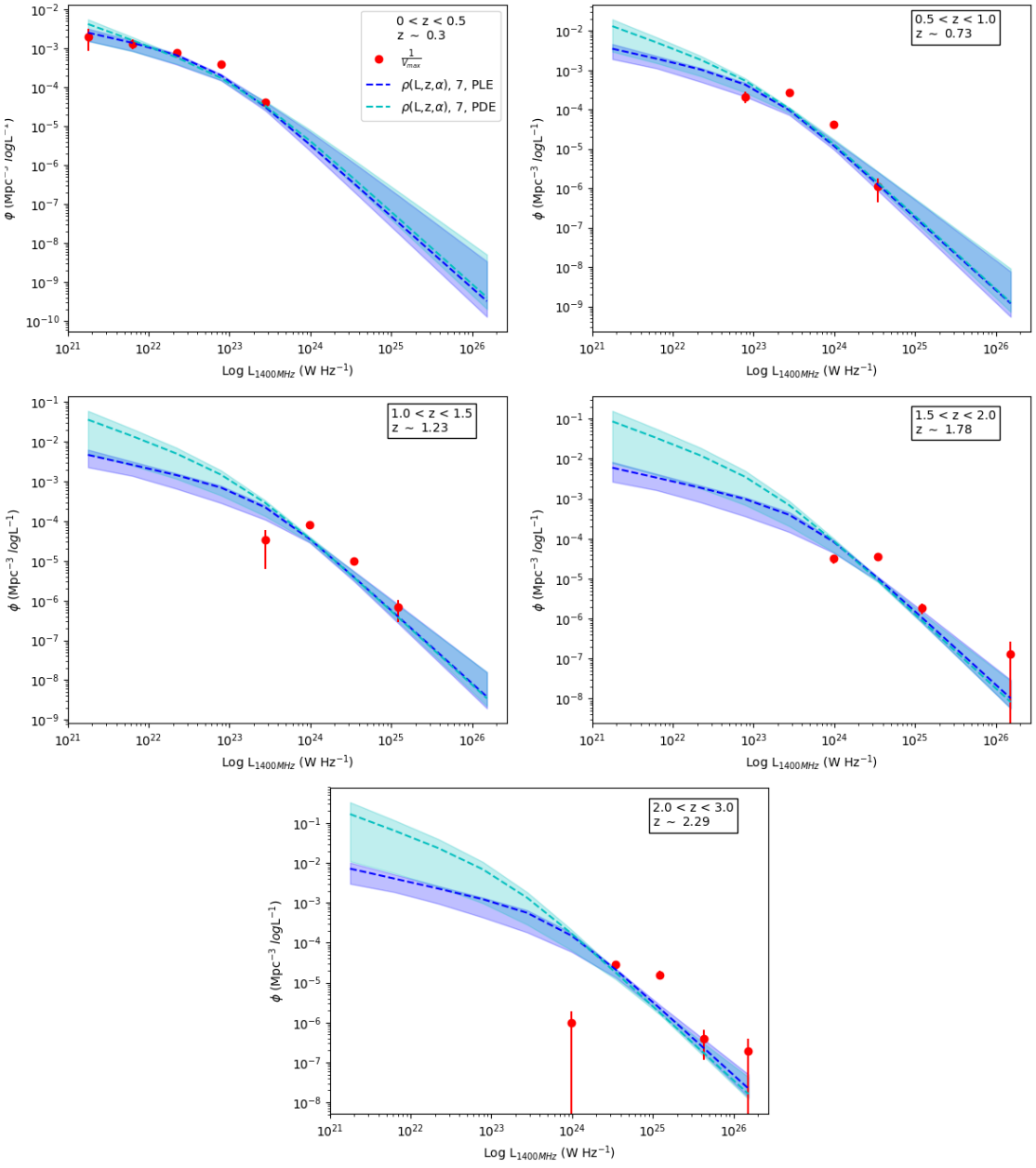

Figure 4.11: The $\frac{1}{V_{max}}$ and ρ(L,z,α) 7 parameter RLFs. *Red points:* $\frac{1}{V_{max}}$ points. *Dashed:* ρ(L,z,α) 7 parameter models based on the median parameter values from the MCMC sampling. The RLFs are plotted based on the mean $\alpha = 0.94$) for the sample, and the median z for the z-bin since individual α and z values are required. *Blue:* PLE model. *Cyan:* PDE model.

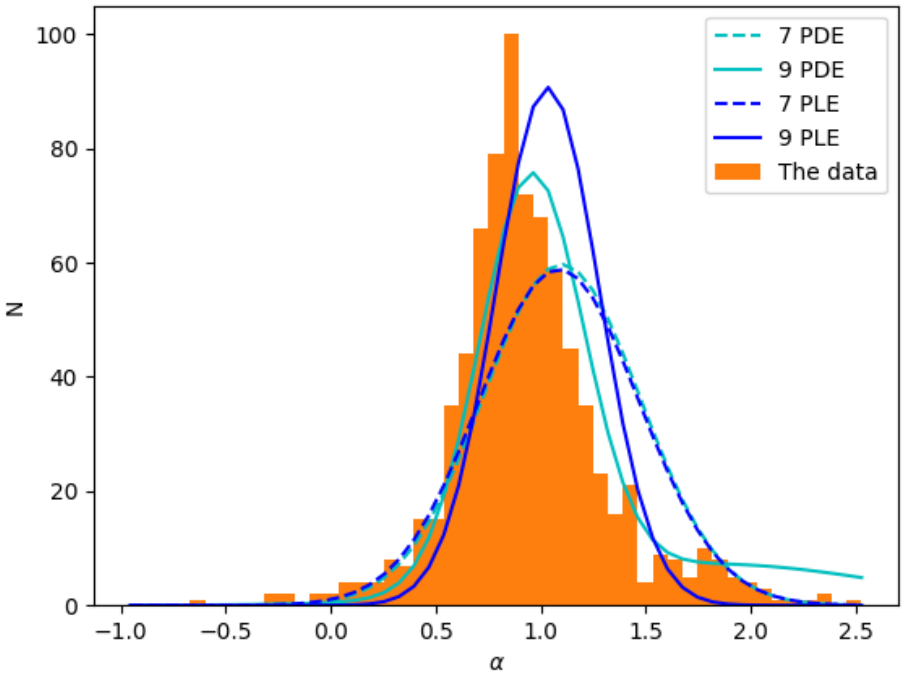

Figure 4.12: The fits of the models that account for the distribution in α compared to the actual distribution of the data.

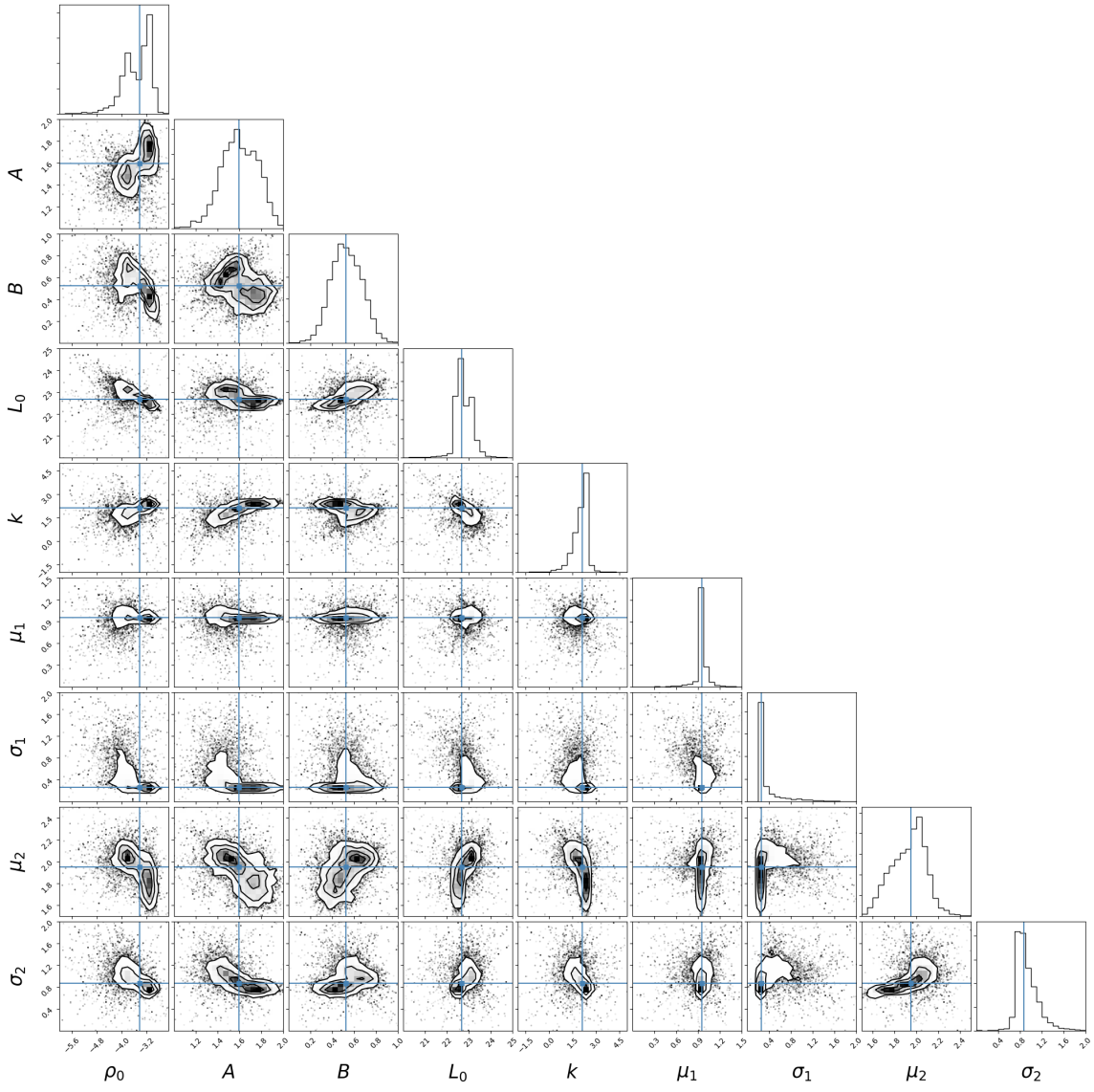

Figure 4.13: The corner plot showing the fits of the parameters for the ρ(L,z,α) 9 parameter PLE model. The blue lines show the median values that are listed in Table 4.4.

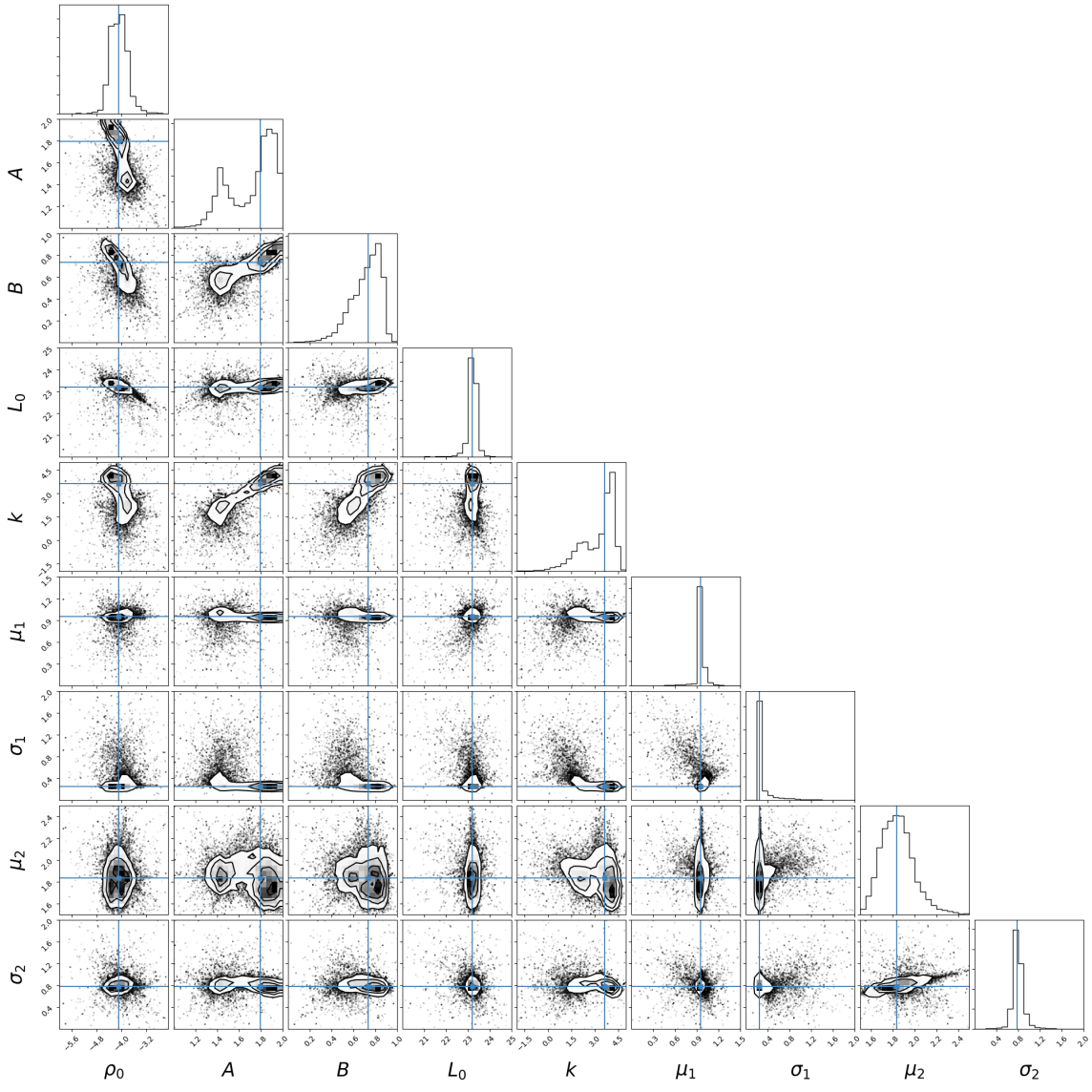

Figure 4.14: The corner plot showing the fits of the parameters for the ρ(L,z,α) 9 parameter PDE model. The blue lines show the median values that are listed in Table 4.4.

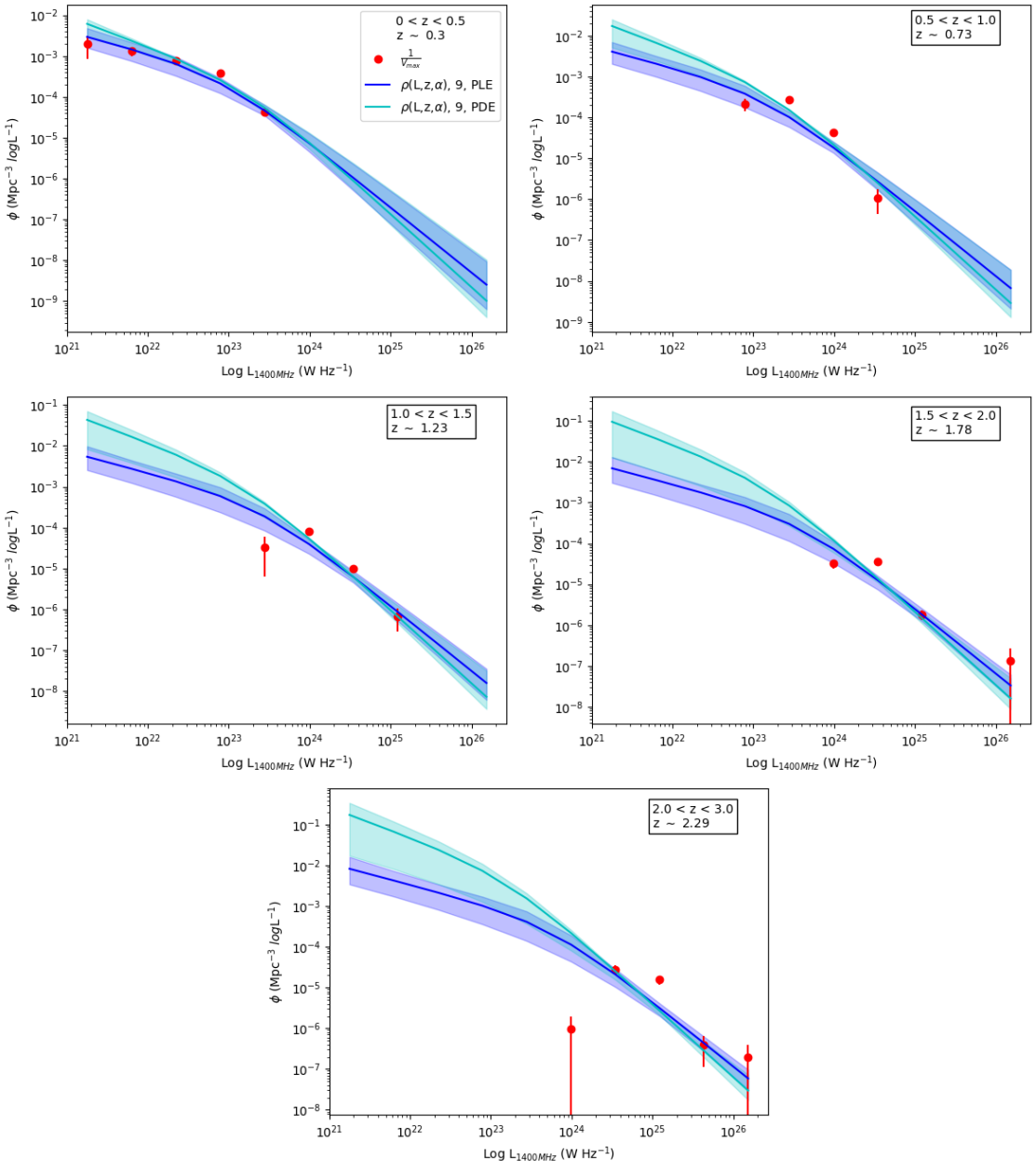

Figure 4.15: The $\frac{1}{V_{max}}$ and ρ(L,z,α) 9 parameter RLFs. *Red points:* $\frac{1}{V_{max}}$ points. *Solid:* ρ(L,z,α) 9 parameter models based on the median parameter values from the MCMC sampling. The RLFs are plotted based on the mean α (0.94) for the sample, and the median z for the z-bin since individual α and z values need to be chosen to display a given RLF. *Blue:* PLE model. *Cyan:* PDE model.

When looking at the fits for the distribution in L individually, the ρ(L,z) PLE model fits the data well (K-S test p value = 0.31) and closely traces the histogram when corrected for the flux limit (Figure 4.8).

4.4.1.2 PDE

The results of the ρ(L,z) PDE model show well defined fits (Figure 4.6, Table 4.4) for each of the parameters. The ρ(L,z) PDE model has the strongest evolution parameter of all of the models that were fitted, with a value of $k = 5.50^{+0.24}_{-0.27}$. A and B are more similar ($A = 2.13^{+0.06}_{-0.07}$, $B = 0.68^{+0.06}_{-0.08}$), resulting in a flatter RLF over the full luminosity range than with the PLE model which predicts fewer low luminosity sources ($L_{1.4\mathrm{GHz}} \lesssim 10^{23}$ WHz^{-1}).

The ρ(L,z) PDE model in also in reasonable agreement with the $\frac{1}{\mathrm{V_{max}}}$ points (Figures 4.7). Some of the distance between the two is accountable for due to the width of the redshift bin which the $\frac{1}{\mathrm{V_{max}}}$ points are evaluated over, compared to the single redshift for the model fits.

Since the ρ(L,z) PDE model accounts for the evolution in z independently of L it is possible to examine how well the model fits the distribution of z in the data on its own (Figure 4.8). Though slightly uneven, the model appears to provide a reasonable fit to the distribution in z by eye, though it fails the K-S test with $p = 0.002$. The fit of the ρ(L,z) PDE model in L closely matches the PLE model and fits well (K-S test p value = 0.57).

The PLE and PDE models separate from one another at the faint-end slope as redshift increases, this is because of the evolution terms. The high value of $k = 5.50^{+0.24}_{-0.27}$ for the PDE model dictates the rate at which the RLF moves down the Φ axis and thus why the PLE and PDE models are so distinct at the faint-end slope at high redshift.

4.4.2 7 parameters

The results of the 7 parameter models can be seen in Figures 4.9, 4.10 and 4.11. I discuss the results of the PLE and PDE models separately below.

4.4.2.1 PLE

The corner plot of the parameters in Figure 4.9 shows ρ_0, B, L_0, μ and σ to be well constrained (summarised in Table 4.4).

This is a little more difficulty in finding conclusive fits for A as there are two peaks in the distribution of parameter values. I inspected whether taking the median value for the parameter A from the second, highest peak makes a substantial difference to the subsequent likelihood. The difference on the likelihood is negligible, an increase by 0.6 up to 16820.9 for the adjusted A value. The value of A itself increases slightly to a median value of 1.93 compared to 1.84. Overall, the fitted range for A is small and the median lies relatively closely to one of the peaks.

Both A and B are degenerate with other parameters, as is evident by their non-circular contour plots in Figure 4.9. When A goes to lower values, and thus flattens the bright end of the RLF, B goes to higher values, steepening the faint end of the RLF. When the two parameters have closer values it gives a near single power-law type RLF. When the values are more distinct the characteristic double power-law shape is more evident. The effect of these degeneracies is also apparent on other parameters; ρ_0 increases as the flattening of the faint end and steepening of the bright end bends the RLF down to fit with the data (exemplified by comparing with the $\frac{1}{\mathrm{V_{max}}}$ points). Simultaneously, L_0 decreases which determines the L value at which the RLF is normalised. k increases with the steepening of A and flattening of B, suggesting that to fit the model a stronger evolution term is required then with an RLF that resembles more closely a single power-law.

In terms of looking at the L and α distributions, the ρ(L,z,α) PLE model fits the distribution in L more accurately than the ρ(L,z) models (Figure 4.8). It follows the shape of the distribution well (K-S test $p = 0.31$). The fit for α is unsatisfactory as the curve is too wide, and has been shifted up towards steep spectral indices due to a small surplus in steep spectrum sources (see Figures 4.12 and 4.2). This is further illustrated by the value for $\mu = 1.09^{+0.02}_{-0.03}$, even though the dominant peak in α lies at ~ 0.8. It also fails the K-S test with a $p = 7.4 \times 10^{-26}$. For this reason I use 9 parameter ρ(L,z,α) PLE models.

4.4.2.2 PDE

The 7 parameter ρ(L,z,α) PDE model is well constrained for parameters ρ_0, L_0, μ and σ (Figure 4.10, Table 4.4). Though the PDE model also shows signs of two peaks in the distribution of parameters A, B and k, the medians lie close enough to the more dominant peak that it is not necessary to consider more strict restrictions on those parameters. The model follows the $\frac{1}{\mathrm{V_{max}}}$ points at all redshifts. The evolution parameter is notably high in this model at $k = 3.99^{+0.48}_{-1.88}$.

Degeneracies are also apparent in the PDE model (see non-circular contours in Figure 4.10). As A and B move to steeper values the model is forced to evolve more strongly with higher k values for a constant ρ_0 and L_0. This suggests that either the model has steep A and B values determined at low-z which forces the RLF to evolve strongly, or there are flatter A and B values where less evolution is required.

For the distribution of the data in L and α the fits closely align with that of the PLE model (Figures 4.8 and 4.2). In terms of L the PDE model is slightly less satisfactory, but still follows the data well (K-S test p value = 0.78). In α the PLE and PDE models are almost identical, with $\mu = 1.10^{+0.02}_{-0.02}$. It also fails the K-S test with a $p = 1.11 \times 10^{-20}$. This further reinforces the need for 9 parameter models and for this reason I use 9 parameter ρ(L,z,α) PDE models as well as PLE models.

The fit of the distribution in z (Figure 4.8) is more reasonable than the 5 parameter ρ(L,z) models giving a K-S test $p = 0.489$.

4.4.3 9 parameters

The results of the 9 parameter models can be seen in Figures 4.13, 4.14 and 4.15. I discuss the results of the PLE and PDE models separately below.

4.4.3.1 PLE

The 9 parameter ρ(L,z,α) PLE model fits well alongside the $\frac{1}{\mathrm{V_{max}}}$ points and shows a definitive fit on the corner plot for all the parameters, although there is some degenracy between ρ_0 and the power-law slopes of the RLF (Figure 4.13, Table 4.4). I find a moderate evolution parameter $k = 2.13^{+0.29}_{-0.56}$ and the double power law to describe the shape of the RLF has a steep end at high luminosities ($A = 1.59^{+0.18}_{-0.16}$) which becomes flatter ($B = 0.52^{+0.15}_{-0.13}$) below $\log_{10} L_0 = 22.68^{+0.46}_{-0.23}$ WHz^{-1}.

The PLE model shows a double peak in the distribution of ρ_0. Though, when taking the median value to focus on the high peak at $\rho_0 > -3.42$ (the median for the overall sample), the likelihood increases from 16780.6 to 16803.6 and the value of ρ_0 goes from -3.42 to -3.19. Distributions appear broad in A and B but the range of the is narrow in both cases compared to other parameters.

A degeneracy appears between ρ_0, A, B and μ_2 in Figure 4.13. As A becomes shallower, B is steeper in turn increasing ρ_0 and μ_2. A shallower A (bright-end) and steeper B (faint-end) brings the two values closer together to mimic a single power-law and requires a smaller normalisation of ρ_0. A higher value for μ_2 means incorporating more steep spectrum sources, which when K-corrected are brighter in the rest-frame

than a flatter-spectrum source observed with the same flux, this coincides with a shallower value for A and steeper value for B as sources previously underestimated in their rest-frame luminosity move along the L axis to higher and brighter values.

The fit of the 9 parameter ρ(L,z,α) model on the distribution of the data in L, lies on top of the 7 parameter model. Of all the models, both the 7 and 9 parameter PLE model fit the L distribution most closely. The K-S test gives a p value = 0.379.

In terms of the α-distribution, there is a marked improvement on the fit from the 7 parameter model. The 9 parameter ρ(L,z,α) PLE model is much close in shape and location of peak than in the 7 parameter case. The value of μ is closer to what the visual inspection of the data suggests, with $\mu = 0.95^{+0.03}_{-0.03}$. The fit also includes the surplus of steep spectrum sources which can be seen in Figure 4.12. However, the location of the peak of the model distribution does not match the data and the model fails the K-S test with a p value = 1.5×10^{-8}.

4.4.3.2 PDE

The 9 parameter ρ(L,z,α) PDE model shows reasonable fits for all parameters (Figure 4.14, Table 4.4) and fits well against the $\frac{1}{V_{max}}$ points. Though some of the parameters show additional peaks in the distribution of the samples for those parameters, the median values lie firmly attached to a peak and not in-between the two, so I will not be investigating these further. This final sample attains the best likelihood, even when going back to smaller numbers of samples in the same run which had more defined peaks, the likelihood was worse.

The evolution parameter of $k = 3.63^{+0.50}_{-1.66}$ suggests that the PDE model is showing stronger evolution in density than the respective PLE model.

Again there are degeneracies between A, B and k for this model. This mirrors the 7 parameter PDE model in that steeper values of A coincide with steeper values of B and increasing the value of k. This decreases the number density at the bright-end and increases the number density at the faint-end. It suggests that a model with steep A and B values is constrained more at low-z and is forced to evolve more strongly to fit with higher redshift data.

The fit of the distributions in L and z closely match the 7 parameter fit and are generally good. The K-S test p values are $p = 0.6979$ for L and $p = 0.346$ for z. In α, the PDE model improves on the corresponding 9 parameter PLE model in that the shape is more like the underlying distribution. However, the PDE model fails to accommodate the surplus in steep spectrum sources (see the upper tail end in Figure 4.12) and subsequently fails the K-S test with $p = 2.21 \times 10^{-9}$.

4.5 Discussion

4.5.1 Parametric modelling vs. $\frac{1}{V_{max}}$

All the models fit well against the $\frac{1}{V_{max}}$ points. In the lowest redshift bin, $z < 0.5$, the parametric models and the $\frac{1}{V_{max}}$ points lie directly on top of one another (see Figure 4.16, Table 4.4). The main discrepancies occur at higher redshift where the number of sources are less numerous. Beyond $z > 0.5$, the parametric models do not turn down severely like the $\frac{1}{V_{max}}$ points do and are smoother. The jumpiness of the $\frac{1}{V_{max}}$ points can be attributed to the lack of data in those particular bins, which is demonstrated by the large error bars at those points. Overall, the parametric models agree well with the empirical method.

4.5.2 5, 7 and 9 parameter models

In Figure 4.16 the 5 parameter RLFs are represented by dotted lines, the 7 parameter RLFs by dashed lines and the 9 parameter RLFs by solid lines. All the models fit reasonably well against the $\frac{1}{V_{max}}$ points.

At the bright-end ($L_{1.4GHz} \gtrsim 10^{23}$ WHz^{-1}), models with greater numbers of parameters predict a higher number density of bright sources. However, this separation begins to decrease with increasing redshift, which is where the higher luminosity bins become more constrained. The 7 and 9 parameter RLFs follow each other closely across all redshifts and over both PLE and PDE models. The 5 parameter model, however, is more extreme than the other two in the regions which are unconstrained. This is evident at the low luminosity end ($L_{1.4GHz} \lesssim 10^{23}$ WHz^{-1}), where the 5 parameter model predicts are large number of sources for the PDE model, but under predicts in the PLE model compared to the 7 and 9 parameter RLFs. It is not possible to ascertain which of these is correct as this only occurs in redshift bins where this region of the RLF is poorly constrained by data.

This severity of the 5 parameter model is exemplified by the k values. Table 4.4 shows the 5 parameter model to have the highest values for k over all models ($2.68^{+0.06}_{-0.07}$ for PLE and $5.50^{+0.24}_{-0.27}$ for PDE). The k values in both PLE and PDE models decrease for 7 parameters ($2.49^{+0.13}_{-0.69}$ for PLE and $3.99^{+0.48}_{-1.88}$ for PDE) and then even further for the 9 parameter model ($2.13^{+0.29}_{-0.56}$ for PLE and $3.63^{+0.50}_{-1.66}$ for PDE). The reduction in the k value could be attributed to the fact that more information, namely the specific distribution of spectral index α, is accounted for in these more complex models. The more simplistic models may be using the k parameter to compensate for ill-fitting elsewhere. A more severe evolution term is likely to be necessary in models which

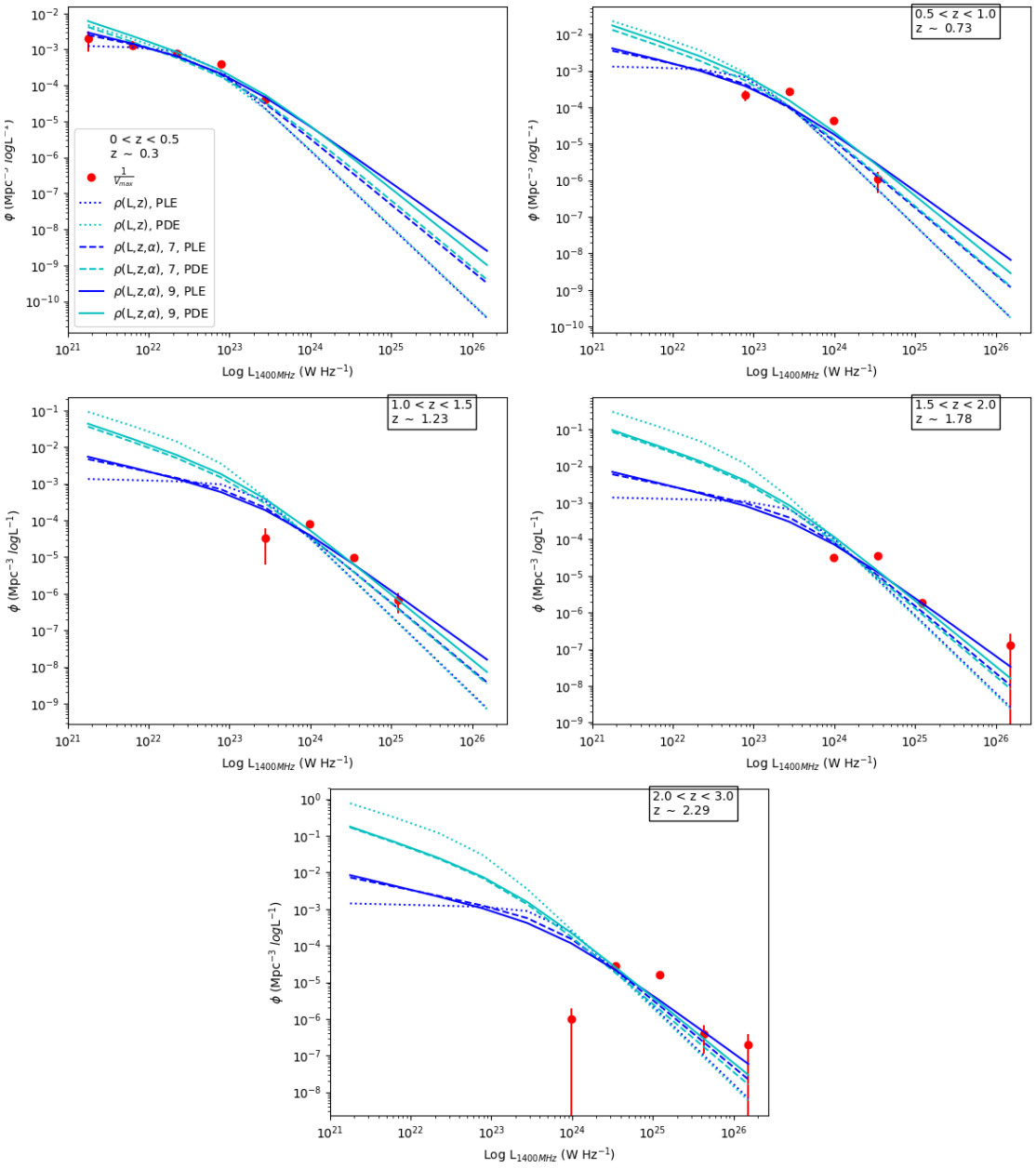

Figure 4.16: The $\frac{1}{V_{max}}$, ρ(L,z) and ρ(L,z,α) RLFs. *Red points:* $\frac{1}{V_{max}}$ points. *Dotted:* ρ(L,z), *Dashed:* 7 parameter ρ(L,z,α), *Solid:* 9 parameter ρ(L,z,α) models based on the median parameter values from the MCMC sampling. *Blue:* PLE models. *Cyan:* PDE models. For ease of comparison I have not included the errors on these plots.

do not account for the small population of sources with steep spectral indices. A population of sources with a steep spectral index populates the bright-end of the RLF when K-corrected accurately, making the parameter A shallower as it includes more sources. Not accounting for these sources can force stronger evolution terms to cope with the shallower bright-end, as the model itself is not expecting this region to be as populated as it is.

Another area which shows the dramatic change the 5 parameter model undergoes to fit the data is in the values for A and B. Though not as extreme as the evolution parameter k, this too shows more pronounced differences between PLE and PDE models that stabilise as the models increase in complexity. A remains consistent over PLE and PDE models, but gradually decreases from $2.12^{+0.07}_{-0.07}$ and $2.13^{+0.06}_{-0.07}$ for 5 parameters, to $1.59^{+0.18}_{-0.16}$ and $1.79^{+0.12}_{-0.36}$ at 9 parameters for PLE and PDE models respectively. It is only with more parameters that the value for A starts to differ for PLE and PDE models. This is expected as the bright-end is modelled more accurately through the inclusion of steep spectral index sources, A is more tailored to each model. The values for B are more variable, especially for PLE models. In the PDE models the value for B increases from $0.68^{+0.06}_{-0.08}$ in the 5 parameter model to $0.74^{+0.11}_{-0.17}$ in the 9 parameter model. Whereas, when modelling for PLE, B begins at a low $0.05^{+0.25}_{-0.13}$ in the 5 parameter model, catching up with the PDE model at 9 parameters as $0.52^{+0.15}_{-0.13}$. B represents the faint-end slope of the RLF. In the PDE models with stronger evolution terms, the faint-end is pinned at low-z where it is most constrained, and is then forced to evolve more strongly. This also ties in with the modelling of the steep spectrum sources as they shift towards the bright-end. A steeper value for B coupled with a more negative value for ρ_0 maintains the relationship at the faintest part of the faint-end but reduces the predicted number density at mid-range luminosities.

Overall, the 9 parameter models show the best fits in the distribution of the data individually, accurately representing the underlying data in L and z, though still unsatisfactory for α. If these models are taken to be the most reliable, it gives evidence to support including an accurate distribution of the spectral index α. The 9 parameter models have more modest evolution parameters and the PLE and PDE models become more similar than the simpler models. The effect is especially dramatic for the PDE models.

Since the 9 parameter models are still unable to accurately fit the α-distribution, in the next section I implement an 8 parameter model using a different form for modelling the α-distribution with the aim to improve the fit further.

4.5.3 8 parameters

The form of the RLF for this 8 parameter model follows previous models, but with a different definition for ρ_α to address the problem with replicating the α-distribution. ρ_α is now defined by a Lorentzian distribution with different widths either side of the peak value, which provides longer tails and a narrower peak than a Gaussian;

$$\rho_\alpha = \left\{ \begin{array}{ll} \frac{1}{\pi} \frac{\frac{1}{2}\sigma_1}{(\alpha-\mu)^2+(\frac{1}{2}\sigma_1)^2} & : \alpha \leq \mu \\ \\ \frac{1}{\pi} \frac{\frac{1}{2}\sigma_2}{(\alpha-\mu)^2+(\frac{1}{2}\sigma_2)^2} \times \frac{\sigma_2}{\sigma_1} & : \alpha > \mu \end{array} \right\} \tag{4.1}$$

where α is the variable and μ, σ_1 and σ_2 are parameters to be fitted.

The results of the 8 parameter models can be seen in Figures 4.17, 4.19 and 4.18. I discuss the results of the PLE and PDE models separately below.

4.5.3.1 PLE

The search for parameter values for the 8 parameter ρ(L,z,α) PLE model appears on the whole well constrained (see Figure 4.17). There are however a degeneracy between parameters A and σ_2. As A moves to lower values and flattens the bright-end slope this correlates with an increase in σ_2. This is to be expected as σ_2 corresponds to steep spectral indices in the α-distribution. A greater value for σ_2 implies a greater population of steep spectrum sources, which when accounted for increases the population at the bright-end of the RLF, of which A represents. A flatter value for A correlates with this increased population.

Figure 4.18 shows the PLE model against the $\frac{1}{\mathrm{V_{max}}}$ points. They appear to agree well over all redshifts.

The fit for L appears reasonable (see Figure 4.20), but only passes the K-S test at the 7% level with $p = 0.072$. The 8 parameter PLE model appears to fit the α-distribution more accurately compared to previous models (see Figure 4.22), however, it still formally fails the K-S test as to whether the model and the data originate from the same underlying distribution with $p = 0.000125$, however this is much higher than the previous models for the distribution for α and it is at least visually more representative than previous models.

The actual parameter values compared to previous models (see Table 4.3), show firstly that μ is for the first time a value ($\mu = 0.77^{+0.04}_{-0.02}$) that corresponds to the expected value from the literature Mauch et al. (0.7, e.g. 2003); Owen et al. (0.7, e.g. 2009); Prescott et al. (0.7, e.g. 2016) as well as locating the peak of the model in

line with the data (Figure 4.22). This newer version of ρ_α is able to account for the dominant population of sources more accurately without being pulled by the steep spectrum sources.

k lies between the 7 and 9 parameter PLE model values at $k = 2.37^{+0.17}_{0.51}$. The more accurate modelling of the steep spectrum side also calls for a slightly steeper A and a flatter B to compensate than the 9 parameter PLE model, since the 9 parameter model gave too much weight to the steep spectrum sources.

4.5.3.2 PDE

The PDE model also appears to be well constrained (see Figure 4.19, Table 4.3). A slight degeneracy exists between k, σ_1 and σ_2. Higher values of σ_2 correspond with higher values of k and lower values of σ_1. Since σ_1 and σ_2 are modelling either side of the α-distribution, it is expected that as one side increases and therefore increases the number of sources it predicts, the other side has to adjust to balance that out. Moving simultaneously towards a lower σ_1 and a higher σ_2 increases the value for k. Since steep spectrum sources drop out of the flux limit of a survey faster than flat spectrum sources, this leads to the evolution term increasing.

Another factor is that a larger population of steep spectrum sources shifts more sources along the L-axis, leading to the flattest value for B of all the PDE models, as well as a flatter value for A depicting the additional steep spectrum sources that are K-corrected to be brighter. When looking back at Figure 4.12 and Table 4.4, this makes sense as each time a PDE model has incorporated a steep spectrum population, A has become flatter and k has decreased. The 8 parameter ρ(L,z,α) PDE model exhibits the weakest evolution term, k, compared to any of the other PDE models.

Figure 4.18 shows an agreement between this model at the $\frac{1}{\mathrm{V_{max}}}$ points. There exists a discrepancy between PLE and PDE models at the faint-end of the RLF, but only in redshift bins where this region is not constrained by data.

The 8 parameter PDE model continues to fit the distributions in L and z well with K-S test probabilities of $p = 0.9406$ and $p = 0.1336$ respectively (see Figures 4.20 and 4.21). However, although the PDE model again seems to closely trace the distribution in α (Figure 4.22), I find $p = 0.00182$ for the K-S test. This could be to do with the fact that the peak of the model in both PLE and PDE iterations does not have as high an amplitude as that of the data, and slightly underestimates the flat-spectrum side of the distribution.

Although there is still yet to be an agreement between the model and the data in α, the 8 parameter models are clearly more representative of the data and the

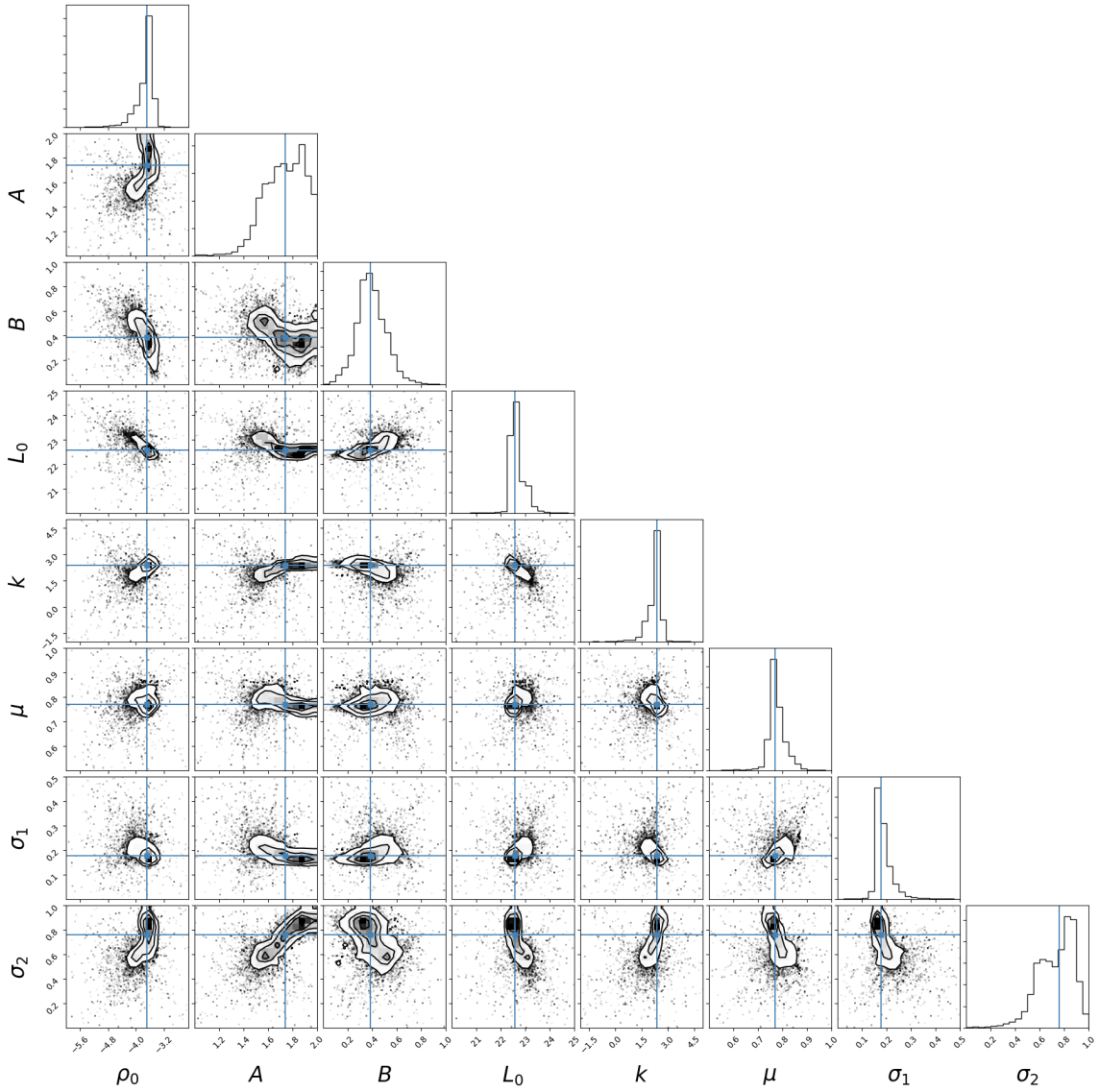

Figure 4.17: The results of the MCMC analysis using the 8 parameter PLE model. For the parameter search I used 150 walkers with 215 steps per walker.

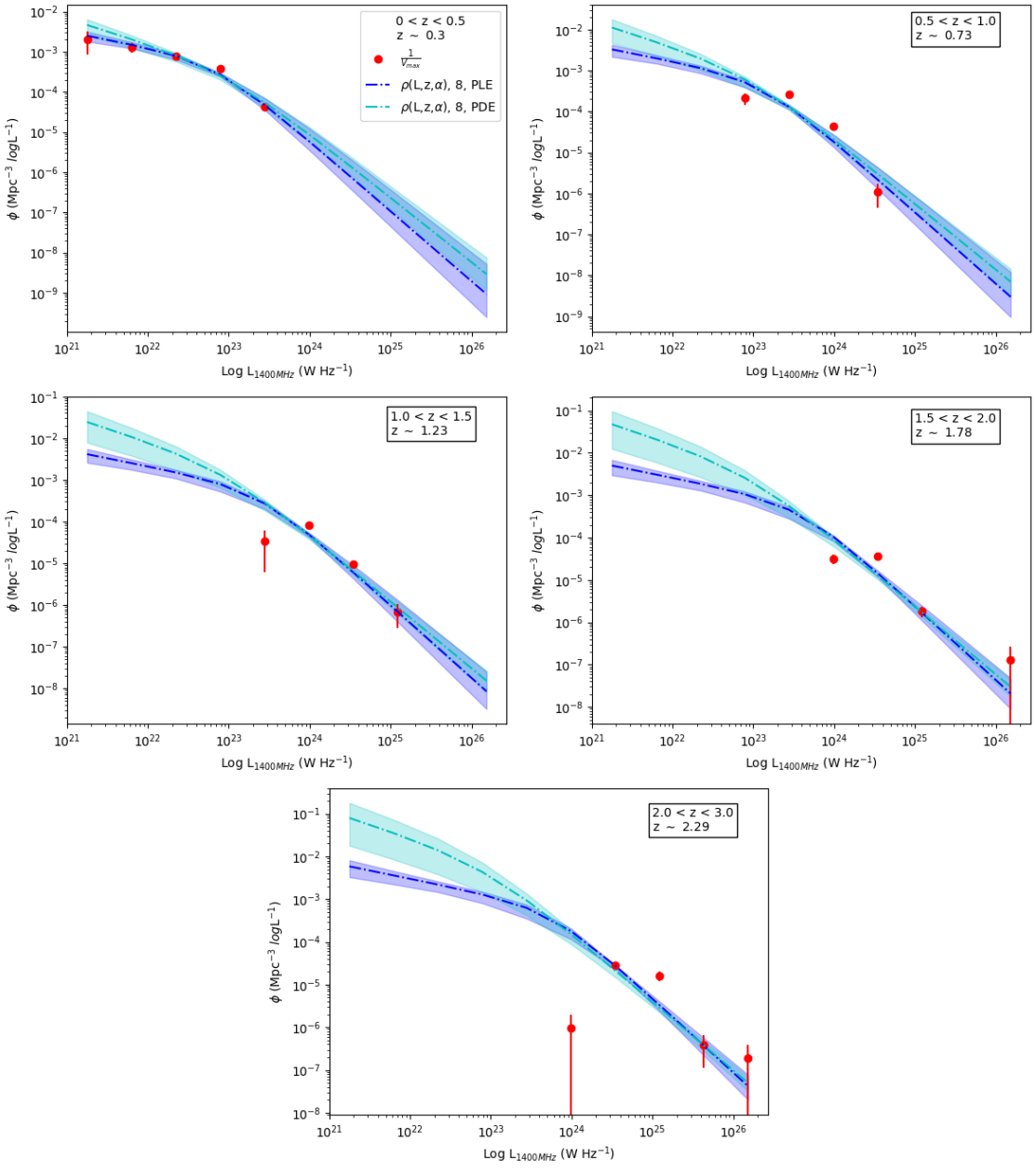

Figure 4.18: The $\frac{1}{V_{max}}$ and ρ(L,z,α) 8 parameter RLFs. *Red points:* $\frac{1}{V_{max}}$ points. *Dot-dashed:* ρ(L,z,α) 8 parameter models based on the median parameter values from the MCMC sampling. The RLFs are plotted based on the mean α (0.94) for the sample, and the median z for the z-bin since individual α and z values need to be chosen to display a given RLF. *Blue:* PLE model. *Cyan:* PDE model.

results are useful for seeing what this more accurate modelling does to the values of the parameters.

As mentioned in the previous Chapter, the PDE model is constrained by the faint end of the RLF. This is particularly of interest here as our sample is populated by more faint sources and with an accurate representation of the distribution of α in the model, this means the truncation boundary which determines when sources drop out of the flux limit of the survey, is properly accounted for. In turn, this informs the rate of evolution. This is visually represented in Figure 4.19. Both values which represent the *distribution* of α (i.e. σ_1 and σ_2) show a degeneracy with k. This exemplifies how vitally important it is to include not only individual values of α for each source, but the distribution for the sample. This is particularly pertinent for this model, which most closely represents the α-distribution.

4.5.4 PLE vs. PDE

From visually examining Figure 4.16, the most obvious difference between the two sets of models occurs at the low luminosity end, $L_{1.4GHz} \lesssim 10^{23}$ WHz^{-1}. The PDE models across all numbers of parameters, predict a greater number of low luminosity sources, with this difference becoming more pronounced as redshift increases. At the high luminosity end ($L_{1.4GHz} \gtrsim 10^{23}$ WHz^{-1}) however, the two sets of models closely follow each other, with the similarity between the two increasing for fewer numbers of parameters. i.e. the ρ(L,z) PLE and PDE models lie on top of one another, whereas it is still possible to distinguish between the 9-parameter ρ(L,z,α) PLE and PDE models.

Since the regions in luminosity where the models diverge are poorly constrained by the data it is difficult to place any confidence in these differences highlighted between PLE and PDE models, although the PDE model is formally the better model for all numbers of parameters. The proximity between the two models over all numbers of parameters at the high luminosity end causes for little discussion, though PDE models appear to predict marginally fewer high luminosity sources.

In terms of the evolution parameter k, a clear trend is that the evolution becomes weaker as the complexity of the model increased. This is predominantly due to the inclusion of modelling the distribution in spectral index and this is expanded upon later.

Another strand to consider is why a PDE model would differ from the PLE model in low luminosity regions of the RLF. Both agree more strongly at the high luminosity

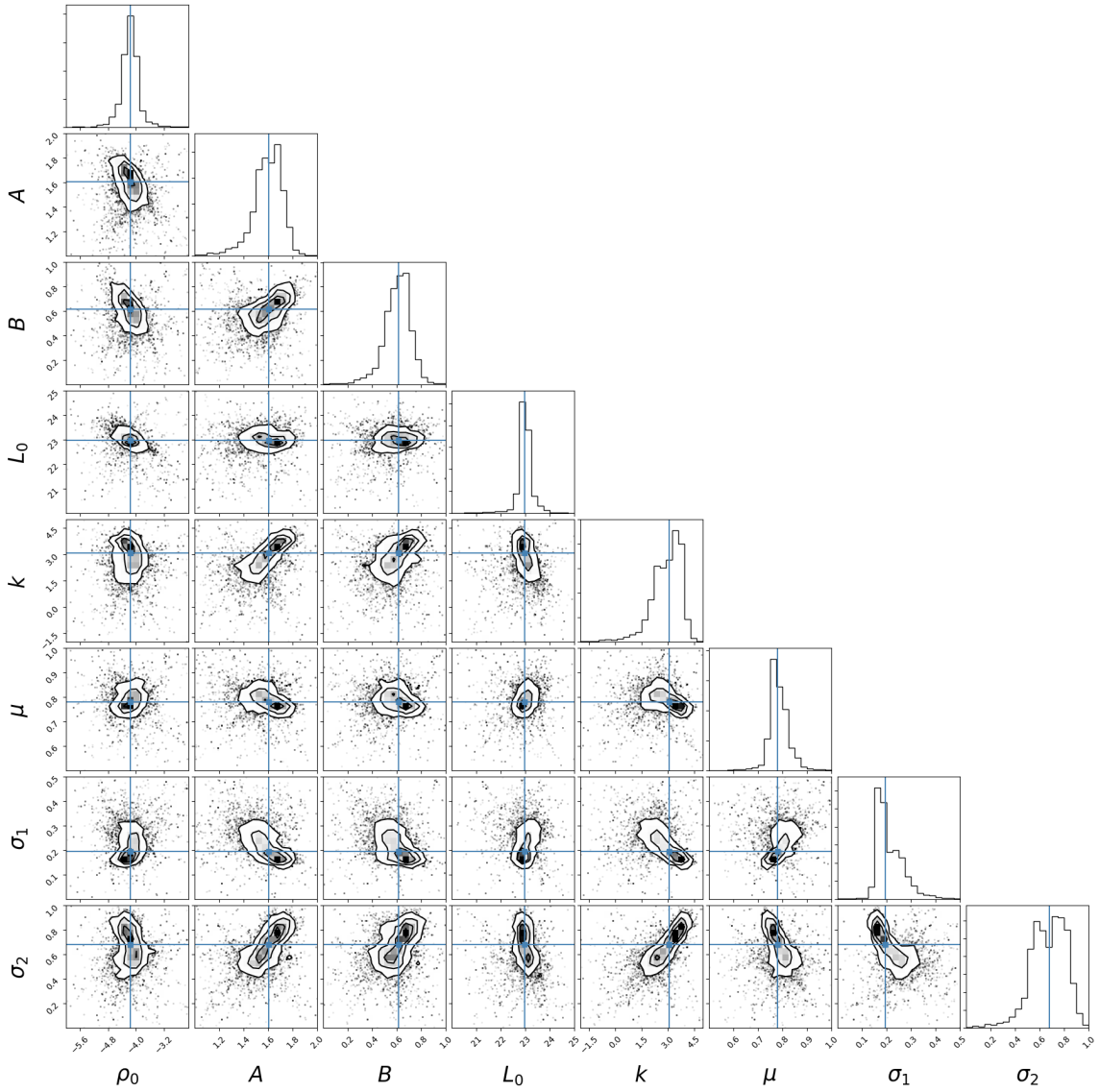

Figure 4.19: The results of the MCMC analysis using the 8 parameter PDE model. For the parameter search I used 150 walkers with 154 steps per walker.

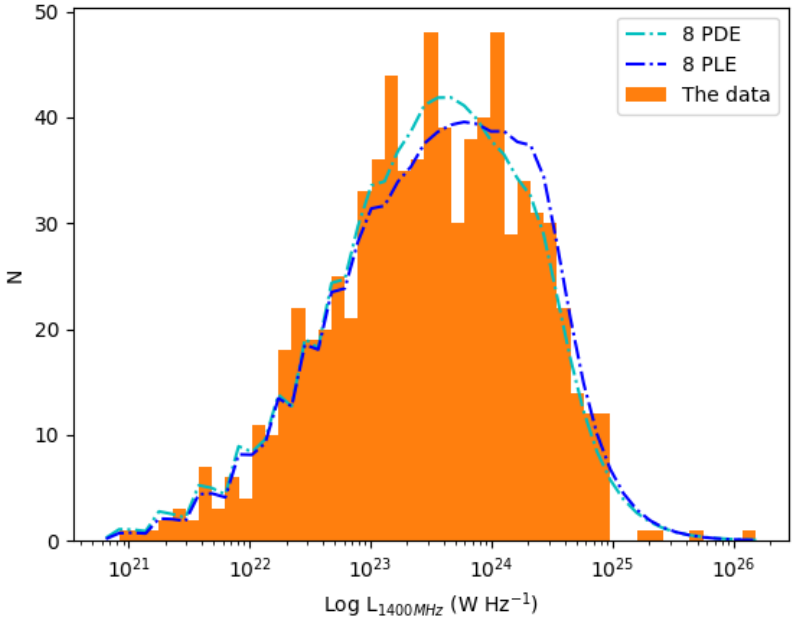

Figure 4.20: The orange histogram shows the distribution of the data. The cyan dot-dash line represents the 8 parameter PDE model and the blue line represents the 8 parameter PLE model.

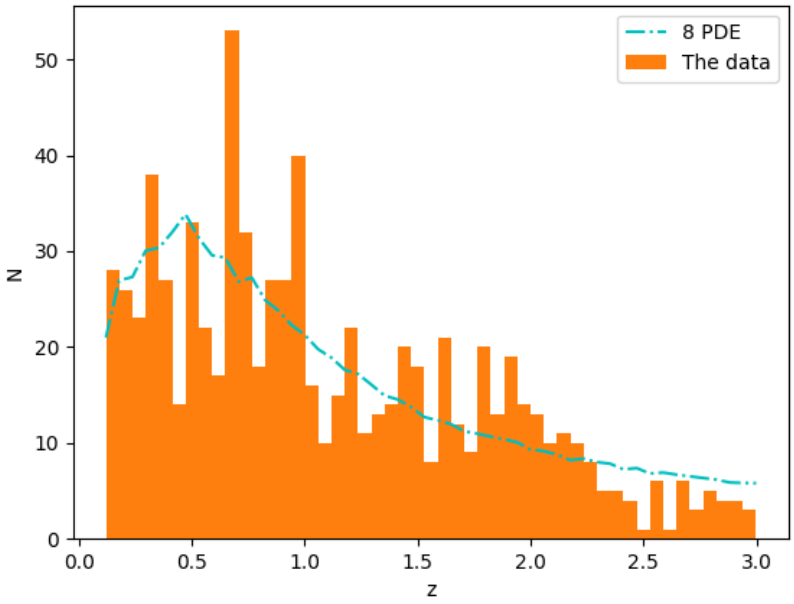

Figure 4.21: The orange histogram shows the distribution of the data. The cyan dot-dash line represents the 8 parameter PDE model.

Parameters	Model	ρ_0	A	B	L_0	k	μ	σ_1	σ_2	-2ln L
8	PLE	$-3.68^{+0.12}_{-0.30}$	$1.74^{+0.16}_{-0.18}$	$0.38^{+0.13}_{-0.10}$	$22.57^{+0.41}_{-0.12}$	$2.37^{+0.17}_{-0.51}$	$0.77^{+0.04}_{-0.02}$	$0.18^{+0.04}_{-0.01}$	$0.76^{+0.12}_{-0.18}$	16717.50
8	PDE	$-4.16^{+0.18}_{-0.22}$	$1.60^{+0.10}_{-0.11}$	$0.61^{+0.09}_{-0.11}$	$22.98^{+0.218}_{-0.18}$	$3.07^{+0.61}_{-0.92}$	$0.78^{+0.04}_{-0.03}$	$0.19^{+0.07}_{-0.03}$	$0.68^{+0.13}_{-0.15}$	16744.23

Table 4.3: The parameter values found for the 8 parameter model.

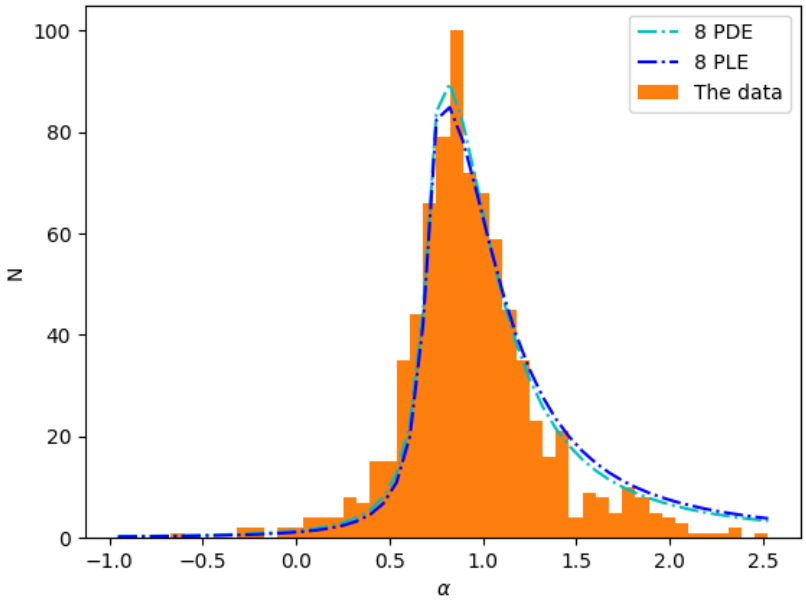

Figure 4.22: The orange histogram shows the distribution of the data. The cyan dot-dash line represents the 8 parameter PDE model and the blue line represents the 8 parameter PLE model.

end due to the existence of more data to constrain them both, so why is there a difference?

The PDE model, by nature, is constrained by the faint end while the PLE model is constrained by the bright end. The faint end of the RLF is the region that is affected most by the inclusion of the spectral index distribution as these are the sources nearest the flux density limit of a survey which can be affected by a steeper or shallower spectral index. The distribution in α prescribes the maximum observable volume for a source, much more accurately than by using a constant value for α. This therefore governs the faint population which are near to the flux limit of the survey. Through this, the PDE is thus affected by the inclusion of the α-distribution. Consequently, it is interesting to witness the difference in the low luminosity end in the PDE and PLE RLF models. Though one is inclined to trust neither at this point due to the lack of low-luminosity sources at high redshift.

Directly comparing the parameters between PLE and PDE models across the 5, 7 and 9 parameterisations, PDE models have lower values for ρ_0.

The value for A, the power law of the bright end in luminosity, is remarkably closely matched across the majority of the models here between PLE and PDE.

Therefore any difference in the bright end will be due to the combination of ρ_0 and L_0 which are degenerate without constraints on the faint end.

On the other hand, when examining the value for B (the faint-end slope) between both sets of models there is a starker difference. The PDE model routinely finds a steeper (higher) value for B. A steeper value typically means more sources. However, this is extremely poorly constrained at high redshift.

In the parameterisations that include the spectral index as a variable, the values for μ or μ_1 are consistent across all models. This is also true of all parameters describing the spectral index distribution (i.e. σ, σ_1, μ_2, σ_2 where appropriate). This is to be expected as the purpose of these parameters is to describe the spectral index distribution.

For our best-fit model, which properly models the distribution in spectral index (the 8-parameter model), we find that the evolution is better described by PLE, which is the opposite to the models where the spectral-index distribution has been modelled by a poorer functional form. The main difference being the improved modelling of the distribution to steep-spectral index sources. As the more powerful sources, due to their preferential selection at low-frequency or due to a real astrophysical effect (e.g. Blundell et al., 1999), tend of have steeper spectral indices (Figure 4.23), this would naturally lead to the PLE model being most affected by these steep spectral index sources, as the PLE evolution is most strongly constrained by the steep part of the RLF at luminosities beyond the break, the opposite of the case for the PDE model in the previous chapter. This therefore suggests that modelling the distribution in spectral index accurately (or inaccurately) can lead to significantly different interpretations of the form of the evolving RLF.

4.5.5 Comparison to the Literature

For the comparisons with the literature (see Figures 4.24-4.27) I use the 8 parameter models since they replicated the distributions in L, z and α most accurately. Across all redshifts the models agree well with the $\frac{1}{\mathrm{V_{max}}}$ points from Novak et al. (2017). There is an excess in the Novak et al. (2017) points at $0.4 < z < 1.0$, but this is likely to be caused by the sample containing a range of redshifts within that bin.

The Mauch & Sadler (2007) Local SF model is plotted at each redshift bin. At $z < 0.5$ for direct comparison, and across higher redshifts as a comparison for how the RLFs both in this work and in the literature move up in number density with redshift. At $z < 0.5$ the models agree with the Mauch & Sadler (2007) Local SF model at $L_{1.4\mathrm{GHz}} \lesssim 10^{22}$ WHz^{-1}, but quickly the Mauch & Sadler (2007) model drops

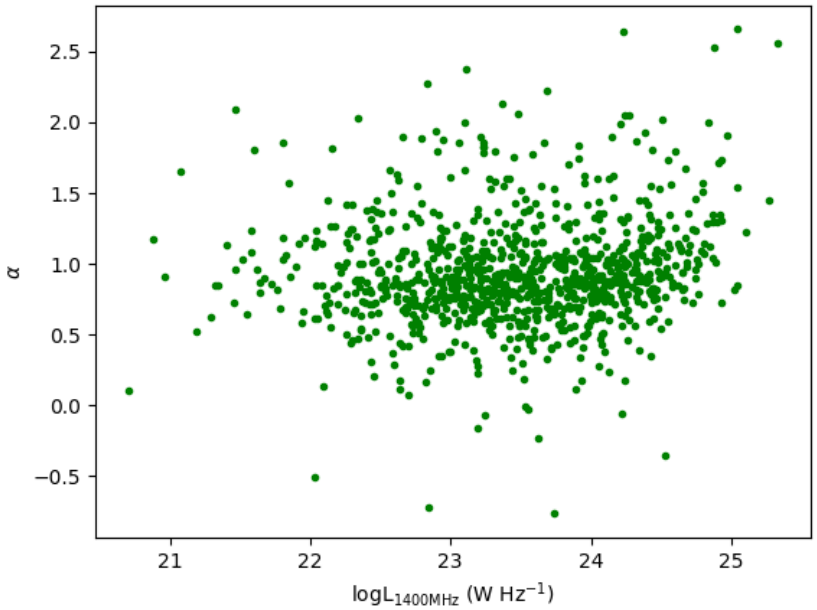

Figure 4.23: The distribution of the sources (green dots) in luminosity and spectral index. A correlation of 12% is found through Pearson's r coefficient between the two variables.

to lower number densities towards higher luminosity. This differs strongly from the $\frac{1}{V_{max}}$ points in this work, as well as the models. The Prescott et al. (2016) points are almost in between, as some of them lie closer to the models presented here, and others closer to the Mauch & Sadler (2007). The McAlpine et al. (2013) points include AGN sources as well as SF galaxies, which explains why occasionally the points from this study are higher than the models from this work. Overall, they generally agree well and are within the errors.

At low redshift, Mauch & Sadler (2007) has the greatest number of sources with 4006 SFGs from the largest survey area (7076 deg°. Novak et al. (2017) has 5915 radio sources overall, but this is distributed over a much wider range ($0 < z < 6$). Thus, the Mauch & Sadler (2007) has the most reliable RLF at low redshift. The data points from McAlpine et al. (2013), Novak et al. (2017) and the work here use data over sky areas of 1 deg^2, 2.6 deg^2 and 0.785 deg^2 respectively, which do not cover enough cosmological volume to accurately measure the RLF at $z < 0.3$.

However, consistency among these models with smaller survey areas, which are the ones that *do* continue to high redshift, is reassuring. McAlpine et al. (2013) and Novak et al. (2017) continue to agree well with increasing redshift. Points from Novak

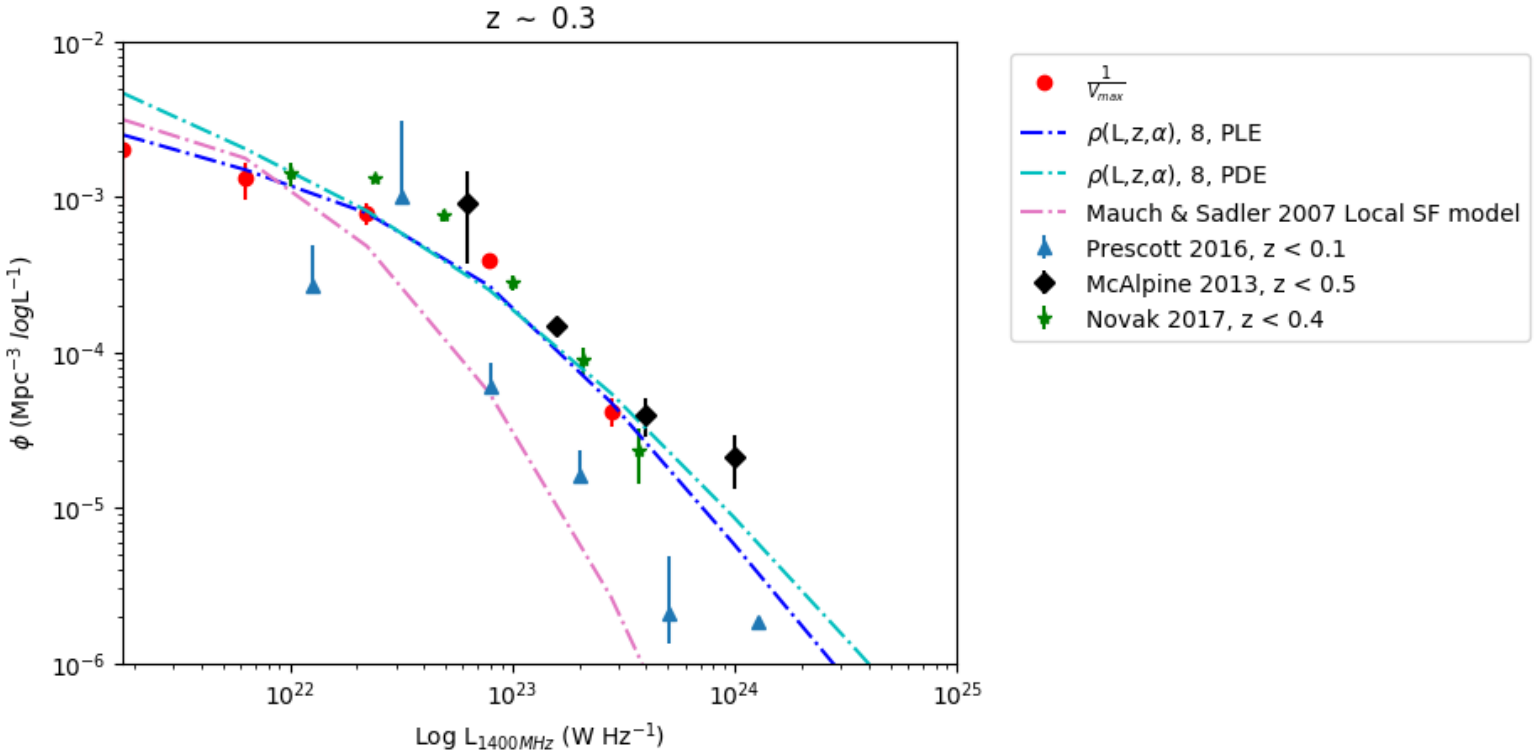

Figure 4.24: RLFs from this work and the literature. *Red points:* $\frac{1}{V_{max}}$. *Blue lines:* PLE models. *Cyan lines:* PDE models. *Dot-dashed lines:* 8 parameter ρ(L,z,α) models. *Pink dot-dash line:* Mauch & Sadler (2007) Local SF model. *Blue triangles:* Prescott et al. (2016) points. *Black diamonds:* McAlpine et al. (2013) points. *Green stars:* Novak et al. (2017) points.

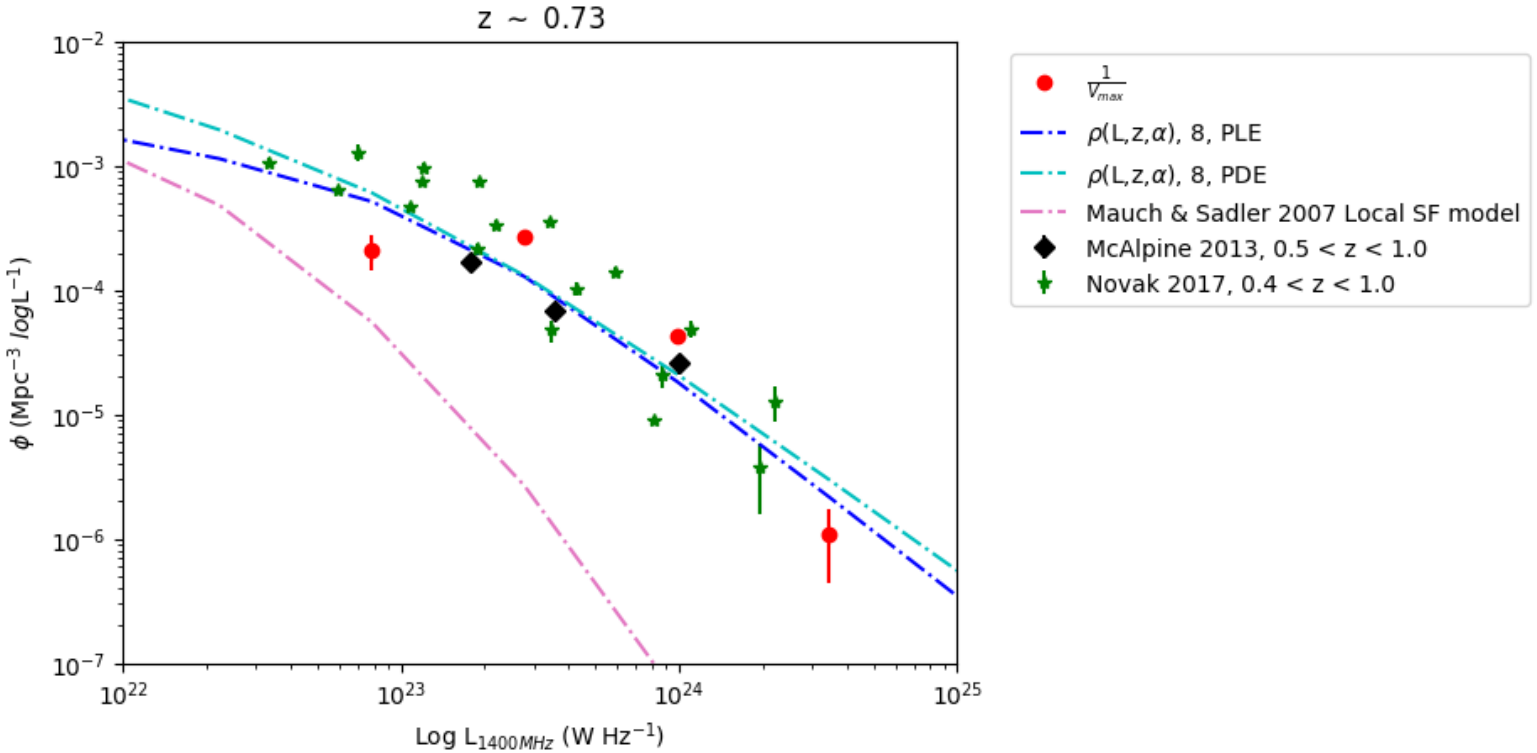

Figure 4.25: RLFs from this work and the literature. *Red points:* $\frac{1}{V_{max}}$. *Blue lines:* PLE models. *Cyan lines:* PDE models. *Dot-dashed lines:* 8 parameter ρ(L,z,α) models. *Pink dot-dash line:* Mauch & Sadler (2007) Local SF model. *Black diamonds:* McAlpine et al. (2013) points. *Green stars:* Novak et al. (2017) points.

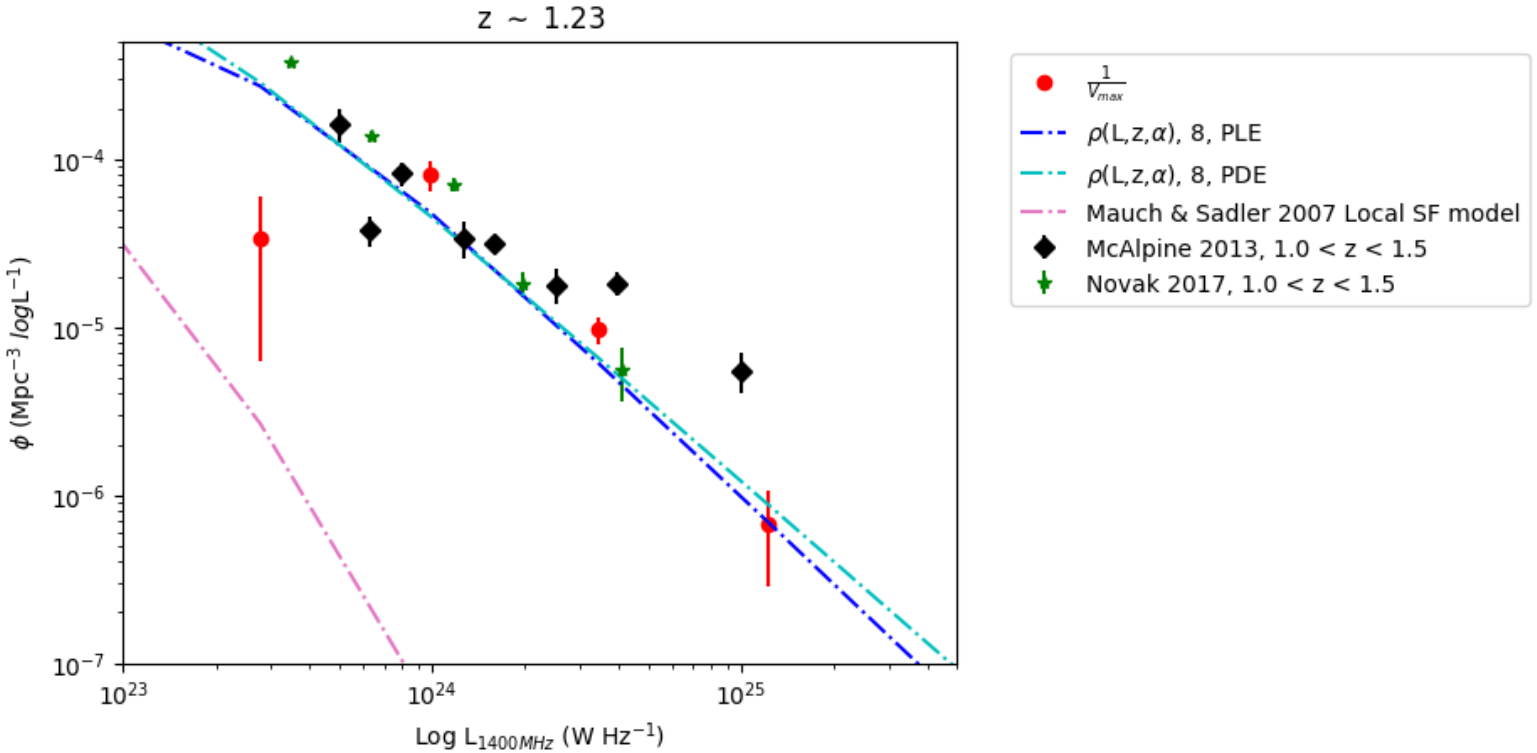

Figure 4.26: RLFs from this work and the literature. *Red points:* $\frac{1}{V_{max}}$. *Blue lines:* PLE models. *Cyan lines:* PDE models. *Dot-dashed lines:* 8 parameter ρ(L,z,α) models. *Pink dot-dash line:* Mauch & Sadler (2007) Local SF model. *Black diamonds:* McAlpine et al. (2013) points. *Green stars:* Novak et al. (2017) points.

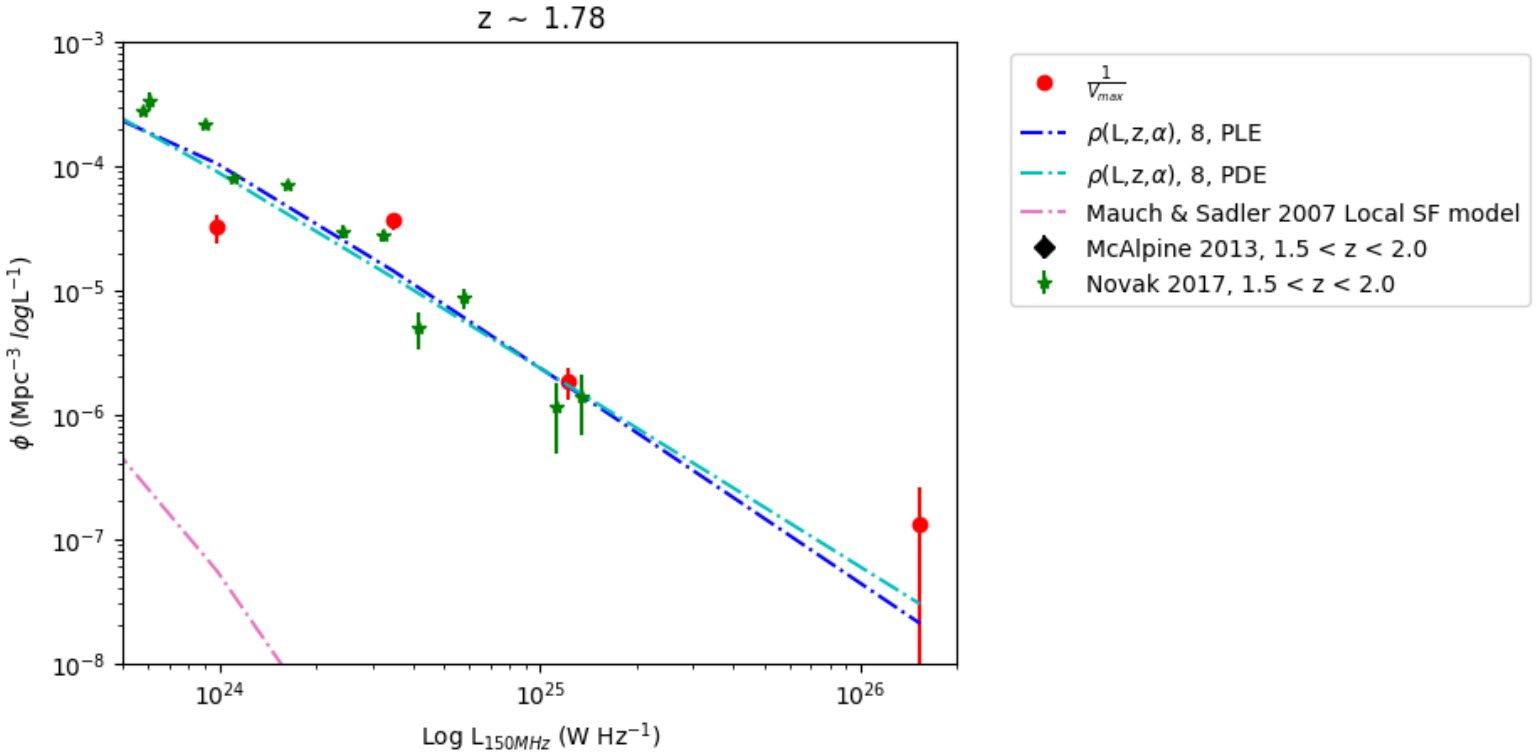

Figure 4.27: RLFs from this work and the literature. *Red points:* $\frac{1}{V_{max}}$. *Blue lines:* PLE models. *Cyan lines:* PDE models. *Dot-dashed lines:* 8 parameter ρ(L,z,α) models. *Pink dot-dash line:* Mauch & Sadler (2007) Local SF model. *Green stars:* Novak et al. (2017) points.

Study	k	PLE/PDE	No. of sources	Sky Area (deg^2)	z range	Frequency (GHz)
This work	$2.37^{+0.17}_{-0.51}$	PLE	792	0.785	$0 < z < 3$	1.5
Mauch & Sadler (2007)	-	-	4006	7076	$z < 0.3$	1.4
McAlpine et al. (2013)	2.47±0.12	PLE	942	1.0	1.4	
Prescott et al. (2016)	-	-	45	138	$0.002 < z < 0.1$	0.325
Novak et al. (2017)	$3.16 \pm 0.20.32 \pm 0.07z$	PLE	5915	2.6	$0 < z < 6$	3.0

Table 4.4: Comparison with the literature for RLFs in SFGs.

et al. (2017) do show a small surplus in the most populated redshift bin ($z \sim 0.73$), although they agree with our $\frac{1}{V_{max}}$ values. This visual underestimate in the model, is actually indicative of the fact that the there is strong redshift evolution within the redshift bin, and plotting the model line at $z \sim 0.73$ does not encapsulate the significant evolution from $z \sim 0.5$ to $z \sim 1$. We should also note that the COSMOS field is known to have a large structure at $z \sim 0.73$ (Guzzo et al., 2007; Iovino et al., 2016), which would effect the binned RLF more than the parametric model fits.

The strength of the evolution for the SFG RLF agree with the most relevant past studies (see Table 4.4). McAlpine et al. (2013) find an evolution term of $k = 2.47 \pm 0.12$ for a best fit PLE model and Novak et al. (2017) find PLE model with an evolution term of $k = 3.17 \pm 0.2 - 00.32 \pm 0.07z$. The result for the 8 parameter PLE model has an evolution term with $k = 2.37^{+0.17}_{-0.51}$, which agrees within the error with McAlpine et al. (2013) and Novak et al. (2017) at $z \gtrsim 1.35$. The generally higher value from Novak et al. (2017) could potentially be influenced by the lack of inclusion of spectral index distribution as it is seen in the results presented in this thesis that the evolution parameter increases to compensate for this lack of information.

A consistent result of finding the PLE model to fit the data more accurately across the literature could suggest that this is what is physically happening. Though it is unlikely that a pure-PLE model is prescriptive and that a mixture of PLE and PDE occurs, it is evident that evolution in the luminosity of sources is the dominant factor in the evolution of SFGs. It would be interesting in future studies to use an adaptable evolution term dependent on z to pin-point peak eras of activity in this domain. It is interesting that PLE models fit the data better as this indicates that the population of SFGs is essentially gradually dimming, rather than star formation being shut off and restarted across the same range in SFRs. This therefore reinforces the view that although there are many more massive galaxies in the local Universe, fewer of them have star-formation rates that would place them on the star-formation main sequence at $z \sim 1$ (e.g. Noeske et al., 2007; Johnston et al., 2015).

An important point to consider is that although in the literature the models show a better fit by PLE models is this in fact a real phenomenon or just a product of inaccurate or non-existent modelling of α? When looking at the best fitting PDE model in this Chapter, there is evidence of a degeneracy between the evolution parameter k and the two parameters (σ_1 and σ_2, see Figure 4.19) which describe the distribution in α. The evolution in PDE models is constrained by faint sources and the α-distribution accurately represents the maximum observable volume of faint sources, unlike an assumption of a constant value for α. Thus the α-distribution affects the

evolution term k in PDE models. The preference for a PLE model in the literature could therefore simply be a side effect of the fact that the faint population in their samples is not properly accounted for and therefore shows a poorer fit.

To disentangle whether a PLE model is truly "the best fit" or simply the best fit given that the PDE is not well accounted for, would require a model where all modelled distributions pass the KS-test to ascertain whether this is the case. Additionally, the PLE models are constrained by the bright end of the RLF , thus a better fit may not imply that this is the physical truth, only that it is easier to obtain a better fit for this part of the populations. This is evident with the comparison of the PDE results of the previous Chapter and with this Chapter. For the most complex models, a lack of sufficient low luminosity sources meant that EMCEE was unable to find a fit for the PDE model. On the other hand, in this Chapter with fainter sources, PDE models are easily found and with almost as much accuracy as the PLE models. While they are different populations, this still rings true. Before jumping to conclusions as to one model is more representative of the Universe, it is imperative to remember that to distinguish these properly, all luminosities must be fairly sampled. This would require a combination of wide surveys to detect bright sources and deep surveys to gather low luminosity sources so that all models can be equally constrained. One may then be in a position to properly account for the evolution across the whole of the RLF, rather than assume a single evolutionary model for the whole population from very low radio luminosities to the very bright. However, it remains that it cannot be disputed that the α-distribution is of upmost importance to obtain a true measure of the evolution of galaxies.

Overall, there are no notable disagreements and the work here is in keeping with other studies in the literature in terms of the measured RLF in each redshift bin. However, introducing the α distribution will inevitably lead to different physical interpretations in the extent of any evolution and what form this evolution takes, i.e. PLE or PDE.

4.5.6 Different selection criteria

The selection criteria for a SFG in the COSMOS sample used here was slightly different from that used in another study with the same data by Novak et al. (2017). The flag that has been used to remove potential AGN contaminants in this work was whether the source had been labelled as being a SFG. Novak et al. (2017) used those galaxies which did not show an excess of radio emission. In the original selection criteria, set out in Smolčić et al. (2017b), a SFG is identified by using a UV/optical

colour cut and selecting those with intermediate or high levels of star formation activity. This does not assess whether AGN activity is also present. The calculation for a radio excess in the catalogue by Smolčić et al. (2017b) is performed using a ratio of the star formation rate (SFR) inferred from infrared emission against 1.4 GHz rest-frame luminosity of each galaxy, with the assumption that any additional radio emission from that predicted from the SFR has its origin in an AGN. This ratio utilises a well known relationship between infrared and radio emission (the far-infrared - radio correlation Helou et al., 1985; Jarvis et al., 2010; Read et al., 2018) that is known to correlate remarkably well for many galaxies over redshift.

To investigate this, I used the 8-parameter PLE model and the sample used in Novak et al. (2017). This changed the number of sources from 792 to 964 sources. The sample has a more even spectral index distribution (see Figure 4.28) and the range of spectral index altered from $-1.02 \leq \alpha \leq 2.53$ to $-0.77 \leq \alpha \leq 2.66$. The redshift range increased slightly from $0.062 \leq z \leq 3.00$ to $0.03 \leq z \leq 3.00$. The maximum luminosity measurement of the sample is reduced by almost an order of magnitude from $20.7 \leq \log L \leq 26.2$ to $20.7 \leq \log L \leq 25.3$.

The resulting corner plot is shown in Figure 4.29. The best-fit parameters are shown in Table 4.5, which also shows that the uncertainties on the parameters are generally smaller than for the original sample. The fit to the distribution of the spectral indices better describes the data (see Figure 4.28), with a KS test p value $= 0.28$.

The model distribution in luminosity is also consistent with the data, with KS-test p value $= 0.09$, with the new selection criteria. The distribution of the data changes in that at the faint end, there is a small increase in the number of sources. However, overall, the change in the sample did not significantly alter the best-fit PLE model, with all parameters consistent within the uncertainties (Table 4.5) and still in agreement with the literature (Figure 4.30). This suggests that the modelling results are robust against small changes in sample selection criteria.

4.6 Conclusions & Summary

In this Chapter I have used 1.4 GHz MeerKAT data and 3 GHz VLA-COSMOS data (Smolčić et al., 2017a) to construct 1.4 GHz RLFs of 0.785 deg^2 of the COSMOS field. I made 6 models to begin with, for numbers of 5, 7 and 9 parameters for PLE and PDE. The inclusion of extra parameters is to accommodate for the distribution in spectral index of the sample. The increasing numbers of parameters model the RLF

Parameters	Model	ρ_0	A	B	L_0	k	μ	σ_1	σ_2	$-2\ln L$
8	PLE	$-3.68^{+0.12}_{-0.30}$	$1.74^{+0.16}_{-0.18}$	$0.38^{+0.13}_{-0.10}$	$22.57^{+0.41}_{-0.12}$	$2.37^{+0.17}_{-0.51}$	$0.77^{+0.04}_{-0.02}$	$0.18^{+0.04}_{-0.01}$	$0.76^{+0.12}_{-0.18}$	16717.50
8	PLE_{new}	$-3.51^{+0.09}_{-0.15}$	$1.94^{+0.04}_{-0.16}$	$0.31^{+0.19}_{-0.13}$	$22.49^{+0.20}_{-0.09}$	$2.47^{+0.11}_{-0.30}$	$0.76^{+0.01}_{-0.03}$	$0.16^{+0.03}_{-0.01}$	$0.71^{+0.19}_{-0.08}$	19797.2

Table 4.5: The parameter values found for the 8 parameter model with the existing selection criteria and new selection criteria. Both models are provided for ease of comparison.

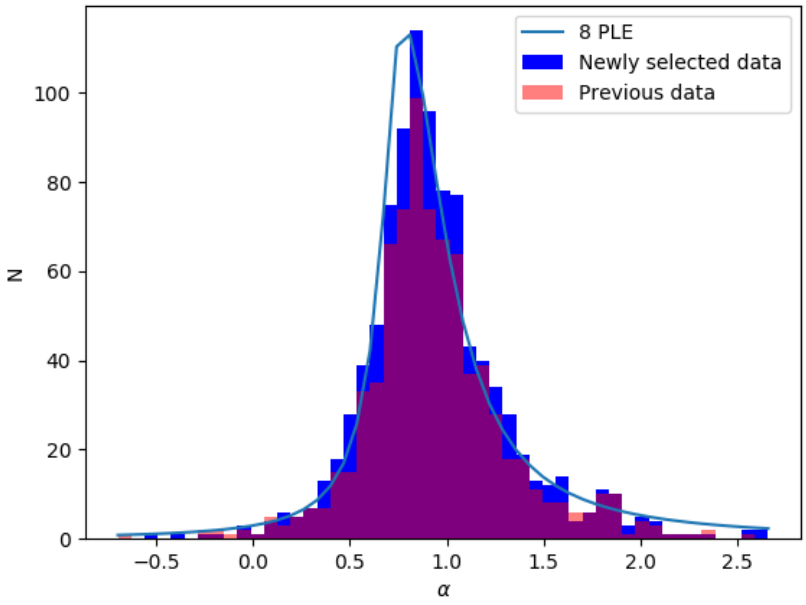

Figure 4.28: The fitting of the 8 parameter PLE model (blue, solid line) to the distribution of the spectral index using new selection criteria (blue histogram) of sources without radio excess as opposed to sources labelled as SFGs (orange/translucent histogram).

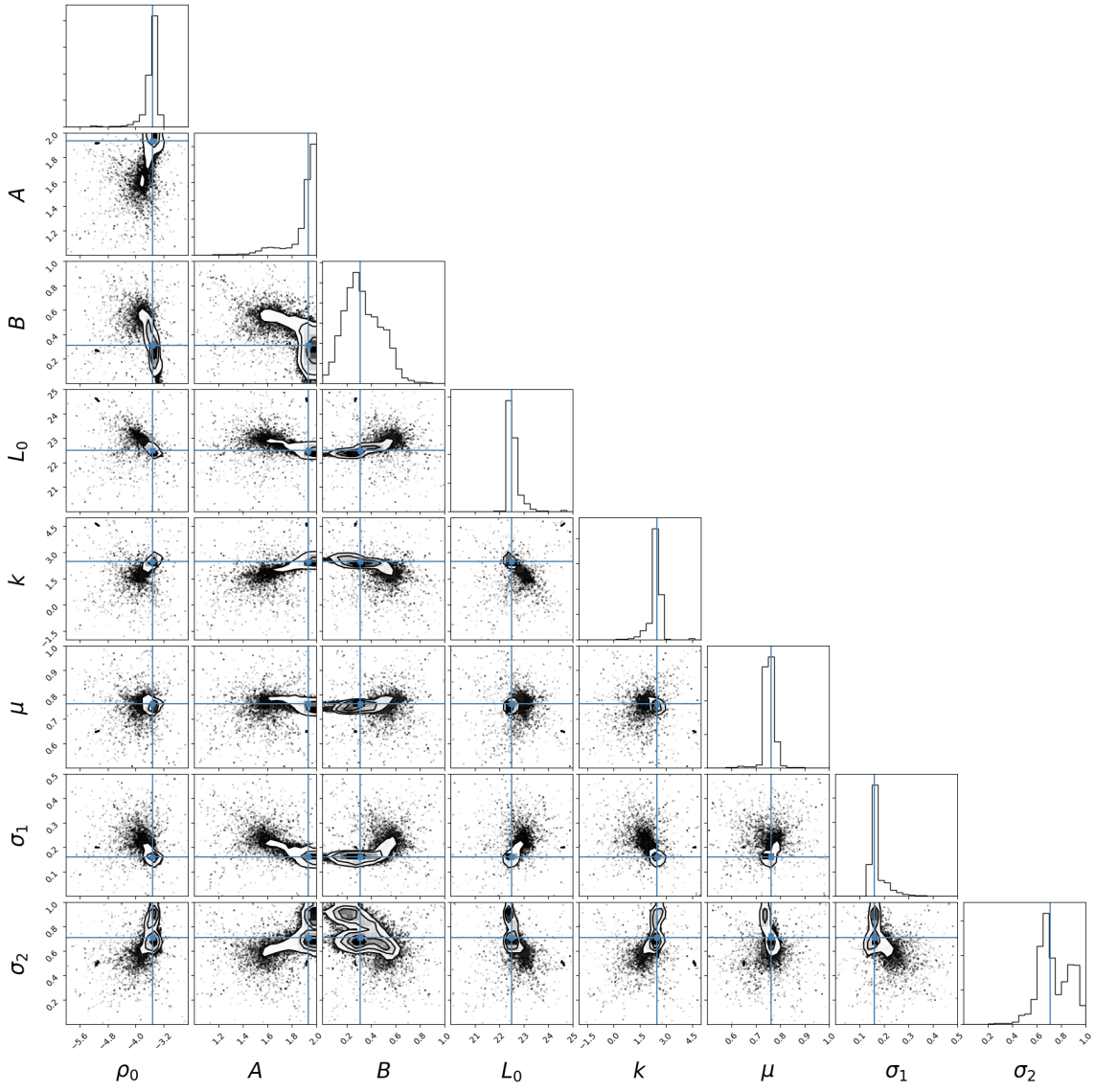

Figure 4.29: The corner plot for the 8 parameter PLE model using the adjusted data set with different selection criteria based on radio excess rather than classification as a SFG.

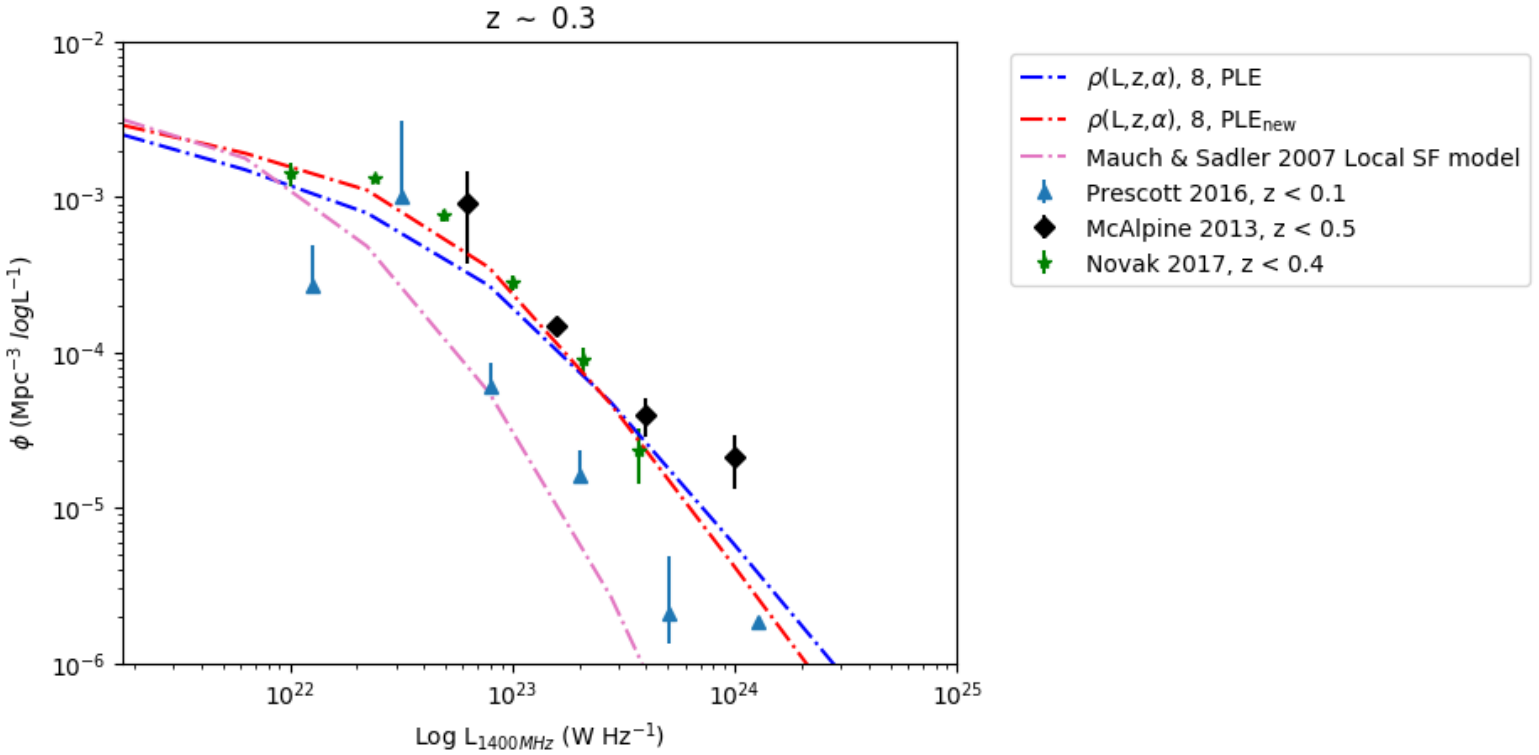

Figure 4.30: RLFs from this work and the literature. *Blue, dot-dashed line:* 8 parameter ρ(L,z,α) PLE model from the previous data set. *Red, dot-dashed lines:* 8 parameter ρ(L,z,α) PLE model using data from the new selection criteria. *Pink dot-dash line:* Mauch & Sadler (2007) Local SF model. *Blue triangles:* Prescott et al. (2016) points. *Black diamonds:* McAlpine et al. (2013) points. *Green stars:* Novak et al. (2017) points.

reasonably well and significantly improve the fits to the individual distributions in L and z. However, none of these modelled the distribution in α with sufficient accuracy. I then also implemented an 8 parameter ρ(L,z,α) model in both PLE and PDE with a new form of ρ_α using a Lorentzian equation. Though it was still insufficient to pass a K-S test, this did improve the fits to α compared to previous models.

In regions where the models are most constrained (see Figures 4.16 and 4.18), all models agree well with the $\frac{1}{\mathrm{V_{max}}}$ points. The consequence on the values of the parameters from including more comprehensive modelling, is a decrease in the severity of the evolution term k and an increase in similarity between PLE and PDE models. From comparing all models it appears this hinges on the accuracy of including the steep spectrum population in α. Higher values of k are present in models which do not include this.

In terms of differences between the PLE and PDE models. An interesting case appears in the 8 parameter version where the PDE model k parameter shows a degeneracy with μ, σ_1 and σ_2. This shows a direct link between accurately modelling the α-distribution and the effect on the evolution of the sample. The PDE model is most effected by the influence of the faint end and thus the distribution of spectral indices, which defines the truncation boundary as to what sources fall above the flux density limit of a survey,

I investigated the impact of using a different selection criteria for what constitutes a star forming galaxy. Instead of selecting whether a galaxy was selected as indicated to have intermediate or high levels of star formation activity, I selected a new subsample of sources to exclude those sources which have an excess in radio emission, indicative of AGN. The new sample contained more sources and an α-distribution that was more evenly distributed. The resulting model fit that was found (for a PLE model) passed the KS-test for the α-distribution. However, all parameters remain within the uncertainties for the original sample for an 8-parameter PLE model, this suggests that the model is robust.

To model the evolution of the RLF without sufficient free parameters that account for the spectral index distribution,(as is especially evident in the 5 parameter ρ(L,z) model) can produce mis-leading parameter values. With more sensitive instruments on the horizon that will be able to detect these sources to higher redshift, it is imperative to account for these variations in spectral index to find a robust and reliable RLF. This is especially prudent as when the aim is to model galaxy evolution, the evolution term k should be measured as accurately as possible.

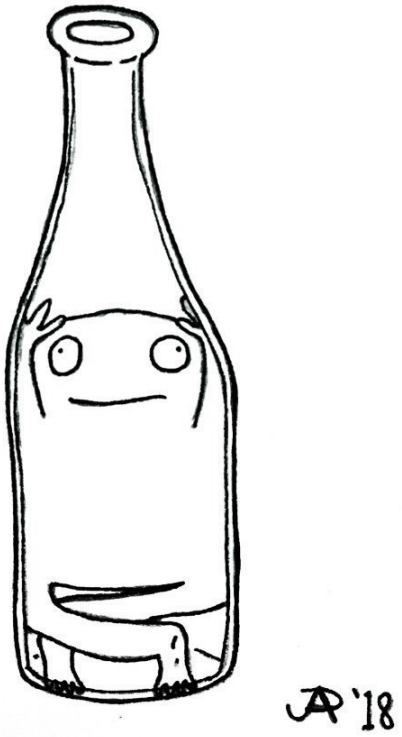
JA '18

Chapter 5

Comparing flux densities of 1.5 GHz VLA data observed in different configurations

As discussed in Chapter 2, the choice of baselines in an interferometer can affect not only the resolution of the resulting images, but also the angular scales that are possible to observe. When using the luminosities of galaxies to fit RLFs or otherwise, it is imperative that the flux measurements that inform these luminosities are reliable and contain the global emission of each galaxy. A lack of short baselines can impede the detection of galaxies with extended emission, likewise a lack of long baselines can result in the confusion of two nearby sources as they are not able to be resolved separately. Between these extremes, extended or point-like components of a galaxy's emission could be lost. With this in mind, the aim of this Chapter is to see how well different antenna configurations observing the same field capture the global emission of a sample of galaxies.

The interferometer used for this work is the VLA with observations taken in B, C and D configuration. B configuration provides the long baselines, while C and D configurations supply short baselines and are combined for comparison against B configuration. The Chapter is outlined as follows. In Section 5.1 I list the observations, in Section 5.2 I describe the data reduction, the results are presented in Section 5.4. Finally, I discuss the results and summarise conclusions in Section 5.6.

5.1 Observations

All of the following observations are of the XMM-LSS field (Pierre et al., 2004), over a 6.8 deg^2 area of the sky, and were observed over 1-2 GHz (L-band). I give the

information the observations separated into the configuration they were observed in.

5.1.1 B-Configuration

Some of the details of the B-configuration observations are already mentioned in Section 3.2.1. However, I will recap and expand.

The B-configuration observations (Heywood et al., prep) were taken by the VLA during September - December 2013 and April 2015. Each of the 32 pointings that make up the final map were observed in 1.5 hour scheduling blocks (SBs). 67.5 minutes of each SB was observing on target. The total observing time is 48 hours.

The primary calibrator for the observations is 3C147, used for calibrating the flux density scale, bandpass and delays. The secondary calibrator for time dependent corrections is J0217+0144.

5.1.2 C and D Configuration

The C-configuration data was observed in 8 SBs that each included 4 of the 32 pointings with 30 minutes per pointing with 23.25 minutes on source. The SBs were observed on 7, 12, 18, 24 - 27 and 30 June 2017. Observations on the 24-26 June 2017 had 26 antennas in operation, while the remainder observed with 27 antennas.

The D-configuration data was observed in 4 SBs that each observed 8 of the 32 pointings. Each SB was 95.6 minutes long and the observation time for 10 minutes per pointing with 8.17 minutes on source. The observations were taken on 17, 19 and 24 February 2017 using 27 antennas, except for the observations on 24 February which had 26 antennas in operation.

The primary calibrator was 3C48 and the secondary calibrator was J0217+0144 for both configurations. The total observing time for both sets of observations is 22 hours.

5.2 Data Reduction

The details of the B-configuration data reduction are described by Heywood et al. (prep), but I provide a summary here. The C and D configuration data was reduced by me for this thesis and is described following the description of the B-configuration data.

5.2.1 B-Configuration

The calibration of the B-configuration observations were first performed using the NRAO CASA pipeline. The pipeline performed an automatic scanning for notable RFI in the data, which was then followed by visual inspection to identify any undetected sources of RFI. After flagging the remaining RFI the pipeline was re-run. The main windows that suffered from RFI in the B-configuration observations were spectral windows (SPWs) in the ranges 1.314-1.412 GHz and 1.506-1.634 GHz (SPWs 5 & 6 and 8 & 9 respectively). SPWs 8 & 9 were flagged for all 32 pointings. SPWs 5 & 6 were flagged in the majority of pointings. This was done for each SB separately. Flux scale calibration is also performed in the pipeline using Perley & Butler (2013).

Following this, each SB was separated into individual measurement sets (MS) for each pointing. The imaging was performed using WSCLEAN (Offringa et al., 2014) to help correct for the wide area of the images. The image size of each pointing is 12,000×12,000 pixels with a cell size of 0.7″. This comes together to create an image size of 2.33 $\deg^2$. A Briggs (1995) weighting with a robust parameter = 0.0 was used to dampen sidelobes and retain sensitivity. The polynomial used to measure the dependence on the sky brightness distribution as a function of frequency was of order 3.

After initially running with 50,000 CLEAN iterations, PyBDSF (Mohan & Rafferty, 2015) was used over the image to catch any particularly bright sources contaminated with PSF-like structures. This catalogue was then visually examined to remove these sources and a cleaning mask was created from the reduced catalogue. The cleaning process was then repeated, this time using a mask for 35,000 iterations as 50,000 was unnecessary from looking at the peak value in the residual map. 5 of the 32 pointings obtained sufficiently good images after phase-only and self-calibration. The remaining 27 pointings required further calibration in both amplitude and phase, as well as direction-dependent calibration to reach acceptable quality.

Once calibration for all pointings were of a good standard, a final round of imaging was performed in two stages. Firstly using cleaning masks, followed by a second shallower CLEAN of 10,000-20,000 iterations without the masks. The restoring beam for each image has a full-width half maximum (FWHM) of 4.5″ and is a 2D circular Gaussian. The individual pointings were corrected for the primary beam, masking emission below 30% and then mosaicked together using `Montage`, weighting each pointing by the square of the primary beam. The final median rms depth of the B-array image is 16 μJy/beam.

To generate the source catalogue ProFound was used (Robotham et al., 2018). ProFound differs from PyBDSF in that it does not assume a shape for the sources it finds, whereas PyBDSF assumes sources are comprised of Gaussians. ProFound has been shown to perform well with extended features in radio images (Hale et al., 2019). The catalogue for the B-configuration image consists of 7,185 sources and is complete to a 5σ flux limit of 100μJy/beam.

5.2.2 D configuration

Each configuration is imaged separately first. For both C and D configurations, each SB was run through the NRAO casa pipeline and then split into a separate MS for each pointing. Since the D configuration observations are shorter and thus faster to image, I reduced the D-configuration data first.

To begin with, all pointings were cleaned for 1000 iterations using casa. These initial images were visually inspected and measurements were taken of the noise to infer a guideline threshold (in mJy) to clean down to for more extensive numbers of cleaning iterations. This was performed by a scripted series of non-interactive cleaning and calibration steps to stop cleaning once it reached this threshold. The first cleaning steps followed a phase calibration at three solution intervals of 30s, 60s and 120s. This was followed by an amplitude and phase calibration at a solution interval of 30s. Images were produced at all of these stages. A summary of the input parameters for various cleaning attempts is provided in Table 5.1.

The number of iterations per clean was 20,000. Combined with the unique threshold parameter for each value this was a high enough iteration value to CLEAN sufficiently deep for first inspection. All were imaged using 'Briggs' weighting (Briggs, 1995) with a robust parameter of 0.0 to balance between sensitivity and resolution. The nterms parameter that defines the polynomial used to model the sky frequency dependence was set to 2.

A cell size of $6''$ is used which sufficiently samples the $46''$ synthesised beam generated by observing in D-configuration at L-band. The initial image size was a square of 900 by 900 pixels as this is slightly greater than twice the size of the primary beam ($\theta_{PB} \sim 1.2 \times \frac{\lambda}{D} = 1.2 \times \frac{0.21}{25} = 2080''$, $2 \times 2080'' = 4160''$ c.f. $900 \times 6'' = 5400''$).

From visual inspection of the data and colourizing by spectral window (SPW), 4 SPWs stood out as being problematic across all pointings. These were SPWs 1, 2, 9 and 15 and were flagged entirely for all further imaging.

Attempt	Iterations	nterms	Robust	Image size	Cell size
1	10000	2	0.0	900	$6''$
2	20000	2	0.0	1400	$6''$
3	20000	3	0.0	1400	$6''$

Table 5.1: A summary of the input parameters for the various attempts at cleaning the D-configuration data alone.

After these initial cleaning stages I visually inspected the results. All of the pointings required deeper cleaning to obtain higher sensitivity and some displayed sidelobe structures over the target area due to bright sources present away from the phase centre. For the first issue, I removed the threshold parameter and re-imaged the pointings with a lower value of 10000 iterations. For the pointings which displayed unwanted features, I expanded the image size to 1400 pixels. Increasing the image size helped with some pointings as there were bright sources on the edges of the images. After various attempts it was clear that 14/32 pointings were failing to improve (pointings 3-8, 11-13, 15, 16, 19, 27 and 28).

The next stage for these pointings was to image using WSCLEAN which is a fast package for cleaning data over wide areas. Some improvement was made from using WSCLEAN but more calibration was required. Cleaning masks were used to construct an error-free model for self-calibration via deconvolution. I used CUBICAL (Kenyon et al., 2018) to self-calibrate pointings over both phase and phase and amplitude.

The final median depth of the D-array image is 108μJy beam^{-1}.

5.2.3 C configuration

To speed up the identification of faulty SPWs in the C-configuration observations each pointing was run through a script which identified any outliers from the mean amplitude across the SPWs (see Table 5.2). Then all pointings were imaged using WSCLEAN. Each image is 4096 pixels square in size, with a cell size of $5.0''$ and was cleaned for 40,000 iterations setting to automatically mask peaks at 6σ and clean down to an automatic threshold of 0.3σ. A Briggs (1995) weighting was used with a robust parameter of 0.0 to balance between sensitivity and resolution.

After this initial cleaning step each pointing was phase self-calibrated using CUBICAL. From this stage, the models were used to mask the pointings for further deeper imaging for another 50,000 iterations.

The final median depth of the C-array image is 52μJy beam^{-1}.

Pointing	SPWs flagged
VLA1	3, 9, 10
VLA2	3, 9, 10
VLA3	2, 3, 4, 9, 10
VLA4	10
VLA5	9, 10
VLA6	2, 3, 9, 10
VLA7	2
VLA8	2, 3, 9
VLA9	2, 7, 9, 10
VLA10	9, 10
VLA11	2, 7
VLA12	2, 8, 9, 10
VLA13	2, 7, 9
VLA14	9, 10
VLA15	2, 3, 10
VLA16	2
VLA17	2, 3, 4, 9, 10
VLA18	10
VLA19	2, 3
VLA20	2
VLA21	2, 9
VLA22	2, 3, 9
VLA23	9
VLA24	9
VLA25	10
VLA26	2, 3, 8, 9, 10
VLA27	2, 3, 4, 9, 10
VLA28	2, 9
VLA29	2, 9
VLA30	2, 9, 10
VLA31	9
VLA32	9, 10

Table 5.2: A summary of the SPWs flaggged for each pointing identified using the mean amplitude of SPWs to identify outliers.

After this a mosaic was created for C and D configuration separately by combining all the pointings, this is described in Section 5.2.5.

5.2.4 C + D images

After imaging the pointings from each configuration separately, I then simultaneously imaged the configurations together. These images make the most of filling the (u,v) plane with all available information and take advantage of the longer baselines from the C-configuration data and the shorter baselines from the D-configuration data to create one image with higher resolution and sensitivity to large scale structure.

All pointings were imaged independently, simultaneously using the C and D configuration MS with WSCLEAN. From earlier imaging of the configurations separately it was evident that WSCLEAN was faster than CASA, so I adopted this for the joint imaging runs. Masks that were used to image the C-configuration data alone were used in the joint imaging process. The initial clean was for 50,000 iterations. The images were individually 4096×4096 pixels in size with a cell size of $5''$. The higher resolution of the C-configuration images is retained because the (u,v) plane is populated with the long baselines from the C-configuration.

After visually inspecting all of the pointings, they were separated by whether the imaging was already satisfactory or images which showed artefacts such as striping and spikes from bright sources interacting with the PSF. These 'problematic' pointings were then manually examined for faulty spectral windows (SPWs), antennas or baselines that were contributing to the artefacts in the images.

When imaging the configurations separately, each MS had been put through a pipeline and an automatic flagging script that identified RFI by calculating the mean amplitude per SPW per pointing and finding outliers. This level of flagging seemed to be largely sufficient for individual images. However, when jointly imaging the MS of both configurations more artefacts appeared to be present. The initial flagging stages removed the worst cases of RFI from the data (e.g. Figure 5.1), though other less severe but still substantial RFI remained when inspected manually (e.g. Figure 5.2).

The severity of the saturation varied across pointing, SPW and configuration. If one had more time or the data were more scarce, it may have been useful to inspect more carefully by plotting Amp vs. Time for each SPW of each pointing of each observation to identify problematic time windows, baselines and antennas. With 32 pointings, 2 configurations and 16 SPWs, unfortunately this is a costly exercise. For brevity and to ensure only high quality data remained, entire SPWs were flagged. For

Pointing	C flags	D flags
VLA2	2, 4, 14	-
VLA3	1, 14	1, 4, 10, 14
VLA4	2, 3, 4, 9	1
VLA5	1, 2, 3, 4, 14	-
VLA7	1, 3, 4, 9	-
VLA8	1, 4, 10, 14	1, 3, 14
VLA12	1, 3, 4, 7, 14	4, 14
VLA14	3, 10	3, 10
VLA15	1, 4, 5, 9	3, 10, 14
VLA16	1, 3, 4, 9, 10	3, 4, 14
VLA20	3, 9,	3
VLA22	10	3
VLA23	4, 10, 14	3, 4
VLA24	4, 10, 14	3, 4, 10, 14
VLA25	3, 9	10
VLA26	4	4, 10
VLA27	1, 14	3
VLA29	1, 3, 4, 5, 10, 14	3, 4, 14
VLA30	1, 3, 4	3, 4, 10, 14

Table 5.3: A summary of the SPWs flaggged for each pointing identified visually from examining SPW against amplitude. Only pointings that required flagging are listed here.

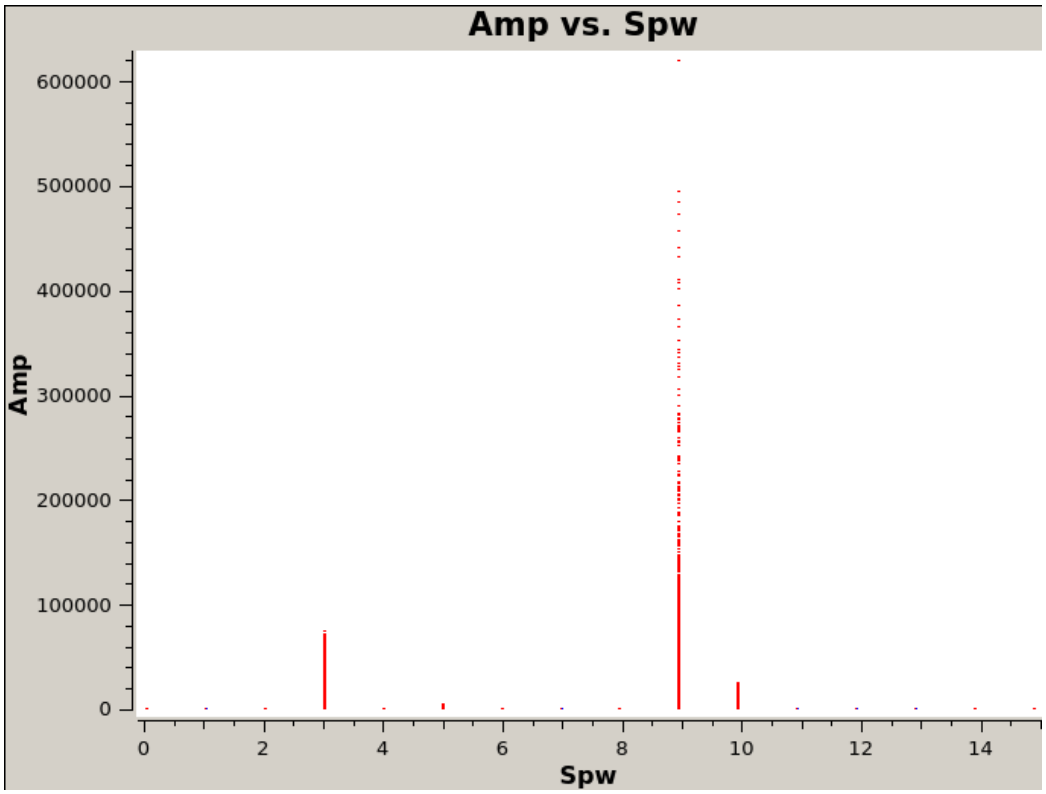

Figure 5.1: Unflagged data for pointing VLA2 observed while the VLA is in C-configuration. The data is separated by spectral window to show which, if any, windows is saturated and contaminates the data. In this example, it is evident that spectral windows 3, 9 and 10 outlie the rest of the data.

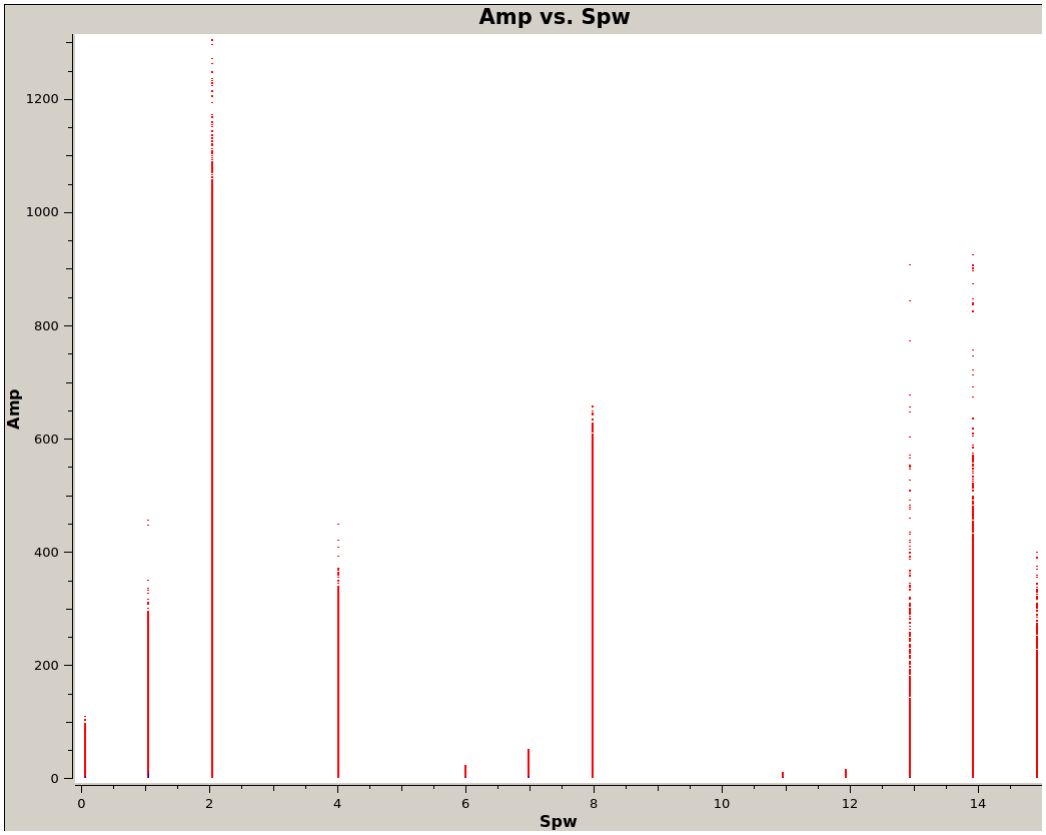

Figure 5.2: C-configuration data for pointing VLA2 after undergoing an initial round of flagging generated by an automatic script.

many pointings as much as 50% of the SPWs were flagged, with SPWs 1, 3, 4, 9, 10 and 14 being the most commonly problematic (for the full list see Table 5.3). After removing these SPWs I re-imaged the data using WSCLEAN with 50,000 iterations, a Briggs (1995) robust parameter of 0.0.

Two pointings (VLA-4 and VLA-29) proved particularly difficult to image due to them both containing bright sources that dominated the individual pointing and produced significant artefacts in the form of PSF like structures. To improve these pointings both were phase self-calibrated using CUBICAL, followed by another round of imaging to update the imaging mask, finished by an application of amplitude-phase self-calibration with CUBICAL and one last imaging run with WSCLEAN.

To ensure the final map had the same resolution and sensitivity across it as well as aiming to improve accuracy when retrieving the catalogue, I restored the final images of the individual pointings with the same restoring beam of $17.5'' \times 17.5''$. At this stage the pointings were ready to be mosaicked together as one image.

5.2.5 Mosaicking

All pointings were mosaicked together to create one image of the XMM-LSS field. Mosaicking involves overlapping the pointings with one another to create a coherent whole. This overlapping needs to be compensated for, since any overlapping regions will increase the flux measurements for those regions and sources lying within them.

The first stage of the mosaicking process, is to correct each pointing for the effects of the primary beam (PB). Sources towards the centre of a pointing, and thus the centre of the PB, will be the most accurate as that is where the beam has the highest sensitivity and lowest noise, the further a source is from this central region, the less reliable the measurement will be as the sensitivity decreases and it is also more likely that a source may lie in a region that is more susceptible to sidelobes. When correcting for the PB this drop in sensitivity needs to be taken into account. As an extension of this, beyond a certain point in the PB it makes sense to crop the image entirely to avoid regions with low signal to noise ratios. For this particular set of mosaics, any emission in regions that were below 30% of the primary beam were masked out.

The next step is to weight each image to ensure that the regions which overlap maintain accurate flux measurements. Each pointing is weighted by the square of the primary beam. This gives the regions at the centre of the beam the highest weight and the edges the lowest weight. The reason for this is to do with the weighting that mosaicking gives to the image, it applies variance weighting in which the variance is

related to the square of the noise. The noise itself scales with the response of the PB in the PB-corrected map.

Finally, all of the individual pointings were re-projected using `Montage`. `Montage` takes the information from the individual FITS headers and conglomerates them into a single table, the information of which is used to re-project the individual pointings into a single mosaic image. This procedure was applied to C, D and C+D configuration images.

The final rms depth of the C+D array data is 40μJy beam^{-1}.

5.2.6 Source catalogue

For the C+D configuration mosaic I used PyBDSF to extract the sources from the final mosaic into a catalogue. PyBDSF uses a flood fill technique that finds peaks in the map that are above a certain threshold and then flood fills down to a second threshold. The threshold values are based on the background emission typically finding peaks that are 5 times the background, flood filling down to a factor of 3 times the background. These islands are then decomposed into point sources and Gaussian components.

Once an initial catalogue was created, I visually inspected the catalogue against the map using `Tigger` to identify any wrongly identified "sources" that were in fact artefacts from the PSF. There were 17 such sources identified around the pointings of VLA-4 and VLA-29 which have particularly bright sources that corrupt those individual regions and were difficult to image. Peaks in diffraction spikes from these bright sources were mis-identified as real sources. By identifying the source ID number these were easily removed from the catalogue. I then visually inspected the catalogue against the mosaic a second time for good measure. The final C+D catalogue contains 1734 sources of all types. There are 1438 sources that are single component sources, denoted S_Code = 'S' by PyBDSF.

5.3 Cross-matching the B and C+D catalogues

The sources in both catalogues are subject to flux density scale errors. The presence of noise contributes to a positive or negative offset in the flux measurements. The data was put through the VLA pipeline to calibrate the flux density scale which is accurate to 2% for all observations[1]. All observations had the same secondary calibrator for

[1]As reported in VLA Documentation for the observing periods 2013B, 2015A and 2017A at L-band: https://science.nrao.edu/facilities/vla/docs/manuals/oss2013B/performance/fdscale,

Image/ Catalogue	Area (deg^2)	Resolution ($''$)	Noise level (μJy/beam)	N^o of sources
B image	6.8	4.3	16	7185
C image	6.8	14	52	-
D image	6.8	46	108	-
C+D image	6.8	17.5	40	1438
B / C+D catalogue	-	-	-	1629

Table 5.4: Details on the final catalogues and images. The number of sources in each catalogue is down to a 5σ threshold.

phase referencing. The consistency of the flux density scale is important for the later step of finding the flux ratios between the two catalogues such that any differences can be reliably attributed to the configuration of the array. Additionally, I confirmed consistency of the scales between the two catalogues by selecting bright sources in the B-catalogue ($> 300\mu$Jy, 7.5σ) where the peak to total flux was the same to within 5% to ensure that they were unresolved, and no other sources are detected within $1'$to ensure that additional source were not within the synthesised beam of the C+D sources. These sources were then cross-matched with the C+D catalogue and the total flux measurements from the two catalogues were compared for any offsets. From the 250 sources that met the above criteria, the mean offset was 0.07%, I am therefore confident that the flux scales are consistent.

To compare the flux values of sources observed in B-configuration with those in C- and D-configuration combined I cross-matched the catalogues from the two maps.

I used TopCat to cross-match the B catalogue with the C+D catalogue using an accuracy of matching sources that are within $8.75''$ of each other. This value is chosen as it is half the diameter of the restoring beam and the poorer resolution relative to the B-configuration image may cause the peak of the emission, and thus associated coordinates, to move within the area of the larger beam (see Figure 5.3 to see the limits of the largest (u,v)-spacings of the C+D configuration compared to B-configuration). This resulted in a cross-matched catalogue of 1,629 sources (for a full list of the sources in each catalogue see Table 5.4). 1,616 are unique C+D sources, and 13 sources in the list had 2 B-configuration matches instead of just 1. This is due to the poorer resolution of the C+D-configuration images which blends sources together. This left 118 single component sources from the C+D catalogue without a match in the B catalogue.

https://science.nrao.edu/facilities/vla/docs/manuals/oss2015A/performance/fdscale,
https://science.nrao.edu/facilities/vla/docs/manuals/oss2017A/performance/fdscale

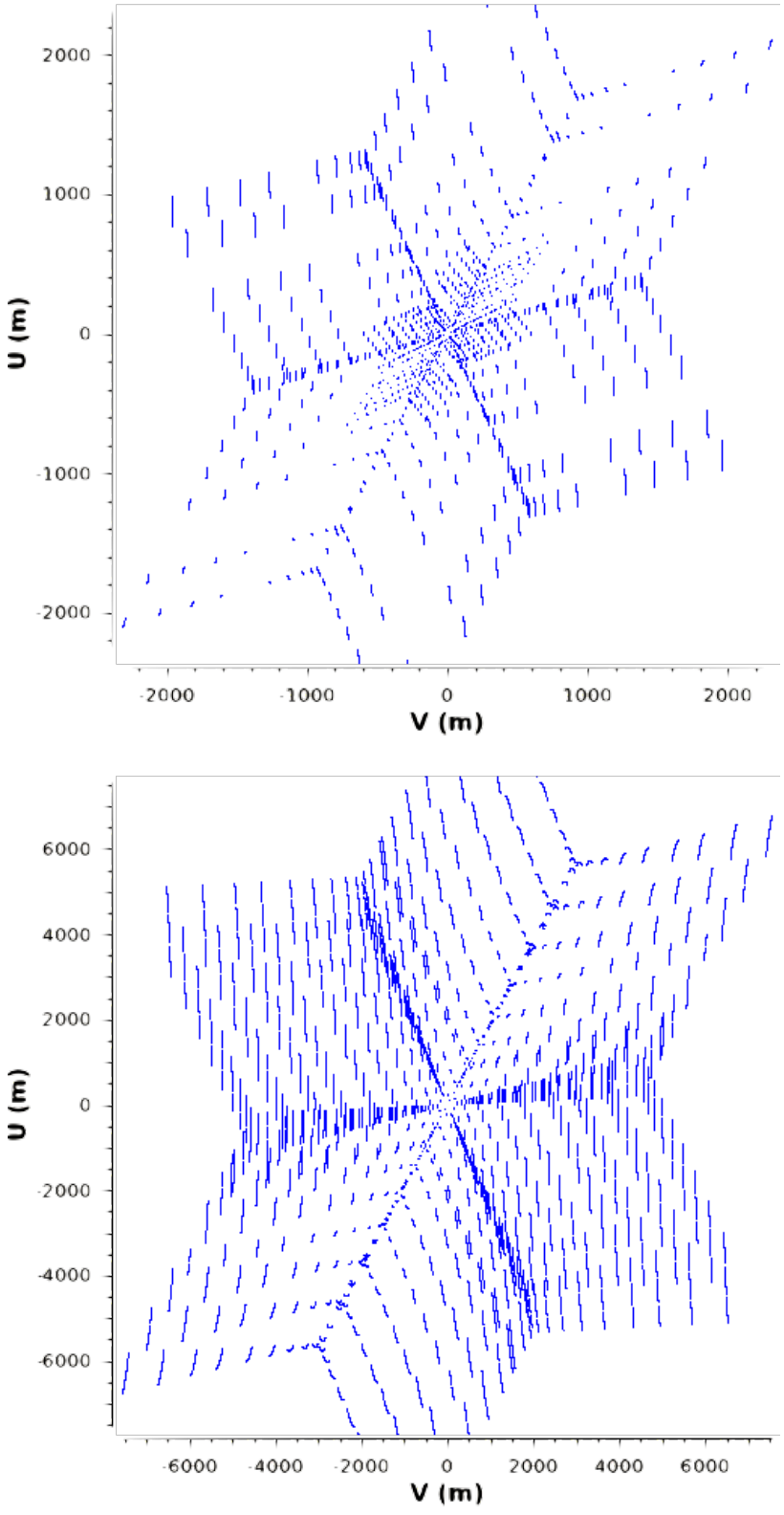

Figure 5.3: The (u,v)-coverage of the C and D-configuration combined (top) and B-configuration (bottom) for pointing 1 of 32. The short baselines of the C+D configuration are evident in the small (u,v) spacings in the top figure.

Classification	N^o of sources
Noise/PSF Artefacts	65
Shifted peaks	25
Extended components	11
New sources	10
Unclassified	7
TOTAL	118

Table 5.5: A list of the classifications for the C+D sources without a match in the B configuration catalog. 'Noise/PSF Artefacts' implies sources that appear to be a spuriously bright region of noise or a previously unidentified artefact originating from the PSF interacting with bright sources. 'Shifted peaks' are sources which have a counterpart in the B catalog, but the peak of the emission is shifted beyond the 8.75″ of the initial cross-match. 'Extended components' are sources which appear to be extended emission associated with a nearby bright source. 'New sources' are sources which appear to be genuine but have no counterpart in the B configuration data. 'Unclassified' sources are not clearly noise or PSF artefacts, but are not obviously new sources either.

Due to the high number of unmatched C+D sources, which is unexpected from the higher sensitivity of the B-configuration catalogue, I investigated each of the sources by eye. First comparing $2' \times 2'$ images of the B and C+D map centred on the RA and Declination of the un-matched C+D source. For any sources that were difficult to identify, I re-examined them in $10' \times 10'$ squares to gain more information on the surrounding image environment. A summary of the classifications of these un-matched sources is provided in Table 5.5.

All objects classified as 'Noise/PSF Artefacts' were ignored from further stages. 'Unclassified' sources too were no longer considered, due to their inconclusive nature they were regarded as artefacts.

Sources that appeared to have 'Shifted peaks' compared to the B-configuration catalogue, were cross-matched with the B-configuration catalogue separately to a radius of within $1.0'$. The larger radius was permitted due to the knowledge that a genuine match would be made. These sources were visually inspected with both B and C+D catalogues to check their cross-matches were accurate. It was found that several sources showing the presence of jets or lobes were labelled as separate components in the C+D catalogue with the RA and Dec centred on the peak of the lobe, whereas the B catalogue listed the combined flux density measurement of the components of the galaxy and its lobes and was centred on a mid-point between all the sources. This is why some of these sources initially failed to partner up successfully as the position in the B catalogue was based on a different criteria than the C+D catalogue position.

Catalogue	μ	σ	min.	max.	N^o of sources
8.75″ cross-match, all	0.98	0.32	0.08	2.38	1616
8.75″ cross-match, 'S'	0.98	0.32	0.08	2.38	1581
Shifted peaks	0.92	0.29	0.31	1.34	17
Extended components	0.47	0.29	0.01	0.978	11

Table 5.6: The mean, standard deviation, minimum and maximum flux ratio measurements from the B-configuration catalogue to the C+D configuration catalogue. The first two rows come from the original catalogue of sources that were cross-matched within 8.75″. The first row gives the statistics on the entire catalogue, the second row on sources that are unresolved (i.e. peak to total flux ratio ~ 1). The third row gives the statistics for the sources which did not have a match in the B-configuration catalogue within 8.75″, but appeared to have a match beyond 8.75″. The fourth row gives the statistics for sources which again had no match within 8.75″, but appeared to be extended components of existing sources.

This makes the number of individual sources in the C+D 'Shifted peaks' list come down to 17, as 16 of the 25 sources were partners.

The opposite of this was also true. A lobe structure may have been separated into several individual components in the B catalogue, whereas the resolution of the C+D image blurred many components together to make only two sources that represented each lobe.

Another consideration was finding that one lobe from the C+D catalogue had been cross-matched in the main catalogue, whereas the other lobe had not. The lobe present in the main catalogue was removed from the main catalogue and transferred to be in the 'Shifted peaks' subsample. This was to add the total flux emission for these sources more easily to compare with the B catalog flux density measurements. This was true for 3 sources.

Sources regarded as being new 'Extended components' of existing sources and entirely 'New sources' were isolated from the rest of the catalogue for further study.

5.4 Results

The final mosaicked images are presented in Figures 5.4-5.7. Below I describe the process of deriving the flux ratios of the catalogues constructed from these images and

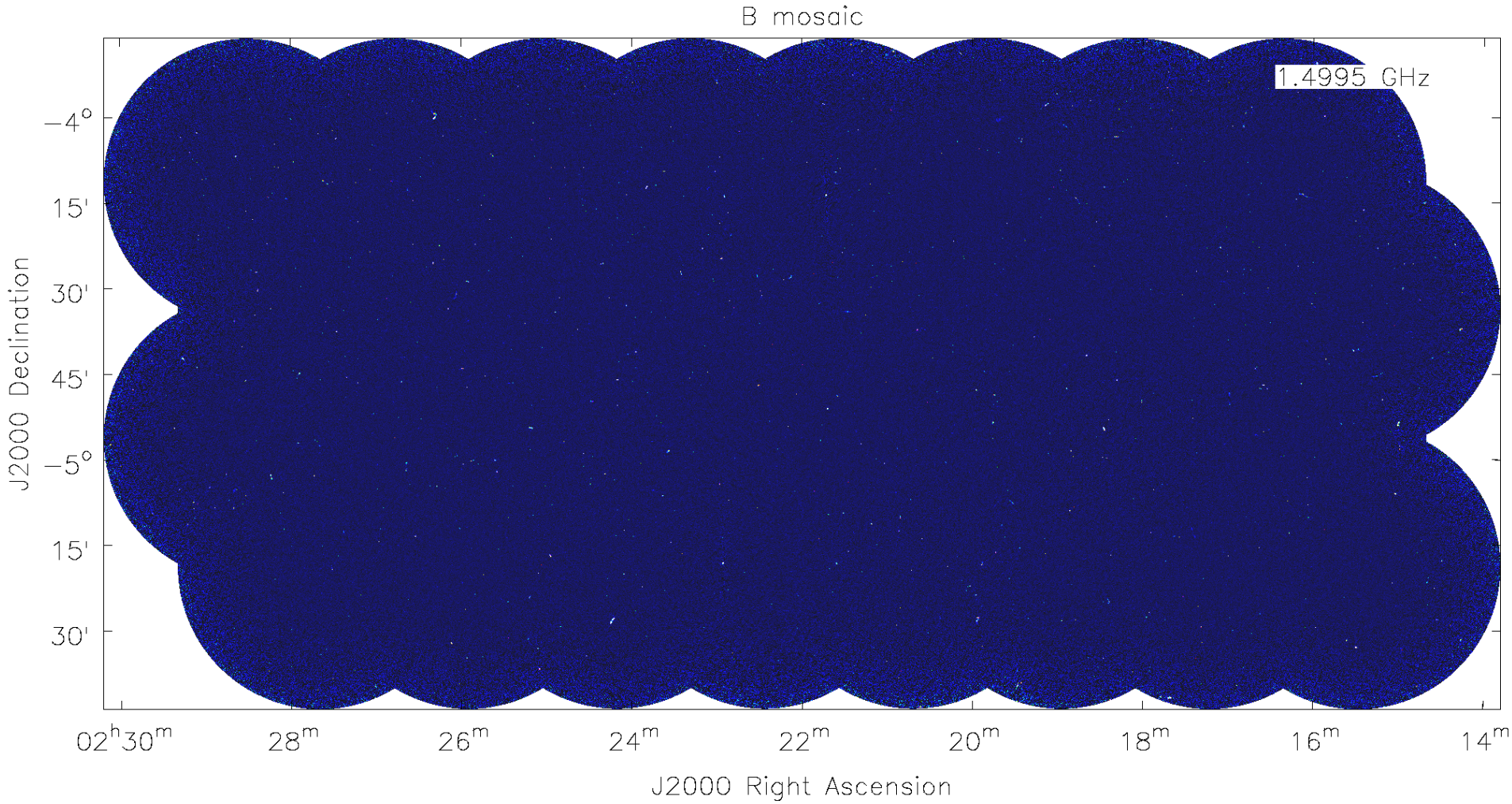

Figure 5.4: The mosaic of the B-configuration pointings. This image was reduced by (Heywood et al., prep). The range of the image is -1.0×10^{-4}-0.001 Jy/beam.

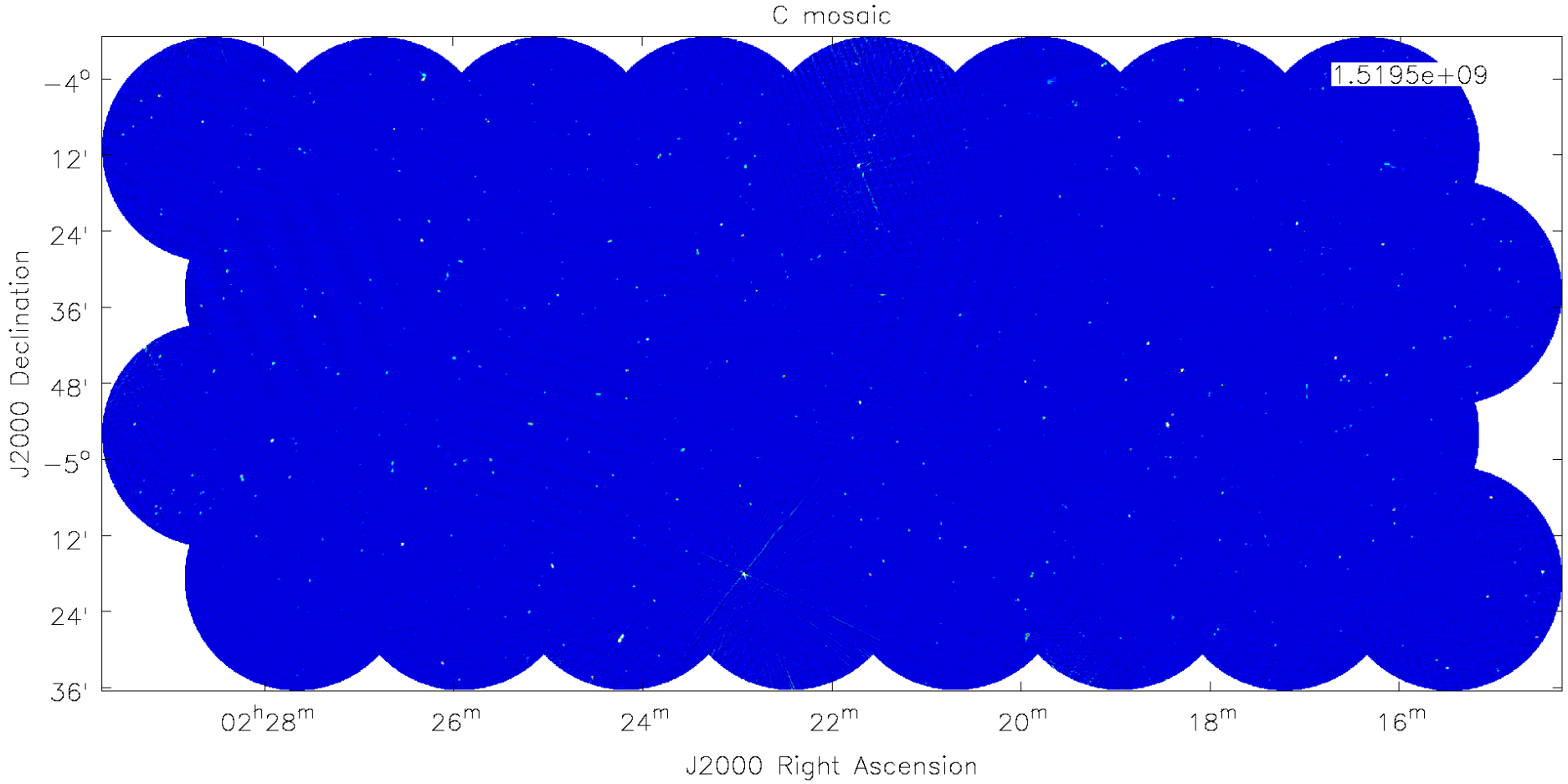

Figure 5.5: The mosaic of the C-configuration pointings. The range of the image is -7.781×10^{-5}-0.002 Jy/beam. The PSF varies across the image as I did not enforce a consistent restoring beam across all pointings until constructing the final C+D image.

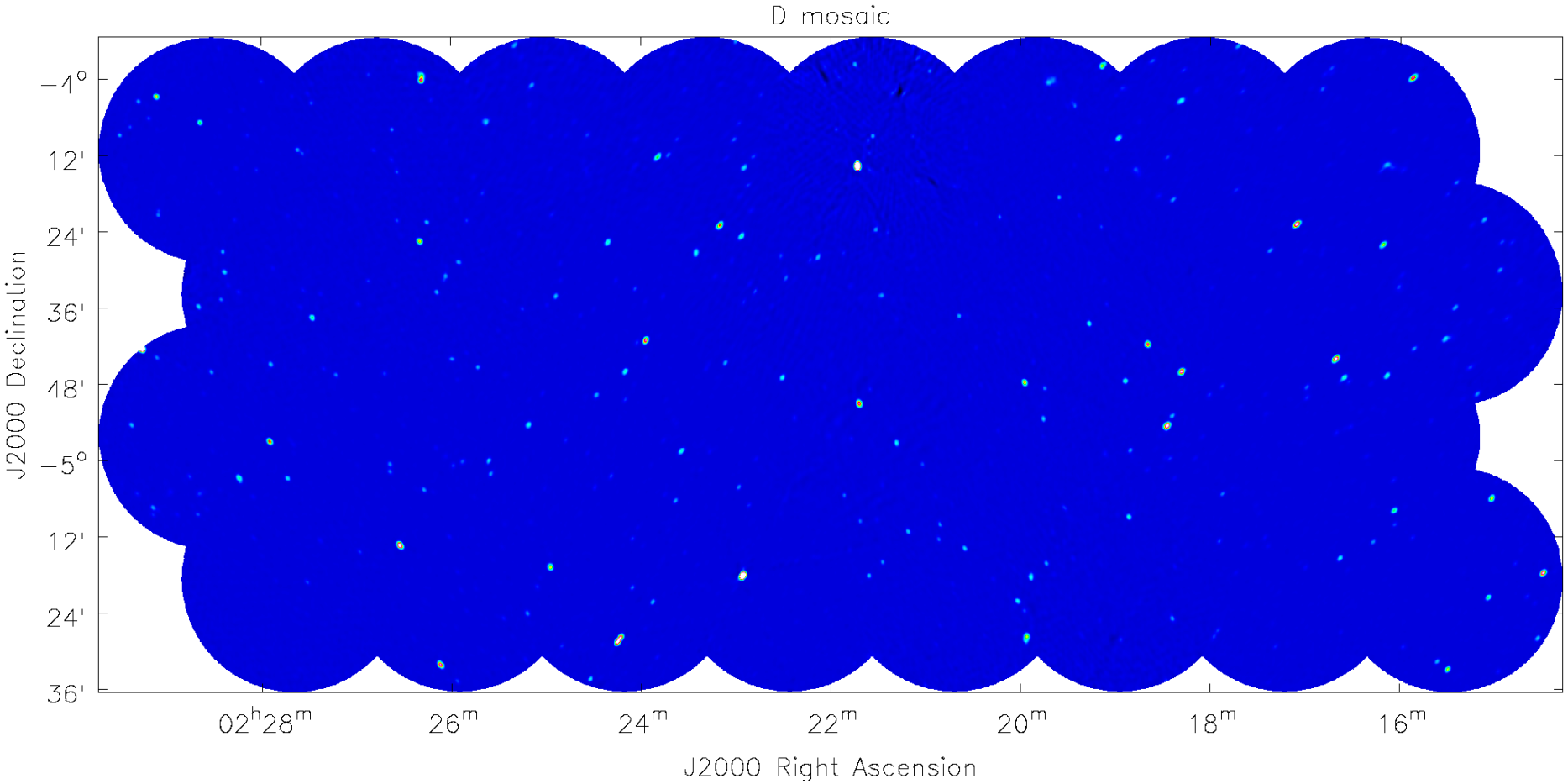

Figure 5.6: The mosaic of the D-configuration pointings. The range of the image is -7.781×10^{-5}-0.002 Jy/beam. The PSF varies across the image as I did not enforce a consistent restoring beam across all pointings until constructing the final C+D image.

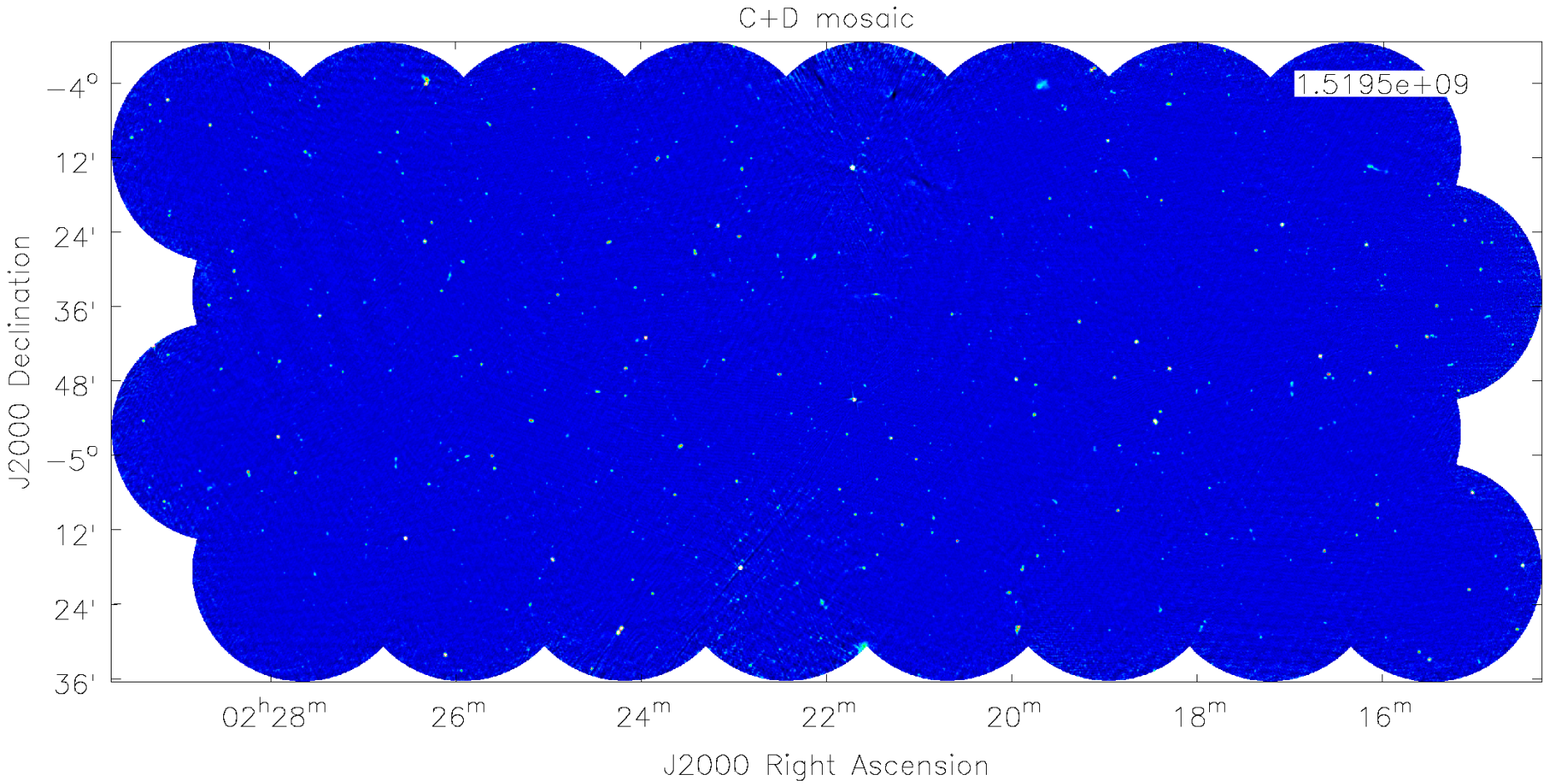

Figure 5.7: The mosaic of the C+D-configuration pointings. The range of the image is -7.781×10^{-5}-0.002 Jy/beam. A consistent restoring beam of 17.5″was implemented in the construction of the image as mentioned in Section 5.2.4

5.4.1 Flux ratios

Before determining the ratios between the flux measurements from the two maps, the 13 C+D sources which had 2 B-configuration cross matches were adjusted as follows. For each source which had multiple matches from the B map, the total flux from both B sources were added together to compare to the single C+D source which encompassed the area of both of them.

Comparing the total integrated flux measurements of the B data to the C+D data shows that on average the two configurations correlate on a 1:1 ratio (see Table 5.6, row 1 and Figures 5.8 and 5.9). The mean ratio of B:C+D for all sources is 0.967 with a standard deviation of 0.33. For the unresolved sources, i.e. sources that have a ratio of S_{peak}:S_{total} $\sim$ 1 (where S_{peak} is peak flux and S_{total} is total flux for the measurement from one map). 1581/1616 of the cross-matched C+D sources are 'unresolved'. 35/1616 are resolved sources.

For the sources that were cross-matched within half the restoring beam width, the results show that the flux measurements on average are just as reliable if observed with the VLA in B configuration or C+D configuration. This agrees with other studies such as Condon et al. (NRAO VLA Sky Survey - NVSS, 1998) who compares NVSS flux density measurements with those from the Westerbork Synthesis Radio Telescope (WSRT) and finds that only a small percentage of sources lie outside the 90% confidence limits. Becker et al. (Faint Images of the Radio Sky at Twenty Centimeters - FIRST, 1995) compares FIRST flux densities of 49 sources $>$ 0.75mJy with those from Mitchell & Condon (1985) and finds a 90% success rate of obtaining similar flux measurements. Interestingly, they find 10% of their sample loses flux that is resolved out by the high-angular resolution of B-configuration.

More recent studies show similar results to those found here. Cohen et al. (2007) find an average ratio of 0.99$\pm$0.01 for 201 sources comparing VLA observations with those from the 6C and 8C catalogues Rees (1990) and Hales et al. (1988) respectively. While Intema et al. (2017) compares to two catalogues, also reporting relatively more sources at faint fluxes for telescopes with more short baselines (similar to Figure 5.8). This is most evident in the plot against Hales et al. (7C catalogue, 2007) observed by the Cambridge Low-Frequency-Synthesis-Telescope which has a minimum baseline of 12m (Rees, 1990). This effect is also likely due to the fact that we do not detect sources in the lower sensitivity data as we move towards these fainter fluxes, there is thus an inevitable bias that ensures that the sources lie above the 1-1 relation due to only detecting sources that lie on positive noise spikes.

Source ID	B total flux (μJy)	CD total flux (μJy)	Ratio	$\text{Ratio}_{\text{err}}$
919	$1410^{\pm 10}$	$2975^{\pm 290}$	0.474	0.046
996	$350^{\pm 10}$	$1137^{\pm 310}$	0.308	0.084
1006	$660^{\pm 10}$	$1725^{\pm 430}$	0.383	0.024

Table 5.7: List of sources with relatively low B:C+D ratios showing brighter emission in the C+D flux density measurements. The source Id, total flux density measurement from the B and C+D catalogue as well as the ratio between them are presented here.

For the sources labelled as having 'Shifted peaks', 14 of the 17 sources showed B:C+D ratios ∼1. The remaining 3 sources continue to have brighter flux density measurements in the C+D catalogue, even when accounting for there being multiple components matched in both B and C+D catalogues (see Figures 5.10, 5.11 and 5.12). These sources with bright extended emission bring the overall average down slightly (see Table 5.6, row 3). The individual flux-density values for the B array, C+D array and the B:C+D ratios are presented in Table 5.7. Each of these sources appears to be more extended than their counterpart in the B image. Sources 919, 996 and 1006 are all individual sources which appear to be galaxies with extended emission.

The mean, minimum and maximum values of the B:C+D flux density ratios of the sources labelled as 'Extended components' of existing sources are listed in Table 5.6. Extended sources are expected to be brighter in the C+D image and catalogue as the short baselines are able to detect extended components by design. This is shown by the low ratio value of 0.468 as the B flux density measurements are less compared to the C+D flux density measurements.

5.4.2 Unmatched sources

In total there are 10 sources in the C+D catalogue that do not have a counterpart in the B catalogue (see Table 5.8 and Figures 5.13, 5.14, 5.15, 5.16, 5.17, 5.18, 5.19, 5.20 and 5.21). I discuss each of these below.

5.4.2.1 Source 108

Source 108 is presented in Figure 5.13. It is fairly bright with a total flux density measurement of 410.11μJy and appears to be extended. The constant amplitude across the source suggests that this could be tracing emission from a cluster in the form of a halo or a relic (e.g. See a recent review on this topic by Feretti et al., 2012). If it were a single galaxy, a clear peak in the emission would be expected and there are no sources nearby that it appears to be associated with.

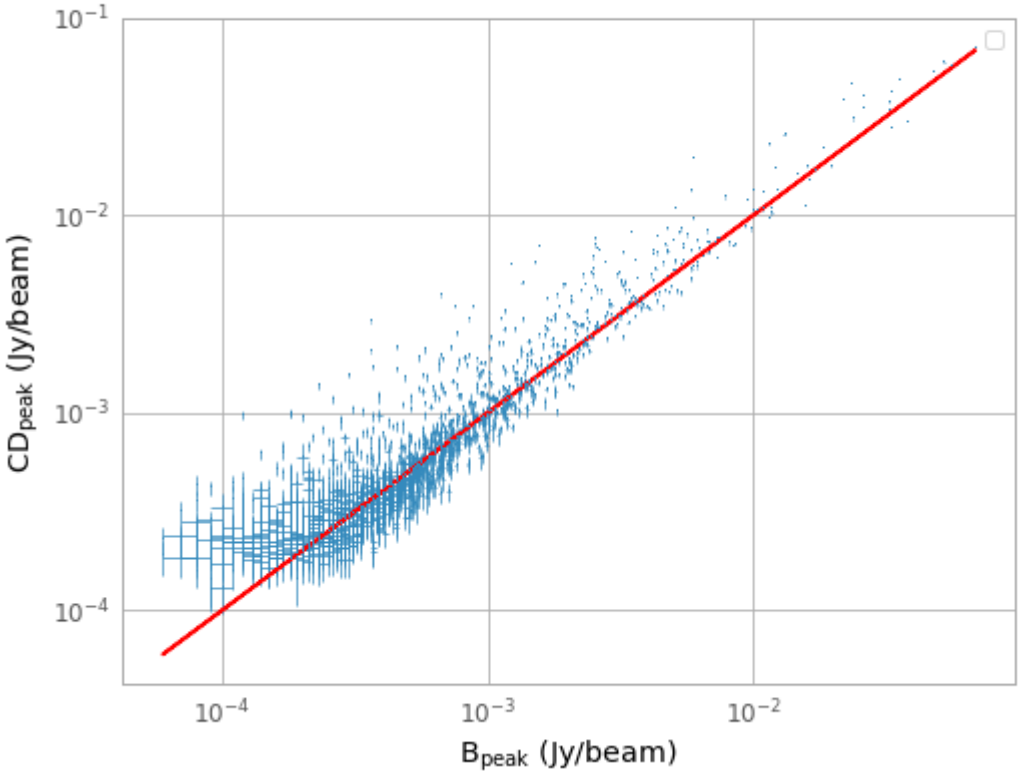

Figure 5.8: A log-log plot comparing the peak flux emission observed in B-configuration and C+D configuration for the full sample. The blue points signify the cross-matched catalogue of sources within 8.75″. The red line represents a 1:1 ratio. Error bars in both directions are shown. Greater errors are present for fainter sources which are nearer the flux limits.

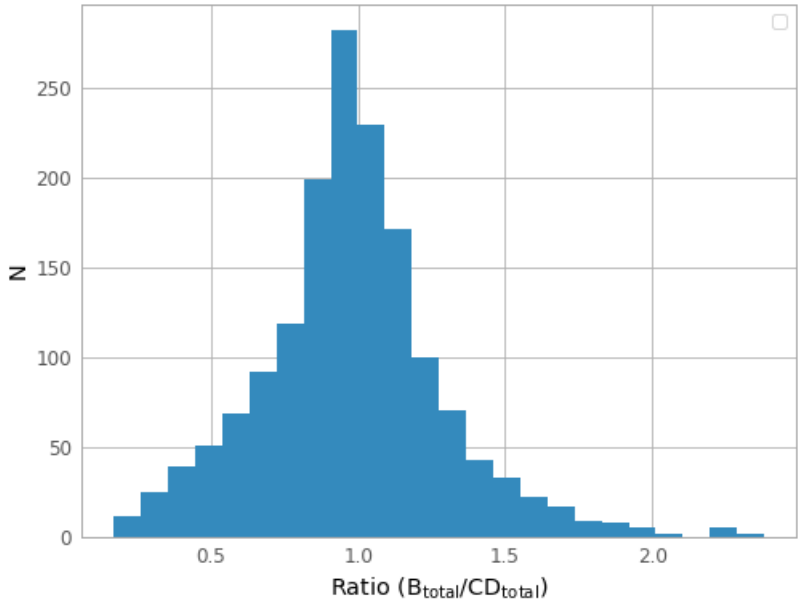

Figure 5.9: A histogram showing the value of the ratio of B-configuration flux measurements to C+D configuration flux measurements of the full sample. The histogram is calculated from the data comparing the total flux for each source from B configuration divided by the measurement from C+D configuration.

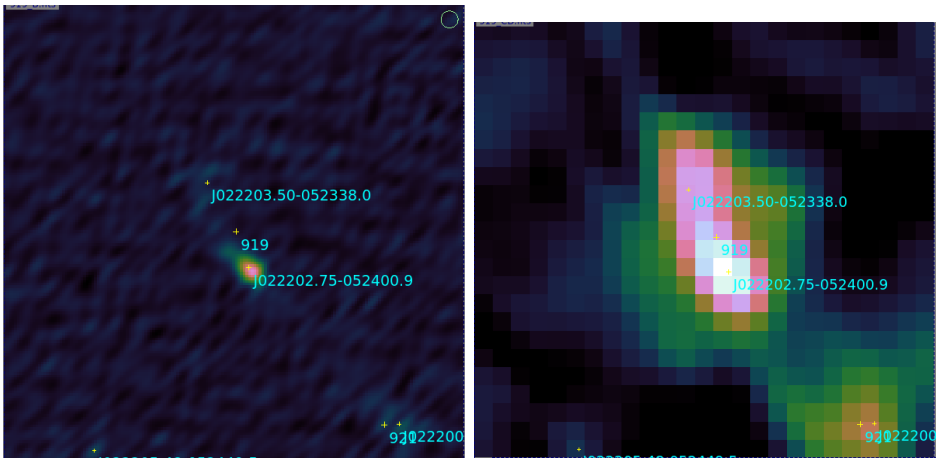

Figure 5.10: C+D source 919. The image is centred on the RA and Dec of source 919 and is a $2' \times 2'$ stamp. *Left:* B configuration image. *Right:* C+D configuration image. The flux range in these images is $-7.781 \times 10^{-5} - 0.0008$ Jy/beam.

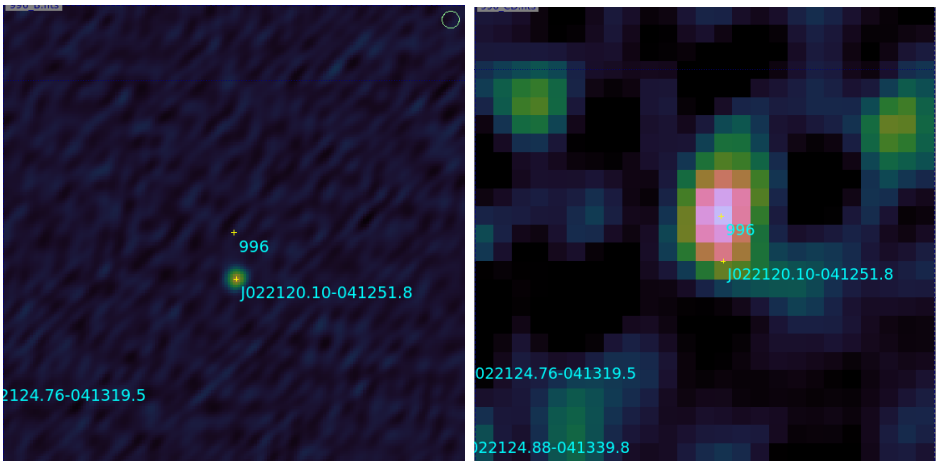

Figure 5.11: C+D source 996. The image is centred on the RA and Dec of source 996 and is a $2' \times 2'$ stamp. *Left:* B configuration image. *Right:* C+D configuration image. The flux range in these images is $-7.781 \times 10^{-5} - 0.0008$ Jy/beam.

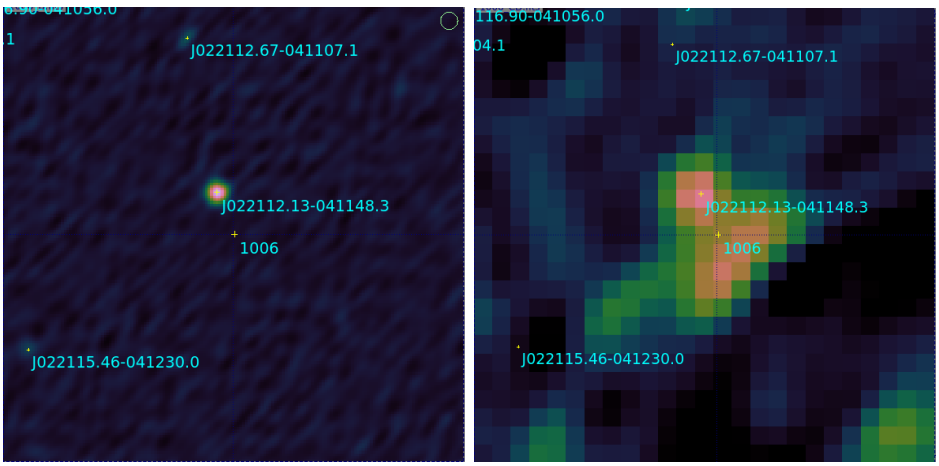

Figure 5.12: C+D source 1006. The image is centred on the RA and Dec of source 1006 and is a $2' \times 2'$ stamp.*Left:* B configuration image. *Right:* C+D configuration image. The flux range in these images is $-7.781 \times 10^{-5} - 0.0008$ Jy/beam.

Source ID	RA (deg)	Dec (deg)	Total flux (μJy/beam)	Peak flux (μJy/beam)	Error (μJy/beam)
108	37.0467	−4.2913	410.11	210.5	110
400	36.4866	−4.3159	1119.13	384.73	150
681	36.0199	−4.5964	303.95	282.18	65.6
849	35.7062	−4.0095	2021.72	540.93	250
952	35.4202	−4.576	1508.13	356.36	280
953	35.4206	−4.5709	221.71	247.57	78.0
1016	35.2862	−4.6523	464.88	261.75	110
1144	35.0244	−3.9248	197.41	339.601	65.4
1258	34.7982	−5.0835	2165.79	244.29	330
1370	34.5605	−5.2483	774.92	381.56	120

Table 5.8: List of sources from the C+D catalogue which do not have a B catalogue counterpart.

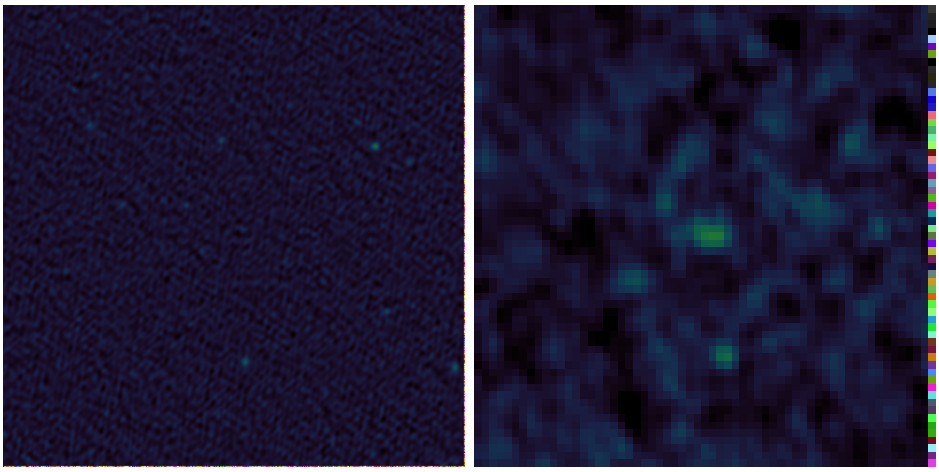

Figure 5.13: Both images are $5' \times 5'$ and are centred on the RA and Dec of source 108 (see Table 5.8). The left-hand side (LHS) shows the B configuration image. The right-hand side (RHS) shows the C+D configuration image. The total flux for this source is 410.11μJy. The flux range in these images is $-7.781 \times 10^{-5} - 0.0008$ Jy/beam.

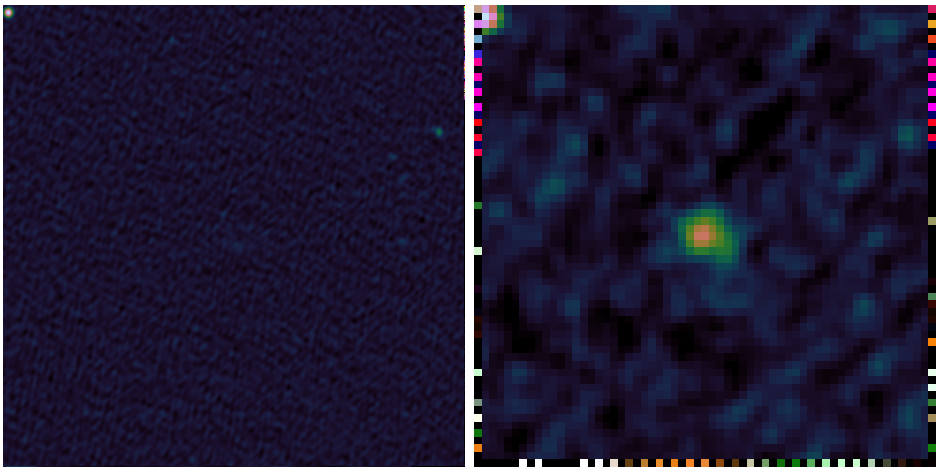

Figure 5.14: Both images are $5'\times5'$and are centred on the RA and Dec of source 400 (see Table 5.8). The LHS shows the B configuration image. The RHS shows the C+D configuration image. The total flux for this source is 1119.13μJy. The flux range in these images is $-7.781 \times 10^{-5} - 0.0008$ Jy/beam.

5.4.2.2 Source 400

Source 400 is shown in Figure 5.14. It shows a bright peak of emission in the centre and has a strong flux density measurement of 1119.13μJy. There is nothing in the B-configuration image in this $5'\times5'$ square that this emission could be associated with. Source 400 may be a somewhat diffuse galaxy with extended components seeing as it is unusually bright and not seen in the B-array data. It could also be a cluster source since it is extended and has a relatively uniform brightness.

5.4.2.3 Source 681

Source 681 can be seen on the RHS of Figure 5.15. Though it appears to be close to a source which can be seen in the B-configuration image, source 681 is brighter (with a flux density measurement of 303.95μJy compared to $\sim$200μJy in the B-array data of the same area) and larger (by visual inspection). The fact that it is brighter makes it unlikely to be an extended component of the nearby source. It is possible it could be lobe emission connected to the bright source to the RHS.

5.4.2.4 Source 849

Source 849 is presented in Figure 5.16. It is a large, bright (2021.72μJy) extended source. Due to the elongated shape it is likely to be lobe emission connected with the source to the south west of the image which is present in both the B and C+D image. It appears to be part of an FRII system.

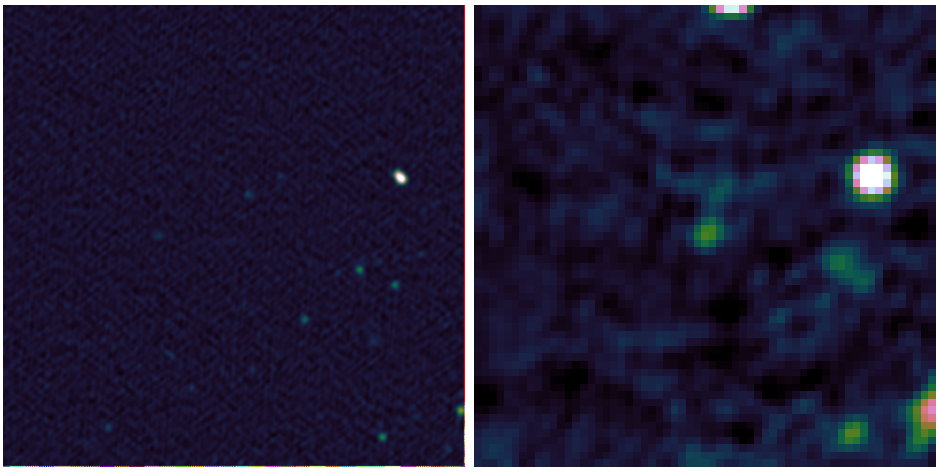

Figure 5.15: Both images are $5' \times 5'$and are centred on the RA and Dec of source 681 (see Table 5.8). The LHS shows the B configuration image. The RHS shows the C+D configuration image. The total flux for this source is 303.95μJy. The flux range in these images is -7.781×10^{-5} - 0.0008 Jy/beam.

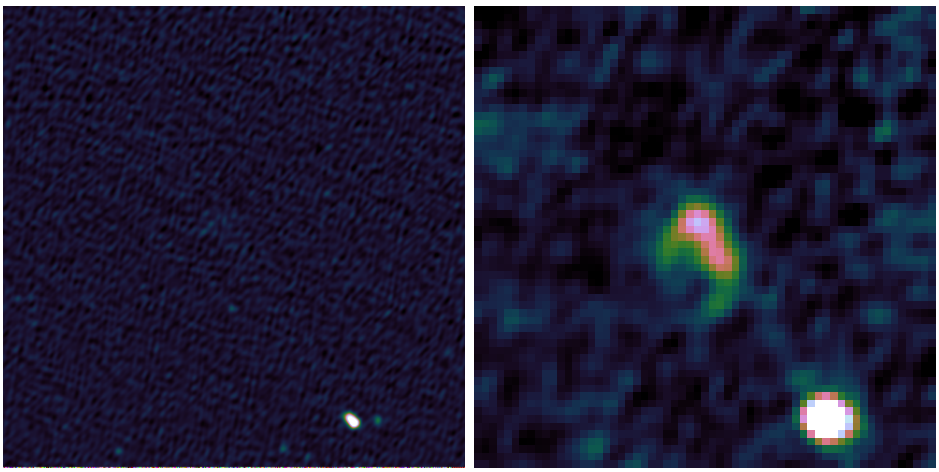

Figure 5.16: Both images are $5' \times 5'$and are centred on the RA and Dec of source 849 (see Table 5.8). The LHS shows the B configuration image. The RHS shows the C+D configuration image. The total flux for this source is 2021.72μJy. The flux range in these images is -7.781×10^{-5} - 0.0008 Jy/beam.

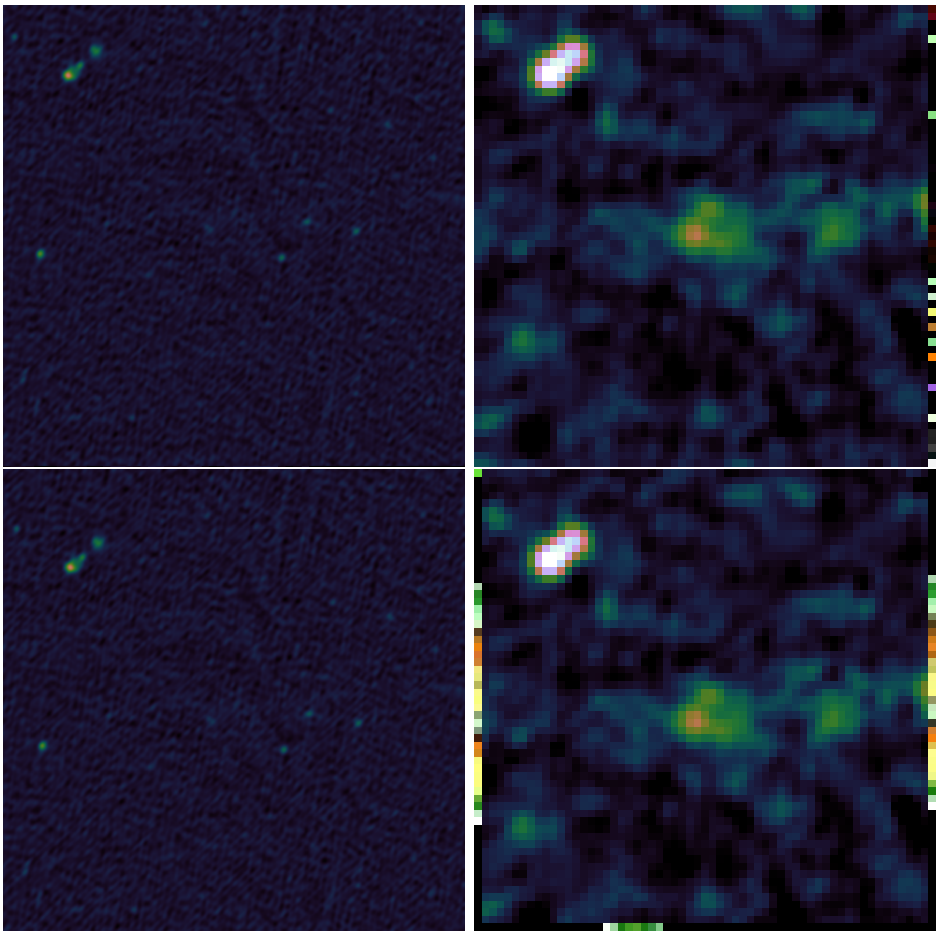

Figure 5.17: All images are 5′×5′. The top two are centred on the RA and Dec of source 952 and the lower two are centred on the RA and Dec of source 953 (see Table 5.8). The LHS shows the B configuration images. The RHS shows the C+D configuration images. Together 952 and 953 comprise components of the same source. The total flux for 952 = 1508.13μJy and 953 = 221.71μJy. The flux range in these images is -7.781×10^{-5} - 0.0008 Jy/beam.

5.4.2.5 Sources 952 & 953

Sources 952 and 953 are shown in Figure 5.17. 952 is the brightest of the two, with a flux density measurement of 1508.13μJy compared to 221.71μJy for 953 in the D-array data. They appear to be components of the same source. There is no other source nearby which could be a potential associated galaxy such that 952 and 953 could be lobe emission. The diffuse and irregular nature of the sources suggests that this may be emission from a galaxy cluster or a very faint, diffuse AGN.

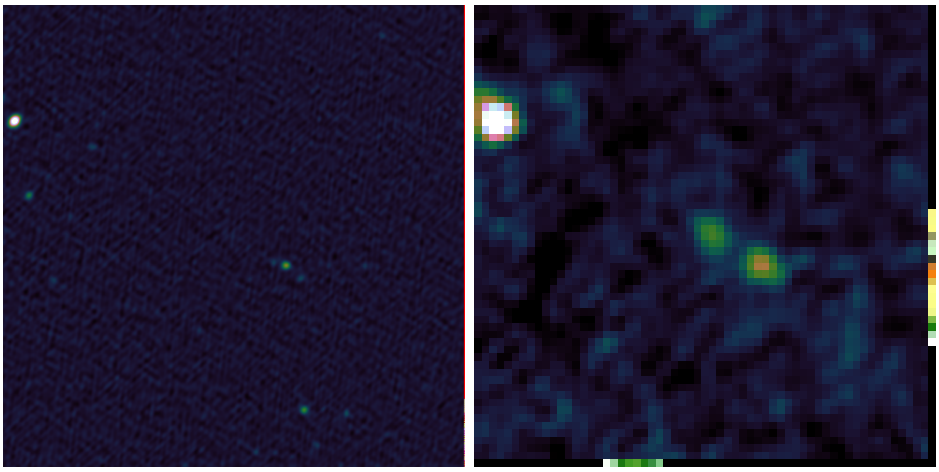

Figure 5.18: Both images are $5' \times 5'$and are centred on the RA and Dec of source 1016 (see Table 5.8). The LHS shows the B configuration image. The RHS shows the C+D configuration image. The total flux for this source is 464.88μJy. The flux range in these images is -7.781×10^{-5} - 0.0008 Jy/beam.

5.4.2.6 Source 1016

Source 1016 is presented in Figure 5.18. Due to the position along a line from the bright source to the north east to the fainter source just to the south west, this may be another example of lobe emission associated with the bright source. It appears to be a fainter, more extended component that is missed by the B-configuration image.

5.4.2.7 Source 1144

Source 1144 is shown in Figure 5.19. The peak is as bright as the source to the south west in the B-configuration image, implies it could be a slightly extended galaxy near to the other source. Due to the comparable nature of the two sources in the C+D image, it seems unlikely that source 1144 is lobe emission associated with the other source. It is unclear what source 1144 is without further information at other wavelengths.

5.4.2.8 Source 1258

Source 1258 is presented in Figure 5.20. It is bright, with a flux density measurement of 2165.69μJy, but with a consistent level of emission across the source. The shape of 1258 is somewhat irregular. Combining these factors it seems that source 1258 is emission from a galaxy cluster halo.

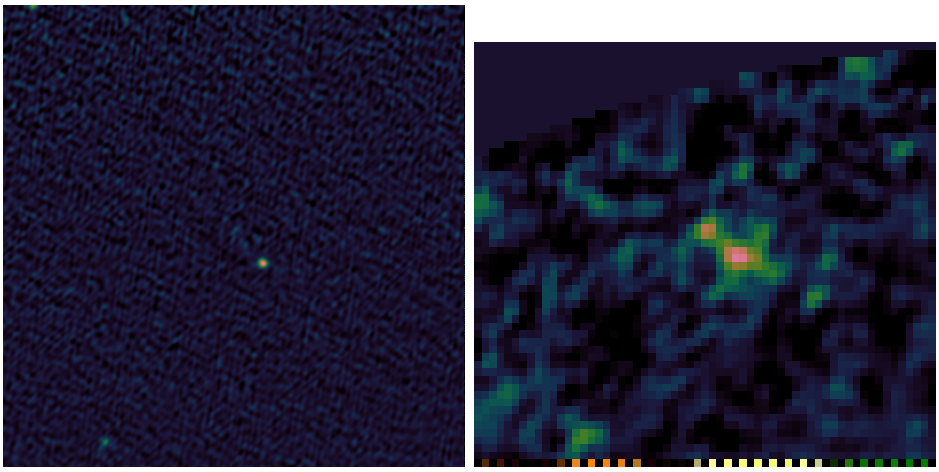

Figure 5.19: Both images are 5′×5′and are centred on the RA and Dec of source 1144 (see Table 5.8). The LHS shows the B configuration image. The RHS shows the C+D configuration image. The total flux for this source is 197.41μJy. The flux range in these images is -7.781×10^{-5} - 0.0008 Jy/beam.

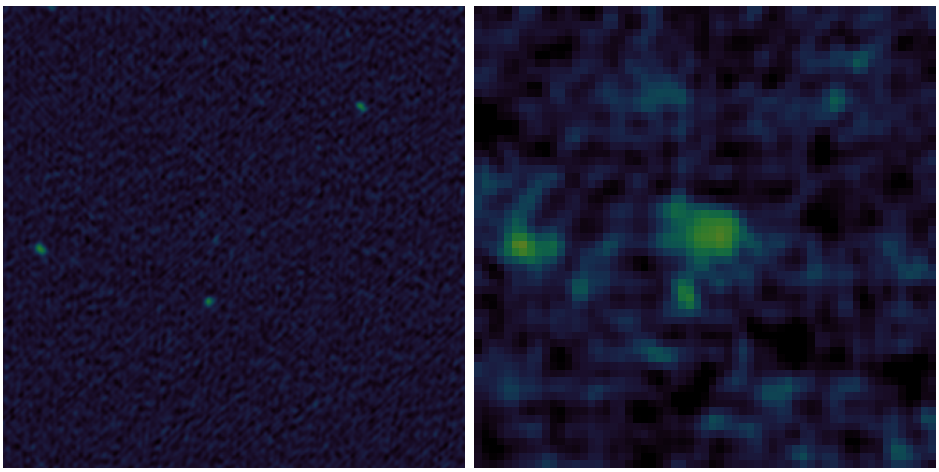

Figure 5.20: Both images are 5′×5′and are centred on the RA and Dec of source 1258 (see Table 5.8). The LHS shows the B configuration image. The RHS shows the C+D configuration image. The total flux for this source is 2165.79μJy. The flux range in these images is -7.781×10^{-5} - 0.0008 Jy/beam.

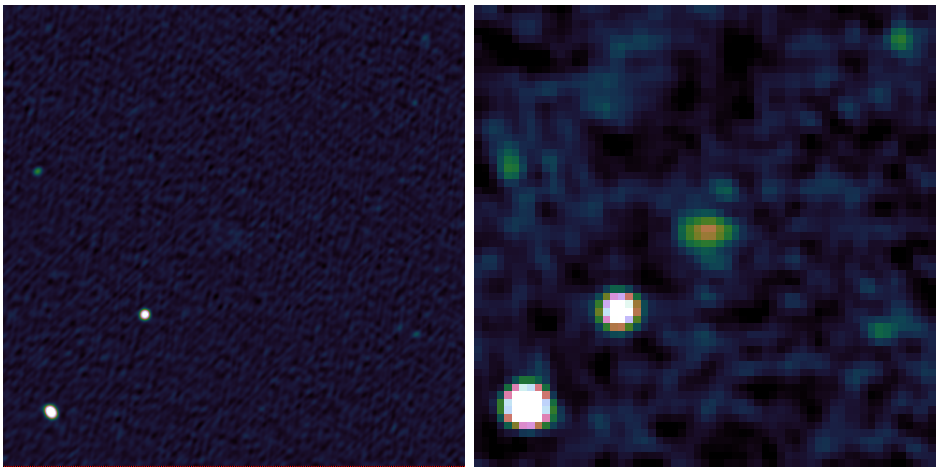

Figure 5.21: Both images are $5' \times 5'$and are centred on the RA and Dec of source 1370 (see Table 5.8). The LHS shows the B configuration image. The RHS shows the C+D configuration image. The total flux for this source is 774.92μJy. The flux range in these images is -7.781×10^{-5} - 0.0008 Jy/beam.

5.4.2.9 Source 1370

Source 1370 is presented in Figure 5.21. It is bright (774.92μJy) and due to its position, appears to be the other side of the lobe emission associated with the source that lies between 1370 and another bright source to the south east.

5.5 Discussion

The primary aim of the work conducted in this Chapter is to assess how well interferometers of different configurations measure the flux of observed sources. The hope was that the relationship would be 1:1 on average between configurations. If so, it would mean that there would be little to no impact on the results of any analysis as the fluxes would be the same.

For sources cross-matched within 8.85″of each other the ratio of fluxes for the B:C+D configuration catalogues give a mean value of 0.975, and for unresolved sources the average is even better with a mean value $\mu = 0.981$ (see Table 5.6). Figure 5.9 is a histogram which shows that the peak of the distribution for the flux ratios is around 1 as expected, however there are clearly more sources at lower flux ratios, which is reflected in the mean values of < 1. This suggests that flux for sources in the C+D array mosaic are higher, specifically for those sources that are resolved in the B-configuration image.

The configuration with the shorter baselines is expected to pick up the emission from more extended features which longer baselines are blind to. The fact that the overall measurement shows a leaning towards the C+D catalogue measurements being higher suggests that sources observed for galaxy samples may be more extended than assumed.

With the C+D measurements exhibiting higher flux it is pertinent to consider the effect that observing in B-configuration may have had in Chapters 3 and 4, which use the more extended VLA configurations. If the B-catalogue is not detecting all the flux from extended sources, then the impact on the earlier analysis could be important. The same analysis but with the C+D catalogue could adjust the placement of the RLF along the L-axis to the bright end of the axis.

However, it is unlikely that this effect would make a large difference to our analysis on the evolution of the RLF. The majority of the sources are at $z > 0.5$ where angular diameter distance becomes fairly constant with redshift, i.e. more distant sources are not expected to have a smaller angular size to those at slightly lower redshift.

Indeed, it is evident in Figure 5.22 that for the subset of the main sample which has redshift information ($\sim 30\%$ of the full sample, used in Chapter 3) there is no statistical evidence for a correlation between the flux ratio B:C+D and redshift. The only tentative evidence of redshift having an effect here is that at very low redshift ($z < 0.5$) there is a dearth of sources where the B-array data gives a higher flux than the C+D data. This can be understood in the context that there are a higher number of extended sources at these low redshifts.

In the likely scenario that it is low redshift sources which contribute to this end of the discrepancy, it would therefore be necessary to conduct studies over a wide range in redshift to minimize the impact of these low redshift sources on the catalogue overall. This is particularly interesting for low-redshift studies that are likely to be investigating the faint end of the RLF. For example, this is likely to effect star forming galaxies (SFGs) the most and is something to consider in the work in Chapter 4. The observations of the VLA-COSMOS project are conducted in both A and C configuration. The balance of short and long baselines should overcome much of the potential issues outlined here. However, if it was observed purely in B-configuration, this could impact the fact that while it was thought that the faint end of the RLF was being observed, corrections would need to be made to adjust it to the correct placement on the L-axis. This may lead to confusion when comparing with the literature, since if a study is conducted using a different frequency with a different set up of baselines and therefore available scales to observe, direct comparison may not

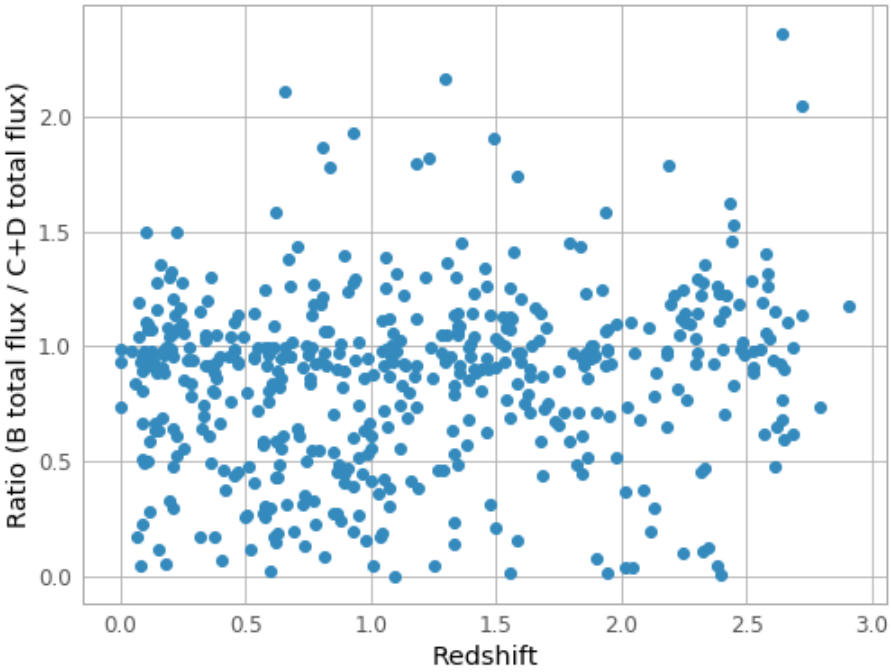

Figure 5.22: The redshift and ratio of flux measurements observed in B configuration to that from C+D configuration. The sample here is the sub-sample used in Chapter 3 which has redshift information. It contains 489 sources ($\sim$ 30% of the full sample).

be possible. As not only does the configuration for a certain observation dictate the scales, but the frequency observed also impacts the distribution of scales possible to be detected with the particular set up of the interferometer. ndeed, recent work with the MeerKAT data suggests that the VLA-3 GHz data missed a significant population of low-redshift, extended star-forming galaxies (Jarvis et al. in prep.).

In terms of the impact on the work conducted in this thesis, B-configuration observations may have been underestimating the flux measurements of the sources in Chapter 3, though because the population sampled in that Chapter is AGN, it is more likely that these are at high redshifts and we would not expect a large difference over the redshift range probed. However, if the fluxes are underestimated, this would move the RLF, at all redshifts, to marginally higher luminosities. This would not effect the evolution of the RLF.

The results of this chapter, which show that the array configuration can have a large impact on the detected flux of extended sources, suggest that comparing results from different studies is difficult. In terms of measuring the RLF, this effect exacerbates the problem of not properly accounting for the spectral index distribution. This is because if we are unable to accurate measure the total flux from an extended source at different frequencies, then the measured spectral index will inevitably be incorrect, and most probably biased towards steeper spectral indices due to the fact that more flux is likely resolved out in observations at higher frequency, if the same array configuration is used, due to the different uv coverage.

5.6 Conclusions

To summarise, I have reduced both C and D configuration VLA data of the XMM-LSS field at L-band (1-2 GHz). Maps of C and D along with an image from a combination of the two configurations were made. The C+D configuration map was compared with a B-configuration map of the same field that was reduced by Heywood et al. (prep).

The aim of this Chapter was to assess whether the flux measurements from long baseline observations capture the same emission as observations from the VLA in configurations with shorter baselines. The ratio of the total flux emission from the B-configuration catalogue to the C+D configuration catalogue is $\sim$1. This remained true for both resolved and unresolved sources. Therefore both configurations are equally reliable for flux measurements though they are sensitive to different scales of emission.

However, 118 sources in the C+D catalogue were not successfully cross-matched with a B catalogue source. Inspection of these showed 65 sources to be previously undetected noise or PSF artefacts, 25 to have a match in the B-catalogue but such that the peak of the emission was shifted by a greater distance than the FWHM of the restoring beam, 11 to be new extended components of existing sources, 10 to be entirely new sources and 7 to be unclassified.

The sources with the peaks of emission shifted were most often (16/25) lobes of jets where the C+D catalogue labelled the individual lobes whereas the B-catalogue summed the total emission and located the position to be the mid-point of the lobes. These were easily rectified and found to have ratios of B:C+D flux densities $\sim$1 also. 3 of these sources had multiple components in the B-catalogue which were single component but extended sources in the C+D image with shifted peak emission. The ratios of these were much lower with an average ratio of 0.388 between them.

Sources labelled as new extended components of existing sources showed an expected ratio of $\sim$0.5 since the C+D observations were able to detect extra extended emission that the B observations were not. Unclassified sources could not confidently be identified as real and so were disregarded with the sources labelled as 'Noise/PSF Artefacts'.

There were 9 individual sources from the C+D catalogue which did not have a match in the B catalogue. Further inspection of these sources suggests that 3 of them may be lobes of jets from bright galaxies, 2 or 3 to be emission from galaxy clusters, 1 is possibly a slightly diffuse galaxy and the remaining 1 is unclear as to what it could be. Comparing observations of these sources from different parts of the electromagnetic spectrum to analyse their morphology and composition at different wavelengths, would be useful to draw stronger conclusions on these sources.

In summary, all sources that were successfully cross-matched with the B configuration data within the FWHM of the C+D observations showed the B and C+D flux density measurements to be in agreement. Care must be taken with remaining sources as the work here has shown there is the possibility of multiple components in either catalogue, the peak of the emission to be shifted, previously unidentified extended components of sources as well as entirely new sources that are not detected by configurations with a lack of short baselines. These undetected sources are likely to be the second lobe of a source with jets or emission from a galaxy cluster. It is therefore imperative to include short baselines when observing for radio galaxy surveys, as extended emission can be missed even when bright.

The impact of resolving out flux from sources due to the lack of short baselines means that spectral index measurements are also less reliable. Taken together with the results presented in Chapters 3 and 4 this could in turn impact on our measurement of the RLF and its evolution.

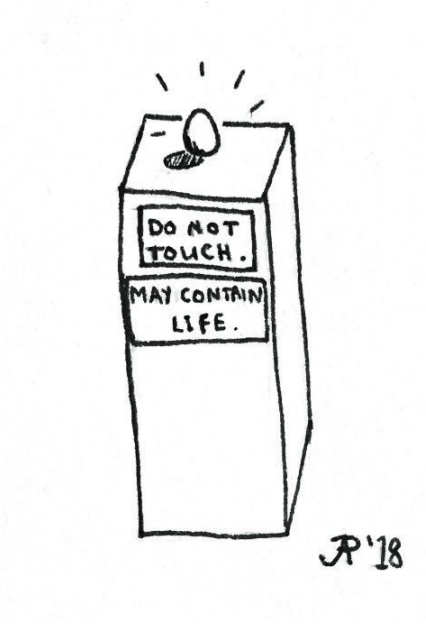
DO NOT TOUCH.
MAY CONTAIN LIFE.
JP '18

Chapter 6

Conclusions and Future work

6.1 Conclusions

The work in this thesis has revolved around radio observations of galaxies using interferometers. Radio Luminosity Functions for both AGN (Chapter 3) and star forming galaxies (SFGs, Chapter 4) were measured using data over the XMM-LSS and COSMOS field respectively. The AGN RLFs were estimated using a combination of 150 MHz LOFAR observations and 1.5 GHz VLA observations, and the SFG RLFs were measured using 1.4 GHz MeerKAT observations combined with 3 GHz VLA observations. This enabled me to account for the distribution in spectral indices for the sources in these fields for determining the RLF.

The key aspect of these RLFs is the inclusion of the distribution of the spectral index α in the model RLF. Not only including the α-distribution, but modelling it to include additional features proved to be important for the interpretation of the RLF and how it evolves with redshift. Both data sets included small populations of steep spectrum sources $\sim$ 10% the size of the main population centred around α $\sim$0.8. The inclusion of steep spectrum sources affected all parameters, but most notably the evolution parameter k, where the evolution is parameterised as $(1+z)^k$ for both pure density and pure luminosity evolution.

In both Chapters 3 and 4, including modelling of the α-distribution had significant effects on the shape and evolution of the RLF. When the primary use of the RLF is to measure the evolution of galaxies, it is therefore crucial to include spectral index information to obtain accurate understanding of the strength and type of evolution with redshift.

When comparing these results to the literature I focused on evaluating the impact on the parameter k for the RLFs. For the case of the AGN, I found that the results of the 9 parameter PLE model agreed well with Smolčić et al. (2009) and McAlpine et al.

(2013) and was within the large errors of Prescott et al. (2016). Pracy et al. (2016) investigated the evolution of radio AGN after splitting their sample into LERGs and HERGs. Given that the radio population is not split in terms of the accretion mode in this thesis, one would expect derived cosmic evolution to fall somewhere between the HERG and LERG evolution terms, weighted according to their redshift distributions. Indeed, I find that the evolution does lie between the extremes of the LERG and HERG populations studied by Pracy et al. (2016). Comparing to the work of Smolčić et al. (2017b), the value for k found in Chapter 3 agrees at $z > 0.78$ in their parameterisation where the k-value can also vary with redshift, which is also the redshift above which the bulk of our sources lie.

On the other hand, for the RLFs determined for SFGs it is generally more difficult to compare to past studies, as fainter nature of the population means that there are only a few studies which measure the RLF out to significant redshifts. Of the works which did track the evolution of the SFG population, I found there to be good agreement. The evolution parameter of McAlpine et al. (2013) was within the error boundaries of the k value found in the work in this thesis, and the evolution term from Novak et al. (2017) also agrees at $z > 1.4$. An interesting addition is that for both models in the literature and in the work here, was that the best fit model was consistently that of the PLE.

A final note on Chapter 4 is the careful consideration of the selection criteria on choosing a certain population and what the effect of that can be on the results. After complete analysis on the variety of models in Chapter 4, it became apparent when performing literature comparisons that the paper of Novak et al. (2017) (which uses data from the VLA-COSMOS 3 GHz catalogue) used slightly different selection criteria to select SFGs and remove unwanted AGN contaminants. When trialling a new data subset constructed using the selection criteria of Novak et al. (2017) it was discovered that the model fitting process sped up, with almost every parameter having smaller errors, as well as for the first and only time in this work the model distribution of the spectral index passed the KS-test for a statistically satisfactory match. The distribution of the spectral index was more even in the new sample with a higher peak at the median. When comparing parameters to the 8 parameter PLE model from the previous sample a shallower value and a steeper value was found for the faint-end and bright-end slopes respectively. This relates to a greater population of faint sources and fewer bright ones. The main difference for parameters related to the spectral index was a reduced σ_2 which determines the fitting of the steep end of the spectral index distribution. σ_2 decreased by 0.5 for the new model and in turn

k increased by 0.1. σ_1 also decreased but by only 0.2. Improved modelling of steep spectral indices will effect the bright end of the RLF which in a PLE model drives the pace of the evolution and so this can explain the increase in k. However, the fits to all the parameters in the PLE model were consistent for both the original and sample defined by these slightly different selection criteria, suggesting that the model fits are robust to moderate changes in the sample selection criteria.

The final science chapter in this thesis (Chapter 5) compares flux densities obtained by observing the same field (XMM-LSS) in different configurations. Observations taken with the VLA in B configuration were compared to images obtained from combining observations in C and D configuration. B-configuration is comprised of many long baselines to achieve high angular resolution images. C and D configurations include more short baselines and few long baselines, they have poorer resolution but the ability to detect larger scale structures. All data was observed at L-band (1-2 GHz).

All sources detected in the C+D configuration that were successfully cross-matched with B configuration sources within the FWHM of the C+D observations exhibited a flux ratio between the B and C+D array data $\sim$1. However, care had to be taken with sources in the catalogues that showed the presence of jets and lobes. The allocation of position and number of components can vary from observing in different configurations using automated source extraction software. It was also found that extended components of existing sources were detected when observing in C+D configuration. 9 individual sources were detected in the C+D catalogue that were not present in the B catalogue. These comprised of lobe components of sources that were not visible in the B configuration image, as well as emission that appears to originate from galaxy cluster halos.

Overall, the flux density measured for sources using both configurations agree, although short baseline observations are still important considerations for gathering full information on sources, especially in the case of galaxies in which the jet morphology can be resolved.

Though the average ratio of the B:C+D configuration catalogues was $\sim$ 1.0, it is worth noting that there is evidence for the flux measurements in the C+D catalogue to be slightly higher for a significant number of resolved sources in the B-configuration data. The results of Chapter 5 show that the array configuration can impact the detected flux of extended sources, suggesting that comparing results from different studies is difficult. When measuring the RLF, this effect exacerbates the problem of not properly accounting for the spectral index distribution. This is because if the

total flux from an extended source is inaccurately measured at different frequencies, then the measured spectral index will consequently be incorrect, and likely biased towards steeper spectral indices due to the fact that at higher frequency observations more flux is likely resolved out, if the same array configuration is used, due to the different uv coverage.

Either way, though the average is ~ 1.0, there is a clear distribution to both sides of the ratio values where there exist sources that the B-catalogue measurement is twice that of the C+D catalogue and vice-versa. In conclusion, the only way to truly account for these variations is to ensure a wide variety of baselines are included in the interferometer observing your data.

6.2 Future Work

The next logical step that follows the work performed in this thesis connects the two themes from Chapters 3 and 4 with Chapter 5. Improving the modelling of the RLF using additional information on the sources in a sample, namely the angular size.

As mentioned in Section 2.1, an interferometer is only sensitive to a subset of angular scales on the sky which correspond to the assortment of baselines in the observing configuration. Examples of this have been demonstrated in Chapter 5. An interferometer with long baselines, and therefore high resolution, may not detect large scale emission. Conversely, an interferometer set-up with lots of short baselines that has poor resolution, can blend sources together or smear sources so that they lie below the flux limit of the survey, which is generally estimated based on the assumption that sources are point like. Indeed, most source extraction software detects sources based on a peak flux above the background noise, rather that on an integrated flux. This is a more complex issue to resolve, as not only must the scales at which the interferometer is sensitive to be considered, given its configuration of antennas and baselines, but also the distribution of angular sizes of sources detected in the observations. Distant bright point-like sources, nearby extended faint sources or those in-between may be missed without proper correction for these effects.

Trends relating L, z, α and D were explored by (Blundell et al., 1999). They found that α increased with linear size (D), α is more dependent on L than z and that D is smaller at higher z. They uncovered that these trends could be explained by not only Inverse Compton Losses, but also the inclusion of synchrotron losses and adiabatic expansion losses on their modelling of double radio lobe sources. However, the discovery of this physical reasoning for these correlations is only possible because they

took into account all possible observational effects to see the real physical happenings underneath.

To implement this approach, it would require observations taken in a variety of configurations to fully fill out the true angular sizes of a sample of sources and be able to measure the variation of the sample. With the data available in this thesis, jointly imaging the B, C and D configuration data from Chapter 5 would provide such information. The models used in Chapters 3 and 4 could be built upon by the addition of another function, this time of the angular size of the sources, D, e.g. a Gaussian distribution

$$\rho_D = \exp\Big[-\frac{1}{2}\Big(\frac{D-\mu_D}{\sigma_D}\Big)^2\Big] \tag{6.1}$$

where μ_D and σ_D are the mean and variance of the angular size distribution respectively. This re-formulates the RLF to be,

$$\Phi_{\rm PLE}\Big(\frac{L}{(1+z)^k}\Big) = \rho_0 \times \rho_L \times \rho_\alpha \times \rho_D \tag{6.2}$$

for the PLE model and

$$\Phi_{\rm PDE}(L) = \rho_0 \times \rho_L \times \rho_z \times \rho_\alpha \times \rho_D \tag{6.3}$$

for the PDE model. These models are identical to Equations 3.5 and 3.6, but with the addition of the distribution of the angular size of sources in the sample, ρ_D. Including the variation in the angular size of each source and the overall distribution of sizes over the sample ensures that sources which may not have observed due to the combination of D and the resolution of the interferometer are accounted for.

D is the last variable of a source that effects whether or not it is detectable by a given interferometer. By including all four variables : L, z, α and D, this is the most extensive and comprehensive way to model the RLF. With the advent of more and more advanced radio telescopes, these measurements will not only be more attainable, but necessary and a model of this kind enables one to truly see the real RLF behind the observational effects and see an unaltered view of galaxy evolution.

The data that I used in Chapter 4 partially came from the MeerKAT. This has a baseline distribution that is centrally concentrated and therefore sensitive to large-scale, diffuse emission. Furthermore, it has baselines that extend to $\sim 8\,$km providing a maximum resolution of around $4.5''$at L-band. Therefore, data from this telescope will allow a full characterisation of the RLF, including angular size, in addition to spectral index distributions.

The MIGHTEE survey (Jarvis et al., 2016) covers some of the most well studied fields of the extragalactic sky, which have some of the deepest multi-wavelength data available, similar to COSMOS (Chapter 4). These data potentially provide redshift information for the vast majority of the radio sources. One could therefore also move away from observed *angular* scale of the radio sources towards a more physically meaningful consideration of the physical size of the sources. One could then relate the various parameters, e.g. α, luminosity, redshift and linear size to each other, based on expectations of physical models of radio sources (e.g. Blundell et al., 1999). This would provide a much deeper understanding of the evolution of radio sources and their relation to galaxy evolution.


No I will not be going to work today
Darren
JR '18

Bibliography

Aird J., et al., 2010, http://dx.doi.org/10.1111/j.1365-2966.2009.15829.x MNRAS, http://adsabs.harvard.edu/abs/2010MNRAS.401.2531A 401, 2531

Ajello M., et al., 2012, http://dx.doi.org/10.1088/0004-637X/751/2/108 ApJ, http://adsabs.harvard.edu/abs/2012ApJ...751..108A 751, 108

Alexander D. M., Swinbank A. M., Smail I., McDermid R., Nesvadba N. P. H., 2010, http://dx.doi.org/10.1111/j.1365-2966.2009.16046.x MNRAS, http://adsabs.harvard.edu/abs/2010MNRAS.402.2211A 402, 2211

Antonucci R., 1993, http://dx.doi.org/10.1146/annurev.aa.31.090193.002353 ARA&A, https://ui.adsabs.harvard.edu/abs/1993ARA

Appleton P. N., et al., 2004, http://dx.doi.org/10.1086/422425 ApJS, http://adsabs.harvard.edu/abs/2004ApJS..154..147A 154, 147

Arav N., Moe M., Costantini E., Korista K. T., Benn C., Ellison S., 2008, http://dx.doi.org/10.1086/588651 ApJ, http://adsabs.harvard.edu/abs/2008ApJ...681..954A 681, 954

Arnouts S., Cristiani S., Moscardini L., Matarrese S., Lucchin F., Fontana A., Giallongo E., 1999, http://dx.doi.org/10.1046/j.1365-8711.1999.02978.x MNRAS, https://ui.adsabs.harvard.edu/abs/1999MNRAS.310..540A 310, 540

Baldi R. D., Capetti A., 2009, http://dx.doi.org/10.1051/0004-6361/200913021 A&A, http://adsabs.harvard.edu/abs/2009A

Baldi R. D., Capetti A., Giovannini G., 2015, http://dx.doi.org/10.1051/0004-6361/201425426 A&A, http://adsabs.harvard.edu/abs/2015A

Baldi R. D., Capetti A., Massaro F., 2018, http://dx.doi.org/10.1051/0004-6361/201731333 A&A, http://adsabs.harvard.edu/abs/2018A

Baldi R. D., Capetti A., Giovannini G., 2019, http://dx.doi.org/10.1093/mnras/sty2703 MNRAS, http://adsabs.harvard.edu/abs/2019MNRAS.482.2294B 482, 2294

Ballantyne D. R., 2007, http://dx.doi.org/10.1142/S0217732307024322 Modern Physics Letters A, https://ui.adsabs.harvard.edu/abs/2007MPLA...22.2397B 22, 2397

Becker R. H., White R. L., Helfand D. J., 1995, http://dx.doi.org/10.1086/176166 ApJ, https://ui.adsabs.harvard.edu/abs/1995ApJ...450..559B 450, 559

Bendo G. J., et al., 2015, http://dx.doi.org/10.1093/mnras/stu1841 MNRAS, http://adsabs.harvard.edu/abs/2015MNRAS.448..135B 448, 135

Best P. N., Heckman T. M., 2012, http://dx.doi.org/10.1111/j.1365-2966.2012.20414.x MNRAS, http://adsabs.harvard.edu/abs/2012MNRAS.421.1569B 421, 1569

Best P. N., Kauffmann G., Heckman T. M., Ivezić Ž., 2005, http://dx.doi.org/10.1111/j.1365-2966.2005.09283.x MNRAS, 362, 9

Beswick R. J., Muxlow T. W. B., Thrall H., Richards A. M. S., Garrington S. T., 2008, http://dx.doi.org/10.1111/j.1365-2966.2008.12931.x MNRAS, https://ui.adsabs.harvard.edu/abs/2008MNRAS.385.1143B 385, 1143

Bhatnagar S., Cornwell T. J., Golap K., Uson J. M., 2008, http://dx.doi.org/10.1051/0004-6361:20079284 A&A, http://adsabs.harvard.edu/abs/2008A

Bhatnagar S., Rau U., Golap K., 2013, http://dx.doi.org/10.1088/0004-637X/770/2/91 ApJ, http://adsabs.harvard.edu/abs/2013ApJ...770...91B 770, 91

Blundell K. M., Rawlings S., Willott C. J., 1999, http://dx.doi.org/10.1086/300721 AJ, http://adsabs.harvard.edu/abs/1999AJ....117..677B 117, 677

Bondi M., et al., 2003, http://dx.doi.org/10.1051/0004-6361:20030382 A&A, https://ui.adsabs.harvard.edu/abs/2003A

Bourke S., Mooley K., Hallinan G., 2014, in Manset N., Forshay P., eds, Astronomical Society of the Pacific Conference Series Vol. 485, Astronomical Data Analysis Software and Systems XXIII. p. 367

Bouwens R. J., et al., 2015, http://dx.doi.org/10.1088/0004-637X/803/1/34 ApJ, http://adsabs.harvard.edu/abs/2015ApJ...803...34B 803, 34

Bower R. G., Benson A. J., Malbon R., Helly J. C., Frenk C. S., Baugh C. M., Cole S., Lacey C. G., 2006, http://dx.doi.org/10.1111/j.1365-2966.2006.10519.x MNRAS, https://ui.adsabs.harvard.edu/abs/2006MNRAS.370..645B 370, 645

Bowler R. A. A., et al., 2014, http://dx.doi.org/10.1093/mnras/stu449 MNRAS, http://adsabs.harvard.edu/abs/2014MNRAS.440.2810B 440, 2810

Bowler R. A. A., et al., 2015, http://dx.doi.org/10.1093/mnras/stv1403 MNRAS, http://adsabs.harvard.edu/abs/2015MNRAS.452.1817B 452, 1817

Boyle B. J., Shanks T., Peterson B. A., 1988, http://dx.doi.org/10.1093/mnras/235.3.935 MNRAS, http://adsabs.harvard.edu/abs/1988MNRAS.235..935B 235, 935

Boyle B. J., Shanks T., Croom S. M., Smith R. J., Miller L., Loaring N., Heymans C., 2000, http://dx.doi.org/10.1046/j.1365-8711.2000.03730.x MNRAS, http://adsabs.harvard.edu/abs/2000MNRAS.317.1014B 317, 1014

Briggs D. S., 1995, in American Astronomical Society Meeting Abstracts. p. 1444

Calistro Rivera G., et al., 2017, http://dx.doi.org/10.1093/mnras/stx1040 MNRAS, http://adsabs.harvard.edu/abs/2017MNRAS.469.3468C 469, 3468

Cappellari M., et al., 2011, http://dx.doi.org/10.1111/j.1365-2966.2010.18174.x MNRAS, https://ui.adsabs.harvard.edu/abs/2011MNRAS.413..813C 413, 813

Caproni A., Mosquera Cuesta H. J., Abraham Z., 2004, http://dx.doi.org/10.1086/426863 , https://ui.adsabs.harvard.edu/abs/2004ApJ...616L..99C 616, L99

Carilli C. L., Perley R. A., Dreher J. W., Leahy J. P., 1991, http://dx.doi.org/10.1086/170813 ApJ, http://adsabs.harvard.edu/abs/1991ApJ...383..554C 383, 554

Chiang J., Mukherjee R., 1998, http://dx.doi.org/10.1086/305403 ApJ, http://adsabs.harvard.edu/abs/1998ApJ...496..752C 496, 752

Cirasuolo M., et al., 2014, MOONS: the Multi-Object Optical and Near-infrared Spectrograph for the VLT. p. 91470N, http://dx.doi.org/10.1117/12.2056012 doi:10.1117/12.2056012

Clark B. G., 1980, A&A, http://adsabs.harvard.edu/abs/1980A

Clewley L., Jarvis M. J., 2004, http://dx.doi.org/10.1111/j.1365-2966.2004.07981.x MNRAS, http://adsabs.harvard.edu/abs/2004MNRAS.352..909C 352, 909

Cohen A. S., Lane W. M., Cotton W. D., Kassim N. E., Lazio T. J. W., Perley R. A., Condon J. J., Erickson W. C., 2007, http://dx.doi.org/10.1086/520719 AJ, https://ui.adsabs.harvard.edu/abs/2007AJ....134.1245C 134, 1245

Condon J. J., 1989, http://dx.doi.org/10.1086/167176 ApJ, http://adsabs.harvard.edu/abs/1989ApJ...338...13C 338, 13

Condon J. J., 1992, http://dx.doi.org/10.1146/annurev.aa.30.090192.003043 ARA&A, http://adsabs.harvard.edu/abs/1992ARA

Condon J. J., Cotton W. D., Greisen E. W., Yin Q. F., Perley R. A., Taylor G. B., Broderick J. J., 1998, http://dx.doi.org/10.1086/300337 AJ, https://ui.adsabs.harvard.edu/abs/1998AJ....115.1693C 115, 1693

Conselice C. J., 2014, http://dx.doi.org/10.1146/annurev-astro-081913-040037 ARA&A, http://adsabs.harvard.edu/abs/2014ARA

Conway J. E., Cornwell T. J., Wilkinson P. N., 1990, MNRAS, http://adsabs.harvard.edu/abs/1990MNRAS.246..490C 246, 490

Cornwell T. J., 2008, http://dx.doi.org/10.1109/JSTSP.2008.2006388 IEEE Journal of Selected Topics in Signal Processing, http://adsabs.harvard.edu/abs/2008ISTSP...2..793C 2, 793

Cornwell T. J., Golap K., Bhatnagar S., 2008, http://dx.doi.org/10.1109/JSTSP.2008.2005290 IEEE Journal of Selected Topics in Signal Processing, http://adsabs.harvard.edu/abs/2008ISTSP...2..647C 2, 647

Crain R. A., et al., 2015, http://dx.doi.org/10.1093/mnras/stv725 MNRAS, http://adsabs.harvard.edu/abs/2015MNRAS.450.1937C 450, 1937

Croom S. M., Smith R. J., Boyle B. J., Shanks T., Miller L., Outram P. J., Loaring N. S., 2004, http://dx.doi.org/10.1111/j.1365-2966.2004.07619.x MNRAS, http://adsabs.harvard.edu/abs/2004MNRAS.349.1397C 349, 1397

Cuillandre J.-C. J., et al., 2012, in Observatory Operations: Strategies, Processes, and Systems IV. p. 84480M, http://dx.doi.org/10.1117/12.925584 doi:10.1117/12.925584

Davies R. L., Efstathiou G., Fall S. M., Illingworth G., Schechter P. L., 1983, http://dx.doi.org/10.1086/160757 ApJ, https://ui.adsabs.harvard.edu/abs/1983ApJ...266...41D 266, 41

De Breuck C., van Breugel W., Röttgering H. J. A., Miley G., 2000, http://dx.doi.org/10.1051/aas:2000181 , https://ui.adsabs.harvard.edu/abs/2000A

Dekel A., Woo J., 2003, http://dx.doi.org/10.1046/j.1365-8711.2003.06923.x MNRAS, https://ui.adsabs.harvard.edu/abs/2003MNRAS.344.1131D 344, 1131

Delvecchio I., et al., 2017, http://dx.doi.org/10.1051/0004-6361/201629367 A&A, https://ui.adsabs.harvard.edu/abs/2017A

Donoso E., Best P. N., Kauffmann G., 2009, http://dx.doi.org/10.1111/j.1365-2966.2008.14068.x MNRAS, http://adsabs.harvard.edu/abs/2009MNRAS.392..617D 392, 617

Dubois Y., Peirani S., Pichon C., Devriendt J., Gavazzi R., Welker C., Volonteri M., 2016, http://dx.doi.org/10.1093/mnras/stw2265 MNRAS, https://ui.adsabs.harvard.edu/abs/2016MNRAS.463.3948D 463, 3948

Duivenvoorden S., et al., 2016, http://dx.doi.org/10.1093/mnras/stw1466 MNRAS, http://adsabs.harvard.edu/abs/2016MNRAS.462..277D 462, 277

Dunlop J. S., Peacock J. A., 1990, MNRAS, http://adsabs.harvard.edu/abs/1990MNRAS.247...19D 247, 19

Dunlop J. S., et al., 2017, http://dx.doi.org/10.1093/mnras/stw3088 MNRAS, http://adsabs.harvard.edu/abs/2017MNRAS.466..861D 466, 861

Ellis S. C., Jones L. R., 2004, http://dx.doi.org/10.1111/j.1365-2966.2004.07338.x MNRAS, http://adsabs.harvard.edu/abs/2004MNRAS.348..165E 348, 165

Emsellem E., et al., 2007, http://dx.doi.org/10.1111/j.1365-2966.2007.11752.x MNRAS, https://ui.adsabs.harvard.edu/abs/2007MNRAS.379..401E 379, 401

Fabian A. C., Crawford C. S., 1990, MNRAS, https://ui.adsabs.harvard.edu/abs/1990MNRAS.247..439F 247, 439

Fanaroff B. L., Riley J. M., 1974, http://dx.doi.org/10.1093/mnras/167.1.31P MNRAS, http://adsabs.harvard.edu/abs/1974MNRAS.167P..31F 167, 31P

Feretti L., Giovannini G., Govoni F., Murgia M., 2012, http://dx.doi.org/10.1007/s00159-012-0054-z , https://ui.adsabs.harvard.edu/abs/2012A

Finkelstein S. L., et al., 2013, http://dx.doi.org/10.1038/nature12657 , https://ui.adsabs.harvard.edu/abs/2013Natur.502..524F 502, 524

Finkelstein S. L., et al., 2015, http://dx.doi.org/10.1088/0004-637X/810/1/71 ApJ, http://adsabs.harvard.edu/abs/2015ApJ...810...71F 810, 71

Foreman-Mackey D., Hogg D. W., Lang D., Goodman J., 2013, http://dx.doi.org/10.1086/670067 PASP, https://ui.adsabs.harvard.edu/abs/2013PASP..125..306F 125, 306

Gallego J., Zamorano J., Aragon-Salamanca A., Rego M., 1995, http://dx.doi.org/10.1086/309804 , http://adsabs.harvard.edu/abs/1995ApJ...455L...1G 455, L1

Gelman A., Rubin D. B., 1992, http://dx.doi.org/10.1214/ss/1177011136 Statistical Science, https://ui.adsabs.harvard.edu/abs/1992StaSc...7..457G 7, 457

Ghisellini G., 2011, in Aharonian F. A., Hofmann W., Rieger F. M., eds, American Institute of Physics Conference Series Vol. 1381, American Institute of Physics Conference Series. pp 180–198 (http://arxiv.org/abs/1104.0006 arXiv:1104.0006), http://dx.doi.org/10.1063/1.3635832 doi:10.1063/1.3635832

Gilli R., et al., 2009, http://dx.doi.org/10.1051/0004-6361:200810821 A&A, https://ui.adsabs.harvard.edu/abs/2009AA...494...33G 494, 33

Griffin M. J., et al., 2010, http://dx.doi.org/10.1051/0004-6361/201014519 A&A, http://adsabs.harvard.edu/abs/2010A

Gunawardhana M. L. P., et al., 2013, http://dx.doi.org/10.1093/mnras/stt890 MNRAS, http://adsabs.harvard.edu/abs/2013MNRAS.433.2764G 433, 2764

Guzzo L., et al., 2007, http://dx.doi.org/10.1086/516588 ApJS, https://ui.adsabs.harvard.edu/abs/2007ApJS..172..254G 172, 254

Hale C. L., et al., 2019, http://dx.doi.org/10.1051/0004-6361/201833906 A&A, http://adsabs.harvard.edu/abs/2019A

Hales C. A., Chiles Con Pol Collaboration 2014, in Exascale Radio Astronomy.

Hales S. E. G., Baldwin J. E., Warner P. J., 1988, http://dx.doi.org/10.1093/mnras/234.4.919 MNRAS, https://ui.adsabs.harvard.edu/abs/1988MNRAS.234..919H 234, 919

Hales S. E. G., Riley J. M., Waldram E. M., Warner P. J., Baldwin J. E., 2007, http://dx.doi.org/10.1111/j.1365-2966.2007.12392.x MNRAS, https://ui.adsabs.harvard.edu/abs/2007MNRAS.382.1639H 382, 1639

Hales C. A., Murphy T., Curran J. R., Middelberg E., Gaensler B. M., Norris R. P., 2012, http://dx.doi.org/10.1111/j.1365-2966.2012.21373.x MNRAS, http://adsabs.harvard.edu/abs/2012MNRAS.425..979H 425, 979

Hardcastle M. J., Krause M. G. H., 2013, http://dx.doi.org/10.1093/mnras/sts564 MNRAS, http://adsabs.harvard.edu/abs/2013MNRAS.430..174H 430, 174

Harwood J. J., Hardcastle M. J., Croston J. H., Goodger J. L., 2013, http://dx.doi.org/10.1093/mnras/stt1526 MNRAS, https://ui.adsabs.harvard.edu/abs/2013MNRAS.435.3353H 435, 3353

Heckman T. M., 1980, A&A, http://adsabs.harvard.edu/abs/1980A

Helou G., Soifer B. T., Rowan-Robinson M., 1985, http://dx.doi.org/10.1086/184556 , http://adsabs.harvard.edu/abs/1985ApJ...298L...7H 298, L7

Heywood I., Hale C. L., Jarvis M. J., Smirnov O. M., Makhathini S., Sebokolodi M. L. L., in prep.

Hill G. J., Lilly S. J., 1991, http://dx.doi.org/10.1086/169597 ApJ, https://ui.adsabs.harvard.edu/abs/1991ApJ...367....1H 367, 1

Högbom J. A., 1974, , http://adsabs.harvard.edu/abs/1974A

Holland W. S., et al., 1999, http://dx.doi.org/10.1046/j.1365-8711.1999.02111.x MNRAS, http://adsabs.harvard.edu/abs/1999MNRAS.303..659H 303, 659

Hopkins A. M., 2004, http://dx.doi.org/10.1086/424032 ApJ, http://adsabs.harvard.edu/abs/2004ApJ...615..209H 615, 209

Hopkins A. M., Connolly A. J., Szalay A. S., 2000, http://dx.doi.org/10.1086/316857 AJ, http://adsabs.harvard.edu/abs/2000AJ....120.2843H 120, 2843

Hopkins P. F., Richards G. T., Hernquist L., 2007, http://dx.doi.org/10.1086/509629 ApJ, http://adsabs.harvard.edu/abs/2007ApJ...654..731H 654, 731

Hopkins P. F., Kereš D., Oñorbe J., Faucher-Giguère C.-A., Quataert E., Murray N., Bullock J. S., 2014, http://dx.doi.org/10.1093/mnras/stu1738 MNRAS, http://adsabs.harvard.edu/abs/2014MNRAS.445..581H 445, 581

Ilbert O., et al., 2009, http://dx.doi.org/10.1088/0004-637X/690/2/1236 ApJ, https://ui.adsabs.harvard.edu/abs/2009ApJ...690.1236I 690, 1236

Intema H. T., van der Tol S., Cotton W. D., Cohen A. S., van Bemmel I. M., Röttgering H. J. A., 2009, http://dx.doi.org/10.1051/0004-6361/200811094 A&A, http://adsabs.harvard.edu/abs/2009A

Intema H. T., Jagannathan P., Mooley K. P., Frail D. A., 2017, http://dx.doi.org/10.1051/0004-6361/201628536 A&A, https://ui.adsabs.harvard.edu/abs/2017AA...598A..78I 598, A78

Iovino A., et al., 2016, http://dx.doi.org/10.1051/0004-6361/201527673 A&A, https://ui.adsabs.harvard.edu/abs/2016AA...592A..78I 592, A78

Jarvis M. J., McLure R. J., 2002, http://dx.doi.org/10.1046/j.1365-8711.2002.05997.x MNRAS, http://adsabs.harvard.edu/abs/2002MNRAS.336L..38J 336, L38

Jarvis M. J., McLure R. J., 2006, http://dx.doi.org/10.1111/j.1365-2966.2006.10295.x MNRAS, http://adsabs.harvard.edu/abs/2006MNRAS.369..182J 369, 182

Jarvis M. J., Rawlings S., 2000, http://dx.doi.org/10.1046/j.1365-8711.2000.03801.x MNRAS, http://adsabs.harvard.edu/abs/2000MNRAS.319..121J 319, 121

Jarvis M. J., Rawlings S., Willott C. J., Blundell K. M., Eales S., Lacy M., 2001, http://dx.doi.org/10.1046/j.1365-8711.2001.04778.x MNRAS, http://adsabs.harvard.edu/abs/2001MNRAS.327..907J 327, 907

Jarvis M. J., et al., 2010, http://dx.doi.org/10.1111/j.1365-2966.2010.17772.x MNRAS, https://ui.adsabs.harvard.edu/abs/2010MNRAS.409...92J 409, 92

Jarvis M. J., et al., 2013, http://dx.doi.org/10.1093/mnras/sts118 MNRAS, 428, 1281

Jarvis M., et al., 2016, in Proceedings of MeerKAT Science: On the Pathway to the SKA. 25-27 May, 2016 Stellenbosch, South Africa (MeerKAT2016). Online at ¡A href=“href=”¿href=“https://pos.sissa.it/cgi-bin/reader/conf.cgi?confid=277¡/A¿, id.6. p. 6 (http://arxiv.org/abs/1709.01901 arXiv:1709.01901)

Johnston R., Vaccari M., Jarvis M., Smith M., Giovannoli E., Häußler B., Prescott M., 2015, http://dx.doi.org/10.1093/mnras/stv1715 MNRAS, https://ui.adsabs.harvard.edu/abs/2015MNRAS.453.2540J 453, 2540

Kennicutt Jr. R. C., 1998, http://dx.doi.org/10.1146/annurev.astro.36.1.189 ARA&A, 36, 189

Kenyon J. S., Smirnov O. M., Grobler T. L., Perkins S. J., 2018, http://dx.doi.org/10.1093/mnras/sty1221 MNRAS, https://ui.adsabs.harvard.edu/abs/2018MNRAS.478.2399K 478, 2399

Kewley L. J., Groves B., Kauffmann G., Heckman T., 2006, http://dx.doi.org/10.1111/j.1365-2966.2006.10859.x MNRAS, http://adsabs.harvard.edu/abs/2006MNRAS.372..961K 372, 961

Koide S., Shibata K., Kudoh T., 1999, http://dx.doi.org/10.1086/307667 ApJ, https://ui.adsabs.harvard.edu/abs/1999ApJ...522..727K 522, 727

Komissarov S. S., Gubanov A. G., 1994, A&A, http://adsabs.harvard.edu/abs/1994A

Kormendy J., Ho L. C., 2013, http://dx.doi.org/10.1146/annurev-astro-082708-101811 ARA&A, http://adsabs.harvard.edu/abs/2013ARA

Kormendy J., Kennicutt Jr. R. C., 2004, http://dx.doi.org/10.1146/annurev.astro.42.053102.13402 ARA&A, http://adsabs.harvard.edu/abs/2004ARA

Korobkin O., Rosswog S., Arcones A., Winteler C., 2012, http://dx.doi.org/10.1111/j.1365-2966.2012.21859.x MNRAS, https://ui.adsabs.harvard.edu/abs/2012MNRAS.426.1940K 426, 1940

Kotilainen J. K., Hyvönen T., Reunanen J., Ivanov V. D., 2012, http://dx.doi.org/10.1111/j.1365-2966.2012.21425.x MNRAS, https://ui.adsabs.harvard.edu/abs/2012MNRAS.425.1057K 425, 1057

Laigle C., et al., 2016, http://dx.doi.org/10.3847/0067-0049/224/2/24 ApJS, https://ui.adsabs.harvard.edu/abs/2016ApJS..224...24L 224, 24

Lake S. E., Wright E. L., Tsai C.-W., Lam A., 2017, http://dx.doi.org/10.3847/1538-3881/aa643a AJ, 153, 189

Landt H., Padovani P., Perlman E. S., Giommi P., 2004, http://dx.doi.org/10.1111/j.1365-2966.2004.07750.x MNRAS, http://adsabs.harvard.edu/abs/2004MNRAS.351...83L 351, 83

Le Floc'h E., et al., 2005, http://dx.doi.org/10.1086/432789 ApJ, http://adsabs.harvard.edu/abs/2005ApJ...632..169L 632, 169

Lilly S. J., Le Fevre O., Hammer F., Crampton D., 1996, http://dx.doi.org/10.1086/309975 , http://adsabs.harvard.edu/abs/1996ApJ...460L...1L 460, L1

Lindroos L., Knudsen K. K., Stanley F., Muxlow T. W. B., Beswick R. J., Conway J., Radcliffe J. F., Wrigley N., 2018, http://dx.doi.org/10.1093/mnras/sty426 MNRAS, https://ui.adsabs.harvard.edu/abs/2018MNRAS.476.3544L 476, 3544

Liu G., Zakamska N. L., Greene J. E., Nesvadba N. P. H., Liu X., 2013, http://dx.doi.org/10.1093/mnras/stt1755 MNRAS, http://adsabs.harvard.edu/abs/2013MNRAS.436.2576L 436, 2576

Lonsdale C. J., 2005, in Kassim N., Perez M., Junor W., Henning P., eds, Astronomical Society of the Pacific Conference Series Vol. 345, From Clark Lake to the Long Wavelength Array: Bill Erickson's Radio Science. p. 399

Lu J., 1991, Chinese Science Bulletin, https://ui.adsabs.harvard.edu/abs/1991ChSBu..36.1580L 36, 1580

Machalski J., Godlowski W., 2000, A&A, http://adsabs.harvard.edu/abs/2000A

Madau P., Dickinson M., 2014, http://dx.doi.org/10.1146/annurev-astro-081811-125615 ARA&A, http://adsabs.harvard.edu/abs/2014ARA

Marshall H. L., Tananbaum H., Avni Y., Zamorani G., 1983, http://dx.doi.org/10.1086/161016 ApJ, http://adsabs.harvard.edu/abs/1983ApJ...269...35M 269, 35

Martini P., Weinberg D. H., 2001, http://dx.doi.org/10.1086/318331 ApJ, https://ui.adsabs.harvard.edu/abs/2001ApJ...547...12M 547, 12

Masters K. L., et al., 2010, http://dx.doi.org/10.1111/j.1365-2966.2010.16503.x MNRAS, http://adsabs.harvard.edu/abs/2010MNRAS.405..783M 405, 783

Matthews T. A., Sandage A. R., 1963, http://dx.doi.org/10.1086/147615 ApJ, https://ui.adsabs.harvard.edu/abs/1963ApJ...138...30M 138, 30

Mauch T., Sadler E. M., 2007, http://dx.doi.org/10.1111/j.1365-2966.2006.11353.x MNRAS, http://adsabs.harvard.edu/abs/2007MNRAS.375..931M 375, 931

Mauch T., Murphy T., Buttery H. J., Curran J., Hunstead R. W., Piestrzynski B., Robertson J. G., Sadler E. M., 2003, http://dx.doi.org/10.1046/j.1365-8711.2003.06605.x MNRAS, https://ui.adsabs.harvard.edu/abs/2003MNRAS.342.1117M 342, 1117

Mauch T., Klöckner H.-R., Rawlings S., Jarvis M., Hardcastle M. J., Obreschkow D., Saikia D. J., Thompson M. A., 2013, http://dx.doi.org/10.1093/mnras/stt1323 MNRAS, https://ui.adsabs.harvard.edu/abs/2013MNRAS.435..650M 435, 650

McAlpine K., Jarvis M. J., 2011, http://dx.doi.org/10.1111/j.1365-2966.2010.18191.x MNRAS, http://adsabs.harvard.edu/abs/2011MNRAS.413.1054M 413, 1054

McAlpine K., Smith D. J. B., Jarvis M. J., Bonfield D. G., Fleuren S., 2012, http://dx.doi.org/10.1111/j.1365-2966.2012.20715.x MNRAS, https://ui.adsabs.harvard.edu/abs/2012MNRAS.423..132M 423, 132

McAlpine K., Jarvis M. J., Bonfield D. G., 2013, http://dx.doi.org/10.1093/mnras/stt1638 MNRAS, 436, 1084

McCracken H. J., et al., 2012, http://dx.doi.org/10.1051/0004-6361/201219507 A&A, https://ui.adsabs.harvard.edu/abs/2012A

McLure R. J., Jarvis M. J., 2004, http://dx.doi.org/10.1111/j.1365-2966.2004.08305.x MNRAS, https://ui.adsabs.harvard.edu/abs/2004MNRAS.353L..45M 353, L45

McLure R. J., Cirasuolo M., Dunlop J. S., Foucaud S., Almaini O., 2009, http://dx.doi.org/10.1111/j.1365-2966.2009.14677.x MNRAS, http://adsabs.harvard.edu/abs/2009MNRAS.395.2196M 395, 2196

McMullin J. P., Waters B., Schiebel D., Young W., Golap K., 2007, in Shaw R. A., Hill F., Bell D. J., eds, Astronomical Society of the Pacific Conference Series Vol. 376, Astronomical Data Analysis Software and Systems XVI. p. 127

Meneses-Goytia S., Peletier R. F., Trager S. C., Vazdekis A., 2015, http://dx.doi.org/10.1051/0004-6361/201423838 A&A, https://ui.adsabs.harvard.edu/abs/2015AA...582A..97M 582, A97

Mitchell K. J., Condon J. J., 1985, http://dx.doi.org/10.1086/113899 AJ, https://ui.adsabs.harvard.edu/abs/1985AJ.....90.1957M 90, 1957

Miyaji T., Hasinger G., Schmidt M., 2000, A&A, http://adsabs.harvard.edu/abs/2000A

Miyazaki S., et al., 2006, in Society of Photo-Optical Instrumentation Engineers (SPIE) Conference Series. p. 62690B, http://dx.doi.org/10.1117/12.672739 doi:10.1117/12.672739

Moe M., Arav N., Bautista M. A., Korista K. T., 2009, http://dx.doi.org/10.1088/0004-637X/706/1/525 ApJ, http://adsabs.harvard.edu/abs/2009ApJ...706..525M 706, 525

Mohan N., Rafferty D., 2015, PyBDSF: Python Blob Detection and Source Finder, Astrophysics Source Code Library (ascl:1502.007)

Molina M., Eracleous M., Barth A. J., Maoz D., Runnoe J. C., Ho L. C., Shields J. C., Walsh J. L., 2018, http://dx.doi.org/10.3847/1538-4357/aad5ed ApJ, http://adsabs.harvard.edu/abs/2018ApJ...864...90M 864, 90

Morabito L. K., Harwood J. J., 2018, http://dx.doi.org/10.1093/mnras/sty2019 MNRAS, http://adsabs.harvard.edu/abs/2018MNRAS.480.2726M 480, 2726

Murgia M., Fanti C., Fanti R., Gregorini L., Klein U., Mack K. H., Vigotti M., 1999, A&A, https://ui.adsabs.harvard.edu/abs/1999AA...345..769M 345, 769

Murphy E. J., 2009, http://dx.doi.org/10.1088/0004-637X/706/1/482 ApJ, http://adsabs.harvard.edu/abs/2009ApJ...706..482M 706, 482

Narayan R., Quataert E., 2005, http://dx.doi.org/10.1126/science.1105746 Science, https://ui.adsabs.harvard.edu/abs/2005Sci...307...77N 307, 77

Natarajan P., Pringle J. E., 1998, http://dx.doi.org/10.1086/311658 , https://ui.adsabs.harvard.edu/abs/1998ApJ...506L..97N 506, L97

Netzer H., 2015, http://dx.doi.org/10.1146/annurev-astro-082214-122302 ARA&A, https://ui.adsabs.harvard.edu/abs/2015ARA

Noeske K. G., et al., 2007, http://dx.doi.org/10.1086/517926 , https://ui.adsabs.harvard.edu/abs/2007ApJ...660L..43N 660, L43

Novak M., et al., 2017, http://dx.doi.org/10.1051/0004-6361/201629436 A&A, 602, A5

Offringa A. R., et al., 2014, http://dx.doi.org/10.1093/mnras/stu1368 MNRAS, http://adsabs.harvard.edu/abs/2014MNRAS.444..606O 444, 606

Oliver S., et al., 2000, http://dx.doi.org/10.1046/j.1365-8711.2000.03550.x MNRAS, http://adsabs.harvard.edu/abs/2000MNRAS.316..749O 316, 749

Orr M. J. L., Browne I. W. A., 1982, http://dx.doi.org/10.1093/mnras/200.4.1067 MNRAS, https://ui.adsabs.harvard.edu/abs/1982MNRAS.200.1067O 200, 1067

Owen F. N., Morrison G. E., Klimek M. D., Greisen E. W., 2009, http://dx.doi.org/10.1088/0004-6256/137/6/4846 AJ, https://ui.adsabs.harvard.edu/abs/2009AJ....137.4846O 137, 4846

Padovani P., Miller N., Kellermann K. I., Mainieri V., Rosati P., Tozzi P., 2011, http://dx.doi.org/10.1088/0004-637X/740/1/20 ApJ, 740, 20

Peacock J. A., 1985, http://dx.doi.org/10.1093/mnras/217.3.601 MNRAS, http://adsabs.harvard.edu/abs/1985MNRAS.217..601P 217, 601

Pedlar A., Ghataure H. S., Davies R. D., Harrison B. A., Perley R., Crane P. C., Unger S. W., 1990, MNRAS, https://ui.adsabs.harvard.edu/abs/1990MNRAS.246..477P 246, 477

Perley R. A., Butler B. J., 2013, http://dx.doi.org/10.1088/0067-0049/204/2/19 ApJS, https://ui.adsabs.harvard.edu/abs/2013ApJS..204...19P 204, 19

Pierre M., et al., 2004, http://dx.doi.org/10.1088/1475-7516/2004/09/011 Journal of Cosmology and Astroparticle Physics, http://adsabs.harvard.edu/abs/2004JCAP...09..011P 9, 011

Pracy M. B., et al., 2016, http://dx.doi.org/10.1093/mnras/stw910 MNRAS, 460, 2

Prescott M., Baldry I. K., James P. A., 2009, http://dx.doi.org/10.1111/j.1365-2966.2009.14859.x MNRAS, http://adsabs.harvard.edu/abs/2009MNRAS.397...90P 397, 90

Prescott M., et al., 2016, http://dx.doi.org/10.1093/mnras/stv3020 MNRAS, 457, 730

Rawlings S., Saunders R., 1991, http://dx.doi.org/10.1038/349138a0 , https://ui.adsabs.harvard.edu/abs/1991Natur.349..138R 349, 138

Read S. C., et al., 2018, http://dx.doi.org/10.1093/mnras/sty2198 MNRAS, https://ui.adsabs.harvard.edu/abs/2018MNRAS.480.5625R 480, 5625

Reddy N., et al., 2012, http://dx.doi.org/10.1088/0004-637X/744/2/154 ApJ, https://ui.adsabs.harvard.edu/abs/2012ApJ...744..154R 744, 154

Rees M. J., 1978, http://dx.doi.org/10.1038/275516a0 , https://ui.adsabs.harvard.edu/abs/1978Natur.275..516R 275, 516

Rees N., 1990, MNRAS, https://ui.adsabs.harvard.edu/abs/1990MNRAS.244..233R 244, 233

Riechers D. A., et al., 2013, http://dx.doi.org/10.1038/nature12050 , http://adsabs.harvard.edu/abs/2013Natur.496..329R 496, 329

Rigby E. E., Argyle J., Best P. N., Rosario D., Röttgering H. J. A., 2015, http://dx.doi.org/10.1051/0004-6361/201526475 A&A, 581, A96

Robotham A. S. G., Davies L. J. M., Driver S. P., Koushan S., Taranu D. S., Casura S., Liske J., 2018, http://dx.doi.org/10.1093/mnras/sty440 MNRAS, http://adsabs.harvard.edu/abs/2018MNRAS.476.3137R 476, 3137

Rodman P. E., et al., 2019, http://dx.doi.org/10.1093/mnras/sty3070 MNRAS, https://ui.adsabs.harvard.edu/abs/2019MNRAS.482.5625R 482, 5625

Roettgering H. J. A., van Ojik R., Miley G. K., Chambers K. C., van Breugel W. J. M., de Koff S., 1997, A&A, https://ui.adsabs.harvard.edu/abs/1997A

Rowan-Robinson M., et al., 2004, http://dx.doi.org/10.1111/j.1365-2966.2004.07868.x MNRAS, http://adsabs.harvard.edu/abs/2004MNRAS.351.1290R 351, 1290

Sadler E. M., et al., 2002, http://dx.doi.org/10.1046/j.1365-8711.2002.04998.x MNRAS, http://adsabs.harvard.edu/abs/2002MNRAS.329..227S 329, 227

Sadler E. M., et al., 2007, http://dx.doi.org/10.1111/j.1365-2966.2007.12231.x MNRAS, http://adsabs.harvard.edu/abs/2007MNRAS.381..211S 381, 211

Sauty C., Tsinganos K., Trussoni E., 2002, Jet Formation and Collimation. p. 41

Saxena A., et al., 2018, http://dx.doi.org/10.1093/mnras/sty1996 MNRAS, https://ui.adsabs.harvard.edu/abs/2018MNRAS.480.2733S 480, 2733

Schawinski K., et al., 2009, http://dx.doi.org/10.1111/j.1365-2966.2009.14793.x MNRAS, http://adsabs.harvard.edu/abs/2009MNRAS.396..818S 396, 818

Schaye J., et al., 2015, http://dx.doi.org/10.1093/mnras/stu2058 MNRAS, https://ui.adsabs.harvard.edu/abs/2015MNRAS.446..521S 446, 521

Schechter P., 1976, http://dx.doi.org/10.1086/154079 ApJ, http://adsabs.harvard.edu/abs/1976ApJ...203..297S 203, 297

Schmidt M., 1968, http://dx.doi.org/10.1086/149446 ApJ, http://adsabs.harvard.edu/abs/1968ApJ...151..393S 151, 393

Schwab F. R., Cotton W. D., 1983, http://dx.doi.org/10.1086/113360 AJ, http://adsabs.harvard.edu/abs/1983AJ.....88..688S 88, 688

Schwarz U. J., 1978, A&A, http://adsabs.harvard.edu/abs/1978A

Scoville N., et al., 2007, http://dx.doi.org/10.1086/516585 ApJS, http://adsabs.harvard.edu/abs/2007ApJS..172....1S 172, 1

Sellwood J. A., 2014, http://dx.doi.org/10.1103/RevModPhys.86.1 Reviews of Modern Physics, http://adsabs.harvard.edu/abs/2014RvMP...86....1S 86, 1

Sellwood J. A., Binney J. J., 2002, http://dx.doi.org/10.1046/j.1365-8711.2002.05806.x MNRAS, http://adsabs.harvard.edu/abs/2002MNRAS.336..785S 336, 785

Shannon C. E., 1949, http://dx.doi.org/10.1109/JPROC.1998.659497 IEEE Proceedings, http://adsabs.harvard.edu/abs/1949IEEEP..37...10S 37, 10

Shim H., Colbert J., Teplitz H., Henry A., Malkan M., McCarthy P., Yan L., 2009, http://dx.doi.org/10.1088/0004-637X/696/1/785 ApJ, http://adsabs.harvard.edu/abs/2009ApJ...696..785S 696, 785

Shimwell T. W., et al., 2017, http://dx.doi.org/10.1051/0004-6361/201629313 A&A, http://adsabs.harvard.edu/abs/2017A

Sijacki D., Springel V., Di Matteo T., Hernquist L., 2007, http://dx.doi.org/10.1111/j.1365-2966.2007.12153.x MNRAS, https://ui.adsabs.harvard.edu/abs/2007MNRAS.380..877S 380, 877

Simpson C., et al., 2012, http://dx.doi.org/10.1111/j.1365-2966.2012.20529.x MNRAS, http://adsabs.harvard.edu/abs/2012MNRAS.421.3060S 421, 3060

Singh R., et al., 2013, http://dx.doi.org/10.1051/0004-6361/201322062 A&A, http://adsabs.harvard.edu/abs/2013A

Smith D. J. B., et al., 2011, http://dx.doi.org/10.1111/j.1365-2966.2011.18827.x MNRAS, https://ui.adsabs.harvard.edu/abs/2011MNRAS.416..857S 416, 857

Smolčić V., et al., 2009, http://dx.doi.org/10.1088/0004-637X/696/1/24 ApJ, http://adsabs.harvard.edu/abs/2009ApJ...696...24S 696, 24

Smolčić V., et al., 2014, http://dx.doi.org/10.1093/mnras/stu1331 MNRAS, https://ui.adsabs.harvard.edu/abs/2014MNRAS.443.2590S 443, 2590

Smolčić V., et al., 2017a, http://dx.doi.org/10.1051/0004-6361/201628704 A&A, 602, A1

Smolčić V., et al., 2017b, http://dx.doi.org/10.1051/0004-6361/201630223 A&A, https://ui.adsabs.harvard.edu/abs/2017A

Smolčić V., et al., 2017c, http://dx.doi.org/10.1051/0004-6361/201730685 A&A, 602, A6

Snellen I. A. G., Schilizzi R. T., Miley G. K., de Bruyn A. G., Bremer M. N., Röttgering H. J. A., 2000, http://dx.doi.org/10.1046/j.1365-8711.2000.03935.x MNRAS, http://adsabs.harvard.edu/abs/2000MNRAS.319..445S 319, 445

Tadhunter C., 2008, http://dx.doi.org/10.1016/j.newar.2008.06.004 , https://ui.adsabs.harvard.edu/abs/2008NewAR..52..227T 52, 227

Tasse C., et al., 2018, http://dx.doi.org/10.1051/0004-6361/201731474 A&A, http://adsabs.harvard.edu/abs/2018A

Tielens A. G. G. M., 2008, http://dx.doi.org/10.1146/annurev.astro.46.060407.145211 ARA&A, http://adsabs.harvard.edu/abs/2008ARA

Timmes F. X., Woosley S. E., Weaver T. A., 1995, http://dx.doi.org/10.1086/192172 ApJS, https://ui.adsabs.harvard.edu/abs/1995ApJS...98..617T 98, 617

Tran H. D., 2003, http://dx.doi.org/10.1086/345473 ApJ, https://ui.adsabs.harvard.edu/abs/2003ApJ...583..632T 583, 632

Tribble P. C., 1993, http://dx.doi.org/10.1093/mnras/261.1.57 MNRAS, http://adsabs.harvard.edu/abs/1993MNRAS.261...57T 261, 57

Urry C. M., Padovani P., 1995, http://dx.doi.org/10.1086/133630 PASP, http://adsabs.harvard.edu/abs/1995PASP..107..803U 107, 803

Vigotti M., Carballo R., Benn C. R., De Zotti G., Fanti R., Gonzalez Serrano J. I., Mack K.-H., Holt J., 2003, http://dx.doi.org/10.1086/375266 ApJ, http://adsabs.harvard.edu/abs/2003ApJ...591...43V 591, 43

Vogelsberger M., Genel S., Sijacki D., Torrey P., Springel V., Hernquist L., 2013, http://dx.doi.org/10.1093/mnras/stt1789 MNRAS, https://ui.adsabs.harvard.edu/abs/2013MNRAS.436.3031V 436, 3031

Vogelsberger M., et al., 2014, http://dx.doi.org/10.1093/mnras/stu1536 MNRAS, http://adsabs.harvard.edu/abs/2014MNRAS.444.1518V 444, 1518

Weiß A., et al., 2009, http://dx.doi.org/10.1088/0004-637X/707/2/1201 ApJ, http://adsabs.harvard.edu/abs/2009ApJ...707.1201W 707, 1201

Westra E., Geller M. J., Kurtz M. J., Fabricant D. G., Dell'Antonio I., 2010, http://dx.doi.org/10.1088/0004-637X/708/1/534 ApJ, http://adsabs.harvard.edu/abs/2010ApJ...708..534W 708, 534

Whittam I. H., Riley J. M., Green D. A., Jarvis M. J., 2016, http://dx.doi.org/10.1093/mnras/stw1725 MNRAS, https://ui.adsabs.harvard.edu/abs/2016MNRAS.462.2122W 462, 2122

Whittam I. H., Jarvis M. J., Green D. A., Heywood I., Riley J. M., 2017, http://dx.doi.org/10.1093/mnras/stx1564 MNRAS, https://ui.adsabs.harvard.edu/abs/2017MNRAS.471..908W 471, 908

Willott C. J., Rawlings S., Blundell K. M., Lacy M., 1998, http://dx.doi.org/10.1046/j.1365-8711.1998.01946.x MNRAS, http://adsabs.harvard.edu/abs/1998MNRAS.300..625W 300, 625

Willott C. J., Rawlings S., Blundell K. M., Lacy M., Eales S. A., 2001, http://dx.doi.org/10.1046/j.1365-8711.2001.04101.x MNRAS, http://adsabs.harvard.edu/abs/2001MNRAS.322..536W 322, 536

Wills B. J., Browne I. W. A., 1986, http://dx.doi.org/10.1086/163973 ApJ, http://adsabs.harvard.edu/abs/1986ApJ...302...56W 302, 56

Yan R., Blanton M. R., 2012, http://dx.doi.org/10.1088/0004-637X/747/1/61 ApJ, http://adsabs.harvard.edu/abs/2012ApJ...747...61Y 747, 61

Yan L., McCarthy P. J., Freudling W., Teplitz H. I., Malumuth E. M., Weymann R. J., Malkan M. A., 1999, http://dx.doi.org/10.1086/312099 , http://adsabs.harvard.edu/abs/1999ApJ...519L..47Y 519, L47

Yuan Z., Wang J., Zhou M., Mao J., 2016, http://dx.doi.org/10.3847/0004-637X/829/2/95 ApJ, 829, 95

Zernike F., 1938, http://dx.doi.org/10.1016/S0031-8914(38)80203-2 Physica, http://adsabs.harvard.edu/abs/1938Phy.....5..785Z 5, 785

da Cunha E., Charlot S., Elbaz D., 2008, http://dx.doi.org/10.1111/j.1365-2966.2008.13535.x MNRAS, https://ui.adsabs.harvard.edu/abs/2008MNRAS.388.1595D 388, 1595

de Jong T., Klein U., Wielebinski R., Wunderlich E., 1985, A&A, http://adsabs.harvard.edu/abs/1985A

van Breugel W., De Breuck C., Stanford S. A., Stern D., Röttgering H., Miley G., 1999, http://dx.doi.org/10.1086/312080 , https://ui.adsabs.harvard.edu/abs/1999ApJ...518L..61V 518, L61

van Cittert P. H., 1934, http://dx.doi.org/10.1016/S0031-8914(34)90026-4 Physica, http://adsabs.harvard.edu/abs/1934Phy.....1..201V 1, 201

van Weeren R. J., et al., 2016, http://dx.doi.org/10.3847/0067-0049/223/1/2 ApJS, http://adsabs.harvard.edu/abs/2016ApJS..223....2V 223, 2